THERMAL AND HYDRAULIC PERFORMANCE OF FINNED TUBE HEAT EXCHANGERS

THERMAL AND HYDRAULIC PERFORMANCE OF FINNED TUBE HEAT EXCHANGERS

by

SAKSHAM GUPTA, B. Tech

A THESIS SUBMITTED TO THE DEPARTMENT OF MECHANICAL ENGINEERING
AND THE SCHOOL OF GRADUATE STUDIES
OF MCMASTER UNIVERSITY
IN PARTIAL FULFILLMENT OF THE REQUIREMENTS FOR THE DEGREE OF
MASTER OF APPLIED SCIENCE

Master of Applied Science (2020)	McMaster University
Mechanical Engineering	Hamilton, Ontario, Canada

TITLE: Thermal and hydraulic performance of finned tube heat exchangers

AUTHOR: Saksham Gupta

B. Tech (Mechanical Engineering).

National Institute of Technology, Kurukshetra, India

SUPERVISOR: Dr. Chan Y. Ching

NUMBER OF PAGES: 159

Abstract

This study numerically examines the heat transfer and pressure drop performance of finned tube heat exchangers with staggered and inline tube layout for a range of tube pitch. The first part of the thesis considers the case where the heat exchanger is placed in fully ducted airflow. The simulations indicate that the performance reduced considerably for the staggered tube layout with an increase in the tube pitch, but a minimal difference for the inline tube arrangement. The effects of other geometrical parameters like fin pitch and the number of tube rows are then presented. Finally, a correlation for fin and tube heat exchangers with inline tube layout is proposed based on 280 simulations for 70 different configurations. The proposed heat transfer correlation can describe the database within $\pm$8% discrepancy while the friction factor correlation can correlate the dataset within a $\pm$10% discrepancy. The mean deviations for heat transfer and friction factor correlations are 4.3% and 5.4%.

An important factor that influences the performance of flat plate and finned tube heat exchangers is when there is bypass flow around the heat exchanger. The next section of this thesis numerically investigates the partially ducted inline fin and tube heat exchanger with side bypass. The effects of the side clearance and the Reynolds number on the heat transfer and the pressure drop performance of the heat exchanger are presented. The simulations indicate that the heat transfer performance depreciates by more than 25% for infinite side clearance. The study then compares the pressure difference observed for entry, exit and the friction pressure drop with the various correlations available in the literature. Finally, the heat transfer and pressure drop performance for staggered and inline tube layouts are compared.

Keywords: Plain fin and tube heat exchanger; Bypass flow; Partially ducted heat exchanger; heat transfer correlation; friction factor correlation

Acknowledgements

I would first like to express my deepest gratitude to my graduate supervisor, Dr. Chan Y. Ching for providing me with his insightful guidance and help during my whole study. This dissertation would not have been possible without him. I am also grateful to Dr. Dan Ewing, for his consistent help during my complete study. His guidance kept me on track and helped me to achieve the objective efficiently.

I would also like to thank my friends and lab mates at McMaster university to make my school life a beautiful journey to remember. Thanks for their help and discussions throughout my study program. At last, I would like to thank my parents and sister for their constant support to chase my dreams.

Table of Contents

List of Tables

List of Figures

Nomenclature

N	------	The number of tube rows.
P_l	mm	Longitudinal tube Pitch
P_t	mm	Transverse tube Pitch
D_o	mm	Outer tube diameter
D_i	mm	Inner tube diameter
D_c	mm	Fin collar outside diameter
D_h	mm	$4*A_c*L/A_o$, Hydraulic diameter
F_p	mm	Fin pitch
δ_f	mm	Fin Thickness
A	mm^2	Area
A_o	mm^2	Total surface area
A_c	mm^2	Minimal cross-sectional area
A_f	mm^2	Fin surface area
A_{fr}	mm^2	Upstream cross-sectional area
$\boldsymbol{\sigma}$	------	Contraction ratio
$\boldsymbol{\sigma}_{ch}$	------	$(F_p - \delta_f)/F_p$, Contraction ratio- Channel entrance
$\boldsymbol{\sigma}_{tu}$	------	$(P_t - D_o)/P_t$, Contraction ratio- tube entance
$\boldsymbol{\sigma}_{ov}$	------	$\boldsymbol{\sigma}_{tu} * \boldsymbol{\sigma}_{ch}$, Overall contraction ratio for finned tube heat exchanger
C_p	$J\ kg^{-1}\ K^{-l}$	Specific heat at constant pressure
k_a	W/(m-K)	Thermal Conductivity of air
k_f	W/(m-K)	Thermal conductivity of fin
$\boldsymbol{\mu}$	kg/(m-s)	Viscosity
$\boldsymbol{\mu}_t$	kg/(ms)	Turbulent viscosity
v_t	m^2/s	Turbulent kinematic viscosity
v	m^2/s	kinematic viscosity
I	%	Turbulent intensity
${}^{\mu_t}/_{\mu}$	------	Viscosity ratio
$\boldsymbol{\rho}$	kg/m^3	density
$\boldsymbol{\rho}_{in}$	kg/m^3	Density at inlet
$\boldsymbol{\rho}_{out}$	kg/m^3	Density at outlet

Pr	------	Prandtl number
τ_w	Pa	Wall shear stress
S_{ij}	1/s	Strain rate tensor
E	J	Energy
u'	m/s	Fluctuating component of velocity
$\bar{U}$	m/s	Mean velocity component
P'	Pa	Fluctuating pressure component
$\bar{P}$	Pa	Mean pressure component
k	$m^2 \cdot s^{-2}$	Turbulent kinetic energy
ω	1/s	The specific rate of dissipation
t	s	time
Ω	1/s	The absolute value of vorticity
$\boldsymbol{\sigma}_{k1}$, $\boldsymbol{\sigma}_{\omega1}$, $\boldsymbol{\sigma}_{\omega2}$, $\boldsymbol{\beta}_1$, $\boldsymbol{\beta}_2$, $\boldsymbol{\beta}^*$, k_1, a_1	------	Constants of turbulence models
Re_k, Re_{β}, Re_{ω}, α_o, α_o^*	------	Constants of turbulence models
U_{up}	m/s	Inlet velocity
U_{app}	m/s	Approach velocity
U_{max}	m/s	$U_{up}/\boldsymbol{\sigma}_{ov}$, Maximum velocity inside the heat exchanger core
U_X	m/s	
U_Y	m/s	Velocity in the Y direction
U_Z	m/s	Velocity in the Z direction
$\dot{M}_{in}$	Kg/s	Inlet mass flow rate
T	K	Temperature
T_{in}	K	Inlet fluid temperature
T_{out}	K	Fluid outlet temperature
T_{sat}	K	Saturation temperature inside the tubes.
$LMTD$	K	$\frac{(T_{sat}-T_{in})-(T_{sat}-T_{out})}{\ln\left(\frac{(T_{sat}-T_{in})}{(T_{sat}-T_{out})}\right)}$, The logarithmic mean temperature difference
Re	------	Reynolds number
Re_{Dh}	------	$\boldsymbol{\rho}^* U_{max}{}^* D_h/\boldsymbol{\mu}$, Reynolds number based on hydraulic diameter
Re_{Do}	------	$\boldsymbol{\rho}^* U_{max}{}^* D_o/\boldsymbol{\mu}$, Reynolds number based on outer tube diameter

Re_{Dc}	------	$\rho * U_{max} * D_c / \mu$, Reynolds number based on outer tube diameter
G_c	kg/sm^2	mass velocity based on minimum free flow area
h	$W\ m^{-2}\ K^{-l}$	Heat transfer coefficient
Q''	$W\ m^{-2}$	Heat flux
Q	W	Heat flow rate
P	Pa	Pressure
P_{fr}	Pa	The area average pressure value in the front of the heat exchanger, considering 0Pa gauge pressure at the outlet.
P_{in}	Pa	The area average pressure value at the inlet of the heat exchanger, considering 0Pa gauge pressure at the outlet.
P_{out}	Pa	The pressure value at the inlet of the heat exchanger, reference pressure.
P_b	Pa	The average pressure value at the exit of the heat exchanger in the central region, considering 0Pa gauge pressure at the outlet.
P'_b	Pa	The average pressure value at the exit of the heat exchanger in the bypass region, considering 0Pa gauge pressure at the outlet.
ΔP	Pa	Pressure difference
ΔP_T	Pa	The pressure drop between inlet and outlet
ΔP_{ex}	Pa	P_{out}-P_b, The average pressure change after exiting from the heat exchanger core.
$\Delta P'_{ex}$	Pa	P_{out}-$P'_{b,}$ The average pressure change at the exit in the bypass region.
ΔP_{fr}	Pa	P_{fr}-$P_{in,}$ The average pressure rise before entrance in the partially ducted heat exchanger.
ΔP_{ae}	Pa	The pressure rise downstream due to abrupt exit from the heat exchanger core
ΔP_{be}	Pa	The pressure rise at the exit of the heat exchanger to the flow stream (similar to pressure behind blunt bodies)
ΔP_{en}	Pa	The pressure loss due to abrupt entrance.
η	------	Fin efficiency
η_o	------	Surface efficiency

C_p	------	$\frac{P-P_\infty}{0.5\rho {U_\infty}^2}$, Pressure coefficient
Nu	------	*h*Do/k,* Nusselt number
j	------	$\frac{h}{\rho * c_p * U_m} Pr^{2/3}$, The Colburn factor
f	------	Friction factor, eq(3-43)
f_{exp}	------	Friction factor including the abrupt entrance and exit, eq(3-44)
f_1	------	Friction factor including the abrupt entrance, eq(5-7)
K_c	------	Abrupt contraction coefficient
K_{c-ch}	------	Abrupt contraction coefficient for channel entrance
K_{c-tu}	------	Abrupt contraction coefficient for tube entrance
K_e	------	Abrupt expansion coefficient
K_{e-ch}	------	Abrupt expansion coefficient for channel entrance
K_{e-tu}	------	Abrupt expansion coefficient for tube entrance
x, y, z	mm	Cartesian Coordinates

Chapter 1.

Introduction

Electric drive technologies, including electric machines and power electronics, represent a key enabling technology for electric vehicles that may cut back petroleum consumption. However, to penetrate the market, these technologies must support vehicle solutions that are economically justified to an average consumer. As these critical components become smaller and lighter, the heat dissipation rates of power electronics continue to increase due to increasing power densities. This makes thermal management of these devices to maintain the operating temperatures below their design value increasingly challenging. There are several methods for cooling these devices. They include air cooling, liquid cooling, and two-phase cooling systems. In many applications, the heat must be transported to a different location to be rejected to the ambient because of space constraints. One common method of accomplishing this is to mount the power electronics on heat spreader plates and transport the heat through heat pipes/thermosyphons to a heat exchanger for rejection to an ambient. Typically, the component with the highest thermal resistance in this network is the heat exchanger and the limiting factor when designing such thermal management systems. A schematic of such a system used by MERSEN, our industrial partner, is shown in Figure 1-1.

The heat exchangers in such systems are typically air-cooled, operating either under free or forced convection conditions. A common heat exchanger used in such systems is the plate-fin and tube heat exchanger. The heat exchanger performance is typically limited by the airside because of the much lower heat transfer coefficient. Plate-fin and tube heat exchangers are effective cooling solutions to the increasing power demand of the power electronics, where current heat dissipation rates can be around 2-6 kW. Such systems are used in many applications, including electric vehicles, as shown in Figure 1-2. It has high efficiency for a given volume since a large surface area is obtained by attaching the thin plates to the tube walls. They are quite lightweight, compact and have low fabrication cost.

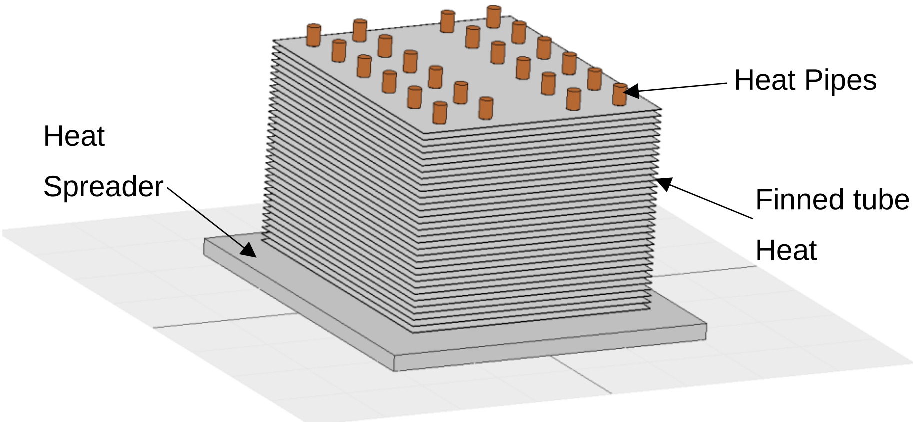

Figure 1-1: The schematic of the thermal management system.

In many applications, the air cooling for the plate-fin and tube heat exchanger is through forced air cooling. The airflow across the tubes and the fin-tube surface can be quite complex and depends on many factors such as the Reynolds number, geometrical parameters such as fin pitch, tube pitch and number of tube rows. In applications such as air conditioning and refrigeration systems, plate-fin and tube heat exchangers with smaller tube pitch ($<2.5D_o$) are typically used. For power electronics cooling, however, flat plate finned tube heat exchangers with larger tube pitch ($>2.5D_o$) are used depending upon the location of heat load on the power electronics surface. Most of the existing heat transfer and pressure drop data, including correlations, have been developed for small tube-pitched heat exchangers. Thus, more comprehensive studies on heat exchangers with large tube pitch are required for the design of heat exchangers typically used for power electronics cooling.

Depending on the application, the heat exchanger can be placed in a fully ducted air-flow or at the other extreme in an open flow, while a more common configuration would be where the heat exchanger is placed in a partially ducted system. Schematics of a fully ducted and partially ducted heat exchanger is shown in Figure 1-3 and Figure 1-4, respectively. When the heat exchanger is placed in a partially ducted system, the performance will be reduced when compared to the fully ducted case as some of the flow bypasses around the heat exchanger. There is a development of high pressure in the front of the heat exchanger and low pressure at the back. Some of the approaching flow circumvents around the heat exchanger due to high pressure in the front and the low pressure at the back helps in the suction of the flow through them.

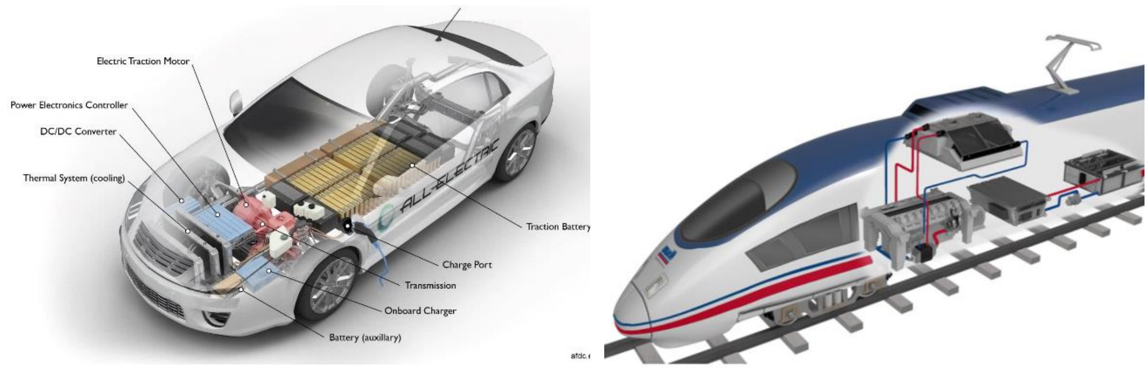

Figure 1-2: Some applications of fin and tube heat exchanger intended for power electronics cooling. (Source: afdc.energy.gov, nissens.com)

The overall objective of this thesis is to model and evaluate the performance of the large-scale heat exchangers used by MERSEN, Canada, in their thermal management systems. The specific objectives are:

(i) Develop computational fluid dynamic simulation methods to analyze large scale, heat exchangers.
(ii) Perform simulations for in-line and staggered heat exchangers under a fully ducted forced convection airflow.
(iii) Develop correlations for predicting the heat transfer for a fully ducted heat exchanger.
(iv) Perform simulations to evaluate the effect of bypass flow on the heat exchanger performance.

This thesis is divided into six chapters that include this introductory chapter. In Chapter 2, a brief review of the literature on plate-fin and tube heat exchangers is presented. The numerical methods are outlined in Chapter 3. The results from the fully ducted case are presented and discussed in Chapter 4. In chapter 5, the effect of the bypass on the heat exchanger is presented, and finally, the conclusion from this study with future recommendations are summarized in Chapter 6.

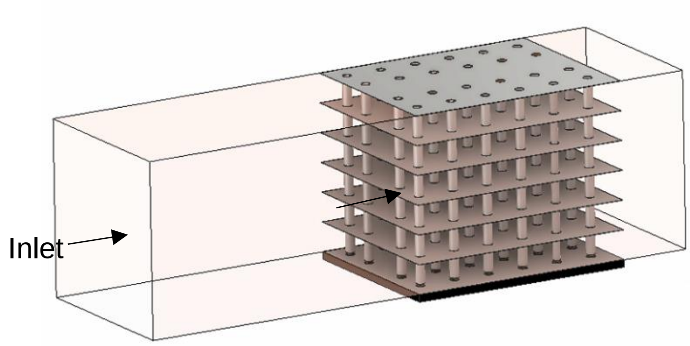

Figure 1-3: Fully ducted heat exchanger.

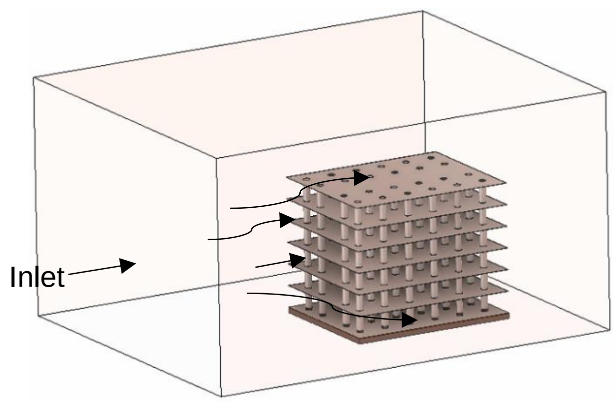

Figure 1-4: Partially ducted heat exchanger.

Chapter 2.

Literature Review

In this chapter, a review of previous work on plain fin and tube heat exchangers is presented. In these heat exchangers, typically hot liquid or gas/vapour flow through the tubes and is cooled by gas (typically air) flowing through the channel formed by flat plates. The tubes are placed in either a staggered or inline layout, as shown in Figure 2-1.

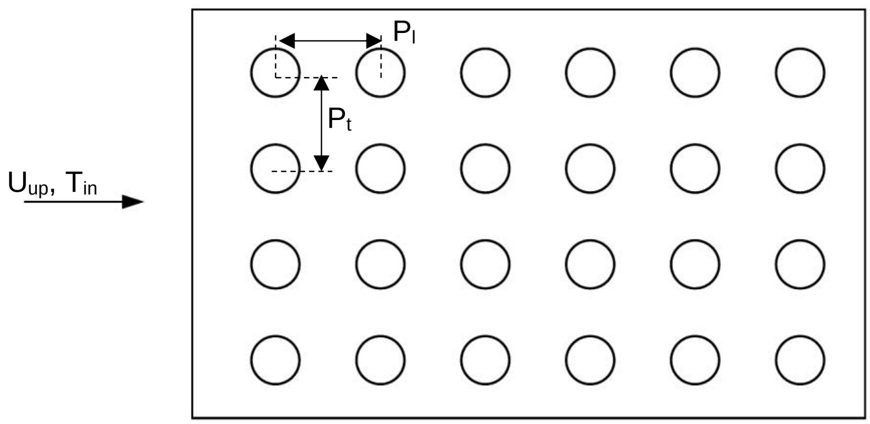

a) Inline tube arrangement

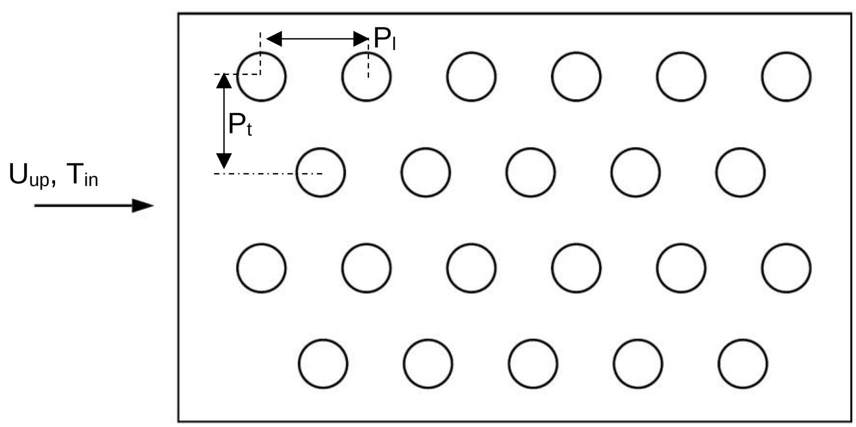

b) Staggered tube arrangement

Figure 2-1: Different tube configurations in the finned tube heat exchanger.

The thermo-hydraulic characteristics of finned tube heat exchangers depend upon many factors such as external velocity, tube diameter, number of tube rows, tube pitch and fin pitch. The heat exchanger performance will also depend on how the airflow is ducted through it. It can be fully ducted where all the airflow is forced through the heat exchanger or partially ducted where there can be bypass flow around the heat exchanger.

There have been several experimental and numerical studies of plate-fin and tube heat exchangers. Most previous work has been focused on the fully ducted plate-fin and tube heat exchangers with a staggered tube arrangement. There are a few studies of the partially ducted system with either plate or tube arrays type heat sinks. However, there is no work on plate-fin and tube heat exchangers for partially ducted systems and very little work on the fully ducted heat exchanger with an inline tube arrangement. This literature review is divided into two main sections; in the first part, the ducted plate-fin and tube heat exchanger is discussed, and in the second part, the case of the partially ducted heat exchanger is reviewed.

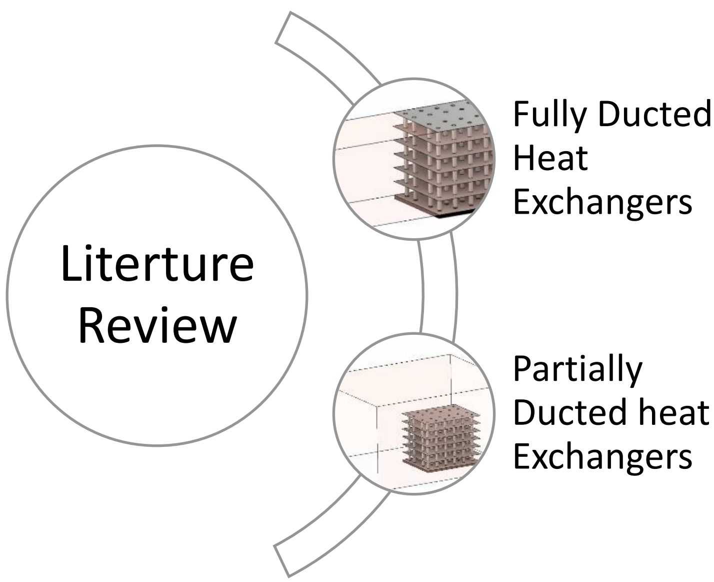

Figure 2-2: Flow chart of literature review.

2.1. Fully Ducted Heat Exchangers

There have been extensive studies on the thermo-hydraulic characteristics of fully ducted fin and tube heat exchangers with a staggered tube arrangement. However, little work exists for the inline tube configuration. Most of the early work was experimental [1-9], but lately, there has been an increasing number of numerical studies [10-13]. McQuiston [1] was the first researcher to experiment on two test samples with a fin pitch of 0.173 & 0.3 diameters with an outer tube diameter of 10.3 mm and an inlet velocity ranging from 0.5-5.9 m/s. Later, Rich [2, 3] concluded from his experimentation on 14 samples that heat transfer is independent of the fin pitch and pressure drop is independent of the number of tube rows. Then, McQuiston [4, 5] established the first and widely known correlation for heat transfer and pressure drop with a deviation of 10% and 35%, respectively, by combing the data of Rich [2, 3] with his data for geometry with a tube diameter of 9.96 mm and fin density from 4-14 respectively. Gray and Webb [6] pointed out the poor accuracy of McQuinston's correlation of the friction factor and proposed a correlation with an RMS difference of 7.3 & 7.8%, respectively. However, the developed correlation is valid only for larger tube diameter with more tube rows. Later, Wang [7, 8, 9] summarized the various parametric effects on the heat exchanger performance and developed correlations for heat transfer and friction factor for a wider range of data with deviations of 7.5 & 8.3%, respectively. The correlation was valid for a staggered geometry with a tube diameter of 6.35 to 12.7mm, fin pitch of 1.19 to 8.7mm, transverse tube pitch of 17.7 to 31.55mm, longitudinal tube pitch of 12.4 to 27.5mm with the tube rows less than 6.

There have been considerable efforts on numerical studies on plain finned tube heat exchangers over the last two decades. Bastani [10] carried out the first computational work on a finned tube bank with an inline arrangement and showed details of the flow field. Jang [11] conducted a numerical study on four-row finned tube banks with tube pitch less than 2.4 diameters and fin pitch less than 0.75 diameters and concluded that the heat transfer coefficient is independent of the number of tube rows if larger than four. They also found out that the heat transfer coefficient and the friction factor for staggered tube arrangement is 15-27% and 20-25%, respectively, higher than the Inline tube arrangement. Bhuiyan [12, 13] conducted numerical studies of inline and staggered tube geometries with tube pitch less than 2.5 diameters and fin pitch less than 0.4 diameters. His results showed a 25-30% higher heat transfer coefficient for the staggered tube arrangement than the inline case but with more than 40% higher friction factor. The major experimental and numerical studies on a flat plate and tube heat exchangers are summarized in Table 2-1.

Table 2-1: Effect of the flow and geometric parameters on the thermal fluid characteristics for the fully ducted heat exchanger.

Experimental study			
Researcher	***Layout***	**Geometrical Parameters**	**Major Findings**
Rich (1973,1975) [3, 2]	Staggered	F_p=1.23-8.7 U_{up}=0.95-21 m/s N=1-6 Do=13.3 P_t=31.8 P_l=27.5 Re_{Do}=1400-32000	• The heat transfer coefficient is essentially independent of the fin spacing. • The pressure drop may be broken into two components, one due to the fin and other due to the tube. • The friction factor is independent of the fin spacing. • The average heat transfer coefficient for the deep coil may be higher or lower than the shallow coil. • The addition of rows downstream has a negligible effect upon heat transfer from upstream rows. • At high Reynolds number, the heat transfer coefficient of the downstream row is higher than the upstream row. • At low Reynolds number, the heat transfer coefficient for the deep coil is substantially lower than the upstream coil. • The unusual trend concerning row depth at low Reynolds number is believed to be due to the influence of stable vortex pattern on the local air temperature distribution within the flow passage.
Chen et al (1988) [14]	Staggered	D_o = 25 F_p = 2.1-12.9 P_t = 60 P_l= 54 N =2 Re_{Pt}=4500-27000	• Flow visualization results to explain the effect of fin pitch • For fin pitch less than 0.33 diameters, heat transfer has no effect of fin pitch for lower Reynolds number. However, it changes significantly with high Re. • For fin pitch greater than 0.33 diameters, no effect of fin spacing on heat transfer at all Reynolds number could be seen.

Wang et al (1996) [7]	Staggered	D_o= 9.97,9.83 F_p = 1.74-3.2 P_t = 25.4 P_l = 22 N = 2-6 V = 0.3-6.5	• The maximum phenomena of Colburn j-factor at low Reynolds numbers occur for plate fin-and-tube heat exchanger at a larger number of tube row and smaller fin spacing. • The experimental data indicate that the number of tube rows does not affect the friction factors. A significant reduction of the heat-transfer coefficients is found for Reynolds number less than 2000 for the six-row coil, and the effect of the number of tube row diminishes for 2000 < Reoc < 7500. • The number of tube rows does not affect the friction factor. • Fin thickness has a negligible effect on both heat transfer and friction characteristics of plate-fin and tube heat exchangers. • Fin spacing has a negligible effect on the heat-transfer.
Wang et al (2000) [8]	Staggered	D_o=7.3,8.28,10 F_p=1.22,1.78,2.23,223,1.23,2.06 P_t = 21, 25.4 P_l=12.7,19.05 N =1-4 Re_{Dc} < 10000	• The effect of fin pitch on the Colburn j factors is negligible for N>4 and ReDc> 2000 owing to the effect of vortex formation along with the fin. The test data indicate that the heat transfer coefficients increase with decrease fin pitch for 300 < Re_{Dc}< 3000 and N=1, 2 • The effect of the tube row on heat transfer performance is especially pronounced at low Reynolds number where the number of tube rows is large, and the fin pitch is small. The effect of the number of tube rows on friction performance is comparatively small. • For Fp=1.2 mm, the effect of tube diameter on the heat transfer coefficients is rather small. However, the pressure drops for Dc = 10:23 mm are 5±15% were observed for Fp=2:2 mm

Jang et al (2002) [15]	Inline, Staggered	D_o = 25.4 F_p=10,15,20 P_t = 60.7,25.4 P_l = 60.7,52.6 N =3 Re_{Dc}=200-2000	• For the in-line arrangement, the shape of the span-averaged heat transfer coefficient on the fin surface along the downstream direction between the transverse tubes is like that of the pipe flow. • The averaged heat transfer coefficient of staggered configuration is 14–32% higher than that of in-lined configuration.
Kim et al (2005) [16]	Inline, Staggered	D_o = 8 F_p = 7.5-15 P_t = 27 P_l = 26 N = 1-4 $\dot{M}_{in}$= 0.8, 1.1, 1.4, 1.7	• For one-row heat exchanger coil, fin pitches had an insignificant influence on the heat transfer coefficient when the fin pitch is large. • However, as tube rows are increased, the heat transfer coefficient was improved with an increase in fin pitches. • For the staggered tube alignment, the heat transfer coefficient was found to be independent of the number of tube rows.
Palez et al(2010)	Staggered	D_o = 10.55 F_p = 2 P_t = 60.7 P_l = 25 N = 2 Re_{Do}=500-5000	• The increase in Re entails the growth of Nu. • Nusselt number increases as fin pitch increases. • An intense dependence of the Nu with the tube diameter is observed. Therefore, a big augmentation of the heat transfer with the tube diameter increases.
Numerical study			
Kundu et al (1991 [17])	Inline single Cylinders between two plates.	F_p/D_o=1.5-10 P_l/D_o= 3 N = 5 Re_{Do} = 50-500	• 2-D Laminar Numerical Simulations • Standing vortices are present between the cylinder in small fin spacing. • With the large tube spacing, the length of the recirculation zone is less than the spacing between the cylinder.
Bastani et al (1992) [10]	Inline	D_o/F_p =3.6 P_t/F_p = 4.5 P_l/F_p = 9	• First 3-d computational work on finned tube bank. • The laminar model is considered.

		N = 2 Re_{Fp} < 2000	• The paper showed the detailed flow field. • Distribution of Nusselt number on the fin surface.
Jang et al (1995) [11]	Staggered and inline	Do = 15.9 Fp = 8-12 Pt = 33 Pl = 38 N =4 Re_{Fp} = 60-900	• The average heat transfer coefficient of the staggered tube arrangement is higher than that of an in-lined array. • The pressure drop of staggered configuration is 20-25% higher than that of in-lined configuration. • The no. of tube row has a minor effect on the heat transfer coefficient as the row numbers are greater than 4.
Sheui et al (1999) [18]	Staggered	Do = 7.5 Fp = 1.4 Pt = 12.75 Pl = 20.4 N =2 Re_{Do} = 83-258	• Fin perforation effect on heat transfer. • There is a trade-off between the benefit of having an improved heat transfer due to the fin perforation and the increase in pressure drop.
Huang et al (2009) [19]	Inline, Staggered	D_o = 25.4 F_p = 10,15 P_t = 60.7 P_l = 60.7, 52.6 N = 3 V = 0.5-1.5	• A three-dimensional inverse heat conduction problem in estimating the local heat transfer coefficients for plate finned tube by utilizing the steepest descent method. • The steepest descent method does not require a priori information for the functional form of the unknown heat transfer coefficients, and the reliable estimations can always be obtained.
Mihir et al (2000) [20]	Staggered	F_p/D_o=0.128-0.240 P_t = 2.12 P_l = 3.1 N =1 V=0.0195-0.1525	• Nusselt number is highest at the leading edge due to the thin boundary layer. • Heat transfer in the wake is slightly increased once the recirculation region opens to the trailing edge and re-entrant fluid comes in.
Tutar et al (2004) [21]	Inline, Staggered	F_p= (0.03-0.365)*Do P_t = 5.37*Do P_l = 2.12*Do	• Higher heat transfer coefficients are obtained on the forward part of the tube, and this can be attributed to the evolution of the horseshoe vortex there.

		N =4 Re_{Do}=600-2000	• For the multirow configuration, the effect of tube row number on the heat transfer coefficient is found to be comparatively small as the tube row numbers are greater than 4. • The peak value of the heat transfer rate occurs at the horseshoe vortex just upstream of the tubes. • The average heat transfer coefficient and pressure drop increase as the Reynolds number is increased, and both are found to be higher for the staggered arrangement than for the in-line arrangement.
Bhuiyan et al (2011) [12]	Inline, Staggered	F_p = 2.53-3.53 Pt = 25.4-30.4 Pl = 19.05-28.575 N = 4 Re_H = 400-1200	• Heat transfer and pressure drop are decreased with an increase in Pl as the flow becomes free and less compact with the increase in the tube pitch. • Heat transfer and pressure drop are also decreased with an increase in Pt. • The effect of fin pitch (Fp) on the heat exchanger performance demonstrates that a decrease in the fin pitch shows opposite performance as the longitudinal and transverse pitches.
Tala et al(2012) [22]	Staggered	D_o =7 F_p = 0.234* Do P_t = 2.134*Do P_l = 1.634*Do N = 2 V = 2.35, 4.70	• The tube shape has a significant effect on the flow topology. • The iso-sectional tube modification increases the thermal-hydraulic performances of the modified heat exchanger tube shape up to 80% when compared to classical circular-shaped finned-tube heat exchangers. • The iso-sectional tube modification reduces the thermal and viscous irreversibility occurring in the modified heat exchanger tube shape, respectively, down to 15% and 50% when compared to classical circular-shaped fin-and-tube heat exchangers.

Bhuiyan et al(2014) [13]	Inline, Staggered	D_o =9.525 F_p = 3.530 P_t = 25.40 P_l = 19.05 N = 4 Re_H = 2000--7000	• Heat transfer and pressure drop are decreased with an increase in Pl as the flow becomes free and less compact with the increase in the tube pitch. • The effects of the longitudinal pitch with the increase in the transverse pitch there is a decrease in heat transfer and pressure drop performance. • The effect of fin pitch on the heat exchanger performance demonstrates that the decrease in the fin pitch shows opposite performance to the longitudinal and transverse pitches.

2.1.1. Correlations

The Colburn j-factor is normally used as a dimensionless parameter for heat transfer and the friction factor is used for friction pressure drop which can be defined as follows.

$$j = \frac{h}{\rho * c_p * U_m} Pr^{2/3} \tag{2-1}$$

$$f_{exp} = \frac{A_c}{A_o} * \frac{\rho_m}{\rho_{in}} [\frac{2\rho_{in}\Delta P_T}{G_c^2} - 2\left(\frac{\rho_{in}}{\rho_{out}} - 1\right)] \tag{2-2}$$

The entry and exit pressure drop is usually lumped into the total pressure drop in the definition of the friction factor. Several correlations have been developed for the heat transfer and pressure drop in plain fin and tube heat exchangers. Colburn [23] suggested a simple correlation between flow and heat transfer for tube banks as follows.

$$Nu = 0.33 * Re_{DO}^{0.6} * (Pr)^{(\frac{1}{3})} \tag{2-3}$$

However, for the plate-fin and tube heat exchanger, Rich [3] showed that the heat transfer and pressure drop depended on the geometrical parameters. McQuiston [5] developed the first known correlation for Colburn j-factor and friction factor for a finned tube heat exchanger which has a dependence on geometrical parameters and Reynolds number and agreed to within +/- 35% with other experimental results. Since then, there has been a considerable effort to develop correlations for heat transfer and frictional characteristics of plain fin and tube heat exchanger. Table 2-2 summarizes the most important correlations developed to date.

Table 2-2: Correlation with the condition and geometrical parameter.

Researcher	**Layout**	**Geometrical Parameters**	**Correlation**
McQuinston (1978) [5]	Staggered Layout	D_o = 9.96 F_p = 1.81-6.35 P_t = 25.4 P_l = 22 N = 4 V = 0.5-4	$\frac{j_N}{j_4} = \frac{1-1280 * N * Re_{Pl}^{-1.2}}{1-5120 * Re_{Pl}^{-1.2}}$ $j_4 = 0.0014 + 0.2618 * Re_{Dc}^{-0.4} * (\frac{A_O}{A_t})^{-0.15}$ $f_{exp} = 0.004094 + 1.382 * Re_{Dc}^{-0.4} * (\frac{P_t - D_c}{4 * F_s})^{-0.8} * (\frac{P_t}{D} - 1)^{-0.8} * (\frac{D_c}{D^*})^{0.5}$ $\frac{D^*}{D_C} = \left(\frac{A_O}{A_t}\right) * \left(\frac{F_p}{P_{t-}D_{c+}F_p}\right)$ **Validity Range**: - Geometry Specification
Gray and Webb (1986) [6]	Staggered Layout		$\frac{j_N}{j_4} = 0.991 * (2.24 * Re_{Dc}^{-0.092} * (\frac{N}{4})^{-0.031})^{0.607*(4-N)}$ $f_{exp} = f_f * \left(\frac{A_f}{A_O}\right) + f_t * \left(1 - \frac{A_f}{A_O}\right) * \left(1 - \frac{\delta_f}{F_P}\right)$ $j_4 = 0.014 * (Re_{Dc}^{-0.328}) * (\frac{P_t}{P_l})^{-0.15} * (\frac{F_s}{D_c})^{0.031}$ $f_f = 0.508 * (Re_{Dc}^{-0.521}) * (\frac{P_t}{D_C})^{1.318}$ **Validity Range**: - Geometry Specification
Kayansayan (1993)	Staggered Layout	D_o = 9.52, 12.5,16.3 F_p = 2.34-4.34	$j_4 = 0.014 * (Re_{Dc}^{-0.28}) * (\frac{A_O}{A_T})^{-0.362}$

		P_t = 25.4,30,31.8,40 P_l = 22,26,32,34.7 N = 4 V = 0.5-10	Note: - No frictional Correlation **Validity Range**: - Geometry Specification
Wang et al (1996a) [7]	Staggered Layout	D_o = 9.97,9.83 F_p = 1.74-3.2 P_t = 25.4 P_l = 22 N = 2-6 V = 0.3-6.5	$j = 0.394 * (Re_{Dc}^{-0.392}) * (\frac{F_P}{D_c})^{-0.212} * (\frac{\delta_f}{D_c})^{-0.0449} * N^{-0.0897}$ $f_{exp} = 1.039 * (Re_{Dc}^{-0.418}) * (\frac{F_P}{D_c})^{-0.197} * (\frac{\delta_f}{D_c})^{-0.104} * N^{-0.0935}$ **Validity Range**: - Geometry Specification
Wang et al (2000a,2000b) [8] [9]	Staggered Layout	D_o = 7.3,8.28,10 F_p = 1.21-2.06 P_t = 21.4,25.4 P_l = 12.7, 19.05 N = 1-4 V = 0.3-6.5	For N=1 $j = 0.108 * (Re_{Dc}^{-0.29}) * (\frac{F_P}{D_c})^{-1.084} * (\frac{F_P}{D_h})^{-0.786} * (\frac{P_t}{P_l})^{P1} * (\frac{F_p}{P_l})^{P2}$ $P1 = 1.9 - 0.23 * Ln(Re_{Dc}^{1})$ $P2 = -0.236 + 0.126 * Ln(Re_{Dc}^{1})$ For N=2 $j = 0.086 * (Re_{Dc}^{P3}) * (\frac{F_P}{D_c})^{P5} * (\frac{F_P}{D_h})^{P6} * (\frac{F_P}{P_l})^{-0.93} * N^{P4}$ $P3 = -0.361 - \frac{0.042*N}{Ln(Re_{Dc}^{1})} + 0.158 * Ln(N * (\frac{F_P}{D_c})^{0.41})$ $P4 = -1.224 - \frac{0.076 * (\frac{P_1}{D_h})^{1.42}}{Ln(Re_{Dc}^{1})}$ $P5 = -0.083 + \frac{0.058 * N}{Ln(Re_{Dc}^{1})}$ $P6 = -5.735 + 1.211 * Ln(\frac{Re_{Dc}^{1}}{D_h})$

			$f_{exp} = 0.108 * (Re_{Dc}^{F1}) * (\frac{F_P}{D_c})^{F3} * (\frac{P_t}{P_l})^{F2}$ F1= $-0.764* 0.739*\frac{P_t}{P_l} + 0.177*\frac{F_P}{D_c} * \frac{0.00758}{N}$ $F2 = -15.689 + \frac{64.021}{Ln(Re_{Dc}^1)}$ $F3 = 1.696 + \frac{15.695}{Ln(Re_{Dc}^1)}$ **Validity Range**: - N = 1-6 D_o = 6.35 -12.7 mm F_p = 1.19 -8.7 mm P_t = 17.7 – 31.75mm P_l = 12.4 – 27.5mm
Bacellar et al (2014) [24]	Staggered Layout	D_o = 2.0-5.0 F_p = 0.3175 - 3 P_t = 3-15 P_l = 3-15 N = 2-10 V = 0.5-7.0	$j = 0.147 * (Re_{DO}^{J1}) * N_t^{J2} * (\frac{P_t}{D_o})^{J4} * (\frac{P_l}{D_o})^{J3} * (\frac{P_l}{P_t})^{-0.28}$ $J1 = -0.38 - \frac{0.043*N}{Ln(Re_{Dc}^1)} + 0.28 * Ln(N * (\frac{F_P}{D_c})^{0.447})$ $J2 = -2.52 - \frac{5.296 * (\frac{P_1}{D_h})^{-0.22}}{Ln(Re_{Dc}^1)}$ $J3 = -1.00 + \frac{0.30 * N}{Ln(Re_{Dc}^1)}$ $J4 = 2.085 - 0.274 * Ln(\frac{Re_{Dc}^1}{D_h})$ $f_{exp} = 1.171 * (Re_{Dc}^{F1}) * (\frac{F_P}{D_c})^{F3} * (\frac{F_P}{D_O})^{F4} * (\frac{F_P}{P_l})^{-0.929} * N_t^{F2}$ $F1 = -0.22 - \frac{0.04*N}{Ln(Re_{Dc}^1)} + 0.04 * Ln(N * (\frac{F_P}{D_c})^{0.0043})$ $F2 = -4.91 - \frac{0.626 * (\frac{P_1}{D_h})^{1.317}}{Ln(Re_{Dc}^1)}$

			$F3 = 0.27 + \frac{-2.429*N}{Ln(Re_{Dc}^{1})}$ $F4 = 0.97 + 0.10375 * Ln(\frac{Re_{Dc}^{1}}{D_h})$ **Validity Range**: - Geometry Specification
Kim et al (2005) [16]	Staggered, Inline Layout	D_o = 8 F_p = 7.5-15 P_t = 27 P_l = 26 N = 1-4 $\dot{M}_{in}$ = 0.8, 1.1, 1.4, 1.7	$j = 0.170 * (Re_{Dh}^{-0.349}) * N_1^{-0.141} * (\frac{F_P}{D_o})^{0.384}$ **Validity Range**: - Geometry Specification; [Re = 600-2000]
Jacimovic et al (2006) [25]	Staggered Layout	D_o = 12 F_p = 1.475-6.207 P_t = 30 P_l = 30 N = 12 V = 0.5-7.0	$f_{exp} = (0.52 + \frac{180}{Re_{D1}^{0.85}}) * (W^{-0.7}) * R_d^{0.65}$ W=ratio of heat transfer area of a row of tubes to the frontal free flow area R_d = ratio of diagonal free cross-sectional area to the frontal free cross-sectional area D1=$\frac{\text{Free heat exchanger volume}}{\text{Area side heat transfer Surface}} = \frac{V_f}{S_{HE}}$
Xie et al (2008) [26]	Staggered Layout	D_o = 16-20 F_p = 2-4 P_t = 38-46 P_l = 32-36 N =3 V = 0.67-4	$Nu = 1.565 * (Re_{Dc}^{0.3414}) * (N * \frac{F_P}{D_o})^{-0.165} * (\frac{P_t}{P_l})^{0.0558}$ $f_{exp} = 20.713 * (Re_{Dc}^{0.3489}) * \left(N * \frac{F_P}{D_o}\right)^{-0.1676} * (\frac{P_t}{P_l})^{0.6265}$ **Validity Range**: - Geometry Specification
Chen et al (1988) [27]	Staggered Layout	D_o = 25 F_p = 2.1-12.9 P_t = 60 P_l =54 N =2	$Nu = 1.565 * (Re_{Pt}^{0.68}) * (Pr)^{0.4}$ **Validity Range**: - Geometry Specification

		Re = 4500-27000	
Kim et al (1999) [28]	Staggered Layout	N>=3 (j-correlation) Re_{Do} = 505-24707 P_t/P_l = 0.857-1.654 P_t/D_o=1.996-2.881 F_p/D_o =0.081-0.641 N<3(j-correlation) Re_{Do} = 591-14430 P_t/P_l = 1.154-1.654 P_t/D_o=2.399-2.877 F_p/D_o =0.135-0.300 Frictional Correlation Re_{Do} = 505-19766 P_t/P_l = 0.857-1.654 P_t/D_o=1.966-2.876 F_p/D_o =0.081-0.641	$j_{N=3} = 0.163 * (Re_D^{-0.369}) * (\frac{F_P}{D_o})^{0.0138} * (\frac{P_t}{P_l})^{0.106} * (\frac{P_t}{D_O})^{0.13}$ $\frac{j(N=3)}{j(N=1,2)} = 1.043 * [(Re_D^{0.14}) * (\frac{F_P}{D_o})^{-0.123} * (\frac{P_t}{P_l})^{0.564} * \left(\frac{P_t}{D_O}\right)^{1.17}\Big] \,\hat{}\,(3 - N$ $f_{exp} = 1.455 * (Re_D^{-0.656}) * (\frac{F_P}{D_o})^{-0.134} * (\frac{P_t}{P_l})^{-0.347} * (\frac{P_t}{D_O})^{1.23}$ Note: - Correlation is provided based on data from various sources.

2.1.2. Heat exchanger pressure drop

In the application of friction factor data for surfaces, it is generally assumed that the total pressure drop of the flow is completely within the matrix. In reality, the flow experiences abrupt contractions at entry and expansions at the exit to the core, as seen in Figure 2-3. These give rise to a net increase in pressure drop.

The entrance pressure drop is made up of two parts. The first is due to the area change at the entrance without considering the friction. The second is the pressure change due to irreversible free expansion, which arise from the boundary layer separation (Vena Contracta), and the consequent pressure change due to change in momentum rate associated with the change of velocity profile downstream from vena contracta. The entrance pressure drop is expressed as [29]

$$\frac{\Delta P_{en}}{\rho} = \frac{V^2}{2g_c}(1-\sigma^2) + K_c\frac{V^2}{2g_c} \qquad \text{2-4}$$

where V is the velocity in the heat exchanger core, and σ is the frontal area ratio. The irreversible component of the pressure drop is contained in the abrupt contraction coefficient $\boldsymbol{K_c}$.

Similarly, the exit pressure drop is divided into two components. The first is the pressure rise, which would occur due to area change alone, without friction and is identical to the corresponding term in entrance pressure drop. The second is the pressure loss associated with the irreversible free expansion and momentum change following an abrupt expansion. Thus,

$$\frac{\Delta P_{ex}}{\rho} = \frac{V^2}{2g_c}(1-\sigma^2) - K_e\frac{V^2}{2g_c} \qquad \text{2-5}$$

where, K_e is the abrupt expansion or exit effects. K_c and K_e are a function of the contraction, the expansion geometry and Reynolds number. The contraction and expansion loss coefficients Kc and Ke are given graphically [29] for parallel plates, and circular tubes and shown in Figure 2-4 and Figure 2-5. Thus, the total pressure drop can be expressed as[29]

$$\frac{\Delta P_T}{p} = \{(1-\sigma^2+K_c) + 2\left(\frac{\rho_2}{\rho_1}-1\right) + f\frac{A_o}{A_c}\frac{\rho_m}{\rho_1} - (1-\sigma^2-K_e)\}\frac{G^2}{2p_1\rho_1} \qquad \text{2-6}$$

The above pressure drop equation includes the pressure drop due to flow acceleration and the core friction pressure drop. Also, the friction factor considers the effect of entrance and exit pressure drop separately, unlike equation (2-2) considered in the most previous work.

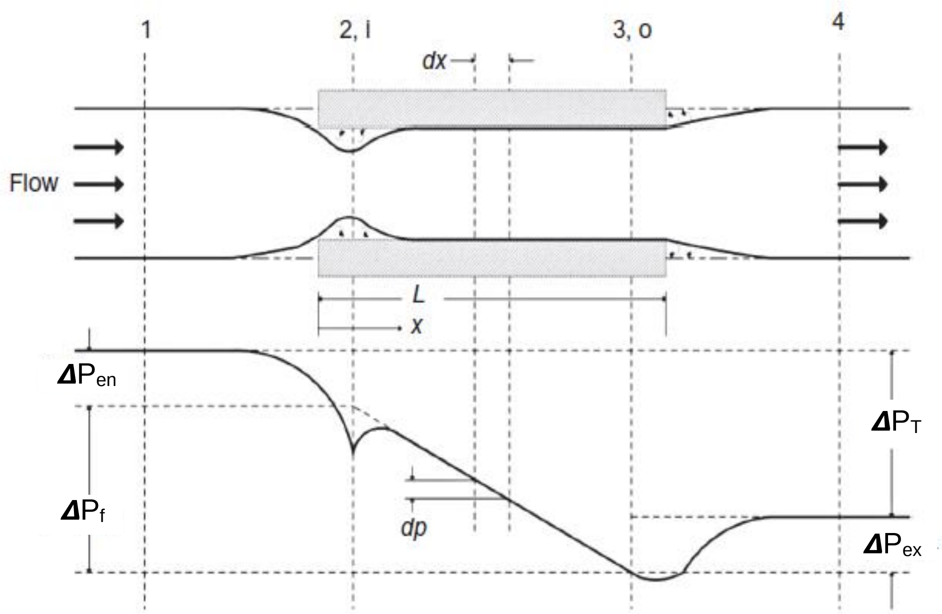

Figure 2-3: The pressure development in the core passage of plate heat exchanger (Compact Heat Exchanger by Richard Law).

2.1.3. Flow and Geometrical Parameter

The geometrical parameters and the flow conditions will significantly affect the performance of the heat exchanger. In this section, these effects are further discussed.

The effects of the fin pitch to diameter ratio have been extensively studied for the staggered geometry for fin pitch to diameter ratio less than 0.625; for the number of tube rows from 2 to 6. Rich [3] concluded that the heat transfer coefficient did not change when the fin pitch was reduced from 0.64 to 0.084 diameters. Chen [14] showed the variation of Nusselt number (based on streamwise tube spacing) with Reynolds number for fin pitch in the range 0.084 to 0.516 diameters, and concluded that the Nusselt number increased with increasing fin pitch for $F_p/D_o < 0.33$, especially at high Reynolds number(Figure 2-6). The Nusselt number did not change with fin pitch beyond fin pitch to diameter ratio of 0.33. Wang [7] found that the heat transfer coefficient is nearly independent of the fin spacing for the fin pitch less than 0.33 diameters, and Reynolds number less than 7000. Overall, for Reynolds numbers less than 7000, the heat transfer performance was found independent of the fin pitch to diameter ratio. For higher Reynolds numbers greater than 7000, the heat transfer performance increased on increasing the fin pitch for fin pitch to diameter ratio less than 0.33. However, the heat transfer performance was unaffected for higher fin pitch to diameter ratio. Chen [14] studied the airflow pattern for a two-row plate and tube heat exchanger to understand the phenomenon behind the behaviour with the fin pitch. He found that the vortex behind the tube became stronger as fin spacing less than 0.336 diameters, and the further increase will no longer influence the intensity of vortices.

Sen [20] analyzed the effect of fin pitch on a single tube row, and the results are summarized in Figure 2-7 for Re=600. Even for this low Reynolds number of 600, the heat transfer coefficient does not change for lower fin pitch to diameter ratio; however, the heat transfer coefficient decreases after a certain value of fin pitch to diameter ratio.

Kim [16] studied the effect of the large fin pitch to diameter ratio (Fp/Do >0.9375) on the performance of the Inline tube arrangement heat exchanger. He concluded that the heat transfer coefficient does not change on increasing the fin pitch for a single tube row geometry, while it increased with the fin pitch for four tube row geometry. He attributed the enhancement of the j- factor with fin pitch to the delay of the boundary layer interruption to the next row in the inline tube alignment.

The effect of the number of tube rows on heat exchanger performance has been studied by many researchers [3] [16] [8] [7]. For a staggered tube arrangement with the number of tube rows less than 6, the Colburn j-factor was shown to decrease with increasing the tube rows at Reynolds numbers less than 2000. However, at Reynolds number greater than 2000, the row effect tends to diminish [7]. The downstream turbulence from the eddies shed from the tube at higher Reynolds number causes mixing, which offsets the decrease in heat transfer. The same trend was observed by Rich [3], Senshimo and Fujii [30]. However, Jang [31] reported that the number of tube rows had a small effect on the average heat transfer coefficient when the row number was greater than 4. Kim [16] also reported the minimal change in Colburn j-factor if the number of tube rows increased beyond four. Kim [16] also studied the effect of the number of tube rows on inline tube arrangement and found that the much higher depreciation in Colburn j-factor by 9.3% than the staggering geometry if the number of tube rows is decreased from four to eight (Figure 2-10). The friction factor was reported to be constant for the staggered tube arrangement with the Reynolds number by Wang [7], as seen from Figure 2-9. In contradiction, Jang [31] reported an increase in pressure drop as the tube rows were increased.

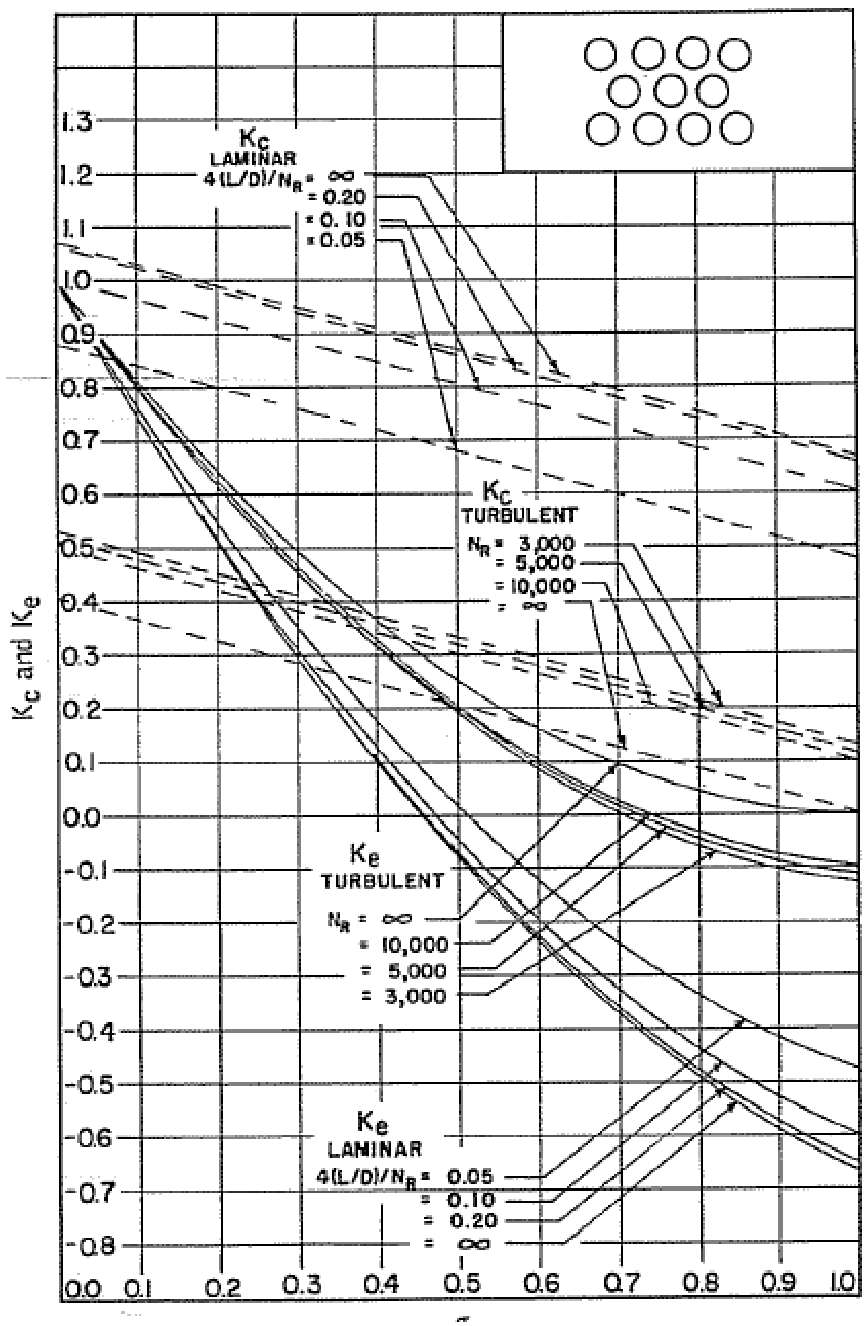

Figure 2-4: Entry and exit loss coefficients, with abrupt entrance and expansion for circular tubes (Kays and London: 1985).

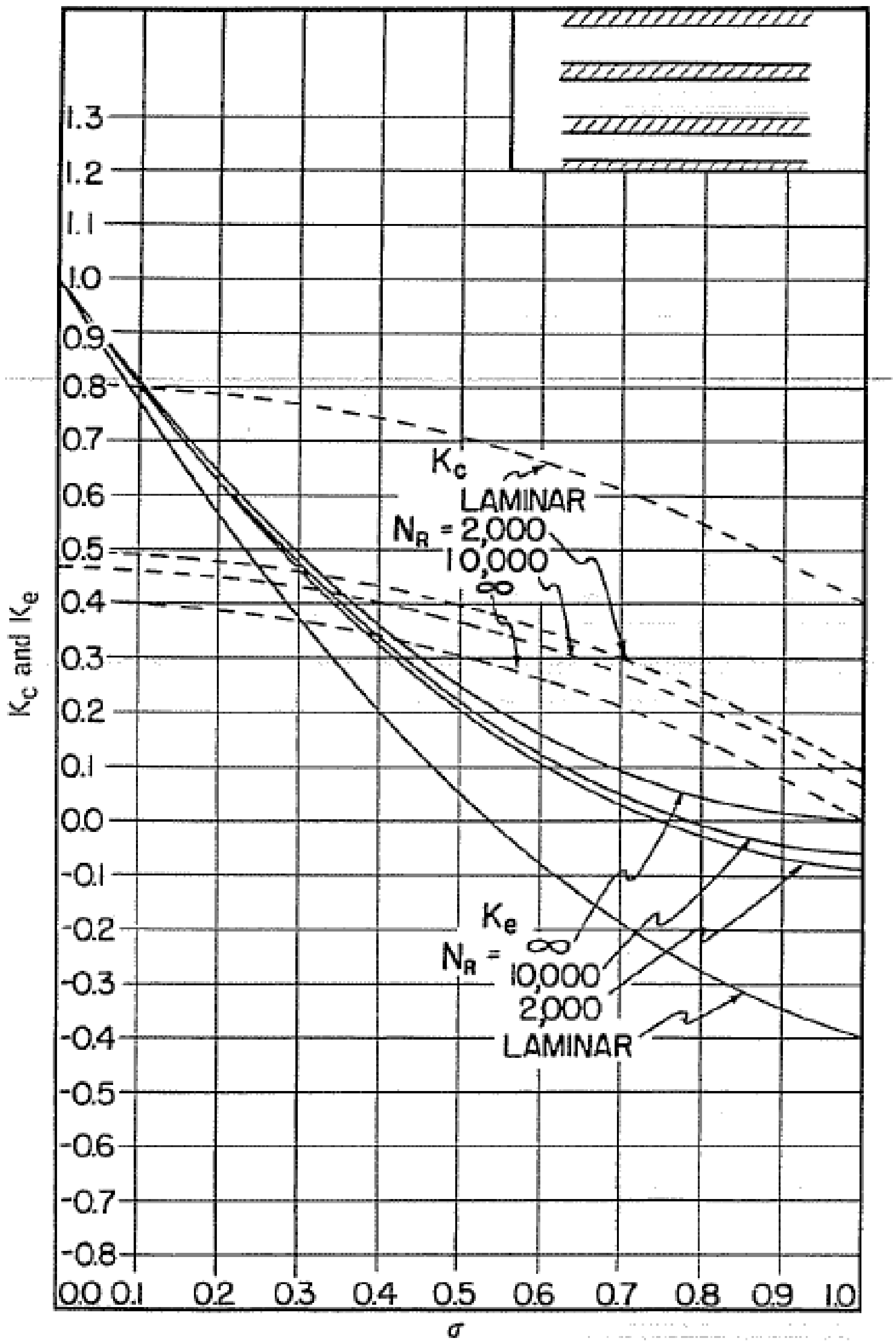

Figure 2-5: Entry and exit loss coefficients, with abrupt entrance and expansion for parallel plates (Kays and London: 1985).

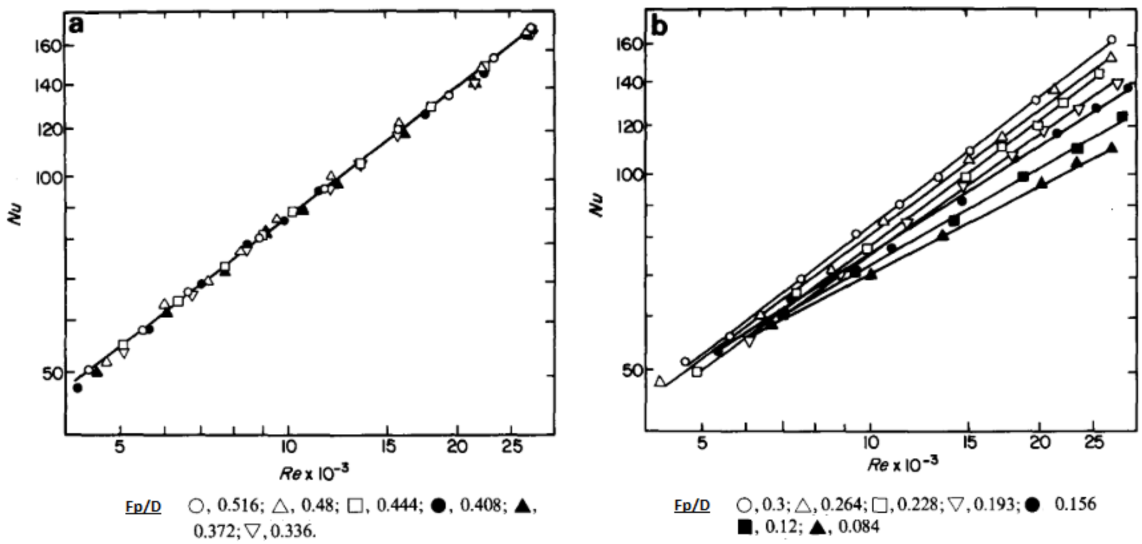

Figure 2-6: Nusselt number (based on tube spacing) variation for different fin pitch on two-row plate-fin and tube heat exchanger(Chen *[14]*).

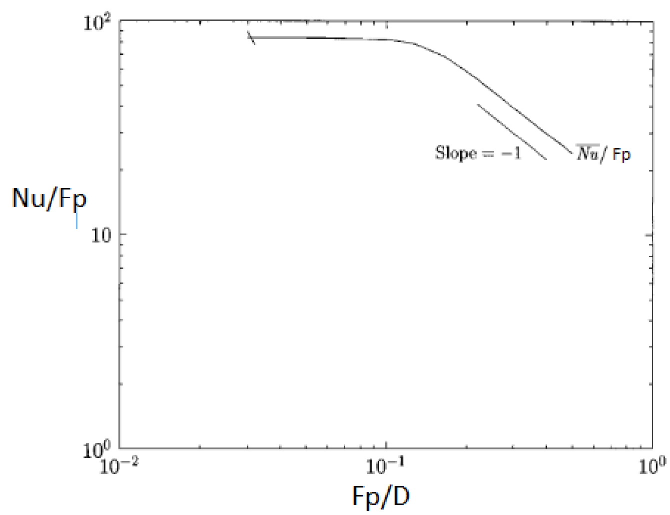

Figure 2-7: Ratio of Nusselt number (characteristics length: fin Pitch) and fin pitch variation for different fin pitch for single-row heat exchanger (Re=600) *[20]*

The effect of the tube arrangement (inline and staggered) has been numerically and experimentally studied by [12] [13] [11] [19]. The difference in the performance of the heat exchanger with tube arrangement seems to be dependent on the tube pitch. Jang [31] studied the effect of tube arrangement for tube pitch less than 38mm (Pt/Do<2.3) and reported that the average heat transfer coefficient of the staggered arrangement was 15-27% higher than that of the in-lined arrangement, but with a higher pressure drop of 20-

25%. Bhuiyan [13] also reported the effect of tube arrangement for tube pitch of less than 25.40mm (Pt/Do<2.3), and showed the Colburn j-factor for the staggered arrangement is 25-30% higher than inline arrangement, while the friction factor is more than 40% higher (Figure 2-11). Huang [19] reported only a 10% difference in the heat transfer coefficient between inline and staggered geometry with tube pitch less than 60.7mm (Pt/Do<2.6). The difference in heat transfer between the staggered and inline tube arrangement appears to reduce on increasing the tube pitch, but it is not very evident from the literature.

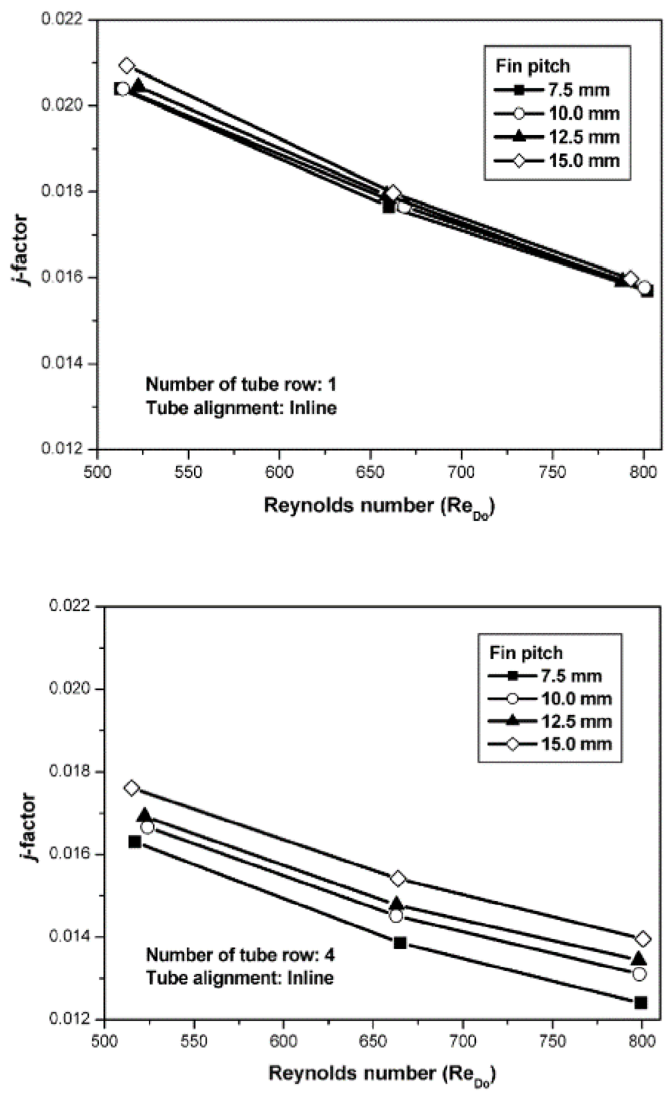

Figure 2-8: Variation of Colbourn j-factor for different fin pitch for 1 row and 4-row inline heat exchanger(Kim *[16]*).

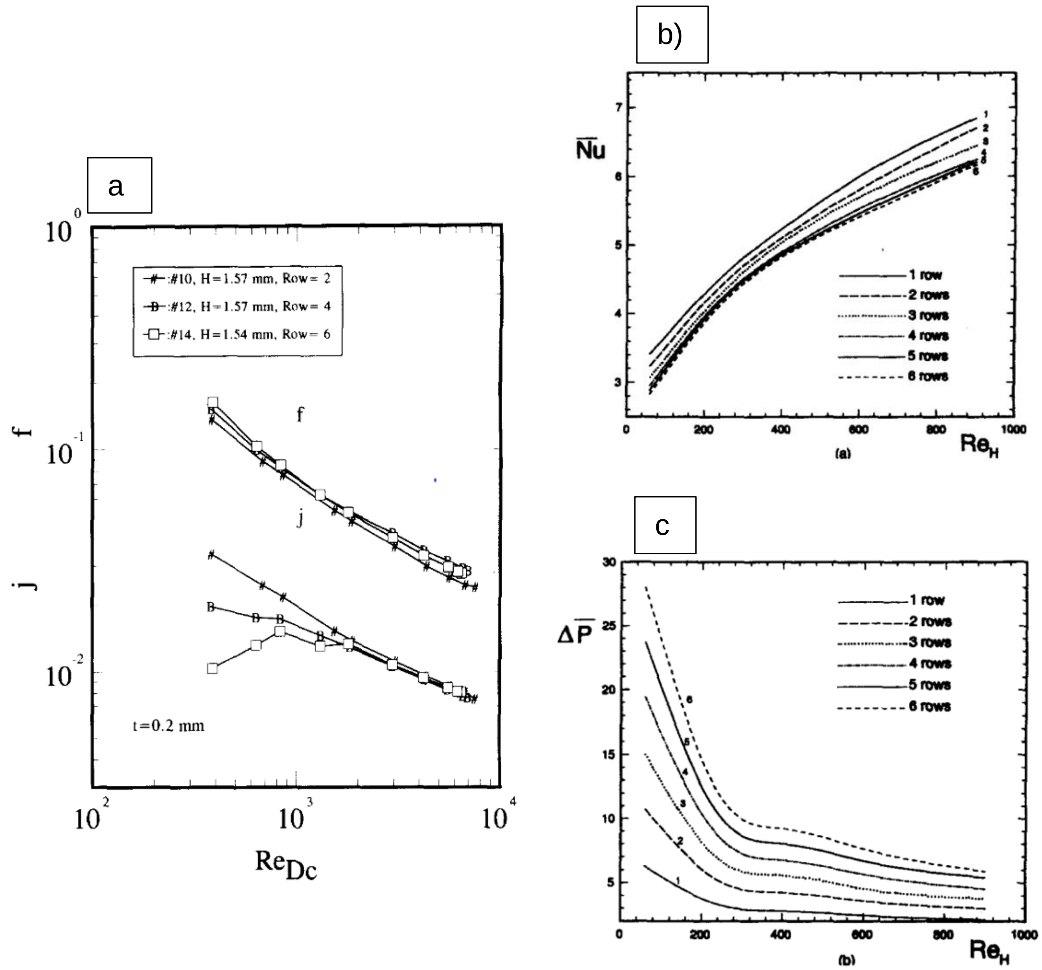

Figure 2-9: a) Variation of Colburn j-factor and friction factor with Re_{Dc} *[7]*, b)Variation of Nusselt number with Re_H *[31]*, c)Variation of friction factor with Re_H *[31]*

Tutar [21] numerically investigated the rationale behind the difference in performance for inline and staggered tube arrangement for Reynolds number from 600 to 2000, and the results for the local Nu around the tube surface are shown in Figure 2-12. The peak value of Nu for the staggered arrangement is also higher than that for the in-line arrangement, especially around the later rows. He concluded that the horseshoe vortex formation behind the tubes is one of the reasons for the higher heat transfer for the staggered tube arrangement compared to the inline tube arrangement, and this would also affect the heat transfer from the fin surface.

The effect of the Reynolds number on heat transfer performance has been extensively studied over the last two decades [12] [13] [14] [11]. The heat transfer coefficient increases with the Reynolds number, but the Colburn j-factor decreases with the Reynolds number.

Similarly, the friction factor was also found to reduce with the Reynolds number (Figure 2-13).

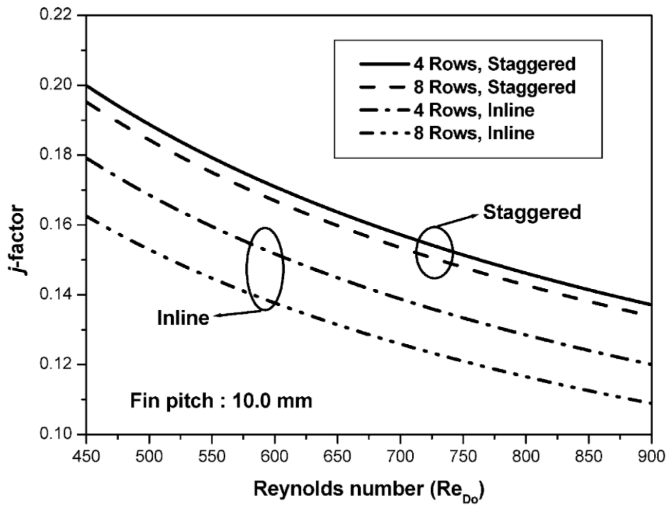

Figure 2-10: The plot of Colburn j-factor with the Reynolds number for staggered and inline geometry *[16]*.

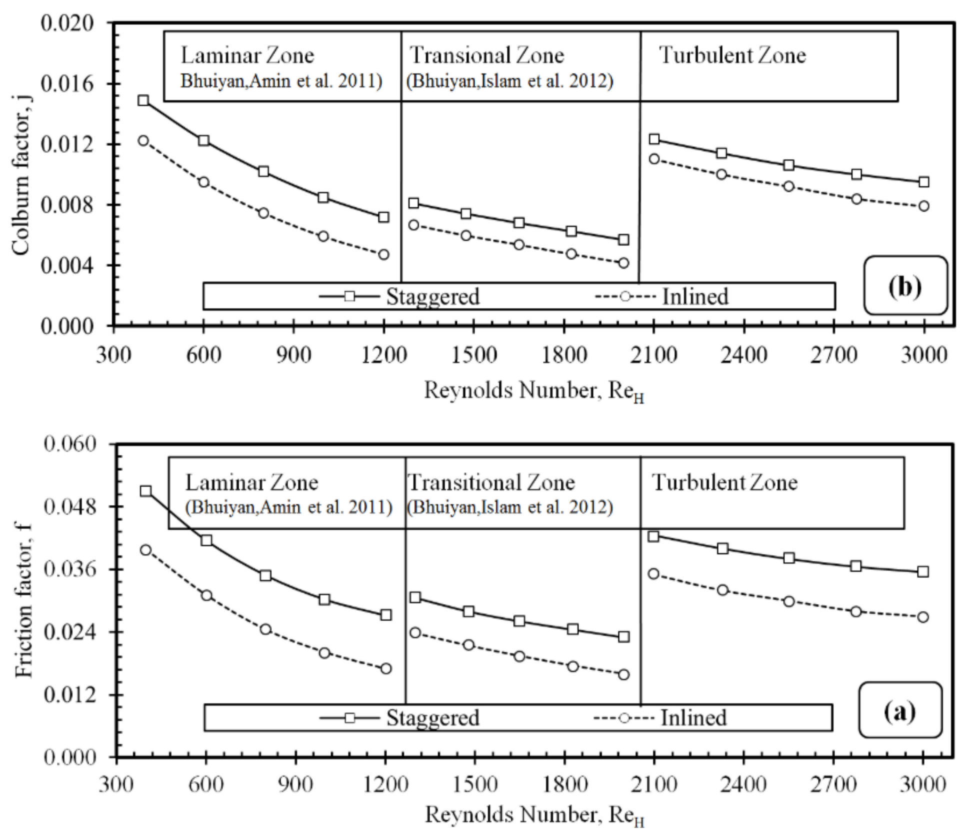

Figure 2-11: The plot of the friction factor and Colburn j-factor with Reynolds number for staggered and inline geometry *[13, 12]*.

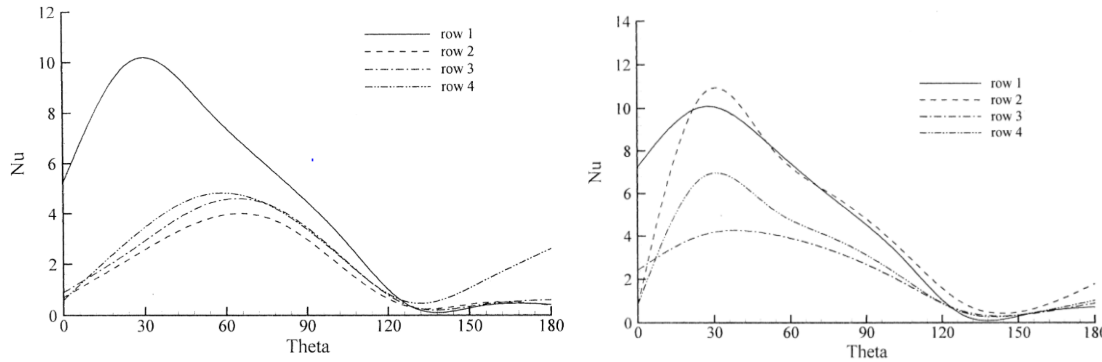

Figure 2-12: a) Variation of Nusselt number around the tube for inline arrangement, b) Variation of Nu around the tube for staggered tube geometry for Re_H=600 *[21]*.

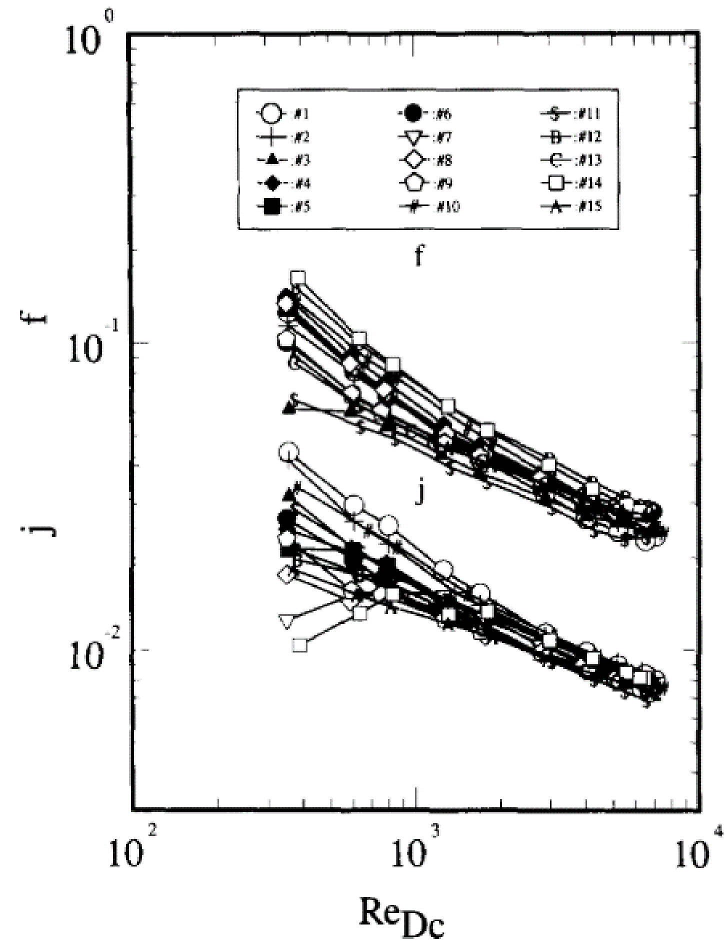

Figure 2-13: The plot of Colburn j-factor and the friction factor with Reynolds number *[7]*.

Most previous work on the ducted plate-fin and tube heat exchanger is for small tube pitch to diameter ratio with little work done for tube pitch to diameter ratio greater than 2-3. The difference in the performance between the staggered and the inline tube arrangement reduces with an increase in tube pitch. The performance of the staggered and the inline tube geometries for the tube pitch of 1.5 to 3.5 diameters will be compared in this study. The effects of different geometrical parameters for the inline tube arrangement will be investigated. Due to the lack of available correlations of the j-factor and the friction factor for the inline tube arrangement, new correlations will be developed for high tube pitch inline geometries.

2.2. Partially Ducted Heat Exchanger

When the heat exchanger is not placed in a fully ducted configuration, some of the approaching air will bypass around the heat exchanger and reduce the performance. There are some studies on the effect of the bypass on tube array heat sinks or plate heat sinks, but none on a flat plate and tube heat sink to the author's best knowledge. Various designs of heat sinks on which the bypass effect has been studied are shown in Figure 2-14. The geometries typically consist of closely spaced fins, which results in pressure drop due to frictional drag from the walls and can be solved by considering a resistance network, as shown in Figure 2-15. The bypass case is far more complex than the fully ducted case. Part of the fluid which enters the heat exchanger leaks out from the Interfin spaces at the fin tip, thus even if the velocity of fluid entering the heat exchanger is known, the flow leaving the heat exchanger from the tip makes it complicated.

The application of flow bypass on the overall performance of plate-fin, pin fin and strip fin heat sinks have been investigated experimentally [34-44], analytically [39,44-46] and numerically [47-51]. Experimentally, the investigation of the top bypass effects on heat transfer and pressure drop characteristics of plate-fin and pin fin was first carried out by sparrow and co-worker [32, 33, 34], Lau and Mahajan [35] examined the top bypass effect of rectangular and convoluted films. Lee [36] considered the tip clearance effects on plate-fin heat sinks. Azar and Madrone [37] studied the effect of pin density on the thermal resistance of the bypass flow. Shaukatullah and Gaynes [38] examined the thermal resistance of the pin fin in open flow. Chapman et al. [39] considered the plate, strip, elliptical pin fin heat sinks in open flow. More recently, Jonsson and co-worker [40, 41] studied the plate, strip, elliptical pin fin heat sinks, developed a bypass correlation.

Analytically, models based on momentum and mass balance to predict the bypass performance is adopted by Lee [36] and Simons and Schmidt [42]. Butterbaugh [43] and

Jonsson and Palm [41] adopted the model based on a pressure balance approach to predict bypass performance.

Barret and Obinelo [44] examined the ability of numerical methods to predict bypass performance. Many researchers, including Sata [45], Obinelo [46], Radmehr [47], Posts [48] numerically investigated the bypass flow effect on the performance of plate-fin heat sinks. Some of the work done on the bypass has been listed in Table 2-3.

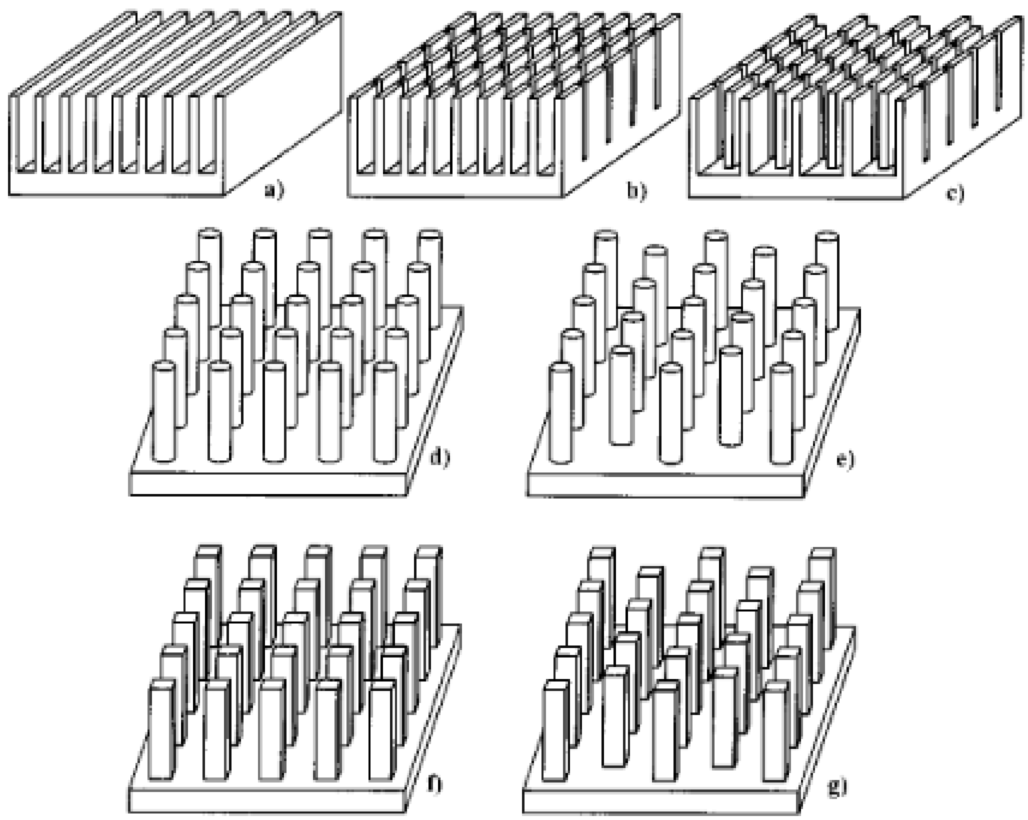

Figure 2-14: Plate fin heat sink (a) strip fin heat sinks with in-line, (b) and staggered, (c) arrays, circular pin fin heat sinks, in-line (d) and staggered (e) arrays and square pin fin heat sinks in-line (f) and staggered (g) arrays [49].

In general, most studies on the partially ducted heat exchanger are done either on the plate or pin heat sinks. In this study, the effect of side bypass on the heat transfer coefficient as well as pressure drop will be investigated for finned tube heat exchanger.

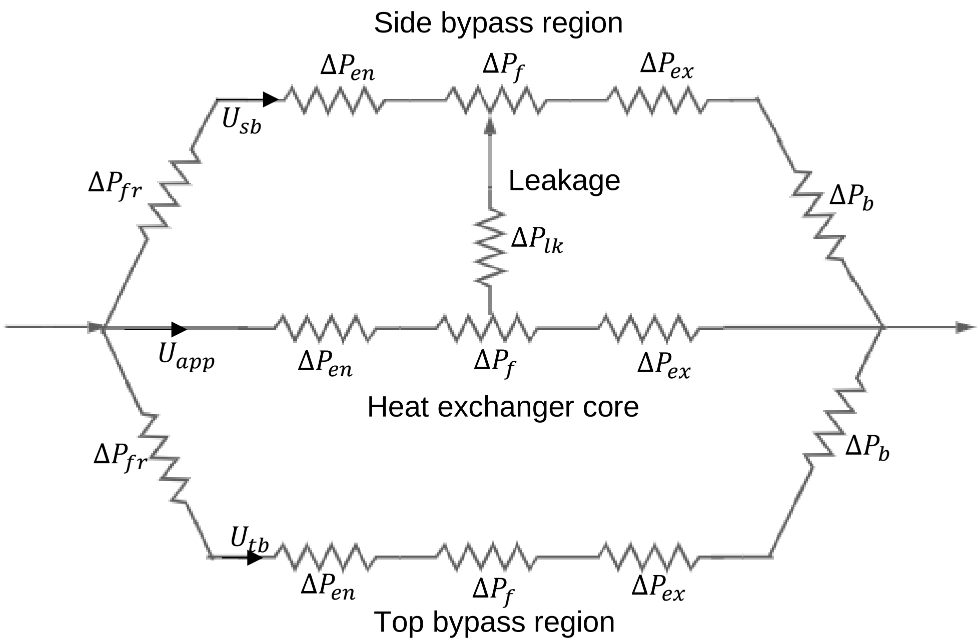

Figure 2-15: Resistance network for fluid flow. Here, $\Delta P_{en}, \Delta P_f, \Delta P_{ex}$ are the abrupt entrance, friction and the abrupt exit pressure drop, respectively, in the various fluid path.

Table 2-3: Top and side bypass effect on heat exchangers.

Lee et al. (1990) [36]	Plate fin	Experimental	• The top bypass is considered only. • As top bypass clearance increases, the heat transfer coefficient decrease by 20% max.
Sparrow and Beckley (1981) [34]	Plate fin	Experimental	• The top bypass is considered only. • Friction factor influence on the heat transfer and pressure drop were analyzed.
Sparrow et al. (1978) [33]	Plate fin	Analytical	• The top bypass is considered only. • Development of a theoretical model to determine thermal resistances by conservation of mass and momentum. • Heat transfer variation from base to tip due to top bypass was analyzed.
Sparrow and Hsu (1981) [50]	Plate fin	Analytical	• The top bypass is considered only. • The laminar model was assumed. • No validation was done

			• They tried to model the heat transfer coefficient of the fin tip and faces of the fin.
Sparrow and Kadle (1986) [32]	Plate fin	Experimental & Analytical	• The top bypass is considered only. • The test their data for turbulent flow conditions • The effect of the top bypass on turbulent heat transfer • Their data did not cover to the limit of a very large bypass.
Lau and Mahajan (1989) [35]	Plate fin	Experimental & Analytical	• The top bypass is considered only. • Effect of top bypass clearance and fin density. • With high fin density, we can obtain improvement in heat transfer with a moderate pressure drop.
Wirtz et al. (1994) [51]	Plate fin	Experimental	• Top and side bypass considered • Derived correlation between inter fin velocity in terms if free stream velocity and fin density. • The proposed overall heat transfer coefficient to be described by Shah et al (1978) • Their experimental results showed up to a 60% flow bypass.
Jonsson et al (2001) [40]	Plate fin, strip fin, circular pin fin, square pin fin	Experimental	• Top and side bypass considered only. • Development of correlation based on experimental results. • $Nu_L = C1 * (Re_{Dh}^{m1}) * (\frac{CB}{B})^{m2} * (\frac{CH}{H})^{m3} * (\frac{\delta}{H})^{m4} * (\frac{\delta f}{H})^{m5}$ • $f = C2 * (Re_{Dh}^{n1}) * (\frac{CB}{B})^{n2} * (\frac{CH}{H})^{n3} * (\frac{\delta}{H})^{n4} * (\frac{\delta f}{H})^{n5}$ • The value of the various coefficient is different for each geometry and is not listed here.
Leonard et al. (2002) [52]	Plate fin	Analytical model	• The top bypass is considered only. • The accuracy of 8% with experimental data.

			• Air leakage effect from the tip. • The influence of top bypass was not included
Coetzer and Visser (2003) [53]	Plate fin	Numerical	• Top bypass considered only • They tried to predict inter-fin velocity accurately. • They investigated the air leakage from the tip by measuring the inlet and outlet inter-fin velocity.
Min et al. (2003) [54]	Plate fin	Numerical	• The effect of Top bypass on the cooling performance of under the fixed power condition. • The presence of an optimal top bypass can improve the cooling performance of a heat sink. • A heat sink does not need to be fully ducted to achieve maximum cooling performance.
Dogrouz et al(2006) [55]	square pin fin	Numerical	• The top bypass is considered only. • A minor effect of tip leakage. • Pin pitch effect on air leakage ratio to diversion ratio.
Khan et al (2007) [56] Hossain et al(2007) [57]	circular pin fin	Analytical	• The top bypass is considered only. • Development of a theoretical model to determine thermal resistances by conservation of mass and momentum. • The formula has not been listed in this review.

Chapter 3.

Numerical Methods

This study aims to numerically investigate the performance of flat plate and tube heat exchangers when placed in a fully and partially ducted system using the finite volume code (ANSYS FLUENT). The flat plate and tube heat exchanger consist of tubes arranged in inline or staggered arrangement intersected by several flat plates. In this chapter, an overview of the conservation equations with details of different turbulence models are first presented. This is followed by a presentation of the computation domain, grid generation, boundary conditions, physical properties for the specific geometries considered in this study. Grid independence and validation studies are finally presented.

3.1. Governing Equation of Fluid Flow

The flow field and temperature field are governed by the conservation of mass, momentum and energy.

Conservation of Mass:

$$\frac{\partial \rho}{\partial t} + \frac{\partial (\rho U_i)}{\partial x_i} = 0 \qquad \text{3-1}$$

Conservation of Momentum:

$$\frac{\partial U_i}{\partial t} + U_J \frac{\partial U_i}{\partial x_j} = \frac{-1}{\rho}\frac{\partial p}{\partial x_i} + \frac{\partial}{\partial x_i}(2\frac{\mu}{\rho}S_{ij}) \qquad \text{3-2}$$

where the strain rate tensor S_{ij} is given by

$$S_{ij} = \frac{1}{2}(\frac{\partial U_i}{\partial x_j} + \frac{\partial U_j}{\partial x_i}) \qquad \text{3-3}$$

Conservation of Energy:

$$\frac{\partial}{\partial t}(\rho E) + \frac{\partial}{\partial x_i}(U_i(\rho E + p)) = \frac{\partial}{\partial x_i}(k\frac{\partial T}{\partial x_i}) \qquad \text{3-4}$$

The equations can be averaged by decomposing the variables U_i and p to mean and fluctuating components.

$$U_i = \overline{U}_i(x_k) + u' \qquad \text{3-5}$$

$$P = \ddot{P}(x_k) + P' \tag{3-6}$$

$$\bar{U} = \frac{1}{T}\int U * dt \tag{3-7}$$

$$\bar{P} = \frac{1}{T}\int P * dt \tag{3-8}$$

$$\frac{\partial \bar{U}_i}{\partial t} + \bar{U}_j \frac{\partial \bar{U}_i}{\partial x_j} = \frac{-1}{\rho}\frac{\partial P}{\partial x_i} + \frac{\partial}{\partial x_i}\left(2\frac{\mu}{\rho}S_{ij}\right) + \frac{\partial(-\overline{u'_i u'_j})}{\partial x_j} \tag{3-9}$$

$$\frac{\partial \bar{U}_i}{\partial t} + \bar{U}_j \frac{\partial \bar{U}_i}{\partial x_j} = \frac{-1}{\rho}\frac{\partial P}{\partial x_i} + \frac{\partial}{\partial x_i}\left(2\frac{\mu}{\rho}S_{ij}\right) + \frac{\partial \tau_{ij}}{\partial x_j} \tag{3-10}$$

where,

$$\tau_{ij} = (-\overline{u'_i u'_j}) \tag{3-11}$$

The solution of the above requires closure for the Reynolds stress τ_{ij}. This is typically done using the Boussinesq hypothesis-based models and Reynolds stress transport model. The Reynolds stress transport model (RSM) uses additional transport equations for the Reynolds stresses and then modelling the higher-order terms. This results in six additional equations and can be computationally expensive. Eddy viscosity models have been used successfully ([10] [12] [24] [21]) for similar geometries, and hence the current work is based on these models.

In the relevant numerical investigation, many previous researchers [20, 12, 21] assumed the laminar flow assumption in the simulation of finned tube heat exchangers. Tsai and Sheu [58] compared the accuracy of the laminar model with the experient for a two-row fin and tube heat exchanger and demonstrated its failure when Re_D is greater than 700. Kritikos [59] indicated the applicability of the low Reynolds number turbulence model for thermal-hydraulic characteristics of transitional flow for tube array heat exchangers. Wang [60] and Huang[69] used the low Reynolds number K-ε model to describe the thermohydraulic characteristics of finned tube heat exchangers for Re_{Do} less than 6000. In recent years, researchers like Tala [61] utilized the low Reynolds number K-ω SST model for Re_{Do} of 1050.

For the finned tube heat exchanger, a strong horseshoe vortex formation is seen behind the fin-tube junction. These horseshoe vortices influence the heat transfer and pressure drop in the system. Khallaki (2005) showed that the k- ω SST model was suitable to describe the horseshoe vortex systems behind single row finned tube heat exchangers. *Table 3-1* shows the comparison of various turbulence models. It can be seen that the k- ω SST model uses the advantages of standard K- ω and K-ε model for prediction of the boundary layer and shear layer, respectively. Hence, in this study the low Reynolds number k- ω SST model is used to model the thermal-hydraulic characteristics behind the finned tube heat exchanger.

Table 3-1: Comparisons of various turbulence models.

	k- ω model	**k- ε model**	**k- ω SST model**
Prediction of Boundary Layer	As per Menter [62], the k- ω model performs better the k- ε in predicting the boundary layer accurately. k-ω model is the model of choice in the sublayer of the boundary layer. It is shown in [63] [64] that k- ω behaves superior to k- ε for predicting the logarithmic part of the boundary layer in equilibrium adverse pressure gradient flows and incompressible flows.	Boundary layer prediction Is less accurate for the k- ε model compared to Menter's k- ω model.	For Menter's SST model, F1 is one inside the boundary layer which switches the SST model to the k- ω model and predicts the boundary layer similar to the k- ω model.
Prediction outside the boundary layer	As per Menter [62], the k- ω model is arbitrarily sensitive to the freestream value of ω specified outside the boundary layer. As per [65], eddy viscosity in the boundary layer and free shear layer can be changed by 100% by reducing the value of ω in the free stream	For the wake region of the boundary layer, k- ε is superior to k- ω model as per Menter [62]. As per [65], k- ε is very less sensitive to the free-stream value of ω specified	However, for Menter's SST model, the blending function made sure that the k- ε model has utilized for free shear layer away from the surface.
Asymptotic behaviour of turbulence	One of the major disadvantages of the k- ω model is that it cannot predict the asymptotic behaviour of the turbulence as it approaches the wall	The asymptotic behaviour of turbulence is comparatively accurately predicted with this model as per [54].	Menter's k- ω SST model does not suffer from this disadvantage since it switches to k- ε model away from the wall.

	unlike the k- ε model [62]. However, this absurd behaviour does not limit this model to predict the mean flow profile and skin friction coefficient accurately.		

3.1.1. K-ω SST model

This model was introduced by Menter [62]. The basic idea behind this model was to combine the best elements of K-ω, k- ε and J-K models by introducing blending functions that combined the various aspects of the different models.

$$\frac{\partial k}{\partial t} + U_j \frac{\partial k}{\partial X_j} = \frac{\partial}{\partial X_j}\left[(v + \sigma_k v_t)\frac{\partial k}{\partial X_j}\right] + \frac{\tau_{ij}}{\rho}\frac{\partial U_i}{\partial X_j} - \beta^* k\omega \quad \text{3-12}$$

$$\frac{\partial \omega}{\partial t} + U_j \frac{\partial \omega}{\partial X_j} = \frac{\partial}{\partial X_j}\left[(v + \sigma_\omega v_t)\frac{\partial \omega}{\partial X_j}\right] + \frac{\gamma}{v_t}\frac{\tau_{ij}}{\rho}\frac{\partial U_i}{\partial X_j} - \beta^* \omega^2 + 2(1 - F_1)\frac{\sigma_{\omega 2}}{\omega}\frac{\partial k}{\partial X_j}\frac{\partial \omega}{\partial X_j} \quad \text{3-13}$$

$$v_t = \frac{a_1 k}{\max(a_1\omega, \Omega F_2)} \quad \text{3-14}$$

Each of the constant is a blend of an inner and outer constant via the equation below

$$\emptyset = F_1\emptyset_1 + (1 - F_1)\emptyset_2 \quad \text{3-15}$$

$$F_1 = \tanh(\arg_1^4) \quad \text{3-16}$$

$$\arg_1 = \min\left(\max\left(\frac{\sqrt{k}}{\beta^*\omega d}, \frac{50v}{d^2\omega}\right), \frac{4\rho\sigma_{\omega 2}k}{CD_{k\omega}d^2}\right) \quad \text{3-17}$$

$$CD_{k\omega} = \max\left(2\rho\sigma_{\omega 2}\frac{1}{\omega}\frac{\partial k}{\partial X_j}\frac{\partial \omega}{\partial X_j}, 10^{-20}\right) \quad \text{3-18}$$

$$\gamma_1 = \frac{\beta_1}{\beta^*} - \sigma_{\omega 1}\frac{{k_1}^2}{\sqrt{\beta^*}}, \quad \gamma_2 = \frac{\beta_2}{\beta^*} - \sigma_{\omega 2}\frac{{k_1}^2}{\sqrt{\beta^*}} \quad \text{3-19}$$

$$\sigma_{k1} = 0.85, \ \sigma_{\omega 1} = 0.5, \ \beta_1 = 0.075, \ \sigma_{k2} = 1.0, \ \sigma_{\omega 2} = 0.856, \ \beta_2 = 0.0828, \ \beta^* = 0.09, k_1 = 0.41, \ a_1 = 0.31 \quad \text{3-20}$$

A low Reynolds number correction was introduced by Wilcox with some modification to the constants of the above model as

$$\beta^* = \frac{0.09\left(\frac{100\beta_o}{27} + \left(\frac{Re_T}{Re_\beta}\right)^4\right)}{\left(\frac{Re_T}{Re_\beta}\right)^4 + 1} \quad \text{3-21}$$

$$v_t = \frac{\alpha^* k}{\widetilde{\omega}}, \quad \widetilde{\omega} = \max\left(\omega, C_{lim}\sqrt{2\frac{\widetilde{S_{ij}S_{ij}}}{\frac{\beta^*}{\alpha^*}}}\right. \quad \text{3-22}$$

Instead of $\boldsymbol{v + \sigma_k v_t}$ in the k-equation diffusive term, the below term is used

$$v + \sigma_k \alpha^* v_t \quad \text{3-23}$$

Instead of $v + \sigma_\omega v_t$ in the ω -equation diffusive term, the below term is used.

$$v + \alpha^* \sigma_\omega v_t \quad \text{3-24}$$

$$Re_T = \frac{\rho k}{\mu\omega}, \quad \alpha^* = \frac{\alpha_o^* + \frac{Re_T}{Re_k}}{1 + \frac{Re_T}{Re_k}}, \quad Re_\beta = 8, \; R_k = 6, \quad R_\omega = 2.61 \quad \text{3-25}$$

$$\alpha_o = \frac{1}{9}, \quad \alpha_o^* = \frac{\beta_o}{3} \quad \text{3-26}$$

3.2. Numerical Simulation

The numerical simulations of the plate-fin and tube heat exchangers were performed using the commercial finite volume package, FLUENT©. The RANS equations were solved using the low Reynolds number k- ω SST turbulence model. Though this model is computationally more expansive than the k- ε model, it limits the disadvantages of both k-ω and k- ε model in the free shear and near-wall region, respectively. The low Reynolds number version of this model was chosen to calculate mixed-flow fields (combined laminar, transition and turbulent flow types), also recommended by Huang [66] and wang [60].

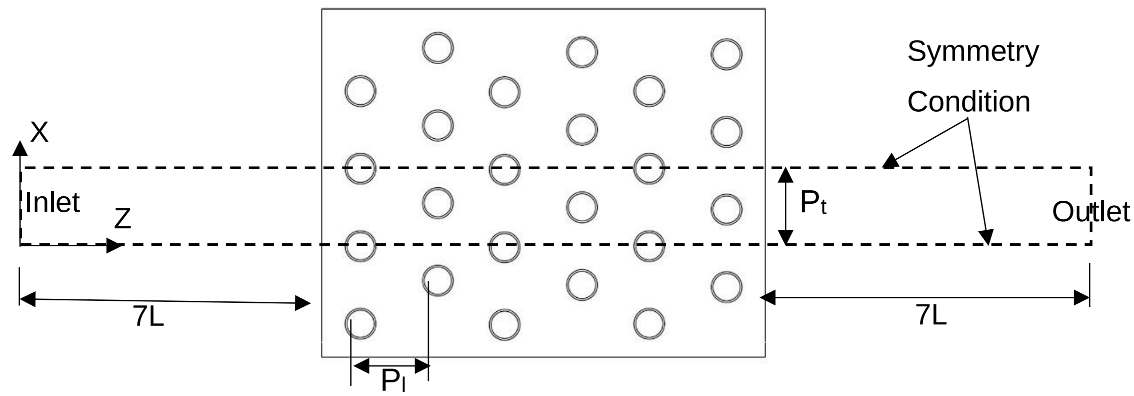

a) Staggered tube arrangement

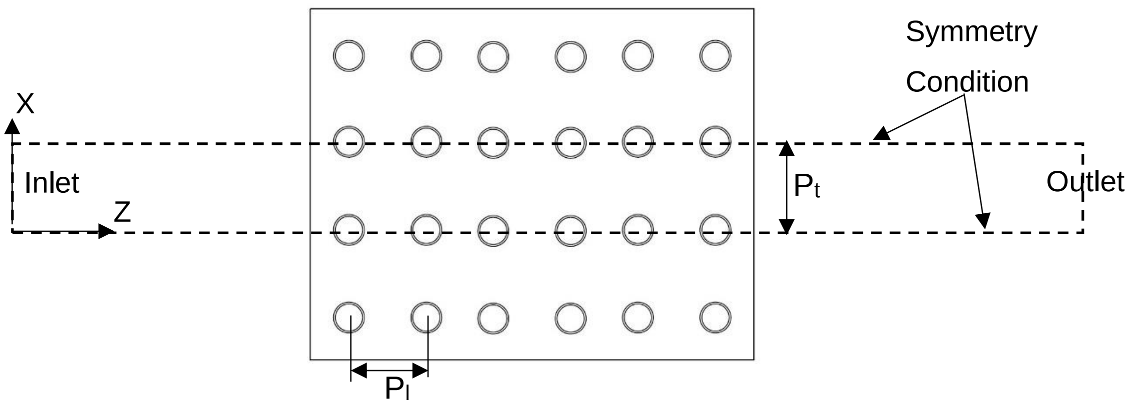

b) Inline tube arrangement

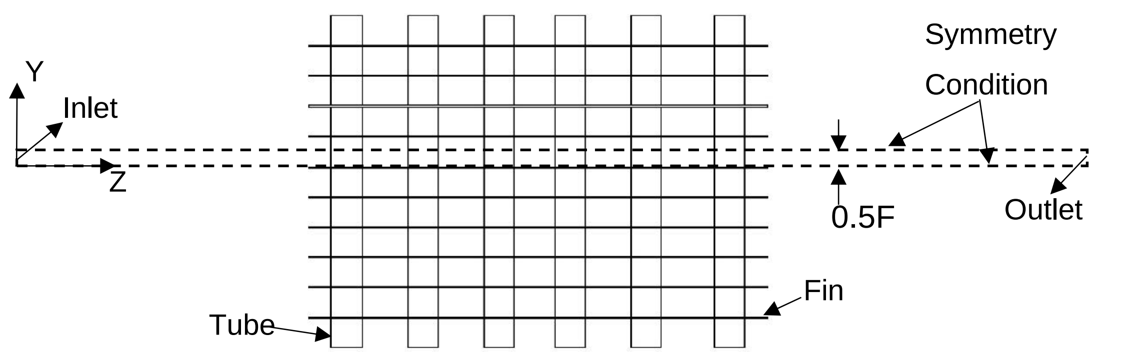

c) Top view

Figure 3-1: Details of the computational domain for *a* fully ducted heat exchanger.

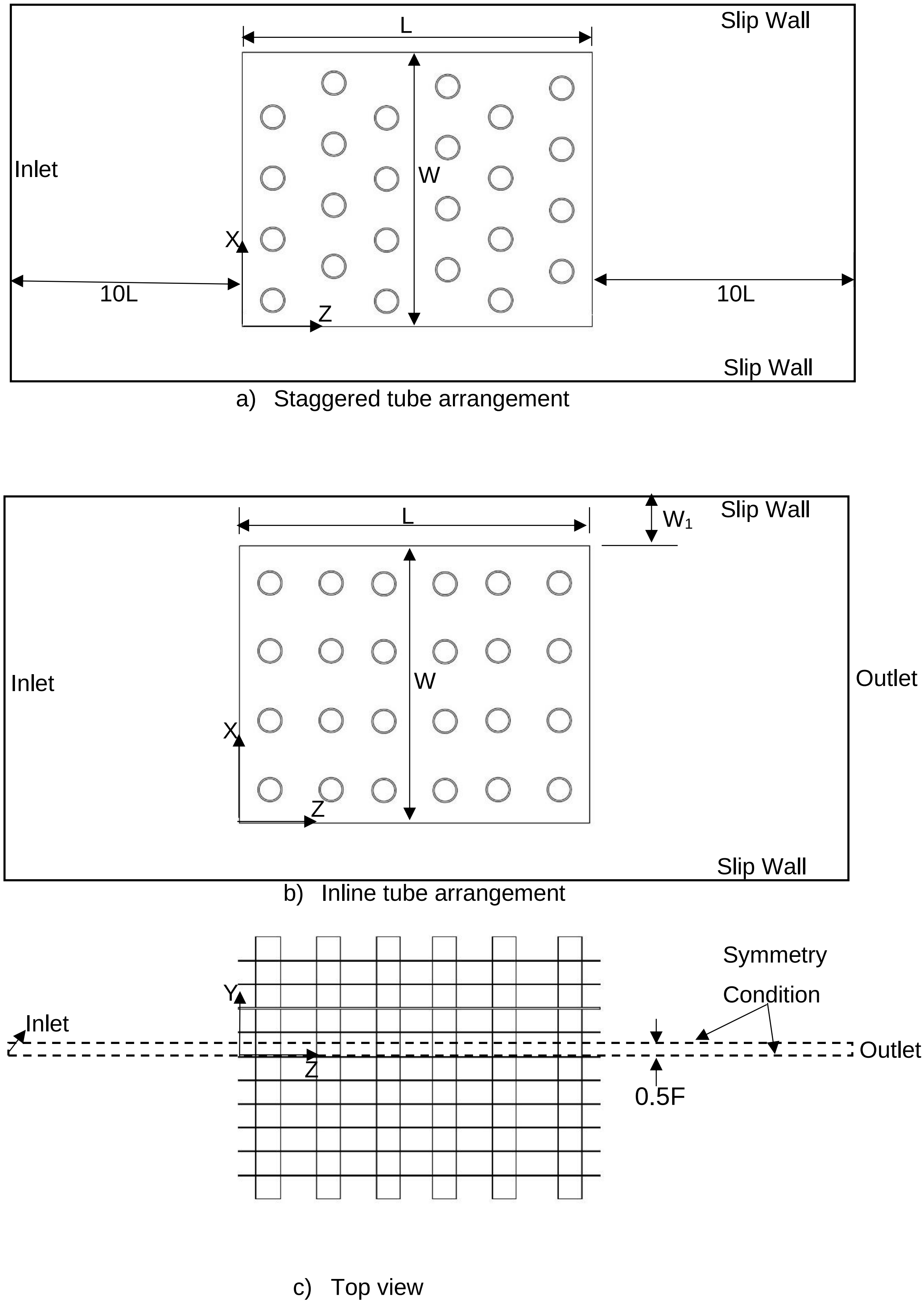

Figure 3-2: The details of the computational domain for a partially ducted model.

3.2.1. Computational Domain

Fully Ducted Model

Schematic views of the plate-fin and tube heat exchangers considered in this study when it is in the fully ducted configuration are shown in Figure 3-1. The symmetry boundary condition, shown by the dashed lines, is used to reduce the computational domain. The total volume of the heat exchanger considered equals to $0.5 * P_t * L * F_p$. An upstream and downstream length of seven times the heat exchanger has been added in the Z direction. The extreme faces in the Z direction of the computational domain are considered the inlet and outlet. This allows us to consider the fin leading edge effect at the upstream of the flow and to stabilize the flow at the outlet to avoid any numerical instabilities due to the potential reversal of the flow. Constant velocity and temperature are used at the inlet and a pressure outlet is used at the outlet.

The numerical simulation with different downstream domain extent was performed. The result did not converge for a very small downstream distance up to 2L. The maximum discrepancy of 0.78% in overall heat transfer was seen for downstream domain length changed from 3L to 4L. There was a change of less than 0.02% in overall heat transfer with a further increase in the downstream domain extent.

Partially Ducted Model

Schematic views of the proposed plate-fin and tube heat exchangers under partial ducting are shown in Figure 3-2. The top and bottom of the heat exchanger are constrained and only the side bypass is considered in this study. Symmetry boundary conditions are used as shown by the dashed lines in the top view. The total volume of the heat exchanger modelled is equal to $(2W_1 + W) * L * F_P * 0.5$. Upstream and downstream distances were taken to be equal to 10 times the length of the fin, which was found sufficient. The corner walls of the duct are considered slip walls similar to previous studies [44, 45]. Constant velocity and temperature have been considered at the inlet and the outlet has been taken as a pressure outlet. The domain of clearance ratio ($\frac{2W_1}{W}$) 35 was considered infinite with slip walls considered as a pressure outlet.

The numerical simulation with downstream and an upstream domain extent of 10L and 13L was performed for the partially ducted geometry with a clearance ratio of 1.5. There was no change observed in approach velocity entering the heat exchanger. The discrepancy of 0.125% and 0.18% was observed in overall heat transfer and pressure drop, respectively. Hence, an upstream and downstream domain size of 10 times the length of the heat exchanger was chosen.

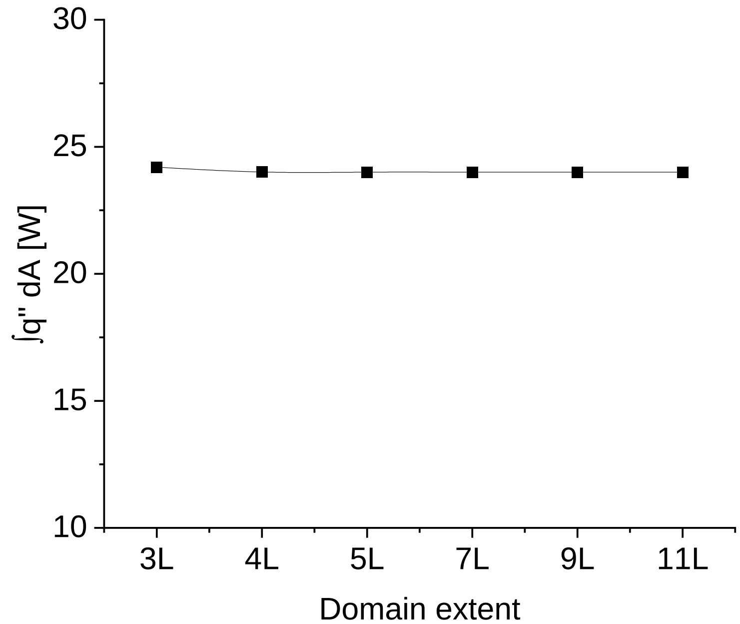

Figure 3-3: The heat transfer variation with the downstream domain extent for a fully ducted heat exchanger.

3.2.2. Grid Generation & Convergence analysis

An appropriate grid with the right resolution is important to predict the flow and heat transfer in complex geometries. In turbulent flow, there is a strong interaction of the mean flow and turbulence and hence the flow tends to be more dependent on the grid optimization than in laminar flow [67].

A significant factor for the precision of the numerical results is the meshing of the near-wall region. As per [67], the possible separation phenomenon due to adverse pressure gradient is captured depending upon the resolution of the boundary layer upstream of the point of separation. For the plate-fin and tube, major areas of refinement are the fin leading edge, fin-tube junction and the tube walls [22]. The purpose of such refinement is to correctly describe the near-wall quantities due to the developing boundary layer at the leading edge of the fin or fin-tube junction due to the development of horseshoe vortices.

Ansys meshing© was used to discretize the domain into a finite number of control volumes. The upstream and downstream meshed with a linearly increasing mesh size. The resultant grid is shown in Figure 3-4 to Figure 3-6. The generated grid near the tube walls and the fin surface is shown in Figure 3-4, near the fin leading edge and corner (for only partially ducted model) is shown in Figure 3-6.

In order to study the grid independence, six grid systems having 1,578,000; 2,670,000; 3,500,000; 5,500,000; 8,500,000; 12,000,000 elements are generated for the fully ducted geometry with tube pitch of 3.5 diameters, fin pitch of 0.5 diameters and Reynolds number of 2300. For the generated grid, attention was paid to ensure that the first centroid distance to the wall y+ <1 following the requirement of the turbulence model. As shown in Figure 3-7, the Colburn j-factor changed less than 0.2% for the grids with 5,500,000 to 12,000,000 elements. In this study, the grid with 5,500,000 is used for the simulations.

The convergence was checked by monitoring the point defined just before the exit from the heat exchanger. The velocity magnitude and turbulent viscosity ratio are checked at each iteration, and the simulations are considered converged once all the residuals drop below 1e-4 and the monitored variable remains constant.

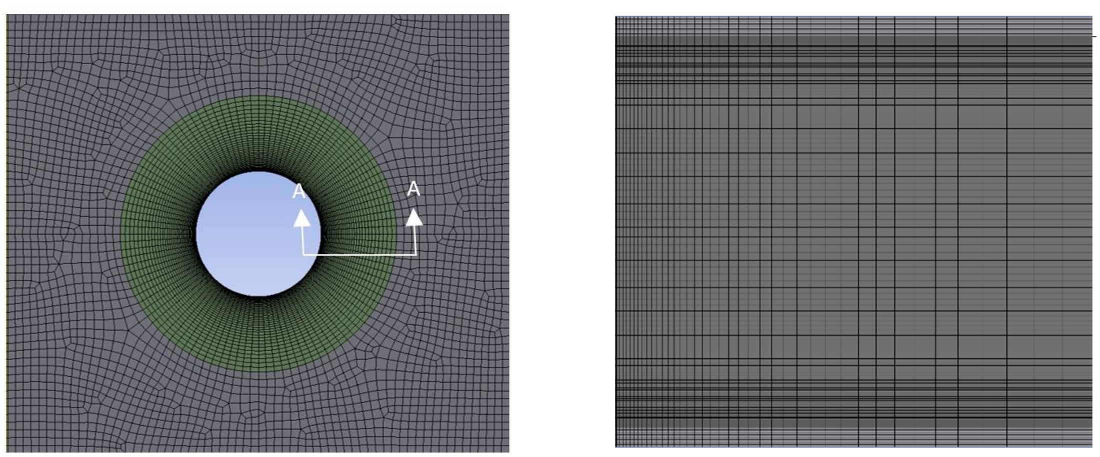

a) Grid near tube walls b) Grid cross-section A-A

Figure 3-4: Grid generation

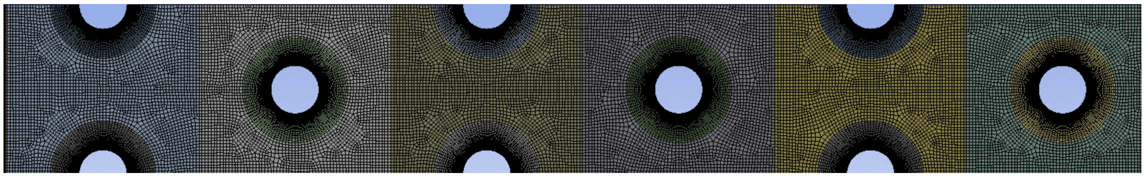

a) Staggered tube arrangement

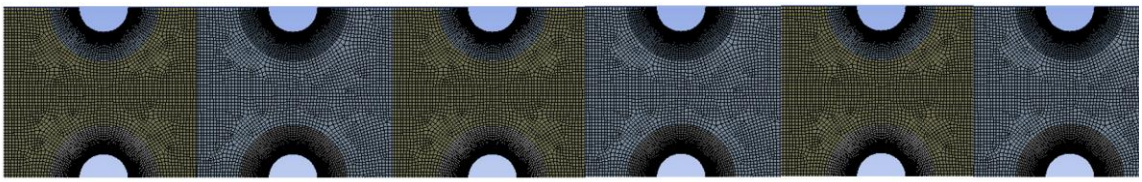

b) Inline tube arrangement

Figure 3-5: Grid generation on the central plane.

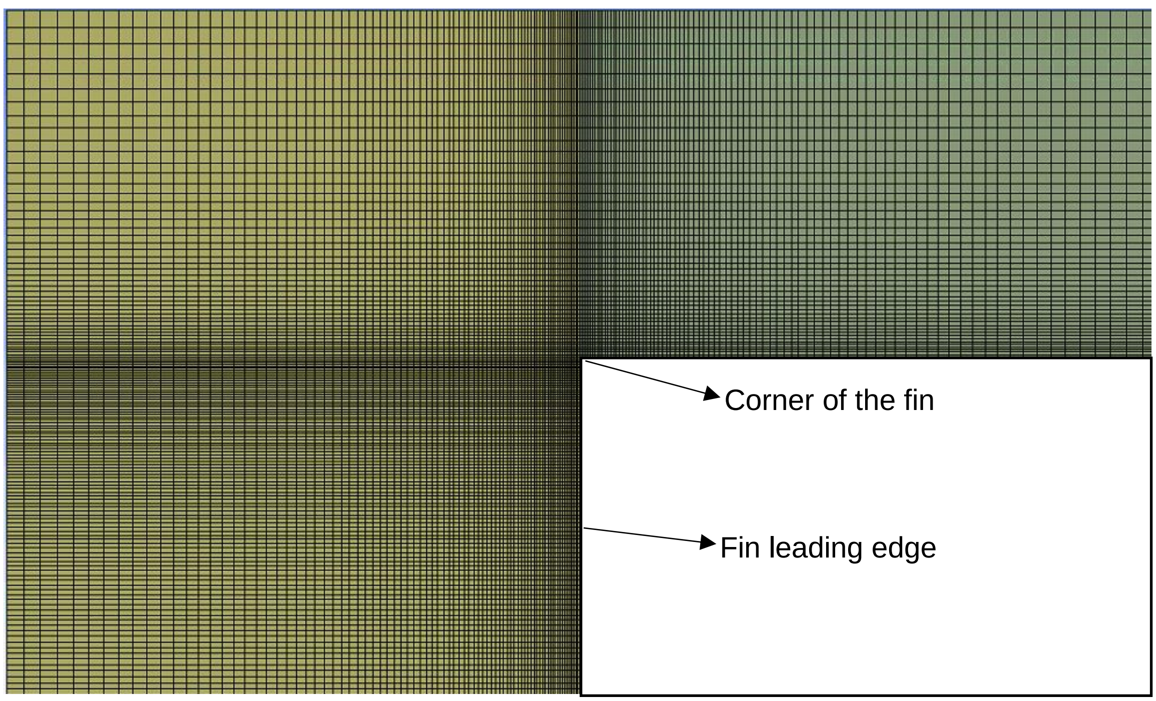

Figure 3-6: Grid generation at the corner and the leading edge of the fin.

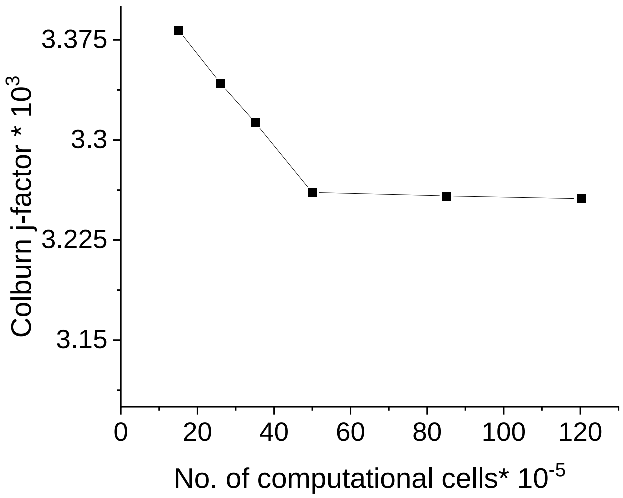

Figure 3-7: Grid independence test for fully ducted geometry.

3.2.3. Physical properties

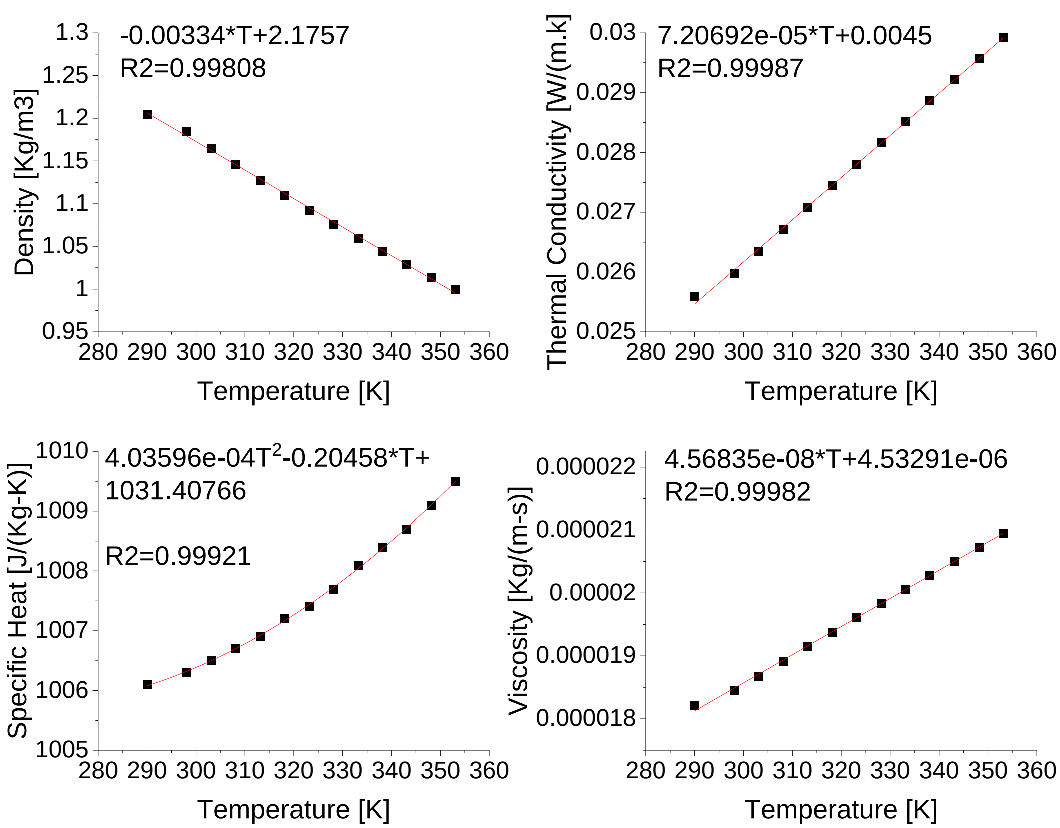

Figure 3-8: Fitted curve for physical properties for air.

In this study, the air was assumed to be dependent on the temperature and its physical properties were obtained by curve fitting the property data over the temperature range of this study, and are shown in Figure 3-8. The minimum R^2 value for the fitted curved is greater than 0.998. The fin is chosen to be aluminum and the tube is chosen to be copper.

3.2.4. Boundary conditions

The boundary conditions used in this study are summarized in Table 3-2.

Table 3-2: Boundary conditions used for the simulations.

Inlet	• Uniform Velocity
Outlet	• Pressure Outlet
Tube	• No-slip boundary condition • The convective boundary condition at inside walls.
Fin	• No-slip boundary condition • Conjugate heat transfer
Symmetry plane or slip walls	• Velocity components in normal direction=0 • Temperature gradients in normal direction =0 • The gradient of tangential components of velocity in normal direction = 0
Steady or Un-Steady	• Steady State

Inlet

A uniform velocity U_o and temperature T_o are imposed at the inlet of the domain. The turbulent intensity of 3% and viscosity ratio of 8.7e-04*Re are specified at the inlet, also specified in Table 3-3.

The decay of turbulent quantities upstream of the domain is not typically calculated accurately [68]. This is likely because the typical grid spacing near the inflow boundary is usually large to resolve the decay and is often underestimated or grid-dependent. High values of viscosity ratio at the upstream junction of the body can contaminate the solution at non-turbulent regions of the domain due to the limitation of the two-equation model and ambient values are often recommended. In this study, different turbulent inlet parameters were tested for the current geometry and final values were selected which yield the ambient values of turbulent viscosity ratio at the upstream junction of the body as suggested by Spalarat [68]. Variation of viscosity ratio at the central plane for different inlet viscosity ratio is shown in Figure 3-9. It can be seen that the flow around the heat exchanger has a strange variation of viscosity ratio if the inlet viscosity ratio is too high. It also has a strong influence on the pressure and the flow pattern in that region. However, the flow inside the fins is not much affected. The variation of viscosity ratio at the central plane for different inlet turbulent intensity can be seen from Figure 3-10. There is a slight variation of viscosity ratio for Intensity up to 3%. For turbulence intensity greater than 3%, the maximum viscosity ratio at the exit edge is affected by a sharp increase in the friction factor. The final values of the viscosity ratio and turbulence intensity are given in Table 3-3. The good agreement of the pressure with the experimental correlation (Refer Validation section of this chapter) supports the selected inlet turbulent boundary condition.

Table 3-3: Inlet flow parameters.

Re	T_{in} (K)	$\mathrm{I}\,\%$	μ_t/μ
1300-5800	290	3	$(8.7\mathrm{E}-4)\mathrm{Re}$

Tube

The main application for the flat plate and tube heat exchanger considered here is to reject the latent heat of condensation of the heat pipes to the outside air. Thus, a convective boundary condition for the tubes was adopted for the current simulations. A saturation temperature of 75°C was assumed inside the heat pipe, and the heat transfer coefficient was calculated using the correlation by Gross [69] for laminar wavy range as

$$\mathrm{Nu}^* = 0.884 * \mathrm{Re}_\varphi^{-1/4} \tag{3-27}$$

where, Nu^* is modified Nusselt number and Re_φ^1 is the modified film Reynolds number [69], shown in Figure 3-11. The correlation yields a heat transfer coefficient of 18,000-20,000 W/m2-K. So, a heat transfer coefficient of 20,000 W/m2-K with a saturation temperature of 75°C was chosen for this study.

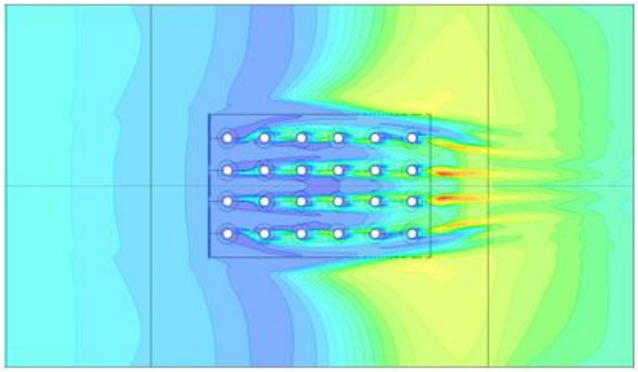

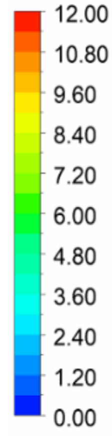

a) I=3%, VR=8.69e-4*Re

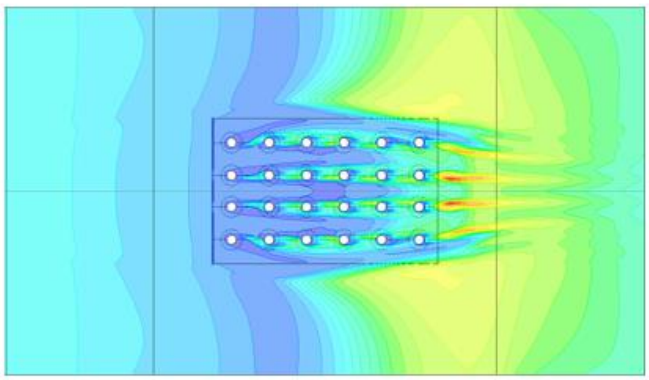

b) I=3%, VR=1.3e-03*Re

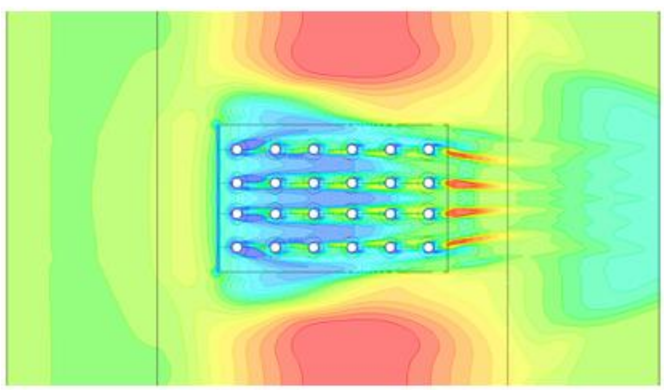

c) I=3%, VR=2.6e-03*Re

Figure 3-9: The variation of viscosity ratio at the central plane for different inlet viscosity ratio.

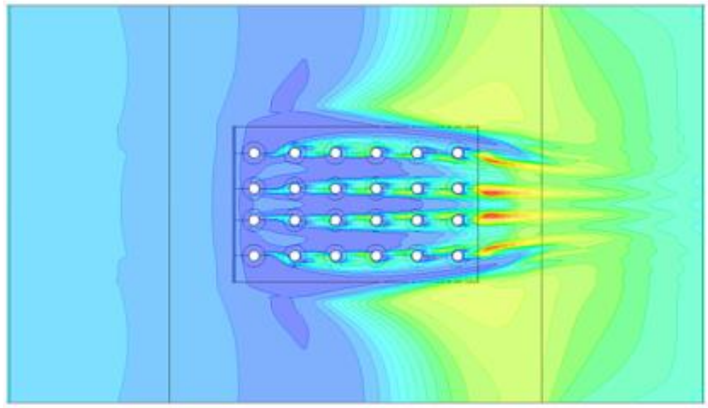

a) I=2%, VR=8.69e-4*Re

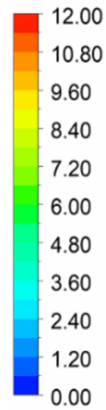

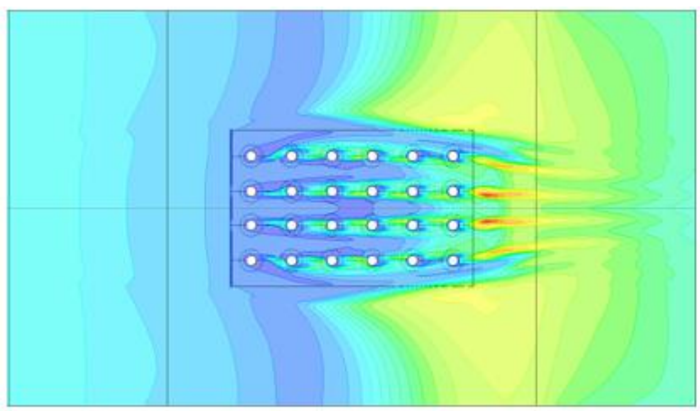

b) I=3%, VR=8.69e-4*Re

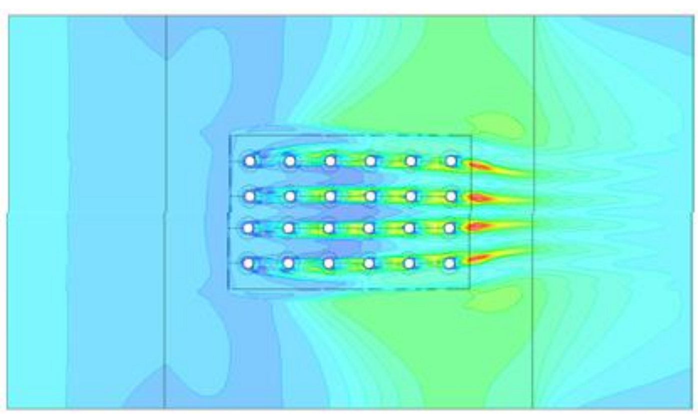

c) I=5%, VR=8.69e-4*Re

Figure 3-10: The variation of viscosity ratio at the central plane for different inlet intensity.

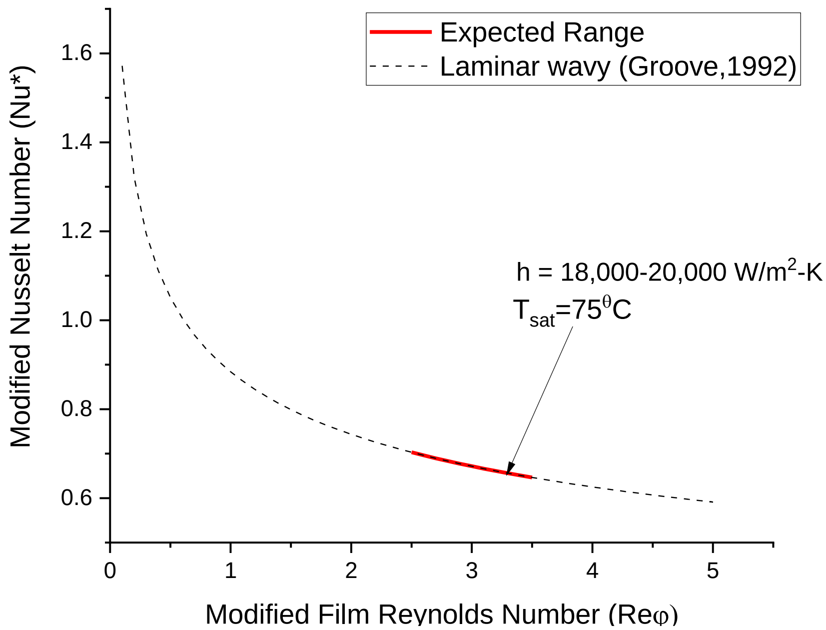

Figure 3-11: The expected range of modified Nusselt number (Gross:1992) for the saturation temperature of 75°C

Symmetry boundary condition

Due to the lack of past numerical studies for partially ducted finned tube geometry, different symmetrical boundary conditions were tested, as shown in Figure 3-12. For the staggered model, case 1 was not feasible due to a lack of symmetry at the central plane. Hence, only case 2 and 3 were considered. The effect of the symmetry boundary condition on the ratio of approach to upstream velocity (Velocity ratio) can be seen in Figure 3-13. There was a marginal change in velocity ratio for staggered as well as inline tube arrangement. Figure 3-14 shows the effect of the symmetry boundary condition on the Colburn j-factor and the friction factor. The Colburn j-factor and the friction factor is almost identical for case-2 and 3 and a little higher for case -1. The velocity profile was plotted at many randomly chosen locations in the domain. Case 2 and 3 produce almost equivalent profiles, unlike case-1. Hence symmetricity was considered at half of the fin pitch (case-3).

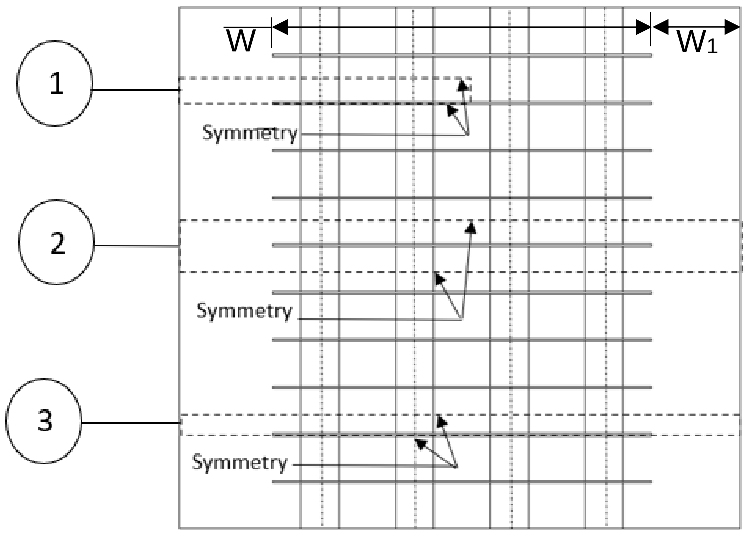

Front View: Inline partially ducted geometry
(Flow direction inwards to plane)

Figure 3-12: The different possible symmetry boundary conditions for partially ducted geometry.

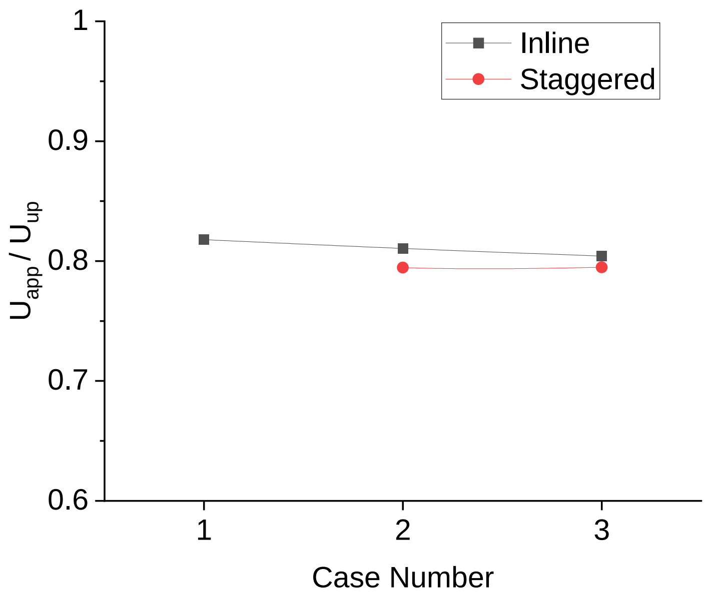

Figure 3-13: The effect of different symmetry boundary conditions on the velocity ratio for a partially ducted model.

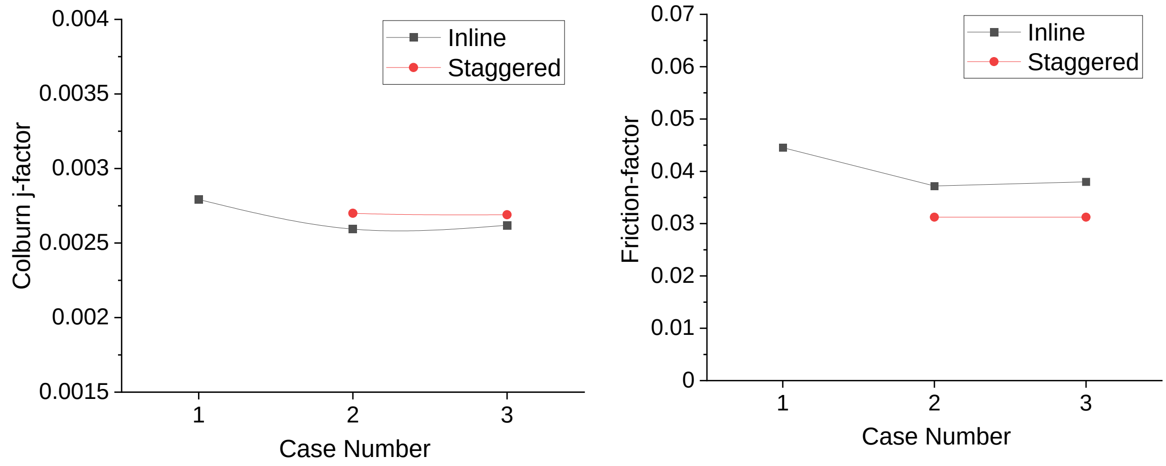

Figure 3-14: The effect of different symmetry boundary conditions on the heat transfer and the friction factor for a partially ducted model.

Nature of the flow: Unsteady Versus steady

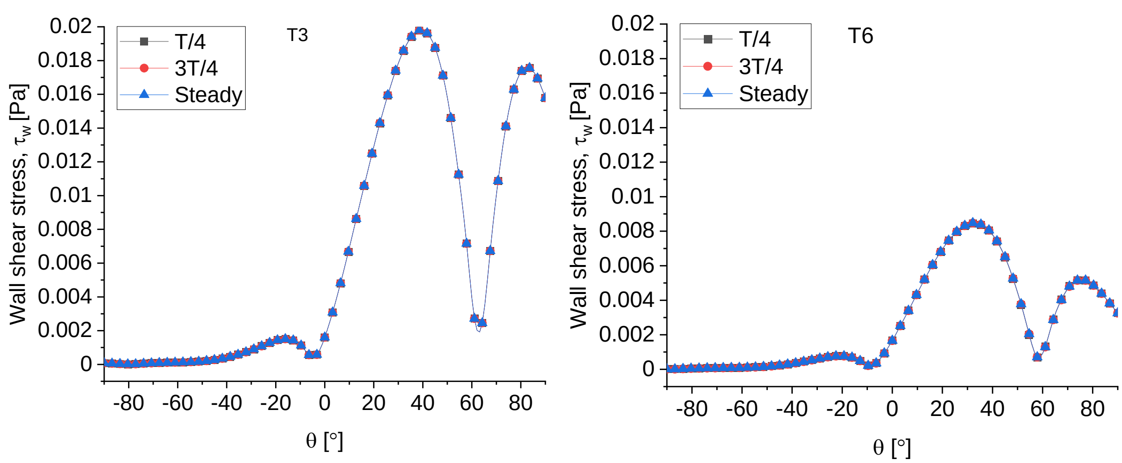

Figure 3-15: Unsteady state instantaneous wall shear stress and steady-state wall shear stress around the third and the sixth row of the tube, where T is the time estimated from strouhal number of 0.2.

This section compares the result from steady and unsteady simulations of typical geometries for a bypass case. In the past, several studies assumed a steady flow behaviour for the finned tube heat exchanger for the fully ducted geometry [12] [24] [22]. However, flow separation downstream can lead to the shedding of vortices. Hence, unsteady simulations were performed in this study to assess the influence of unsteadiness in the flow. The time step was set to 1/20 times the time estimated for shedding at a Strouhal number of 0.2. Unsteady flow behaviour was seen in the exit wakes after exiting from the fins. The fin seemed to limit the unsteadiness for the partially ducted case as well, as seen by Tala for the fully ducted case [61]. Instantaneous and steady-state wall shear stress around the center tube and the last tube are compared in Figure 3-15. There is no difference in the unsteady and steady results. Hence, a steady flow was assumed throughout the study.

3.2.5. Evaluation of Colburn j-factor and Friction Factor

The mass-weighted average temperature at the outlet of the calculation domain was assumed as the outlet temperature T_{out}.

$$T_{out} = \frac{\int T\rho\overrightarrow{u.dA}}{\int \rho\,\overrightarrow{u.dA}} \tag{3-28}$$

The air-side heat transfer rate was calculated using the areal integral from the tube inner walls, as specified below.

$$\dot{Q} = \iint (\text{Wall Heat Flux})\; 2 * \pi * r * dr * dz \tag{3-29}$$

From the air-side heat transfer rate, the heat transfer coefficient is evaluated by the following equation, where A_o is the overall heat transfer area and η_o is the fin effectiveness.

$$h = \frac{\dot{Q}}{\eta_o * A_o * LMTD} \tag{3-30}$$

where LMTD is the logarithmic mean temperature difference given by.

$$LMTD = \frac{T_{in} - T_{out}}{\ln \frac{T_{in} - T_{sat}}{T_{out} - T_{sat}}} \tag{3-31}$$

The Colburn j-factor has been defined as per the following correlation as adopted by

$$j = \frac{h}{\rho * c_p * U_m} Pr^{2/3} \tag{3-32}$$

where,

$$U_m = U_{up}\frac{A_{fr}}{A_c} \tag{3-33}$$

The finned surface effectiveness, η_o is the ratio of actual heat transfer to the heat transfer rate occurring when both fin and base are at the same temperature. This term may be written in terms of fin efficiency, η, fin surface area A_f and the total surface area A_o.

$$\eta_o = 1 - \frac{A_f}{A_o}(1 - \eta) \tag{3-34}$$

In the present investigation, the Schmidt (1949) approximation for inline and staggered plain fin geometry has been used. The iterative process has been used using equations from 3-35 to 3-42.

$$\eta = \frac{\tanh(m * r * \emptyset)}{m * r * \emptyset} \tag{3-35}$$

$$m = \sqrt{\frac{2 * h}{K_f F_t}} \tag{3-36}$$

$$\emptyset = \frac{R_{eq}}{r}\left[1 + 0.35 * \ln\left(\frac{R_{eq}}{r}\right)\right] \tag{3-37}$$

$$\frac{R_{eq}}{r} = 1.28 * \frac{X_m}{r}\left(\frac{X_l}{X_m} - 0.2\right)^{0.5}, \text{Inline} \tag{3-38}$$

$$\frac{R_{eq}}{r} = 1.27 * \frac{X_m}{r}\left(\frac{X_l}{X_m} - 0.3\right)^{0.5}, \text{Staggered} \tag{3-39}$$

$$X_L = \frac{P_L}{2}, \text{Inline} \tag{3-40}$$

$$X_L = \sqrt{\left(\frac{P_L}{2}\right)^2 + \frac{P_l^2}{2}}, \text{Staggered} \tag{3-41}$$

$$X_M = \frac{P_t}{2} \tag{3-42}$$

The friction factor for fully ducted geometry has been defined as per Kays and London's (1994) definition. ΔP is the pressure difference between inlet and outlet.

$$f = \frac{A_c}{A_o} * \frac{\rho_m}{\rho_{in}}\left[\frac{2\rho_{in}\Delta P}{G_c^2} - \underbrace{(K_c + 1 - \sigma^2)}_{\text{Entrance Effect}} - \underbrace{2\left(\frac{\rho_{in}}{\rho_{out}} - 1\right)}_{\text{Fluid Acceleration}} + \underbrace{(-K_e + 1 - \sigma^2)\frac{\rho_{in}}{\rho_{out}}}_{\text{Exit Effect}}\right] \tag{3-43}$$

Entrance and exit effects are often neglected in the definition of the friction factor for most of the experimental work. So, to compare against the experimental data, the friction factor is defined using the below equation.

$$f_{exp} = \frac{A_c}{A_o} * \frac{\rho_m}{\rho_{in}}[\frac{2\rho_{in}\Delta P}{G_c^2} - 2\left(\frac{\rho_{in}}{\rho_{out}} - 1\right)] \quad 3\text{-}44$$

For partially ducted geometry, the fin effectiveness has not been used in the heat transfer coefficient definition and the friction factor is defined as per the below equations. ΔP_f is the pressure drop between the extreme ends of the heat exchanger core.

$$f_1 = \frac{(\Delta P_f)}{0.5\rho U_{max}{}^2} \frac{A_c}{A_o} \quad 3\text{-}45$$

3.3. Code Validation

The validation was conducted at low velocity (0.1 m/s) and high velocity (5 m/s), to make sure that the low Reynolds number model can mimic the laminar model and the k- ω SST turbulence model, respectively. The solution was found to be the same for the laminar case and a maximum discrepancy of 0.7% was observed in overall the pressure drop and the heat transfer for the turbulent case. The eddy viscosity was found to be very low in the case of a laminar flow field using low Reynolds number k-ω SST turbulence model. Hence, this model can be applied to a mixed flow field for this geometry.

The present simulations were validated by comparing the numerical results for fully ducted plain fin and tube heat exchangers with the published experimental results. The validations were done for various geometrical configurations for heat transfer and pressure drop, while the flowfield was validated against PIV data.

Table 3-4: Geometrical parameters for code validation

Case	**Fp**	**Do**	**N**	**Pt**	**Pl**	**Tin(°C)**	**Vin(m/s)**	**T_w(°C)**	***Layout***
1	7.5	8	3	27	26	3	0.86, 1.1, 1.4	33	Inline
2	10	8	2	27	26	3	1.1, 1.25, 1.4	33	Inline
3	15	8	2	27	26	3	1.1, 1.25, 1.4	33	Inline

Note: All non-specified dimensions are mm.

The validation for higher fin pitch geometry was done against the experimental data of Kim et al [16]. The geometry and other parameters for the model used for validation are given in Table 3-4. The j-factor from the simulations are compared to the correlation of Kim et al [16] given by

$$j = 0.170 * (Re_{Dh}^{-0.349}) * N_1^{-0.141} * (\frac{F_P}{D_o})^{0.384} \tag{3-46}$$

In Kim et al [3], ethylene glycol water mixture with a mass flow rate of 150 Kg/hr with 33°C inlet temperature was inside the tubes, and humid air (60%) was on the outside. In the simulations, the tube temperature is assumed constant as 33°C and dry air is used. Figure 3-16 shows the Colburn j-factor for the numerical simulations and the experimental correlation. There is good agreement between the correlation and the computed values, with a maximum difference of approximately 7%. The simulation results are lower than the experiment values because dry air has lower thermal conductivity than the wet air.

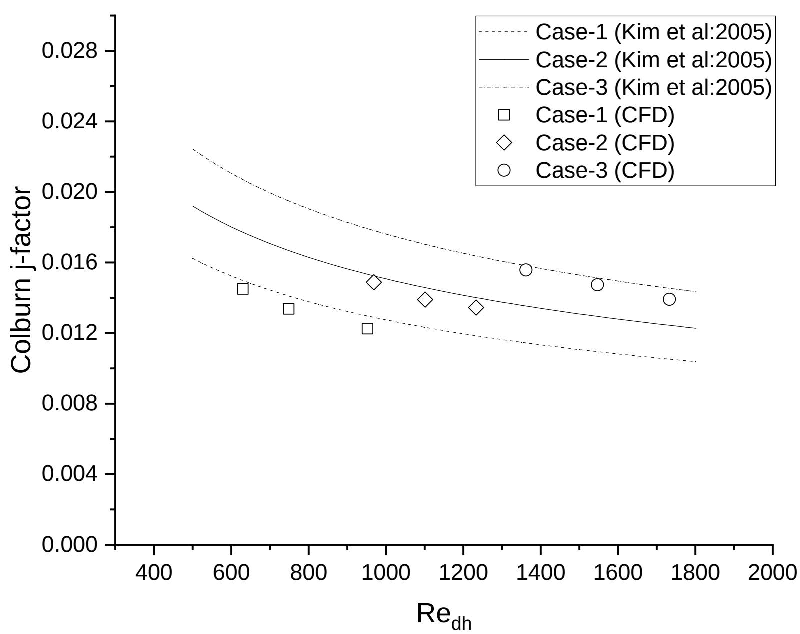

Figure 3-16: The Colburn j-factor for plain fin and tube heat exchanger compared with the correlation of Kim-et al *[16]*.

Table 3-5: Geometry for code Validation (All dimension in mm)

Fp	**Ft**	**Dc**	**Pt**	**Pl**	**N**
3.16	0.13	10.23	25.4	22	6

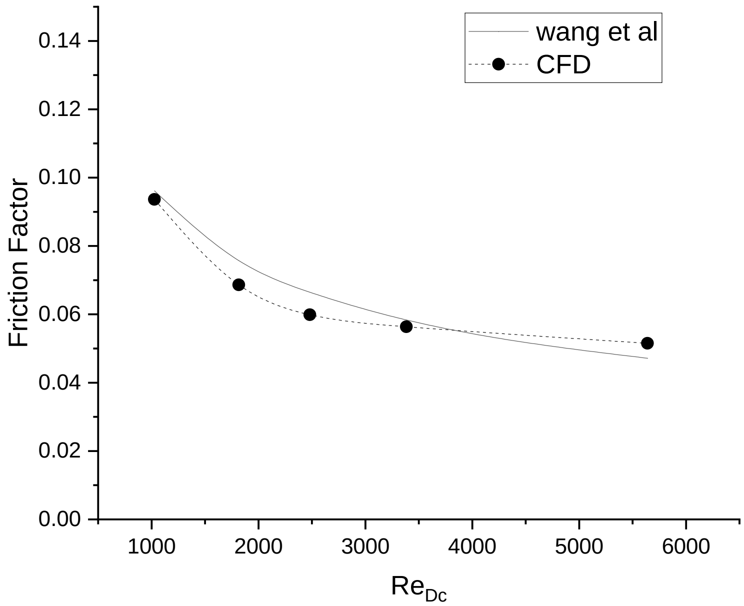

Figure 3-17: The friction factor for plain fin and tube heat exchanger compared with the correlation of wang-et al [7].

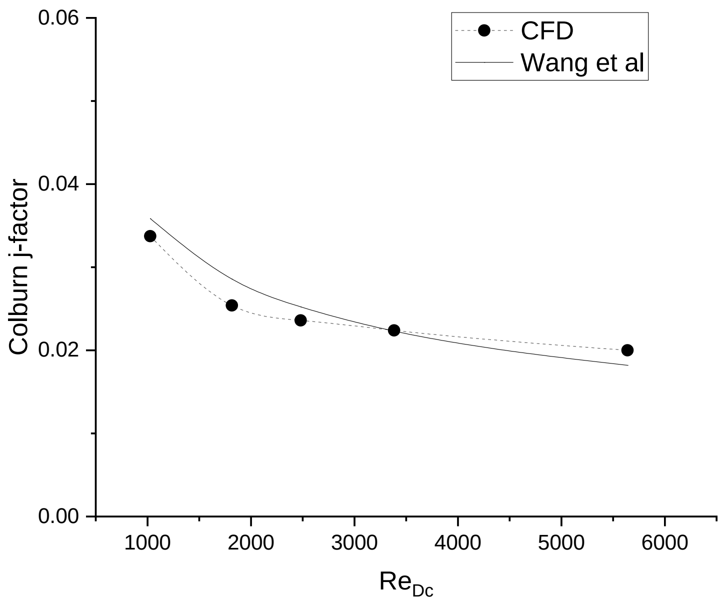

Figure 3-18: The Colburn j-factor for the plain fin and tube heat exchanger compared with the correlation of wang-et al [7].

Validation for lower fin pitch geometry was done against the experimental data of Wang et al *[7]*. The geometry used for the simulation is specified in Table 3-5. Figure 3-17 and

Figure 3-18 show the comparison of computed values for the j-factor and friction factor with the experimental correlation of Wang et al *[7]*. The maximum difference between the numerical results and the experimental correlation was found to be 10% for the friction factor and Colburn j-factor respectively which is equivalent to the correlation accuracy of 10%.

Table 3-6: Geometrical specification for flow field validation *[70]*.

Fp/Do	Ft/Do	Pt/Do	Pl/Do	Pl	N	Do (mm)
0.234	0.0143	2.143	1.643	22	2	7

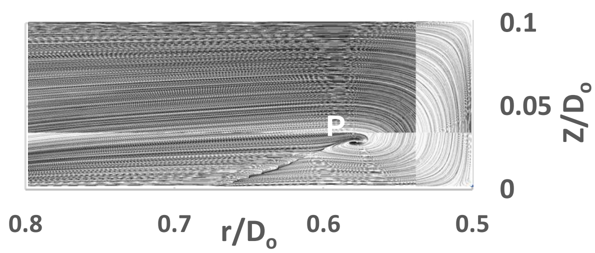

a) First tube (CFD)

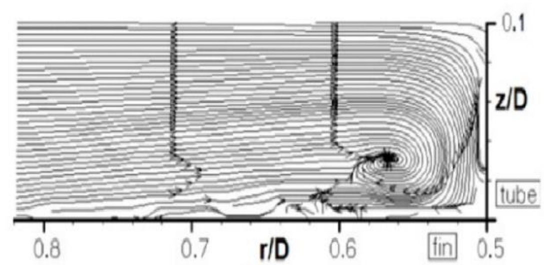

b) First tube (PIV measurement [70])

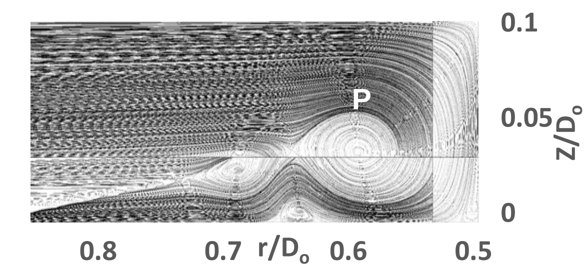

c) Second tube (CFD)

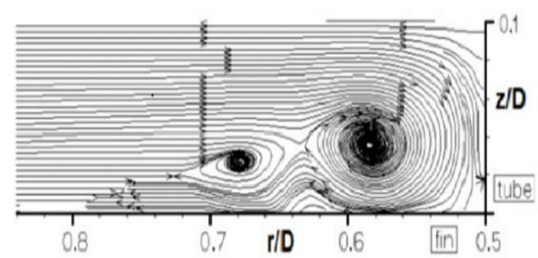

d) Second tube (PIV measurement [70])

Figure 3-19: Comparison of the simulated streamlines in the frontal planes with PIV derived streamlines.

To check the reliability of the simulation to capture the flow field, the mean flow structure was locally compared at each tube junction to the PIV data on the staggered fin and tube heat exchanger by *[70]*. The geometry specification used for simulation is shown in Table 3-6. The results are presented in Figure 3-19, where streamlines are shown in the front plane of each tube-fin junction. The flow pattern in front of the first tube consists only of a single primary vortex P1 (see Figure 3-19 (a), (b)). A complex structure is observed in the front plane of the second tube where the horseshoe vortex is made up of two primary vortices P1 & P2 and a secondary vortex S1. The comparison of the numerical streamlines to PIV data shows good agreement between the position of the vortices. The position of primary vortex P1 is quantitatively confirmed to PIV measurement in Table 3-7.

Table 3-7: The validation of the primary vortex core (P1) located on the frontal plane of the second tube

Location	**Present study**	**PIV measurement** [70]	**Discrepancy**
r/Do	0.594	0.59	0.6%
Z/Do	0.0396	0.0379	4.2%

Chapter 4.

Fully Ducted Heat Exchangers

This chapter presents the results of the fully ducted large tube pitch inline plain fin and tube heat exchanger (PFTHE). These geometries are not as frequently considered as the staggered geometry. The results are compared with a staggered geometry for a range of pitch sizes and Reynold numbers. The heat transfer and pressure drop for different tube configurations are compared. The development of horseshoe vortices that increases the heat transfer and the wall shear stress are characterized and compared. The effect of these vortices on the heat transfer and pitch sizes are discussed.

The effect of the geometrical parameter like fin pitch on the heat transfer and pressure drop for the large pitch in line geometries is then considered. The results are presented in the form of friction factor and Colburn-j factor for Reynolds number based on outer tube diameter ranging from 1450-7000, typical of many practical applications. The different components of pressure drop, including the effect of abrupt contraction effects, the abrupt expansion effects and the friction pressure loss, are considered and compared with correlations. A correlation for the Colburn j-factor and friction factor is developed for a fully ducted finned tube heat exchanger based on 280 different samples to fill the design space for 3 to 6 tube rows with a tube pitch of 3 to 4 diameters; a fin pitch of 0.25 to 0.65 diameters and Reynolds number of 1450 to 7000.

4.1. Identification of flow regime

The different flow regimes were identified by performing simuations for the geometry with 6 number of tube rows, fin pitch of 0.25 diameters, transverse tube pitch of 3.5 diameters, longitudinal tube pitch of 4 diameters for the Reynolds number ranging from 800 to 10000. The plot of Colburn j-factor with Reynolds number on a log-log plot (Figure 4-1) shows the change from laminar to transition at Reynolds number of approximately 1450 and transitional to turbulent regimes at Reynolds number of approximately 4500. Plots of eddy viscosity on the central plane for the laminar, transitional and turbulent regimes are shown in Figure 4-2. The model estimates the eddy viscosity in the range of 10^{-13} for the laminar flow for Reynolds number less than 1450. For Reynolds number in the range of 1450-

4500, the flow in the central channel region is transitional with the transitional to turbulent wakes from the tube. For higher Reynold numbers, the flow is completely turbulent in the channel region as well.

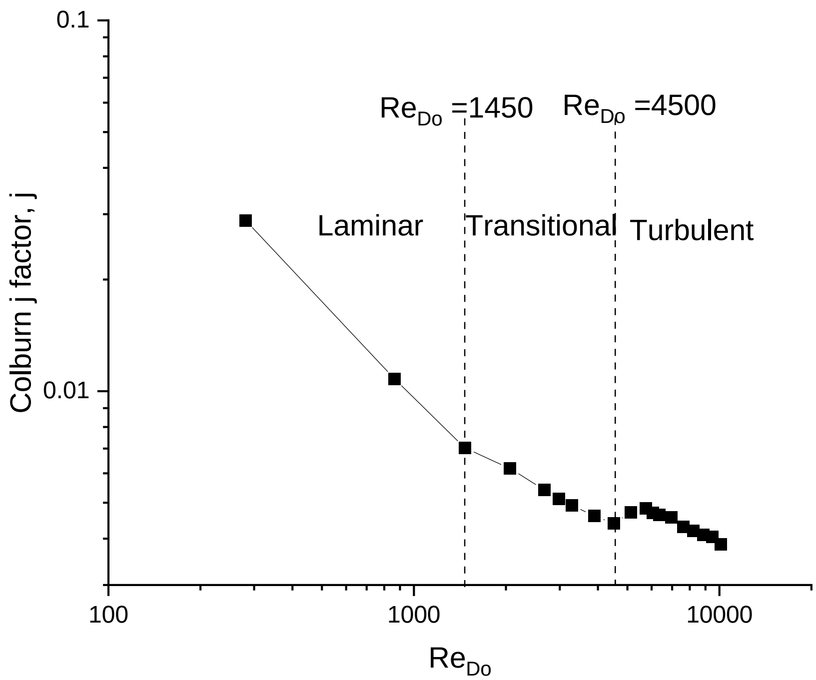

Figure 4-1: The plot of Colburn j-factor with Reynolds number showing different flow regimes.

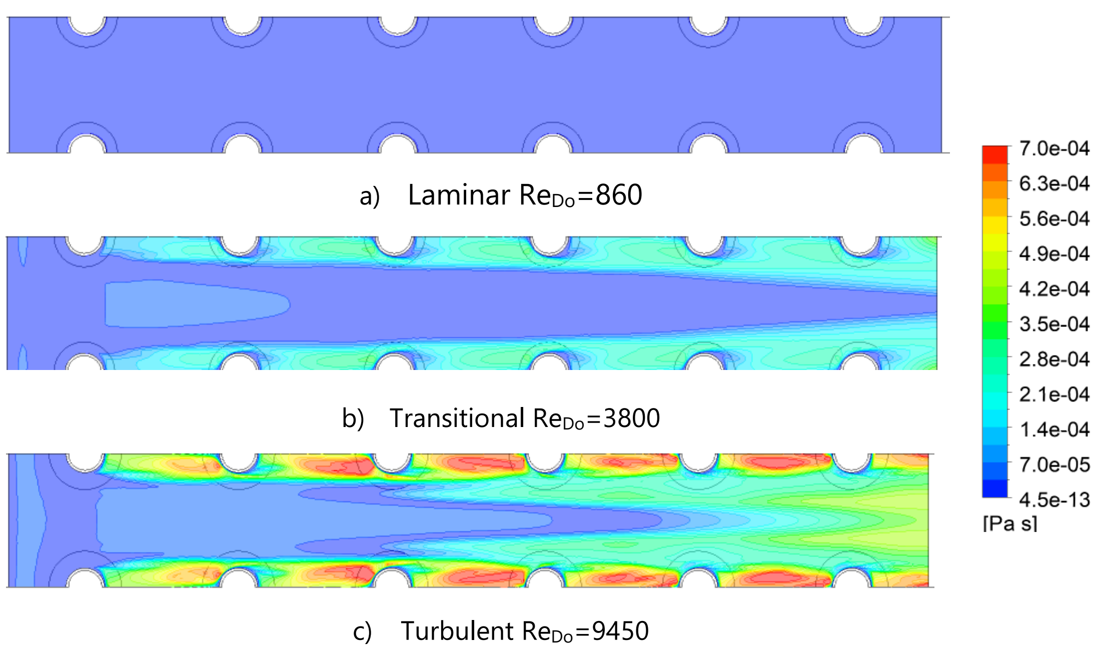

Figure 4-2:Eddy viscosity on the central plane for different flow regimes based on low-Reynolds number k-ω SST turbulence model.

Figure 4-3 shows the heat transferred with streamwise tube rows for laminar, transitional and turbulent regimes. For laminar flow, the heat transfer from the downstream row is always less than the upstream row. For transitional flow, the exiting wakes from the tube slightly improves the heat transfer in the downstream row of the tube and the effect increases on increasing the Reynolds number as the exit wakes from the tube changes from laminar to turbulent. The decrease in heat transfer with tube rows becomes less as the Reynolds number is increased, and at Reynolds number of 4500, the heat transfer increases slightly in the last two rows than in the preceding row. For turbulent flows, the heat transfer in the latter tube rows is higher than the upstream tube row since the turbulence creates a good mixing and increases the heat transfer.

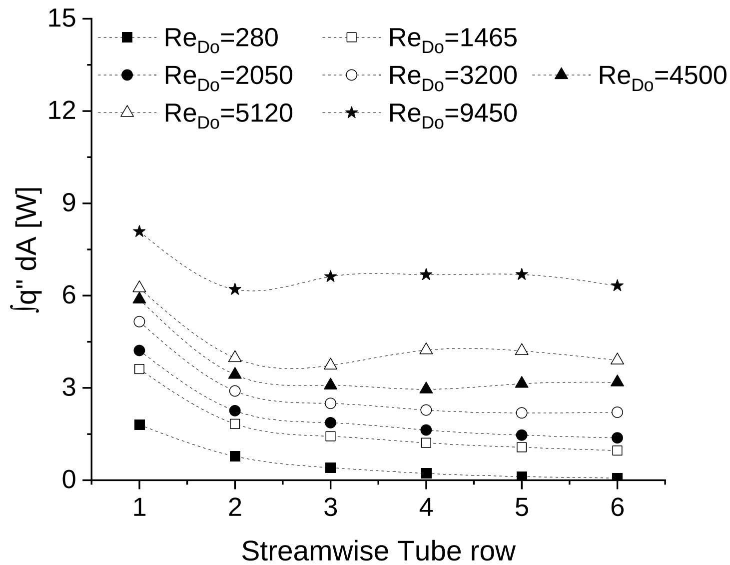

Figure 4-3: Total heat transferred with streamwise tube row for different Reynolds numbers.

4.2. The Effect of the tube configuration

The effect of the tube configuration was compared for the geometries summarized in *Table 4-1*. The first two are typical of the compact geometries used in many staggered configurations ([6] [3] [28] [7] [9] [8]) while the third reflects large pitch typical of the inline geometry of interest here. All the geometries have six tubes.

Figure 4-4 shows the streamlines on the central plane for the large tube pitch case for inline and staggered geometry with a tube pitch of 2.5 diameters. For the Inline geometry, the flow circulates the first tube but passes through the channel between the remainder of the tubes to the outlet contacting a small fraction of each tube. The longitudinal space between the two tubes is enclosed entirely within the recirculation zone. However, for the staggered tube arrangement, the flow circulates each tube. Successive accelerating regions and decelerating regions are formed as the flow moves downstream. A recirculation zone is present behind each tube.

Table 4-1: The geometrical specification

Case study	$\frac{P_t}{D_o}$	$\frac{P_l}{D_o}$	$\frac{F_P}{D_o}$	N	D_o
1	1.9	1.9	0.625	6	15.88
2	2.5	2.5	0.625	6	15.88
3	3.5	4	0.625	6	15.88

Note: All dimensions in mm

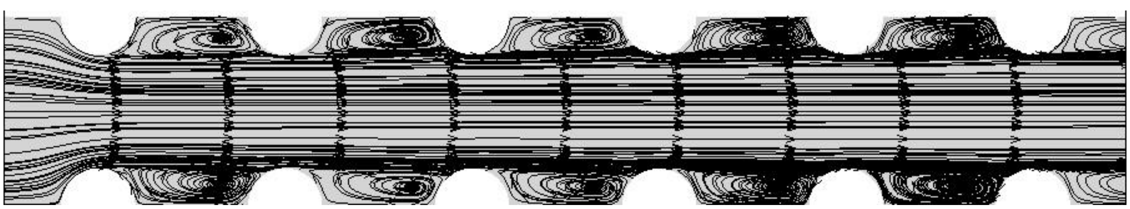

a) Inline tube layout

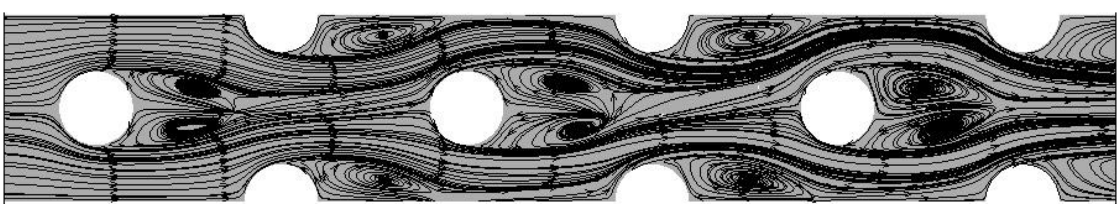

b) Staggered tube layout

Figure 4-4: The streamlines on the central plane for staggered and inline geometry with the tube pitch to diameter ratio of 2.5 for Re_{Do}=3000.

Figure 4-5 shows the heat flux on the fin surface for inline and the staggered tube arrangement with the tube pitch to diameter ratio of 2.5 for Re_{Do}=3000. For the inline case, there is a high heat transfer rate at the entrance and around the first tube due to the flow separation at the entrance, the developing boundary layer and the development of a horseshoe vortex behind the finned tube junction. There is not a similar increase in heat transfer around subsequent tubes. In the staggered tube arrangement, there is a high heat transfer rate around the successive rows of tubes, though it starts to diminish after the second row. Figure 4-6 shows the wall shear stress magnitude on the fin for the inline and the staggered tube arrangement with the tube pitch to diameter ratio of 2.5. For the Inline case, there is high wall shear stress around the first tube and at the entrance between the tubes. However, for the staggered tube arrangement, a high wall shear stress can be seen in front of the downstream tubes as well.

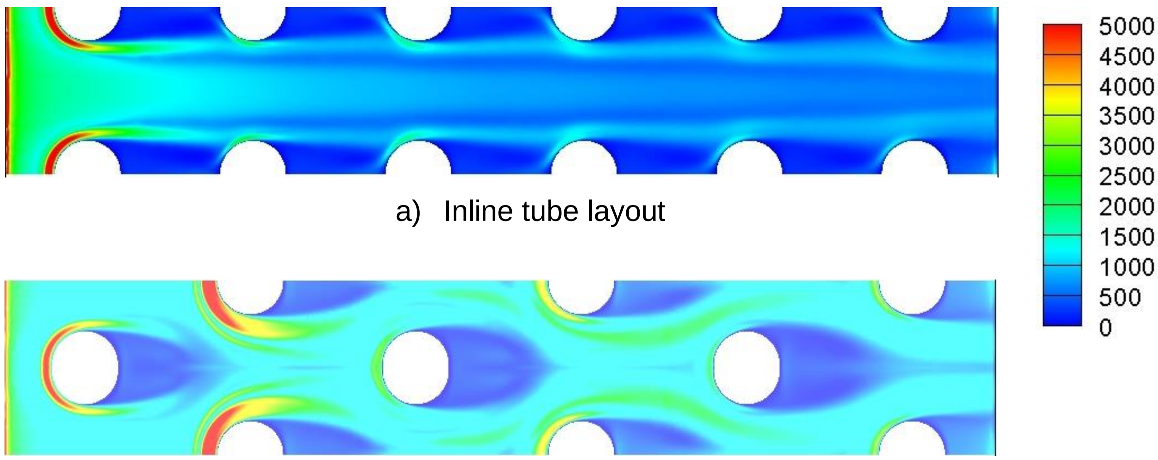

a) Inline tube layout

b) Staggered tube layout

Figure 4-5: Wall heat flux on the fin surface for an inline and staggered case with the tube pitch to diameter ratio of 2.5 for Re_{Do}=3000.

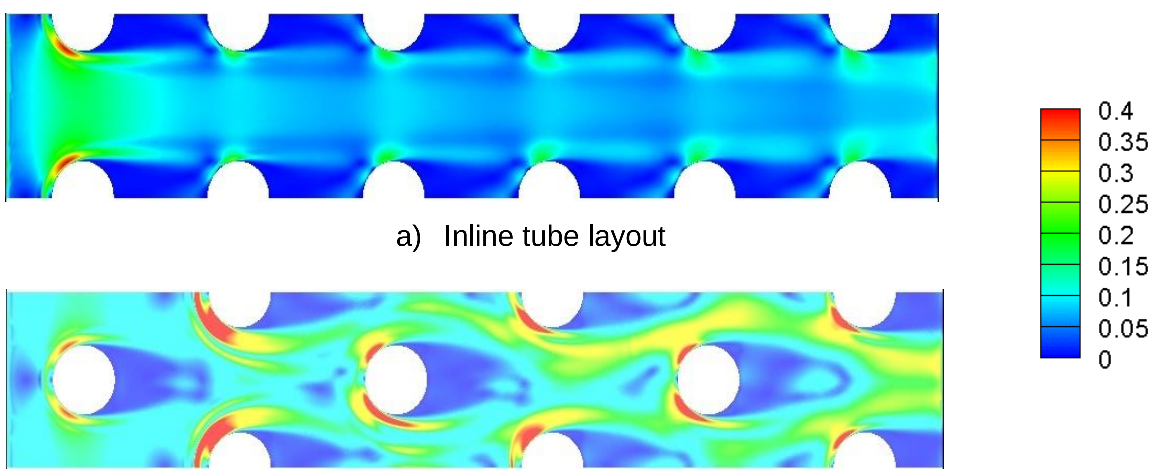

a) Inline tube layout

b) Staggered tube layout

Figure 4-6: Wall shear stress magnitude on the fin surface for the inline and staggered case with the tube pitch to diameter ratio of 2.5 for Re_{Do}=3000.

The increase of heat flux and wall shear stress around the tube for the inline and the staggered tube arrangement is due to the presence of horseshoe vortices. Figure 4-7 & Figure 4-8 shows the streamlines on the different planes around the tube overlapped with the contours of heat flux on the fin for inline and staggered geometry for the tube pitch of 2.5 diameters. Around the first tube, the horseshoe vortex system consists of two co-rotating primary vortices, a counter-rotating secondary vortex and a corner vortex for both inline and staggered geometry. The second primary vortex completely disappears after 0° planes for the inline case. The corner vortex was observed only at 30° and 60° planes. For inline geometry, there is a single primary vortex at 30° planes around the subsequent row. For staggered geometry, the horseshoe vortex system is less developed around T1 than T2, which may be a consequence of a smaller boundary layer thickness around the first tube. It is evident from Baker (1979) that the horseshoe vortex depends on the boundary layer. The horseshoe vortex system has three primary vortices, two secondary vortices and a corner vortex around the second tube. Around the later rows, there are two primary vortices, a secondary vortex and a corner vortex. The single primary vortex is visible at the 0° plane around the third tube and completely disappears at the 0° plane around the last tube. The corner and a secondary vortex are visible at a 90° plane. It is interesting to note the spatial evolution of these vortices. The primary vortex wraps around the tube from 0-90° and progressively disappears with an increase of azimuthal angle. The corner vortex is observed at 30° and 90° planes and not seen at 0° plane.

Figure 4-9 & Figure 4-10 shows the streamlines on the different planes around the tube on the contours of heat flux for inline and staggered geometry for the large tube pitch of 3.5 diameters. The results in both cases show that the horseshoe vortex system around the first tube consists of two co-rotating primary vortices, a counter-rotating secondary vortex and a corner vortex. For inline, a weak second primary vortex was observed at 0° plane but not evident at a 30° plane or later. The corner vortex was observed only at 30° and 60° planes. For succeeding tubes, there is a single primary vortex on 30° planes, and the strength decreases for the next rows. For the staggered tube geometry, the horseshoe vortex system has three primary vortices, two secondary vortices and a corner vortex around the second tube. For succeeding tubes, there is a presence of the single primary vortex. However, for the last two tubes, the presence of the vortex can only be seen at a 60° plane. The primary vortex wraps around the tube from 0-90° and progressively disappears with the increase of azimuthal angle. The corner vortex is observed at 30° and 90° plane and not seen at 0° plane.

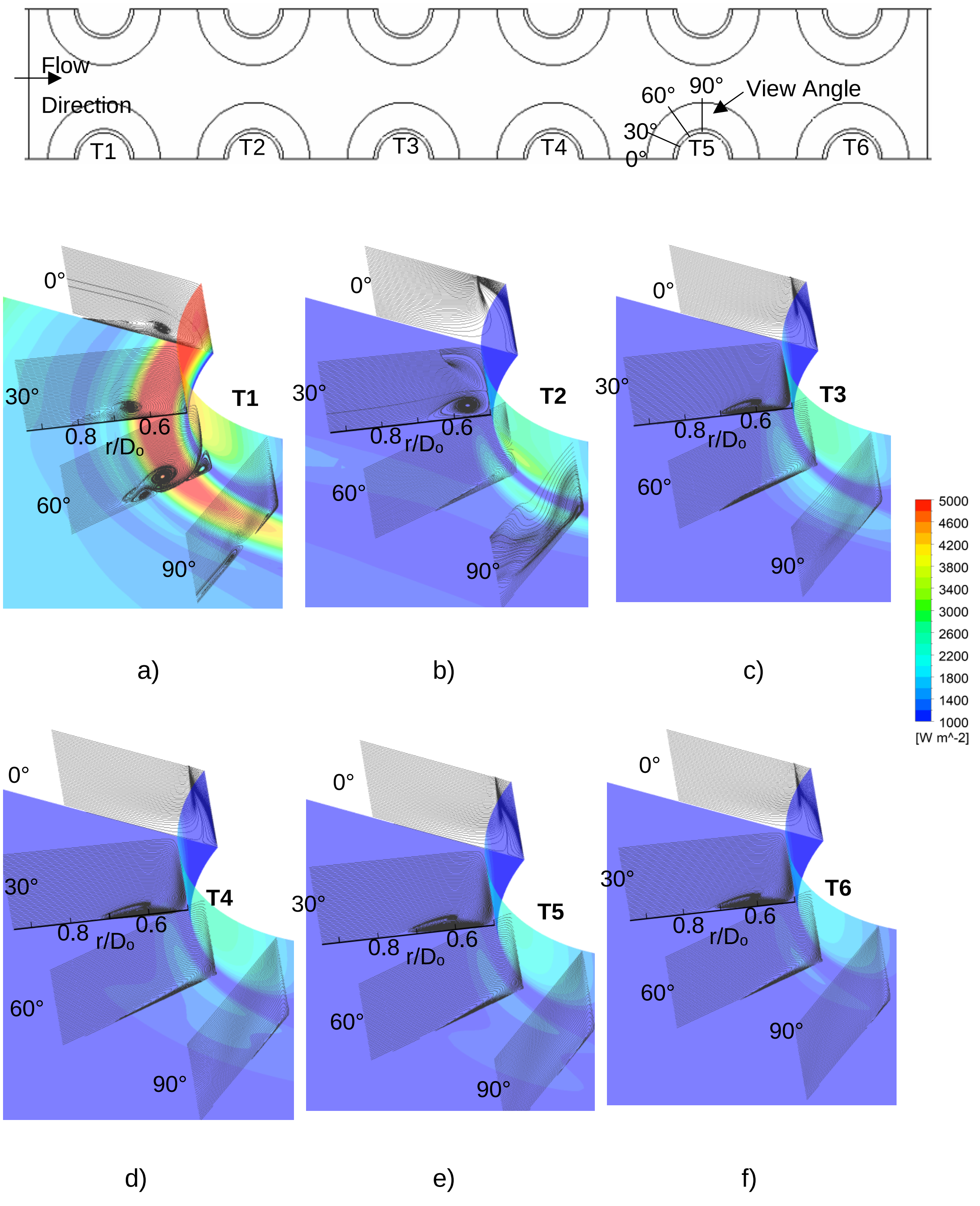

Figure 4-7: Identification of the horseshoe vortices around each tube for an inline geometry with the tube pitch of 2.5 diameters with overlapping contours of heat flux for Re_{Do}=3000

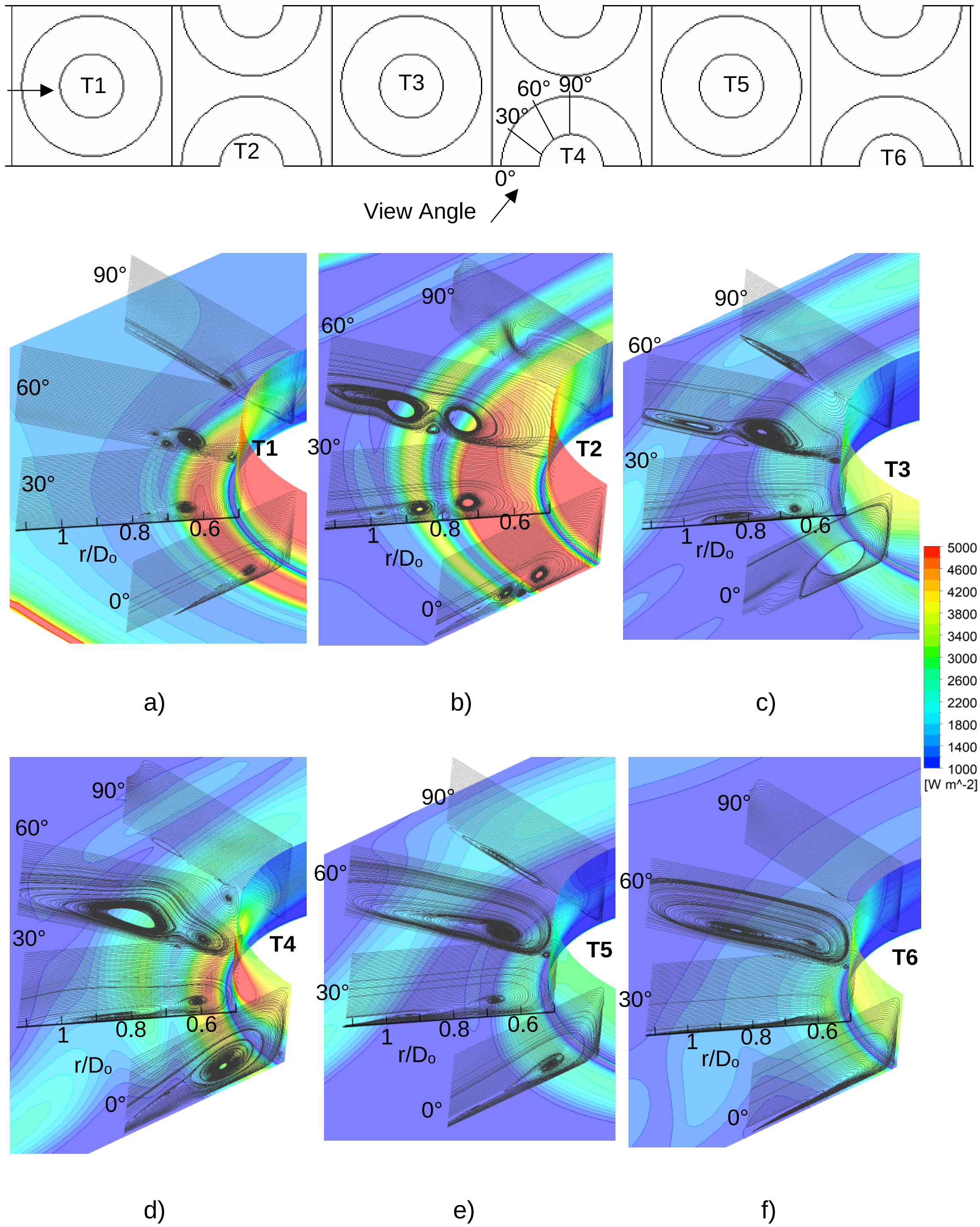

Figure 4-8: Identification of the horseshoe vortices around each tube for a staggered tube arrangement for tube pitch of 2.5 diameters with overlapping contours of the heat flux for Re_{Do}=3000.

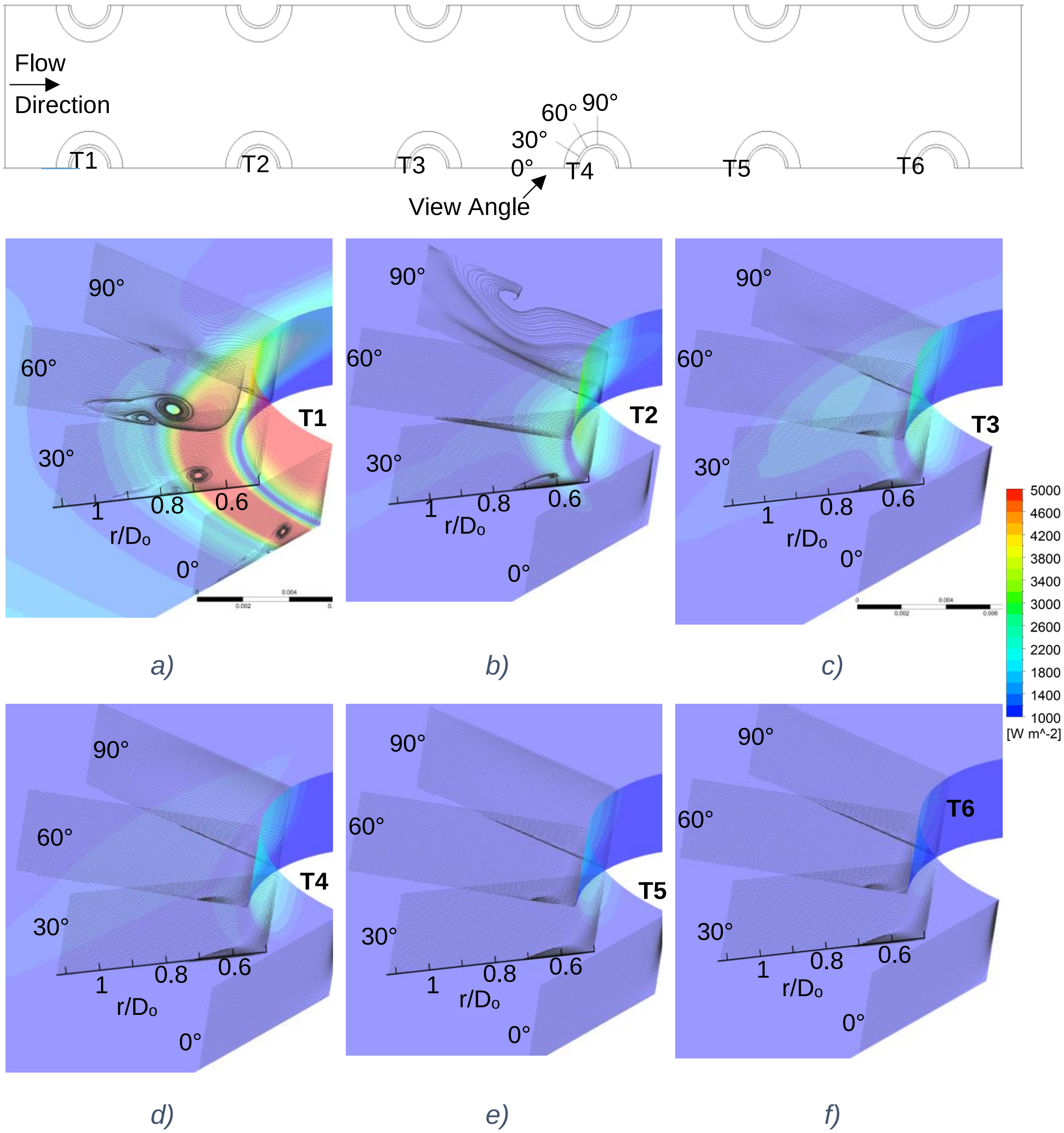

Figure 4-9: Identification of the horseshoe vortices around each tube for an inline geometry with the tube pitch of 3.5 diameters with overlapping contours of heat flux for Re_{Do}=3000.

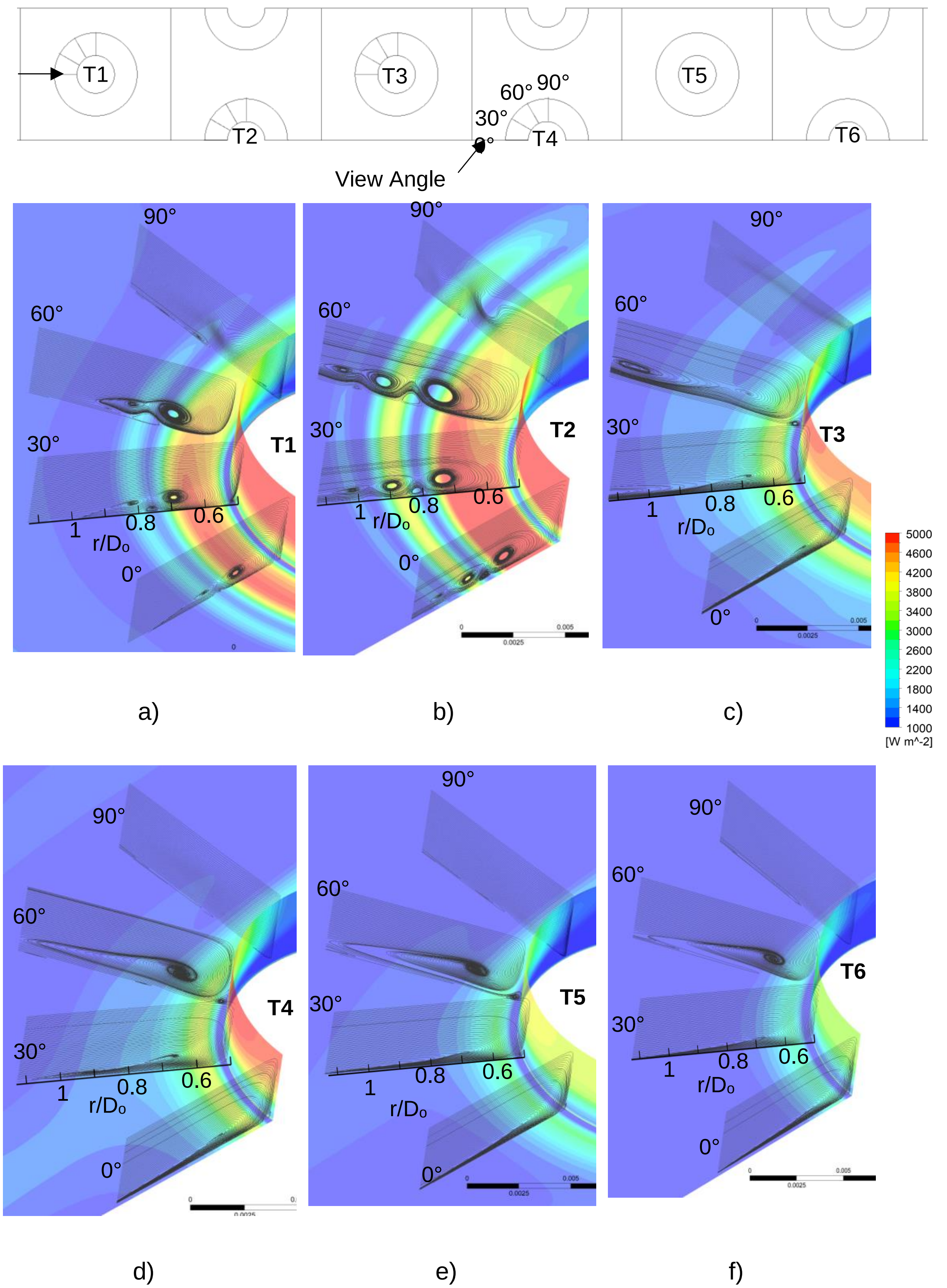

Figure 4-10: Identification of the horseshoe vortices around each tube for staggered tube arrangement for large tube pitch cases with overlapping contours of the heat flux for Re_{Do}=3000.

Figure 4-11 & Figure 4-12 shows the streamlines on the different planes around the tube on the contours of heat flux for inline and staggered geometry for the small tube pitch of 1.9 diameters. The results in both cases show that the horseshoe vortex system around the first tube consists of two co-rotating primary vortices, a counter-rotating secondary vortex and a corner vortex similar to the previous two cases. A weak second primary vortex was observed at 0° plane but not evident at a 30° plane or later for both tube arrangements. The corner vortex was observed only at 30° and 60° planes. For succeeding tubes, there is a single primary vortex on 30° planes. For staggered geometry, the horseshoe vortex system has two primary vortices, one secondary vortex and a corner vortex behind the second row. The increase in height of the second primary vortex can be seen at a 60° plane. Around the third tube, a single primary vortex can be seen on at 0° plane. The inclusion of the second primary vortex can be seen at a 30° plane. Around the fourth and the fifth tube, one primary and a corner vortex can be seen with no vortex at 0° plane. No primary vortex is seen at a 0° plane in the vicinity of the fourth tube. Around the last tube, the horseshoe vortex system consists of two co-rotating primary vortices, a counter-rotating secondary vortex and a corner vortex. The second primary vortex completely disappears after a 30° plane. The formation of the horseshoe vortex system behind the later tubes is influenced by the streamlines emerging from the vortices behind the previous tube if the tube pitch is small. It is evident from the contours of the heat flux that there is a rise in heat flux before the location of each primary vortex, and there is a fall in heat flux before the location of each secondary vortex.

Figure 4-13 to Figure 4-15 shows the radial wall shear stress and wall heat flux at the different positions around each streamwise rows of the tube in staggered and Inline geometries for the tube pitch of 2.5 diameters. The positive and the negative signs of the radial wall shear is due to the clockwise or anticlockwise rotation of the flow associated with vortices. Around the first tube, the staggered and inline case shows a similar variation of the radial wall shear stress and heat flux. The local maxima of the radial wall shear stress are associated with the primary vortices. The maximum radial wall shear stress is also decreasing with the angle and is not evident at 90°. Local minima can be seen around r/D_o =0.5-0.55, which is a result of the counter-rotating vortex. The effect of counter-rotating vortex is negligible at 0° plane and increases with angle up to the 60° plane, which shows that the corner vortex becomes more and more intense with an increase of angle. The effect of the second primary vortex can be seen from the local maxima around r/Do=0.75. The effect is less significant than the first primary vortex. Local minima can be observed between two local maxima, which correspond to the secondary vortex. High heat flux can be seen in front of the location of primary and corner vortices. The local minima for the heat flux can be seen in front of the location of the secondary vortex. For the staggered geometry, around the second tube, three local maxima for the radial wall shear stress can be seen corresponding to each primary vortex. The radial distance of the local maxima is increasing with the angle. The effect of the third primary vortex is very small compared with other vortices, which occurs between a radial distance of 0.95 to 1.1 Three local minima can be observed corresponding to the two secondary vortices and one corner vortex. At the 90° plane, two local maxima correspond to the two secondary vortices and show the opposite sense of rotation to the secondary vortices at a lesser angle plane. However, for inline, the effect after the first streamwise tube is less significant. The peak can be seen corresponding to a single primary vortex at the 30° and 60° plane. High heat flux corresponding to each primary and corner vortices and the low heat flux corresponding to the secondary vortices can be seen. Around the third tube, there is the presence of one maximum for radial wall shear at 0° plane corresponding to the single primary vortex. However, at a 30°plane, two local minima and two local maxima in radial wall shear can be seen. For the 60° plane, the radial wall shear continues to be the same value after the rise at a radial distance of 0.95 diameter due to a stretch of the second primary vortex for a long distance. High heat flux can be seen for each corner, and primary vortices and low heat flux can be noticed around the secondary vortex. For 60° and 90° planes, the heat flux continues to rise until last due to the second primary vortex. Around the fourth tube, there are two local maxima and two local minima in radial wall shear stress for the 30° and 60° plane corresponding to two primary, secondary and corner vortices, respectively. A single peak can be noticed at a 0° plane due to a single primary vortex. The peaks in the heat flux corresponding to primary & corner vortices and valleys corresponding to a secondary vortex can be noticed. Around the fifth tube, there are two maxima and two minima in radial wall shear stress for a 0° and a 30° plane corresponding to two primary, secondary and corner vortices, respectively. At a 60° plane, the presence of a corner and primary vortices causes the maxima and minima in the radial wall shear stress profile. The continuous rise in the radial wall shear stress till r/D_o of 0.95 is due to the stretch of the second primary vortex till the end. Around the sixth tube, there is one local minimum and one local maximum in radial wall shear stress associated with the corner and a primary vortex. The peaks and valleys in radial wall shear stress and heat flux for other tube pitch corresponding to each primary, secondary, and corner vortices change similarly.

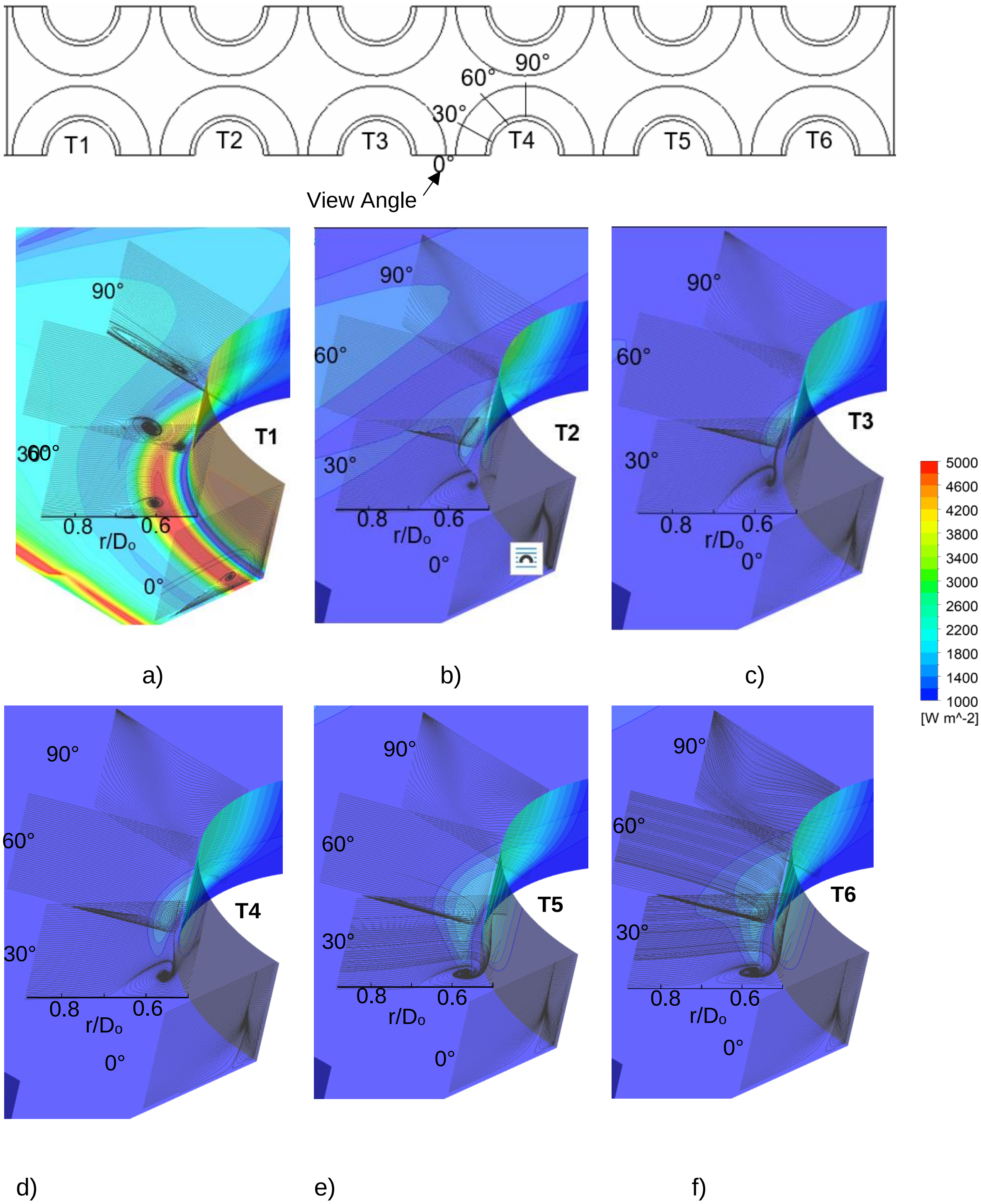

Figure 4-11: Identification of the horseshoe vortices around each tube for an inline geometry with the tube pitch of 1.9 diameters with overlapping contours of heat flux for Re_{Do}=3000

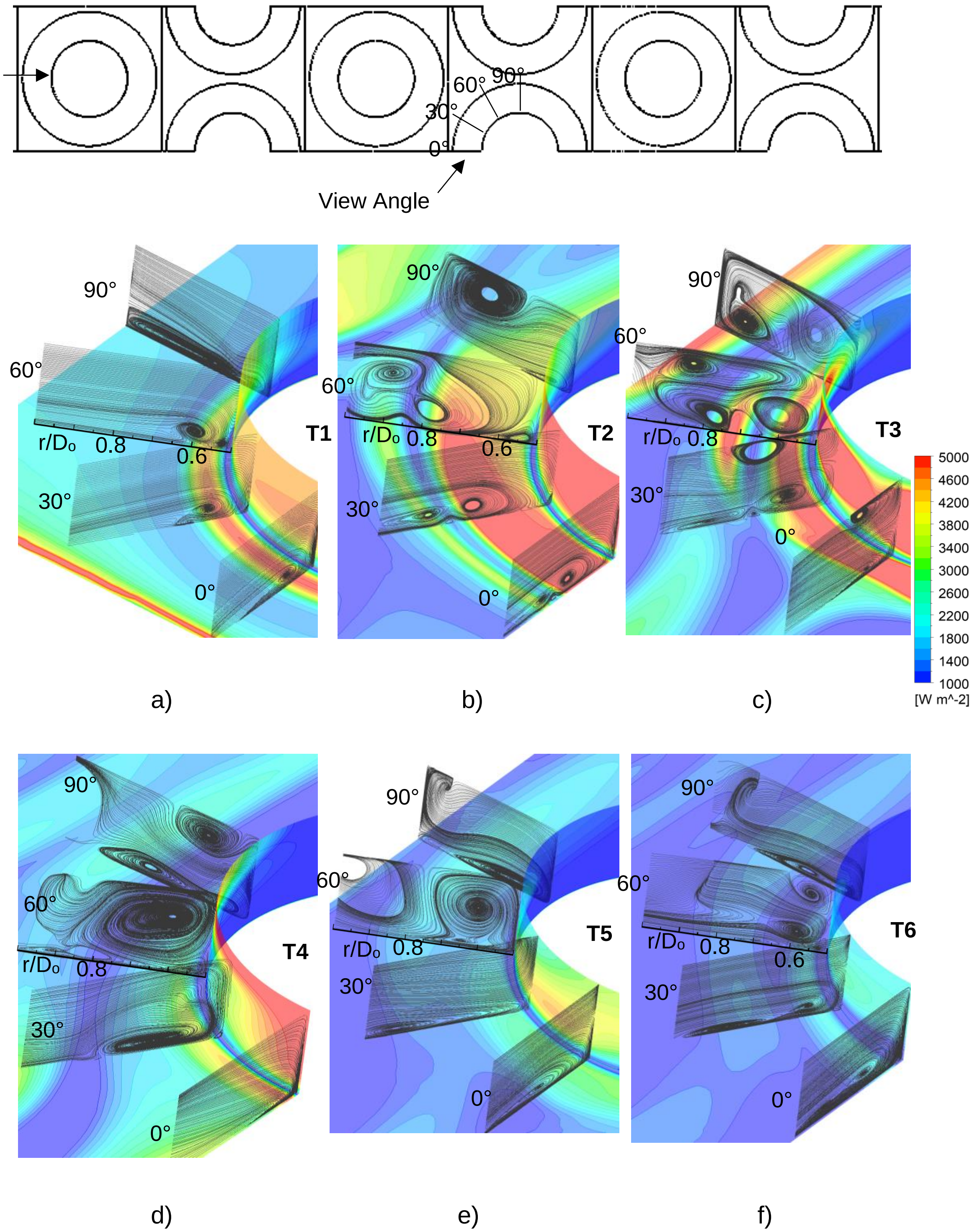

Figure 4-12: Identification of the horseshoe vortices around each tube for a staggered tube arrangement for tube pitch of 1.9 dimeters with overlapping contours of the heat flux for Re_{Do}=3000.

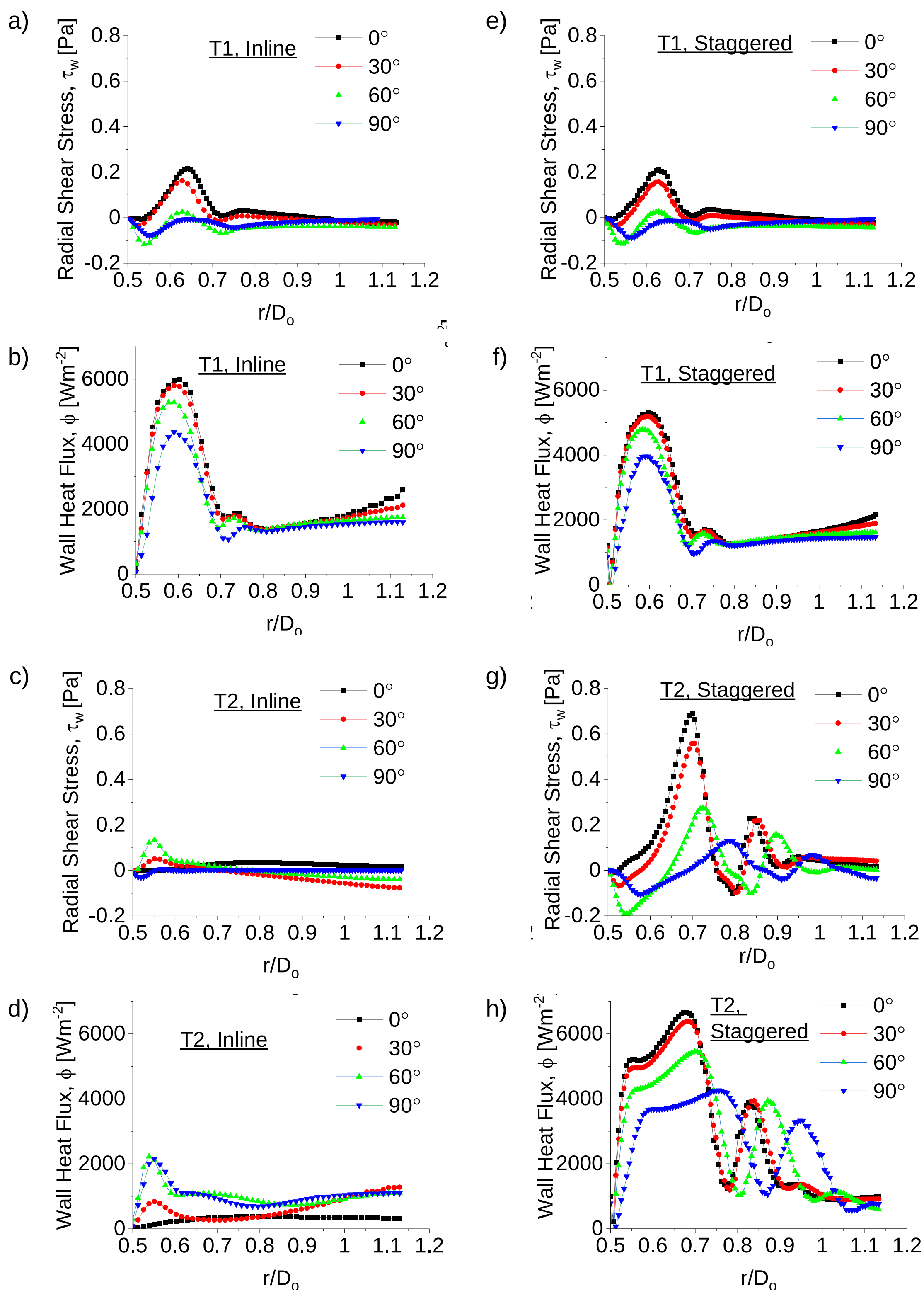

Figure 4-13: Radial wall shear and heat flux vs the radial distance on 0-90° plane for tube T1, T2 for the Inline (Left) and the staggered tube arrangement (right) for tube pitch of 2.5 diameters for Re_{Do}=3000.

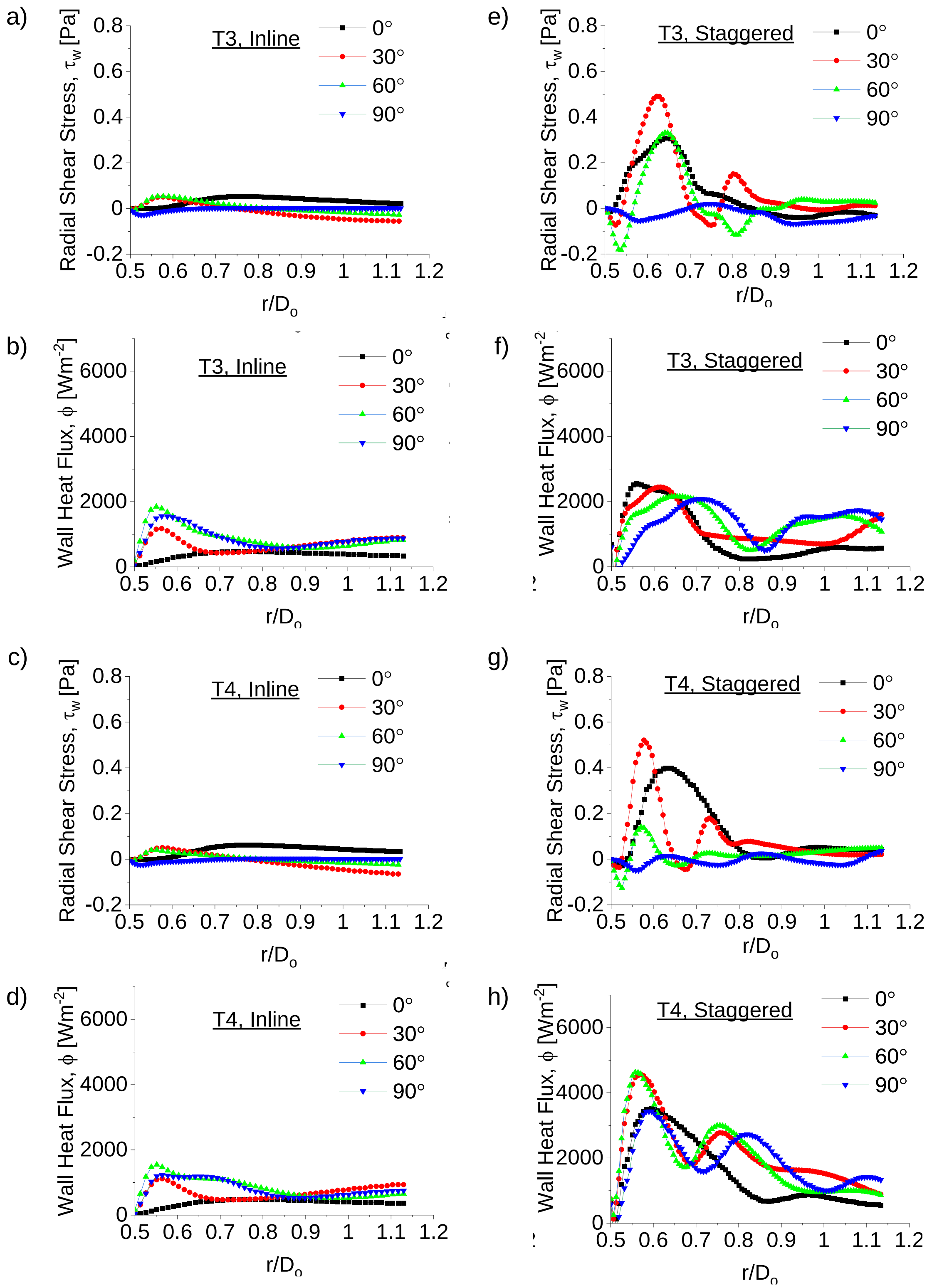

Figure 4-14: Radial wall shear and heat flux vs the radial distance on 0-90° plane for tube T3, T4 for the inline (Left) and the staggered tube geometry (right) for tube pitch of 2.5 diameters for Re_{Do}=3000.

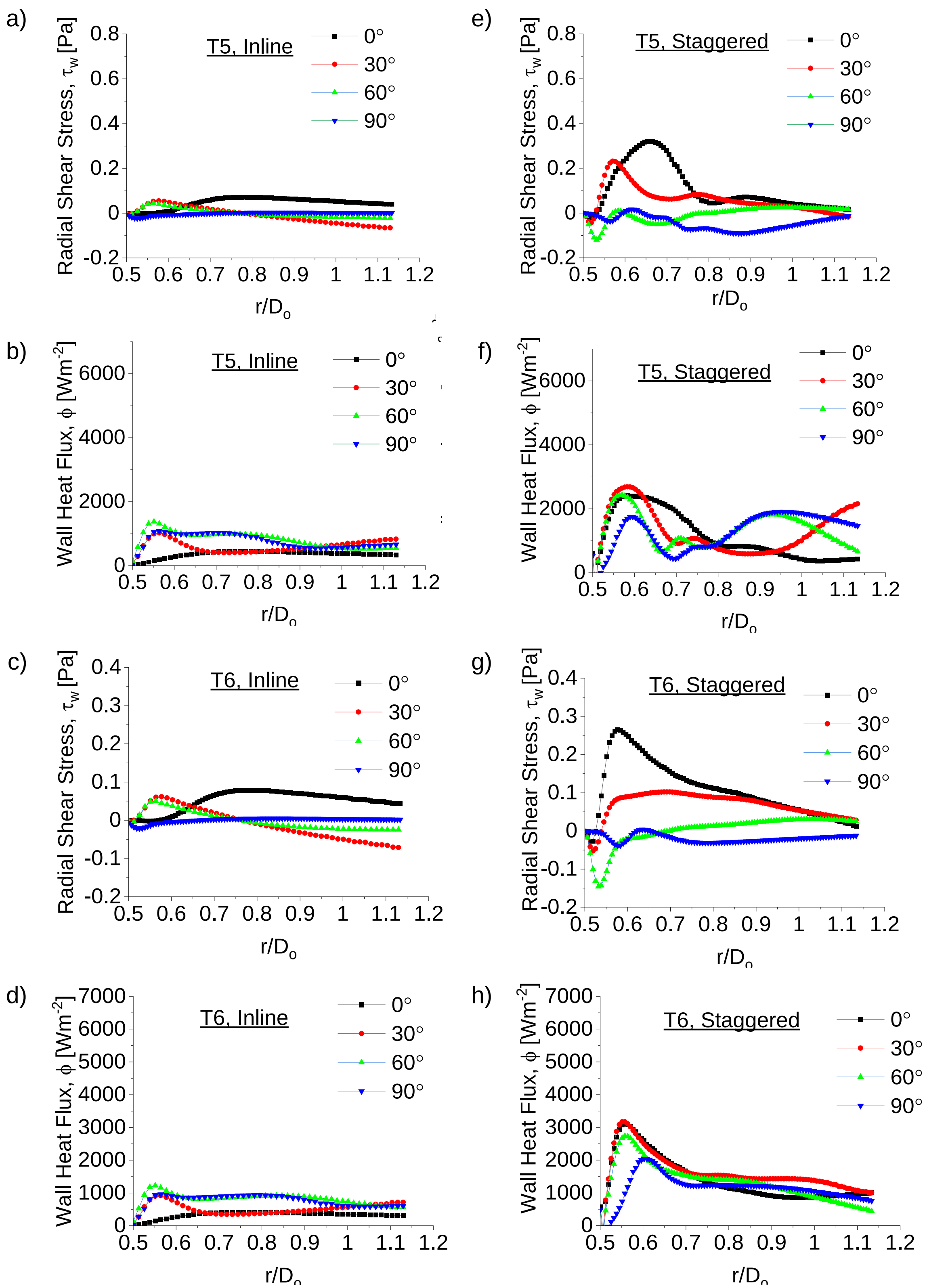

Figure 4-15: Radial wall shear and heat flux vs the radial distance on 0-90° plane for tube T5, T6 for the inline (Left) and the staggered tube arrangement (right) for tube pitch of 2.5 diameters for Re_{Do}=3000.

Figure 4-16 shows the wall heat flux with the radial distance at the frontal fin-tube junction for different tube pitch around each streamwise rows of the tube. Around the first tube, the maxima of the wall heat flux are consistent with the tube pitch but the recovery is delayed for higher tube pitch. Around the later tubes, the wall heat flux is increasing with a decreasing tube pitch. The maximum difference is observed around the third streamwise tube.

To quantitatively compare the effect of vortices on the heat transfer from the fins for different tube pitch, a near tube region on the fin surface is defined. It can be seen that the effect of the vortices stretches up to a radial distance of almost D_o around the second tube. However, it cannot be defined as the smallest tube pitch since it exceeds the longitudinal tube pitch. Hence, the near tube region of the fin is identified by a square of length $1.8D_o$ centred around each tube. The rest of the fin area is referred to as the extended region.

Figure 4-17 shows the total heat transferred from the near-tube region (square area of length $1.8D_O$), the extended region and tube surface around each streamwise tube for different tube pitch for the staggered and inline geometries. From the near tube region, the heat transfer is highest around the first tube for the inline tube arrangement; there is a sudden drop around the second tube, followed by a more gradual change downstream. For the staggered tube arrangement, the peak in heat transfer can be seen around the second tube with a gradual change on either side. There is a small decrease in heat transfer with the decrease in the tube pitch for the inline geometry, especially around the middle rows. However, for the staggered geometry, there is a small increase in heat transfer with the reduction in tube pitch around the third and the fifth-row. There is minimal change around the other rows. Overall, the heat transfer is roughly consistent with the tube pitch for inline and the staggered tube geometry.

From the tube surface, the heat transfer is highest around the first tube for the inline arrangement, and there is a gradual reduction for the later tubes. For the staggered geometry, the highest heat transfer is around the second or the third tube with a gradual decrease on either side. The heat transferred from the tube surface does not change much with the change in tube pitch for both tube configurations.

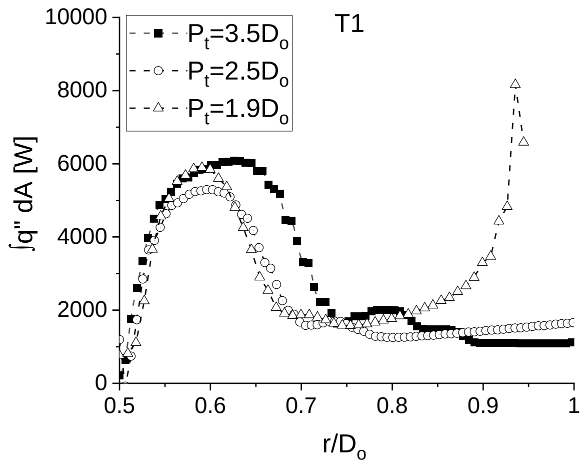

a) First streamwise tube

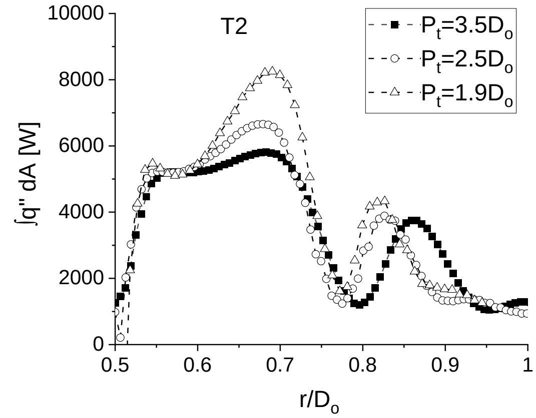

b) Second streamwise tube

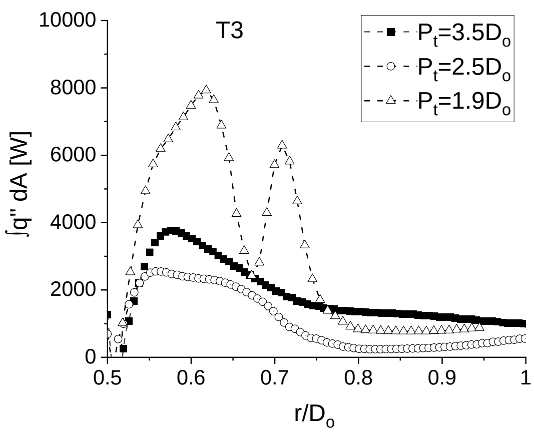

c) Third streamwise tube

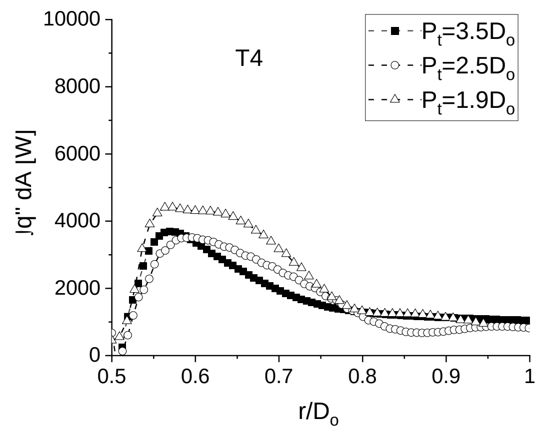

d) Fourth streamwise tube

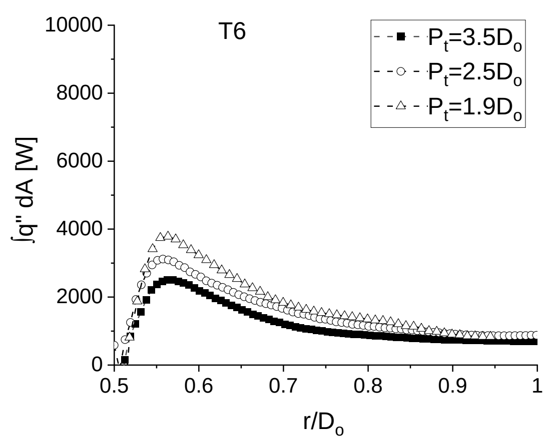

e) Sixth streamwise tube

Figure 4-16: Radial wall heat flux with the radial distance at the frontal fin-tube junction for different rows of the tube for the staggered tube arrangement for Re_{Do}=3100.

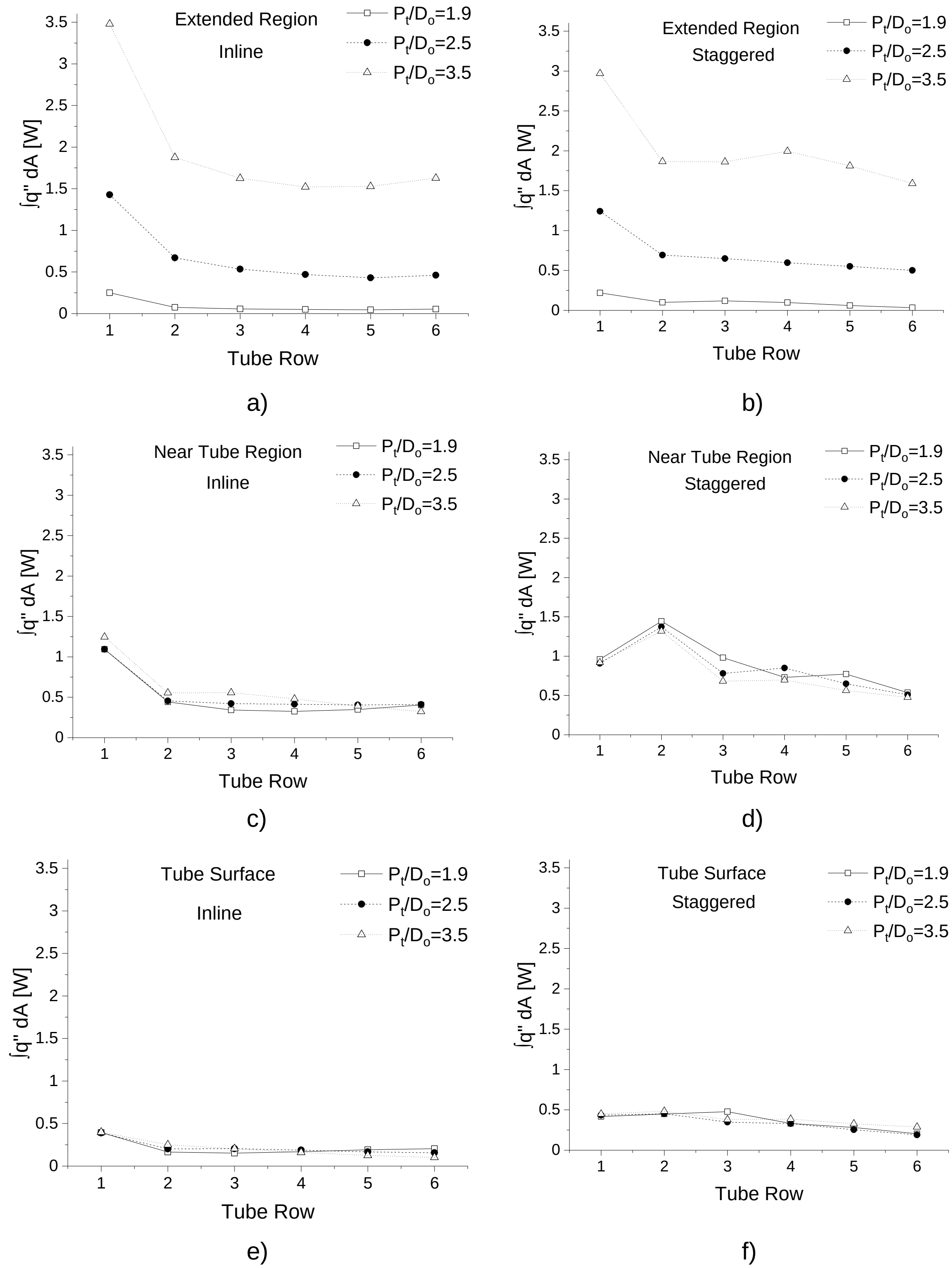

Figure 4-17: The effect of tube pitch on the heat transfer from near tube region, extended region and tube surface for inline and the staggered geometry for Re_{Do}=3100.

From the extended region, there is a peak in heat transfer around the first tube for both the tube arrangements, with a gradual change downstream after the sudden drop around the second tube. The heat transfer decreases with a decrease in tube pitch for both the staggered and inline geometries. Since the area of this extended region increases with increasing tube pitch, Figure 4-18 shows the heat transfer per unit area from the extended region for both tube arrangements. Around the first tube, there is an increase in overall heat flux with a decrease in tube pitch for both tube arrangements. Around the later tubes, the overall heat flux increases with the reduction of tube pitch for staggered geometry while there is a minimal change for the inline arrangement. This is due to the effect of the vortices from the near tube region on the extended region around the later tubes.

Overall, the effect of the vortices on the heat transfer from the near tube region is roughly consistent with the tube pitch for both staggered and the inline geometries. However, due to the effect of vortices on the heat flux from the extended region and decrease in the heat transfer area of the extended region with the tube pitch, the heat transfer coefficient increases with an increase in the tube pitch. The presence of the vortices around the downstream tube rows for the staggered tube configuration makes this change significant but is not significant for the inline case.

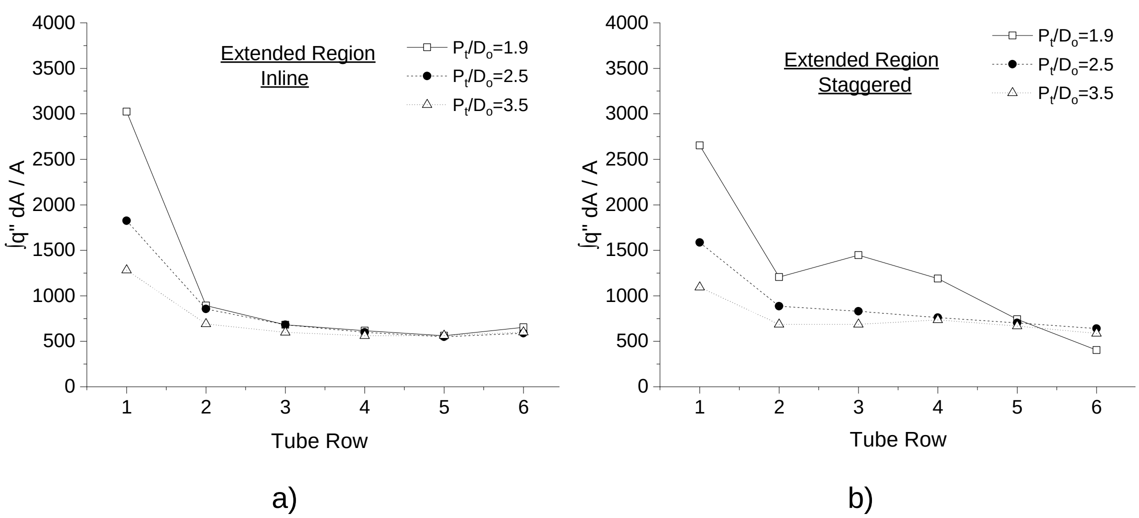

Figure 4-18: The effect of tube pitch on the overall heat flux from the extended region inline and the staggered geometry for Re_{Do}=3100.

4.2.1. Variation with the Reynolds number

Figure 4-19 shows the streamlines around the first fin tube junction for Reynolds number of 1450 and 6000 for both tube arrangements. The horseshoe vortex system consists of one primary vortex and one secondary vortex for low Reynolds number for the staggered as well as the inline geometry. There is the addition of another primary vortex at the higher Reynolds number for both tube arrangements, which suggests that the boundary layer causes the development of a horseshoe vortex system around the tubes, as originally postulated by Baker (1979). Also, the vorticity of the primary vortex (P1) increases with Reynolds number, as shown in Figure 4-20.

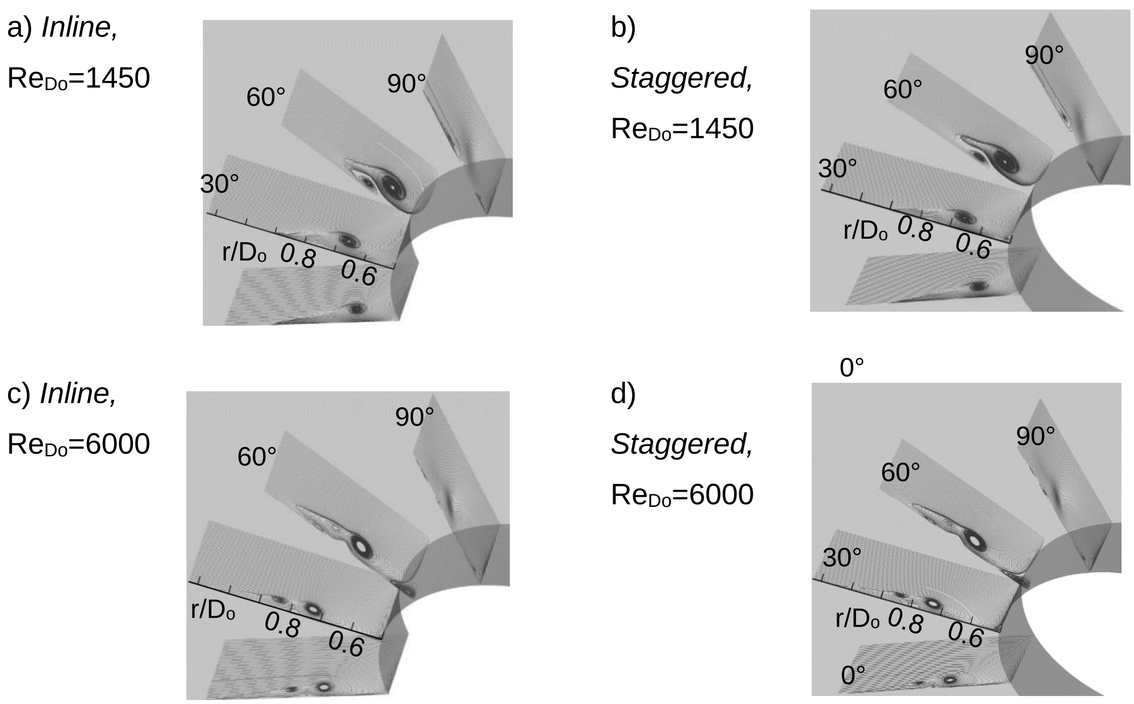

Figure 4-19: The effect of the Reynolds number on the streamlines around the first tube for inline and staggered large tube pitch geometry.

Figure 4-21 shows the wall heat flux and radial shear stress with the radial distance on the frontal fin-tube junction. The heat flux and wall shear associated with the primary vortex increases with the Reynolds number. It also increases due to the strong development of the horseshoe vortex system for higher Reynolds numbers. The total pressure, as well as the heat transferred for both tube arrangement, increases with Reynold number, but the increase is proportional to $Re^{X<0.7}$. Hence, the j-factor and f-factor decrease with the Reynolds number.

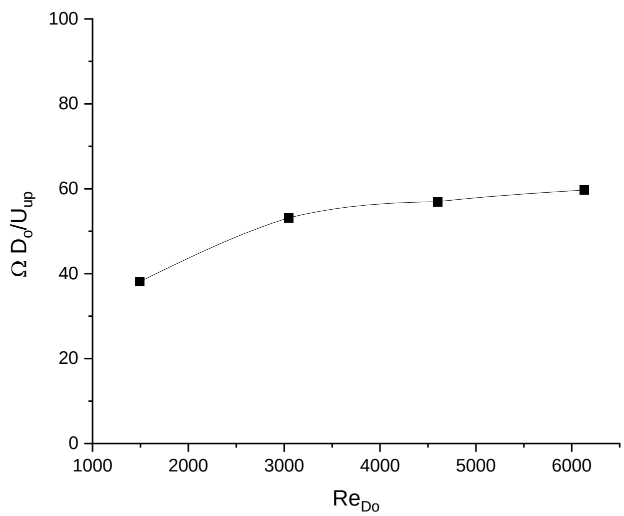

Figure 4-20: The effect of the Reynolds number on the $\Omega D_o/U_{up}$ for Inline or staggered geometry for primary vortex (P1) on the frontal plane of the first fin tube junction for large tube pitch case.

Figure 4-22 shows the total heat transferred from the near tube region, the extended region and tube surface around each streamwise tube for large tube pitch staggered and inline geometries for several Reynolds Numbers. The vortices around the second tube stretch up to the radial distance of Do around the second tube for large tube pitch. A square of the length $2D_O$ defined the near tube region in this case. This region transfers around 25 to 32% of the total heat for both tube arrangements but accounts for 18% of the area. For the near tube region, the inline geometry has the highest heat transfer around the first tube and then gradually decreases till the last tube for all Reynolds numbers. For the staggered tube geometry, the peak is around the second tube and then it drops till the last tube for all Reynolds numbers. Except around the first tube, the staggered geometry transfers a higher heat from near tube region. For the tube surface, there is a peak at the second tube for staggered geometry and at the first tube for inline. Staggered geometry transfers higher heat from the tube-fluid interface than Inline geometry. For the extended region, there is no change in heat transfer from the staggered and the inline geometry for the lowest Reynolds number. However, inline has 5-15% higher heat transfer for the highest Reynolds number from the extended region. It is interesting to note the sudden increase in heat transfer around the middle of the heat exchanger for staggered and the inline geometry, and there is a gradual reduction later. There is no sudden rise seen for the lowest Reynolds number. This rise is due to the start of the turbulence regime for the inline and staggered case. The transition is much more evident for the inline geometry starting at 4500, and the transition moves upstream with an increase of the Reynolds number. For the inline geometry, the transition seems to be more gradual, starting from the back half at Reynolds number of 3000. Figure 4-23 shows the turbulence intensity and viscosity ratio for staggered and inline geometry on the center plane at Reynolds number for 1450 & 6000, respectively. For ReDo=1450, the exit wake flow is transitional. For ReDo=6000, the fully turbulent regime starts in the middle of the heat exchanger.

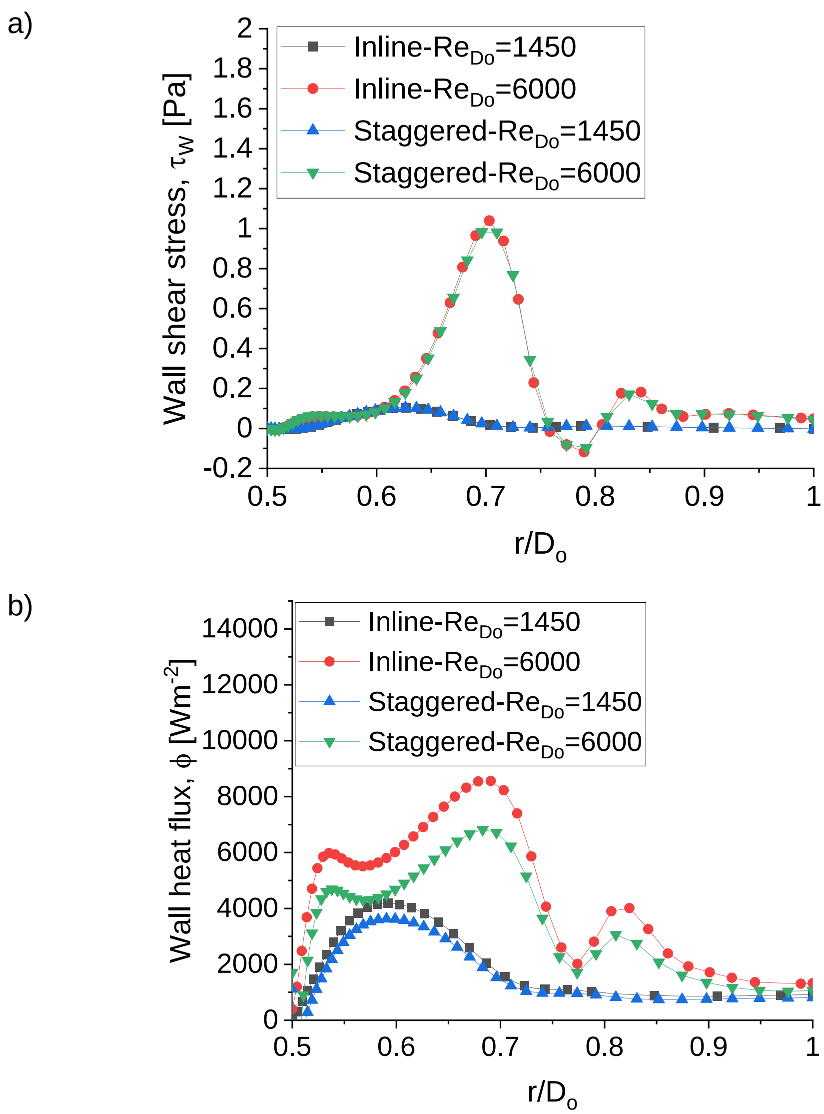

Figure 4-21: The effect of the Reynolds number on the radial wall shear stress and the wall heat flux on the frontal junction of the first fin-tube for staggered and inline geometry for large tube pitch case.

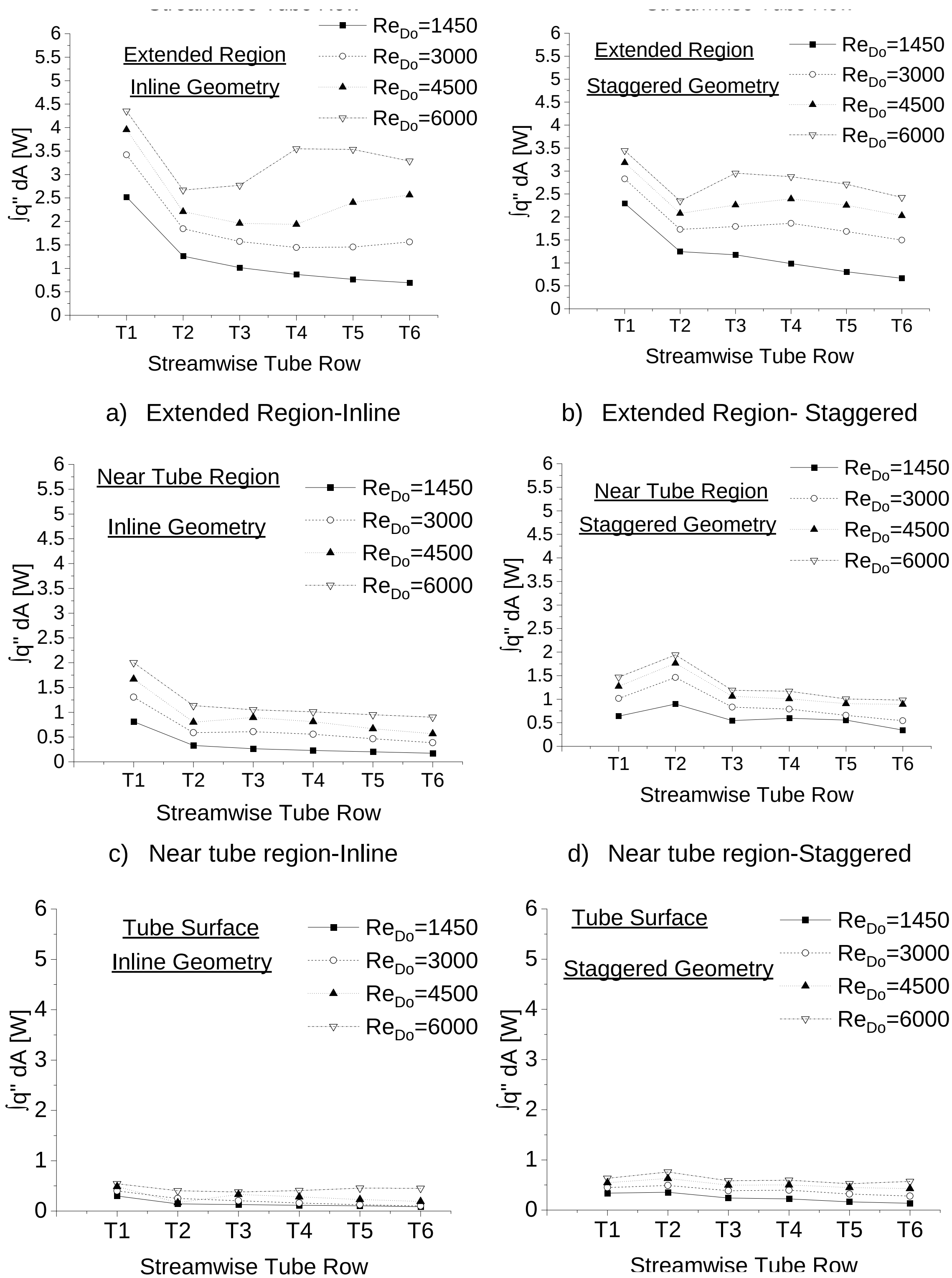

a) Extended Region-Inline

b) Extended Region- Staggered

c) Near tube region-Inline

d) Near tube region-Staggered

e) Tube surface- Inline

f) Tube surface-Staggered

Figure 4-22:The effect of the Reynold numbers on the heat transfer from near tube region, extended region and the tube surface for inline and the staggered tube arrangement.

a) Turbulent Intensity Inline, Re_{Do}=1450

b) Viscosity Ratio Inline, Re_{Do}=1450

c) Turbulent Intensity Staggered, Re_{Do}=1450

d) Viscosity Ratio Staggered, Re_{Do}=1450

e) Turbulent Intensity Inline, Re_{Do}=6000

f) Viscosity Ratio Inline, Re_{Do}=6000

g) Turbulent Intensity Staggered, Re_{Do}=6000

h) Viscosity Ratio Staggered, Re_{Do}=6000

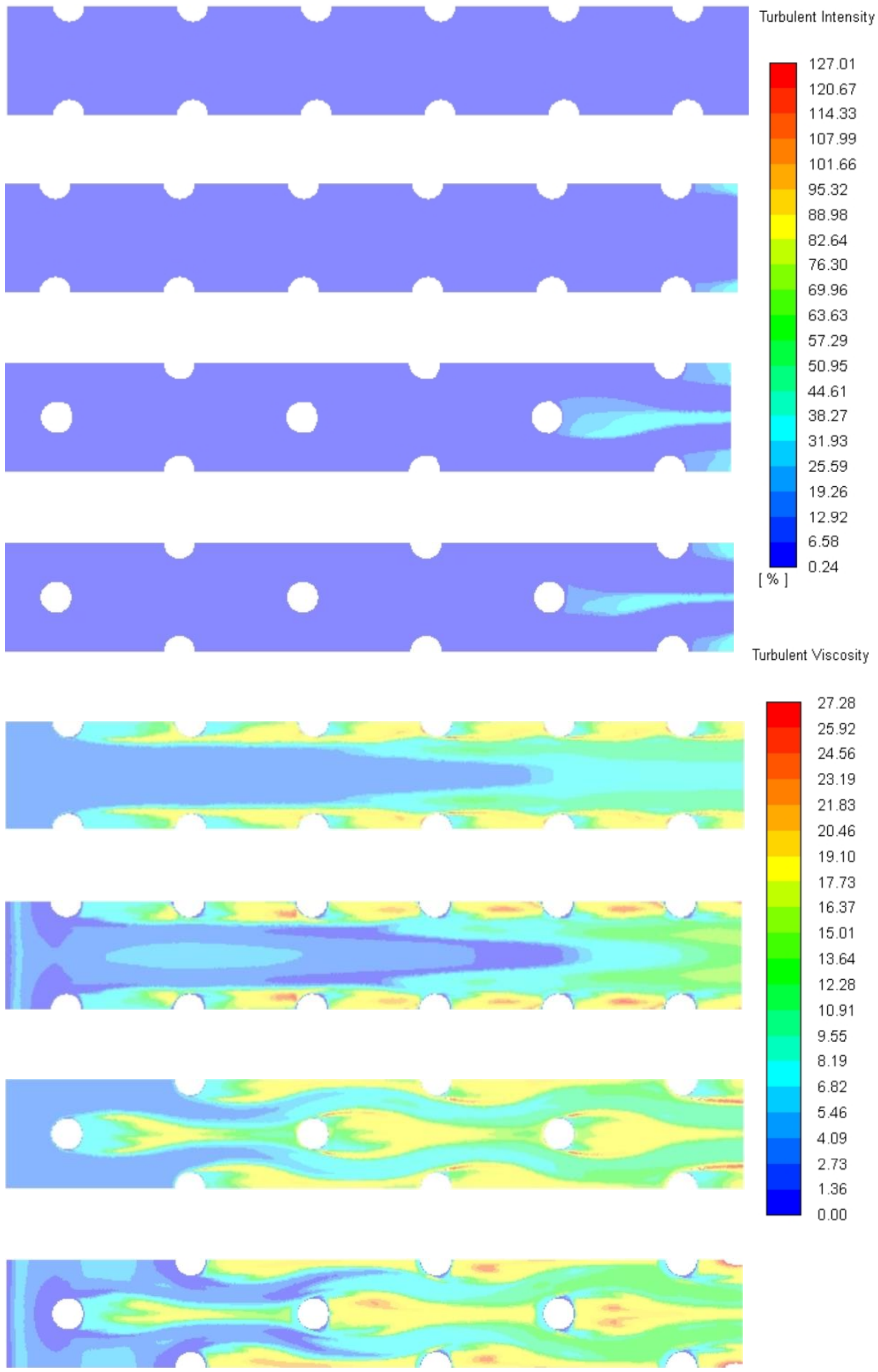

Figure 4-23: The effects of the Reynolds number on the turbulent intensity and turbulence viscosity ratio for inline and the staggered tube geometry at the central plane where the viscosity ratio is μ_t/μ.

Figure 4-24 & *Figure 4-25* shows the variation of the Colburn j-factor and friction factor for the inline and staggered geometries for various tube pitch with Reynolds number (Re_{Do}<4500). The figure also shows the experimental data from Wang [9] for comparison. The friction factor definition is modified as per the experimental data [31, 9] for comparison purposes, which does not separate the entrance and exit effects from the overall pressure drop, and the following definition is used.

$$f_{exp} = \frac{A_c}{A_o}\frac{\rho_m}{\rho_{in}}\left(\frac{2\Delta P \rho_1}{{G_c}^2} - (1+\sigma^2)\left(\frac{\rho_{in}}{\rho_{out}} - 1\right)\right) \quad 4\text{-}1$$

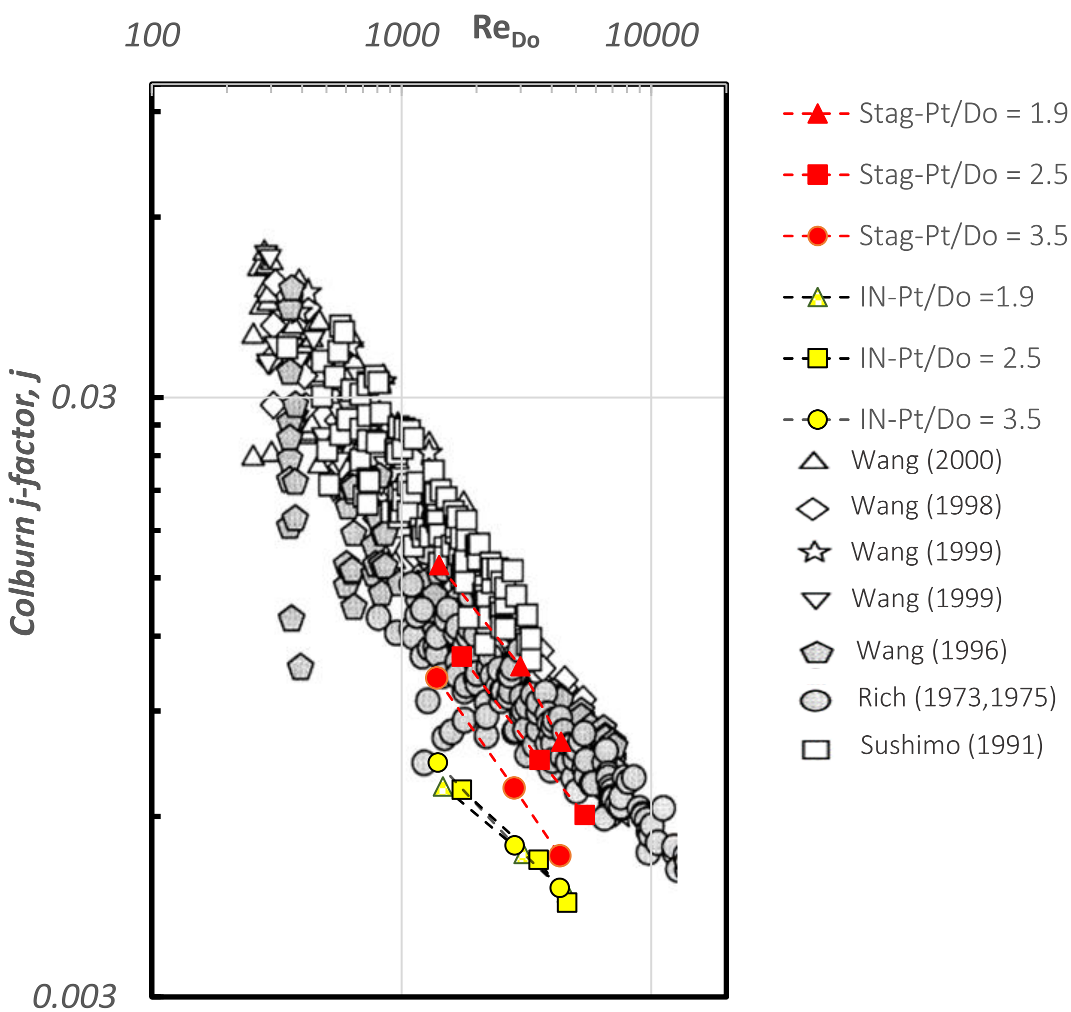

Figure 4-24: The effect of tube pitch on the Colburn j-factor for the inline and the staggered tube arrangement and comparison with past experimental data *[9]*.

As seen in Figure 4-24 & Figure 4-25, the Colburn j-factor and friction factor decrease with an increase in the tube pitch for the staggered tube arrangement. For the inline geometry, however, there is a negligible change in the Colburn j-factor with the tube pitch, and the friction factor decreases slightly with an increase in tube pitch. The high tube pitch inline geometry has a Colburn j-factor of almost 40-70% less than the experimental data, and the low tube pitch staggered geometry, but there is less than 30% difference with the high tube pitch staggered geometry. Similarly, the friction factor for higher tube pitch inline geometry is 40-80% lower than the past experimental data. Still, there is less than a 45% difference between the high tube pitch staggered and inline geometry.

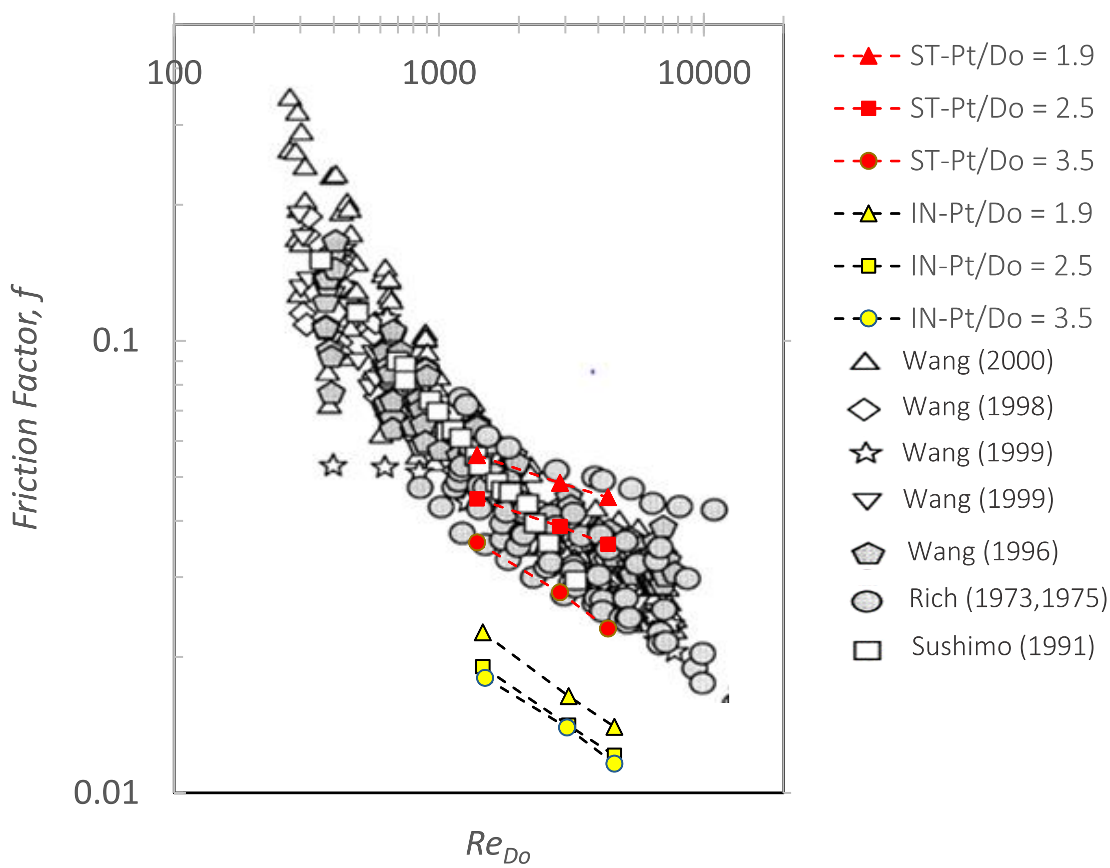

Figure 4-25: The effect of tube pitch on the friction factor(f_{exp}) for inline geometry and staggered tube arrangement and comparison with past experimental data *[9]*.

Figure 4-26 shows the area goodness factor for staggered and inline geometry for the range of tube pitch. If $Q/\Delta P$ is taken to be the design criteria, inline is always better than staggered for the complete range of tube pitch. At lower tube pitch, due to a large difference in heat transfer, staggered was always preferred, but at higher tube pitch, Inline could also be a design choice because of the low-pressure drop and the lower difference in heat transfer with the staggered tube arrangement.

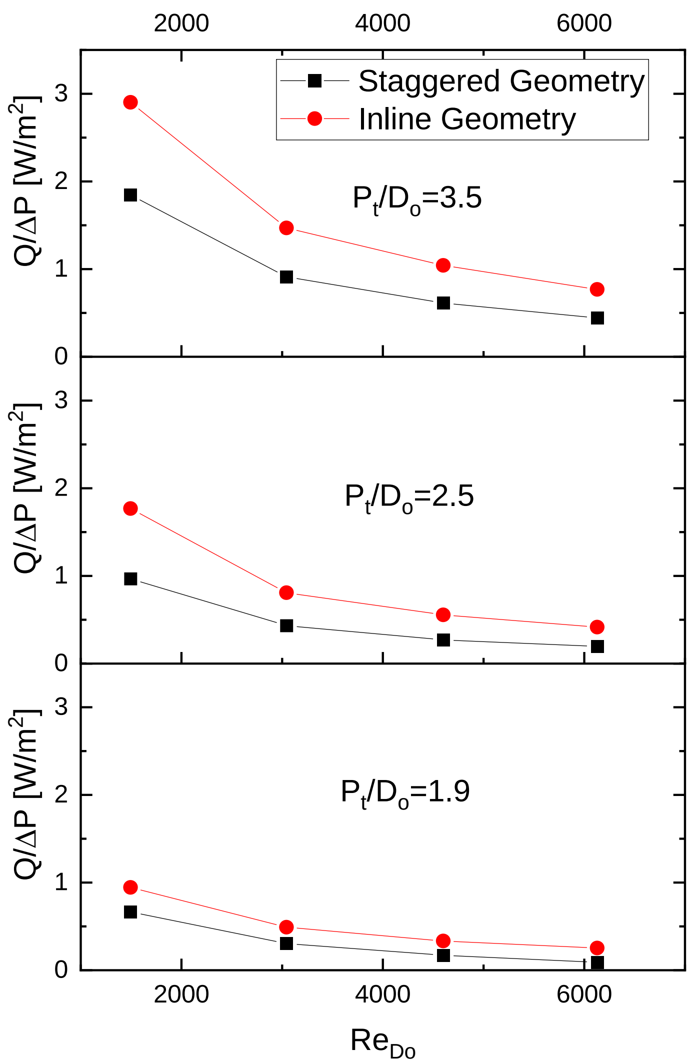

Figure 4-26: Area goodness factor for staggered and inline for different tube pitch.

4.3. Characterization of the large-pitch inline heat exchanger

The effect of other design parameters, like the effect of the fin pitch and number of tube rows, was considered in detail for the large pitch inline heat exchanger. The abrupt contraction and the expansion pressure drop are also considered. Correlations for the friction factor and the Colburn j-factor are finally developed.

4.3.1. Effects of fin pitch

The variation of Colburn j-factor and friction-factor with fin pitch for several Reynolds numbers are presented in Figure 4-27. The j-factor and friction factor decreases as the fin pitch increases for all Reynolds numbers. The ratio *j/f,* which simultaneously accounts for heat transfer and pressure drop, is the area goodness factor. The area goodness factor increases slightly up to a fin pitch of 0.375 diameters and then decreases, as seen in *Figure 4-28*. For the staggered tube arrangement, Tala [61] found the optimum value occurred at F_p/D_o=0.25.

Figure 4-29 and Figure 4-30 shows the streamlines around the first tube for the different fin pitch for the various Reynolds numbers. It can be seen that the structure of the horseshoe vortex is consistent with the fin pitch for the highest Reynold number. However, for Reynold numbers of 3100 & 4800, a second primary vortex cannot be seen after the 0° plane for higher fin pitch. The radial and vertical position of these vortices change with the fin pitch. Figure 4-31 shows the radial position of the primary vortex P1 with the fin pitch. It is seen that the radial position increases with the fin pitch. Figure 4-32 shows the vorticity of the first primary vortex with the fin pitch for the 0° plane behind the first tube. It can be seen that the strength of the vorticity also decreases as the fin pitch increases. This follows Tala et al [61], which found that the strength of the vorticity decreases on increasing the fin pitch for Fp/Do>0.2. It differs from the results of Chen et al [14] that the strength of the primary vortex does not change after Fp/Do>0.336.

Figure 4-33 shows the wall shear stress and the wall heat flux on the frontal plane at fin tune junction at 0°. The maxima in the wall shear and heat flux is associated with the primary vortices. The maximum value of the radial wall shear stress and wall heat flux decreases as the fin pitch increases due to a reduction in vorticity. The radial position of the maxima is also increasing with the Reynolds number. This is due to the change in the radial position of the vortex.

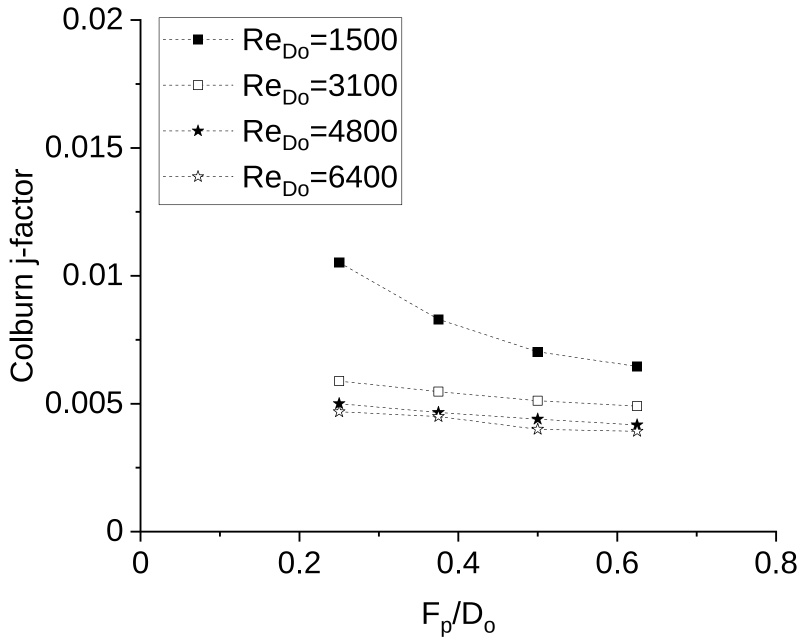

a) Colburn j-factor

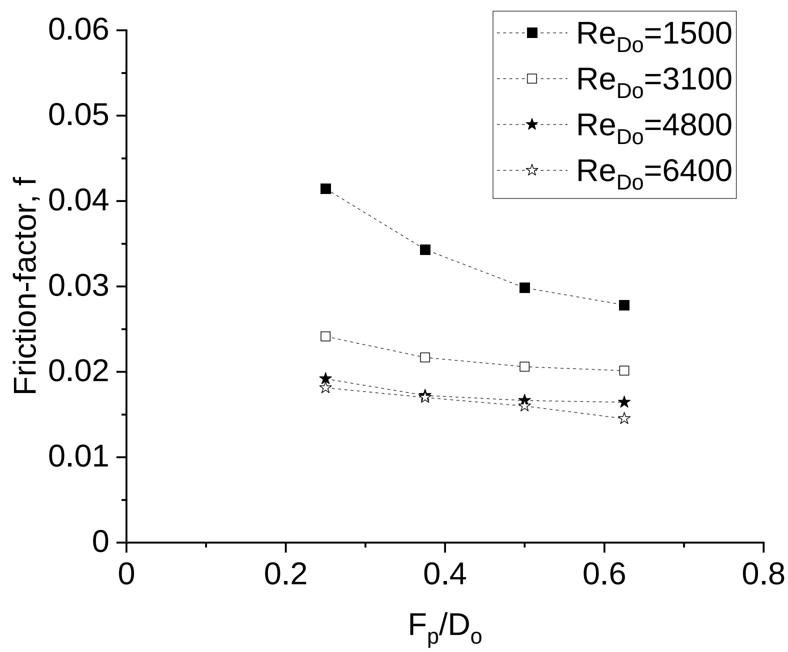

b) Friction factor

Figure 4-27: The effect of fin pitch on the Colburn j-factor and friction factor for different Reynolds numbers.

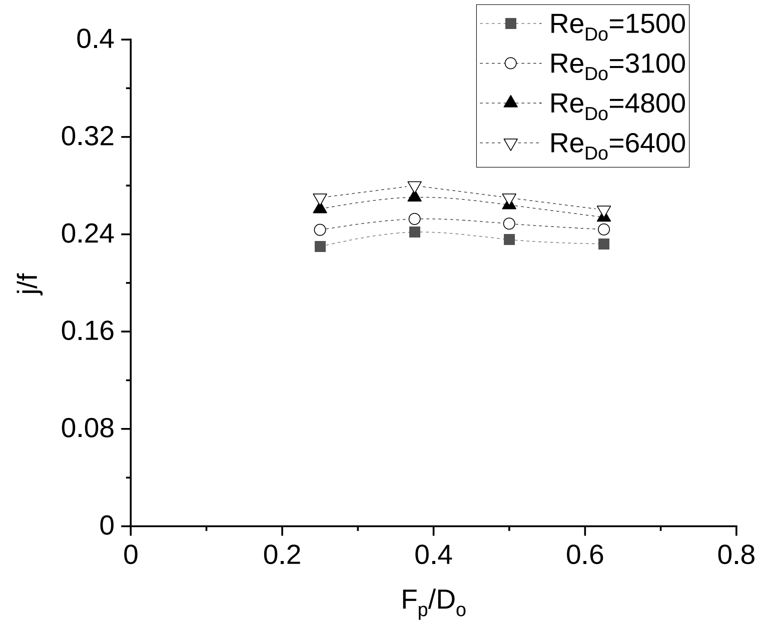

Figure 4-28: The effect of fin pitch on the area goodness factor for different $Re_{Do.}$

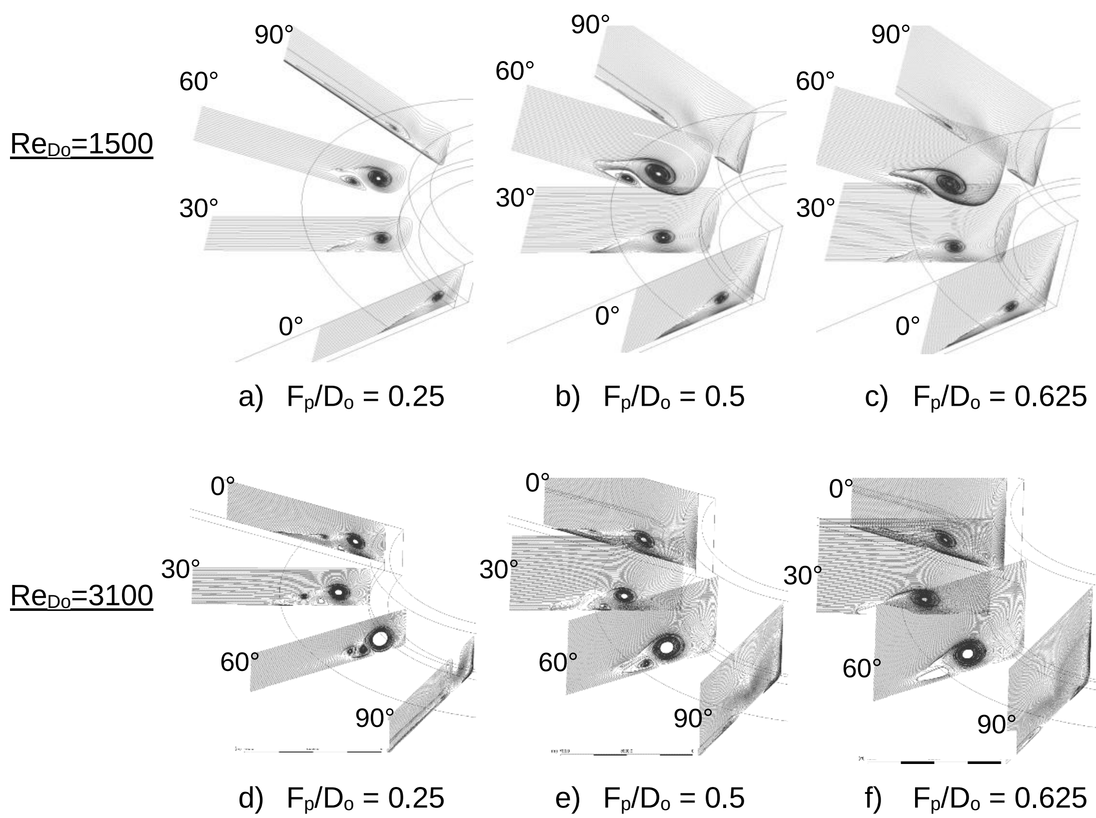

Figure 4-29:The effect of fin pitch on the streamlines around the first fin-tube junction for the Reynolds number of 1500, 3100.

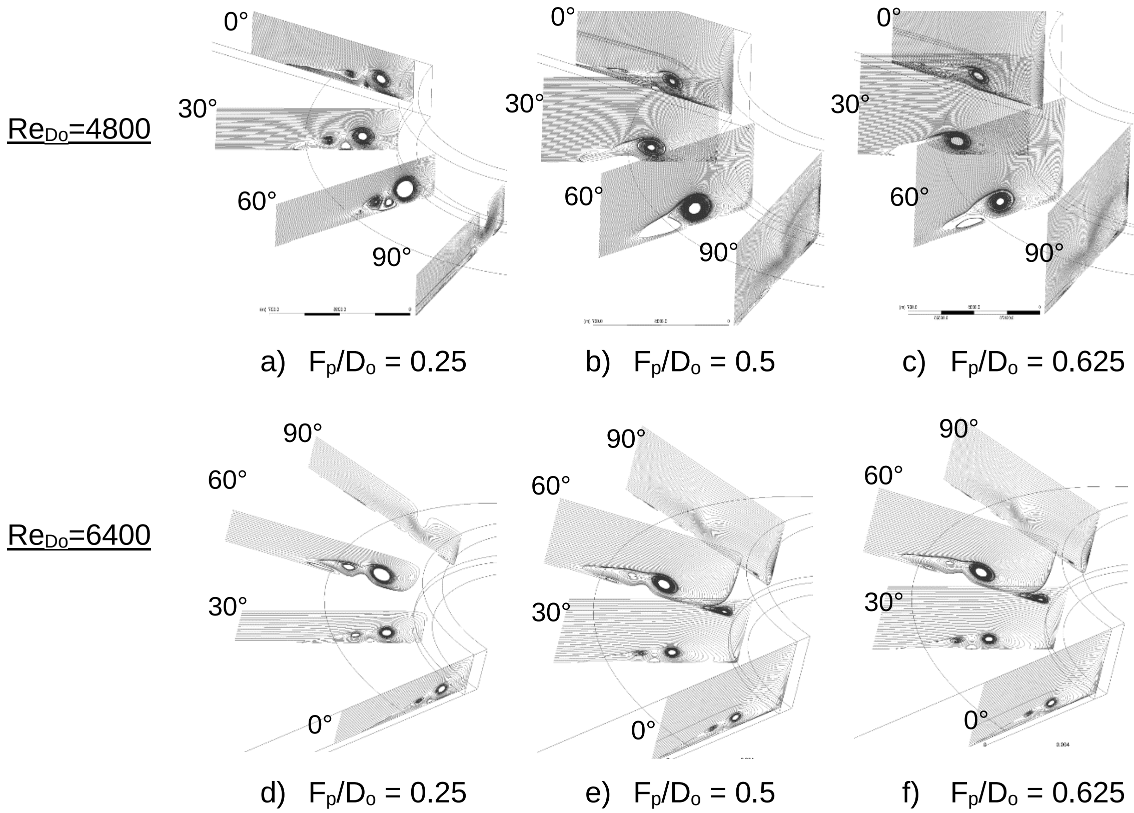

Figure 4-30: The effect of fin pitch on the streamlines around the first fin-tube junction for the Reynolds number of 4800, 6400.

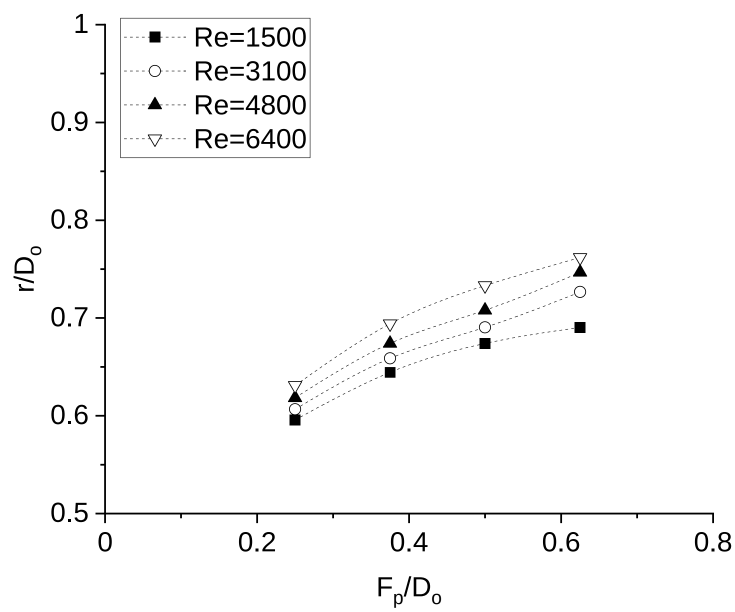

Figure 4-31: The effect of fin pitch on the radial distance to diameter ratio of Primary vortex (P1) for different Re$_{Do.}$

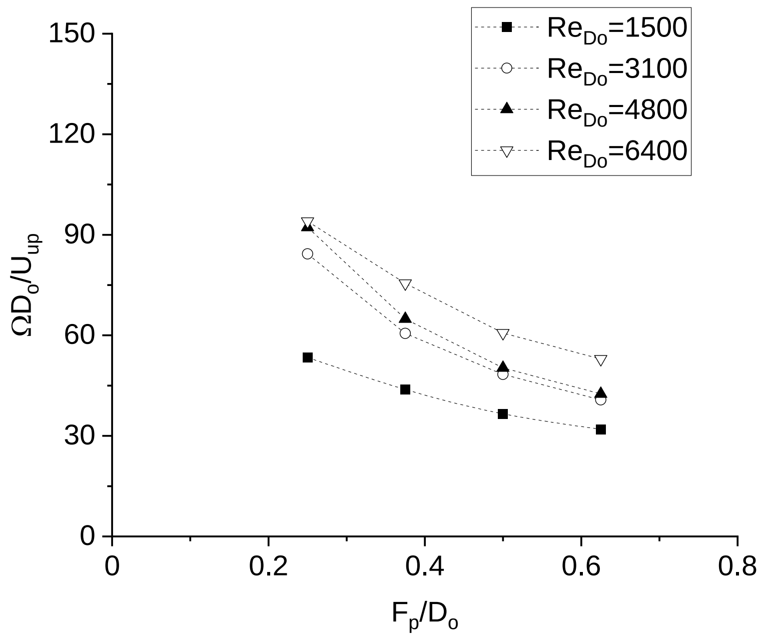

Figure 4-32: The effect of fin pitch on $\Omega D_o/U_{up}$ for first primary vortex (P1) for different Reynolds number.

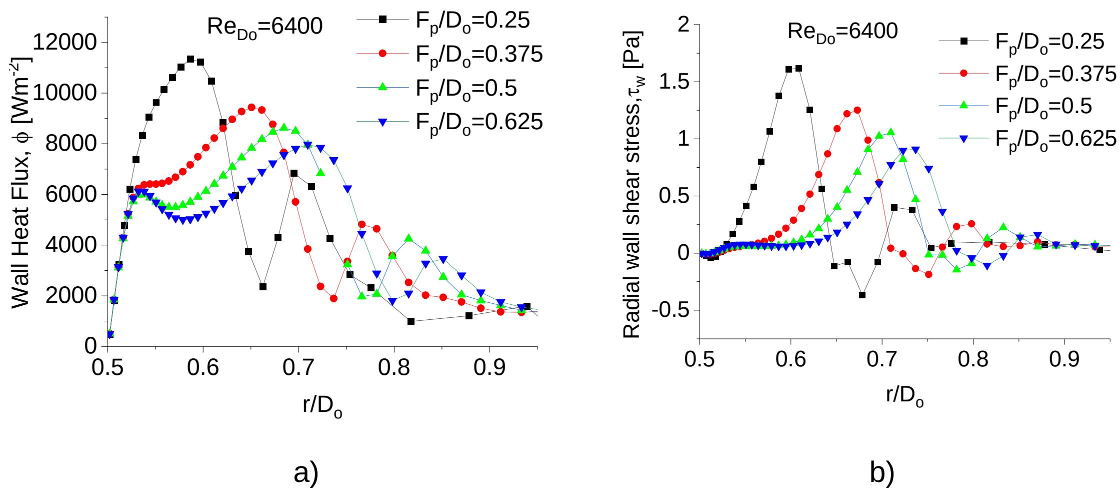

Figure 4-33: The effect of fin pitch on wall heat flux and wall shear stress with radial distance at Re$_{Do}$=6400.

The variation of local Colburn j-factor with streamwise tube row for different fin pitch at different Reynolds numbers is presented in Figure 4-34. It is seen that the j-factor decreases with increasing fin pitch for any tube row for all Reynolds numbers. The horseshoe vortex and the increasing heat capacity of the fluid with the fin pitch may be responsible for the change in j-factor with fin pitch. For the lowest Reynolds number, the j-factor decreases as we move downstream. As the Reynolds number is increased, there is a rise in j-factor beyond the third or fourth tube row. This rise is due to the start of the turbulence regime, as seen earlier.

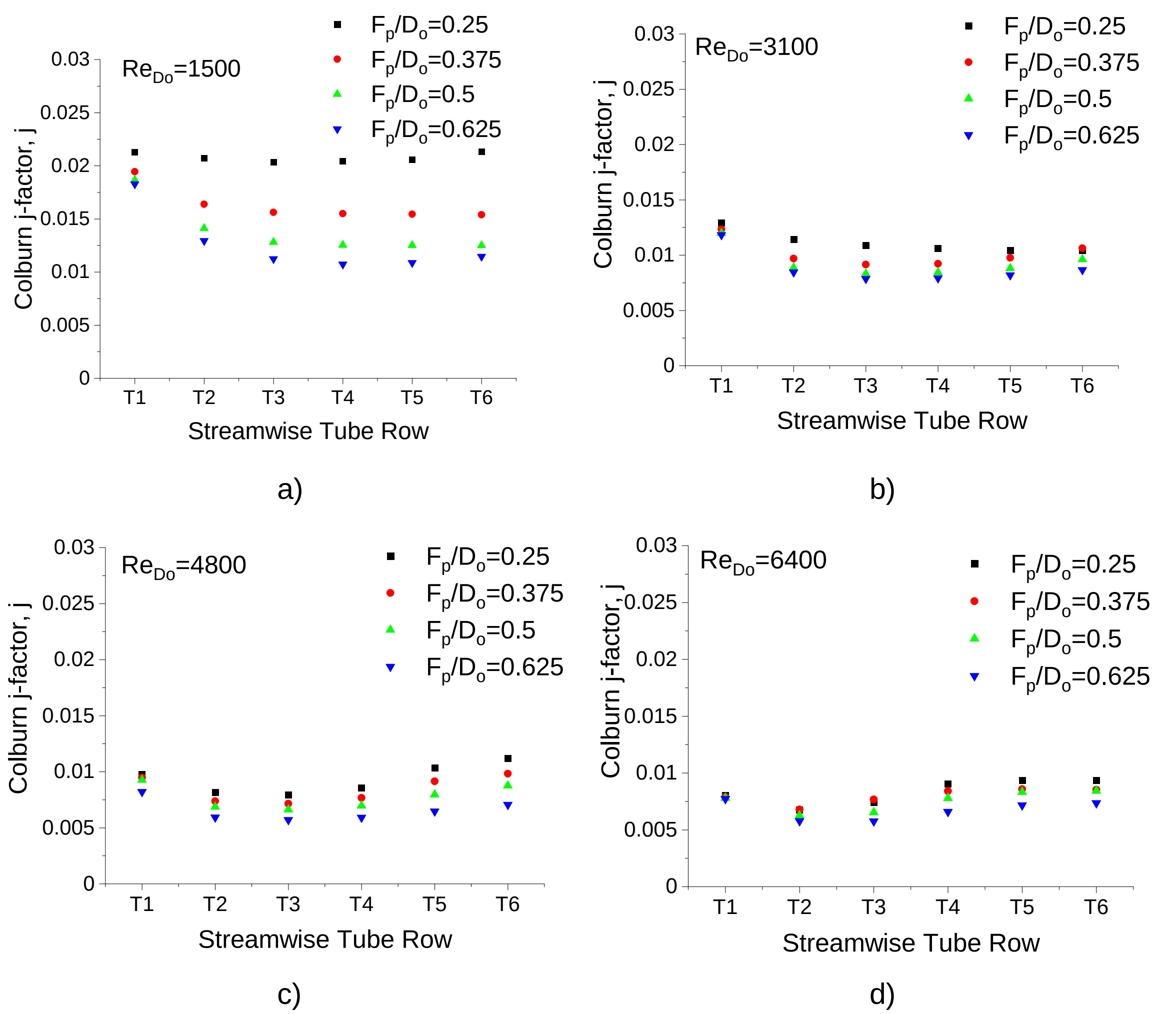

Figure 4-34: The effect of fin pitch for the Colburn j-factor with streamwise tube row for different Reynolds numbers.

4.3.2. Effect of the number of tube rows

The Colburn j-factor and the friction factor with the Reynolds number for a different number of tube rows are presented in Figure 4-35 and *Figure 4-36*. It can be seen that the Colburn j-factor slightly decreases with an increase in the number of tube rows for Reynolds numbers less than about 3000. The effect is diminished as the Reynolds number is increased further. Similarly, the friction factor decreases slightly with an increase in the number of tube rows for Reynolds number less than about 2000 and is not pronounced at higher Reynolds numbers.

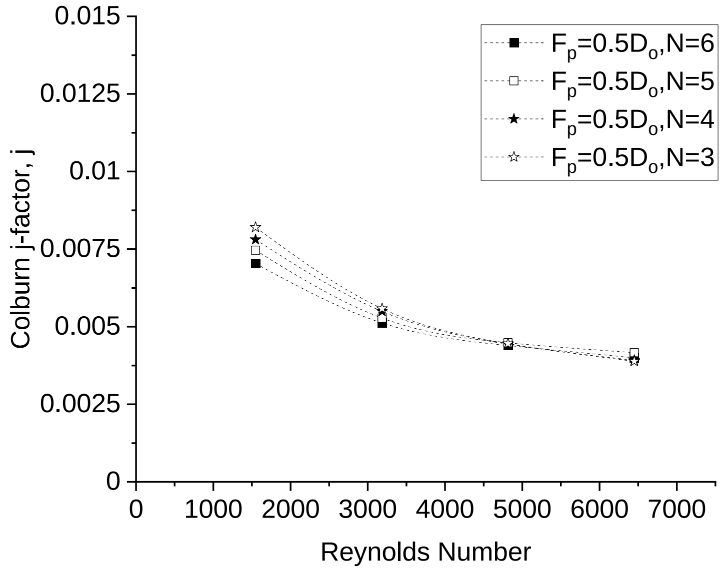

Figure 4-35: The effect of the number of tube rows for the Colburn j-factor.

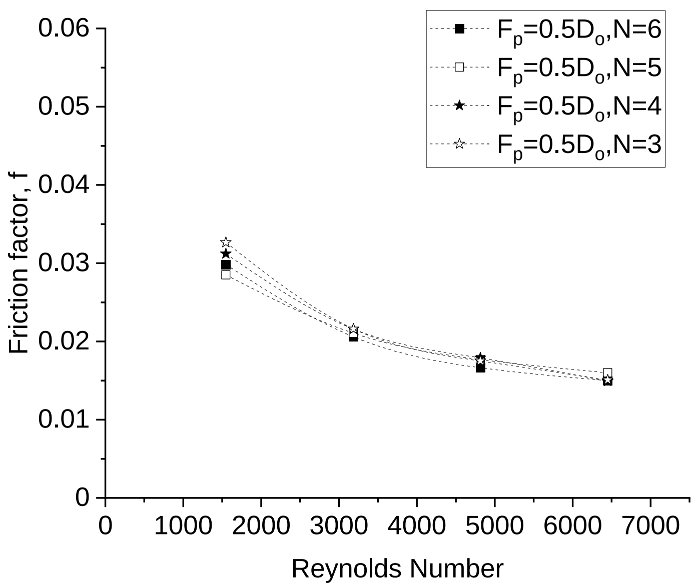

Figure 4-36: The effect of the number of tube rows on the friction factor.

Figure 4-37 shows the heat transfer from tube rows along the streamwise direction as the number of rows is increased at three different Reynolds numbers. At Reynolds's number of 1550, the heat transfer from each tube row decreases, leading to a decrease in j-factor with an increase in the number of tube rows. At the higher Reynolds numbers, after an initial decrease, the heat transfer increases in subsequent tube rows. This occurs because the turbulence causes a good mixing in the downstream fin region. Figure 4-38 shows the eddy viscosity on the central plane for the different number of tube rows for Reynolds number of 6500. A higher eddy viscosity around each tube rows than the previous row can be seen with the addition of a new tube row. Thus, the turbulence causes the local heat transfer coefficient to recover instead of decreasing, leading to no change in the overall Colburn j-factor.

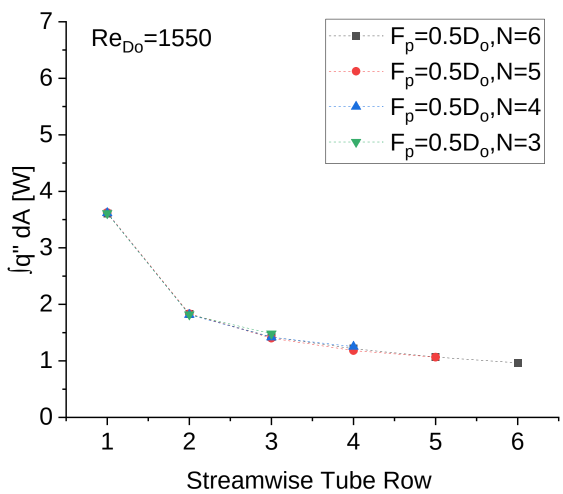

a)

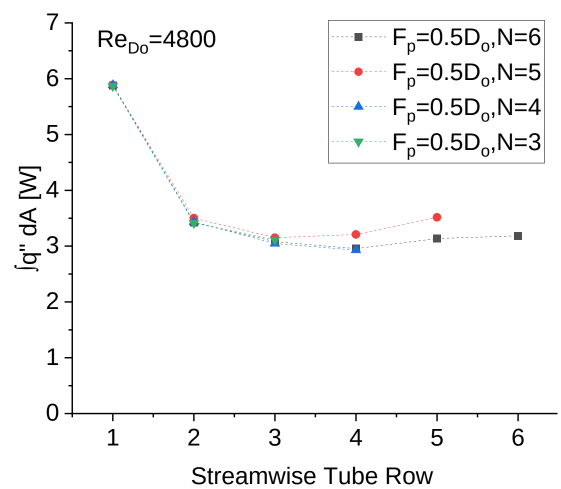

b)

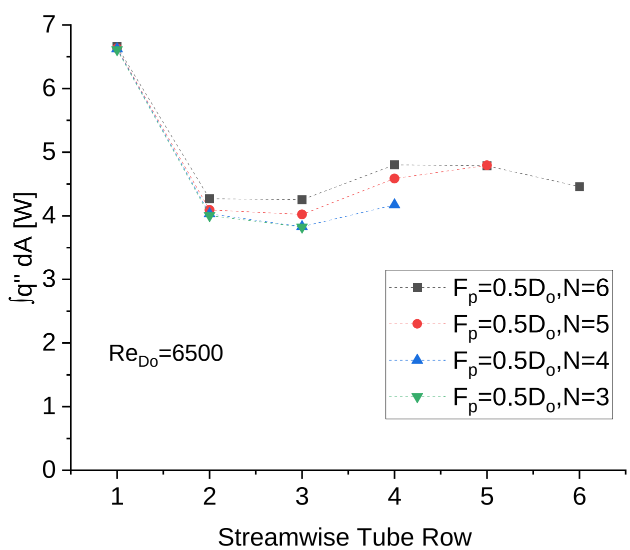

c)

Figure 4-37: The effect of the number of tube rows on the heat transferred for each streamwise tube row for different Reynolds numbers.

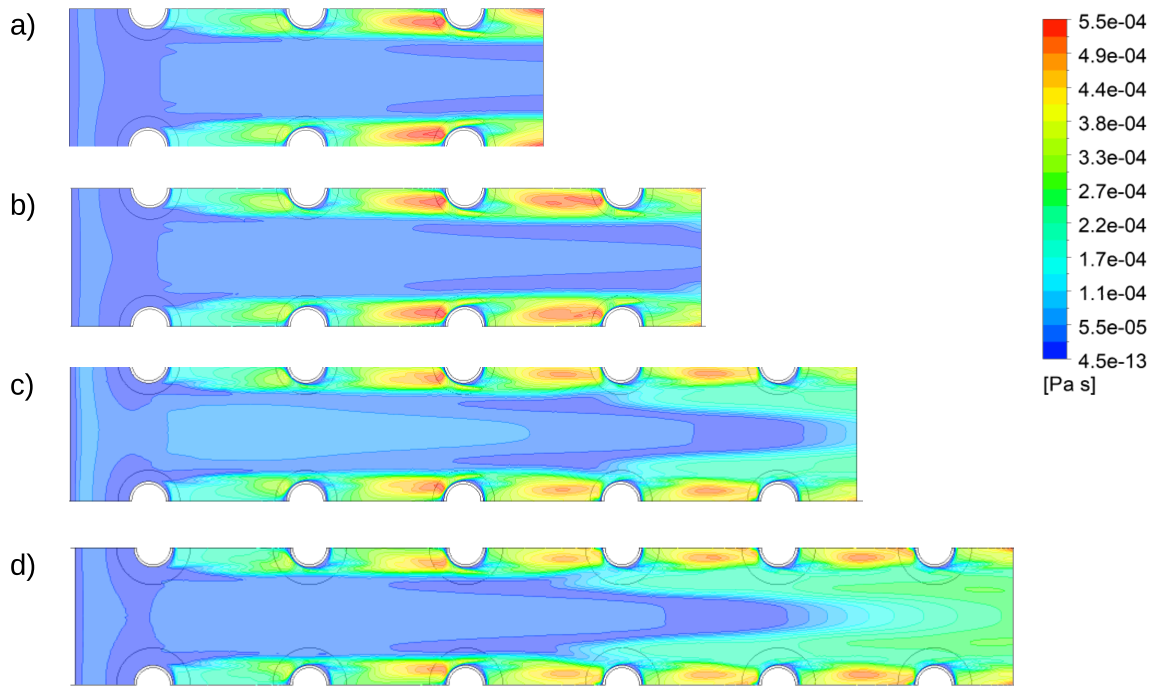

Figure 4-38: The effect of the number of tube rows on the eddy viscosity on the central plane for Re_{Do}=6500

4.3.3. The various elements of pressure drop

The various elements of pressure drop are: (i) abrupt contraction and expansion pressure drop, (ii) friction pressure drop. In the flat plate and tube heat exchanger, there are two consecutive abrupt entrances. First is the contraction through the flat plates and then the contraction due to the tubes. The variation of pressure with streamwise distance is shown in Figure 4-39 and these two different contraction effects on the pressure drop are seen in this figure.

Figure 4-40 shows the variation of the entrance pressure loss coefficient for the channel entrance (Kc-ch) with the frontal contraction ratio. The loss coefficient for the laminar and turbulent flow (Re=2000,10000) from Kays and London (1984) is also plotted in this figure. The turbulent pressure loss coefficient from Kays and London underestimates the entrance loss, and the laminar pressure loss coefficient overestimates the entrance pressure loss.

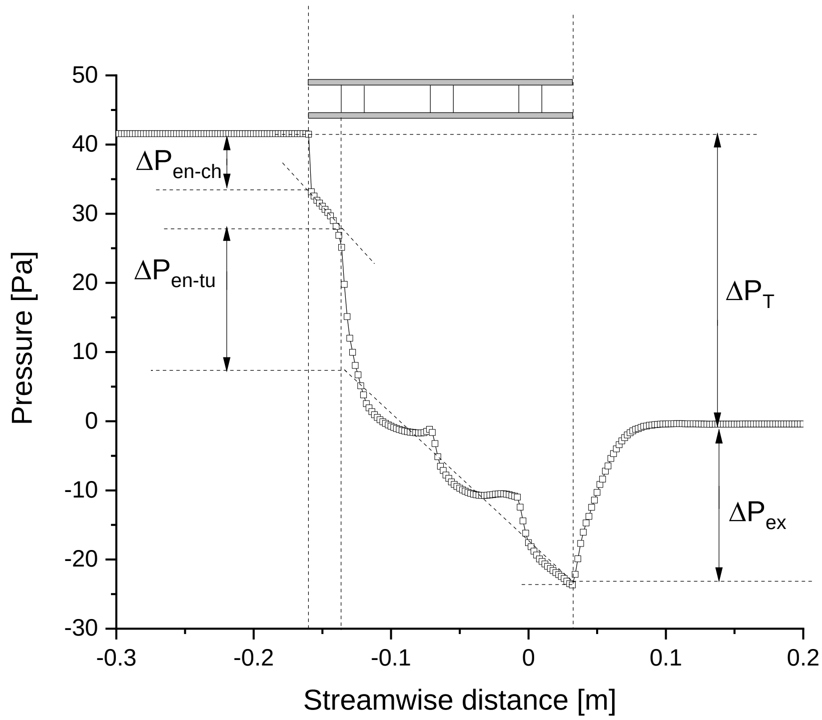

Figure 4-39: The variation of pressure with streamwise distance. $\triangle P_{en\text{-}tu}$ is an approximate measurement.

Hence, a correlation was developed for the loss coefficient by multiple regression analyses using the Gauss-Newton iterative algorithm *[71]* considering a quadratic polynomial variation with $\boldsymbol{\sigma}$ and ReFp, as given below.

$$K_{c-ch} = C_1 {\sigma_{ch}}^2 + C_2 \sigma_{ch} + C_3 {Re_{Fp}}^2 + C_4 Re_{Fp} + C_5 \qquad \text{4-2}$$

where,

$$\sigma_{ch} = \frac{F_p - F_t}{F_p} \qquad \text{4-3}$$

The coefficients are listed in *Table 4-2*.

Table 4-2: Coefficients of the correlation of the channel abrupt contraction effect.

C_1	C_2	C_3	C_4	C_5
-4.776273201	6.846610792	3.42918E-08	-0.000139838	-1.972382239

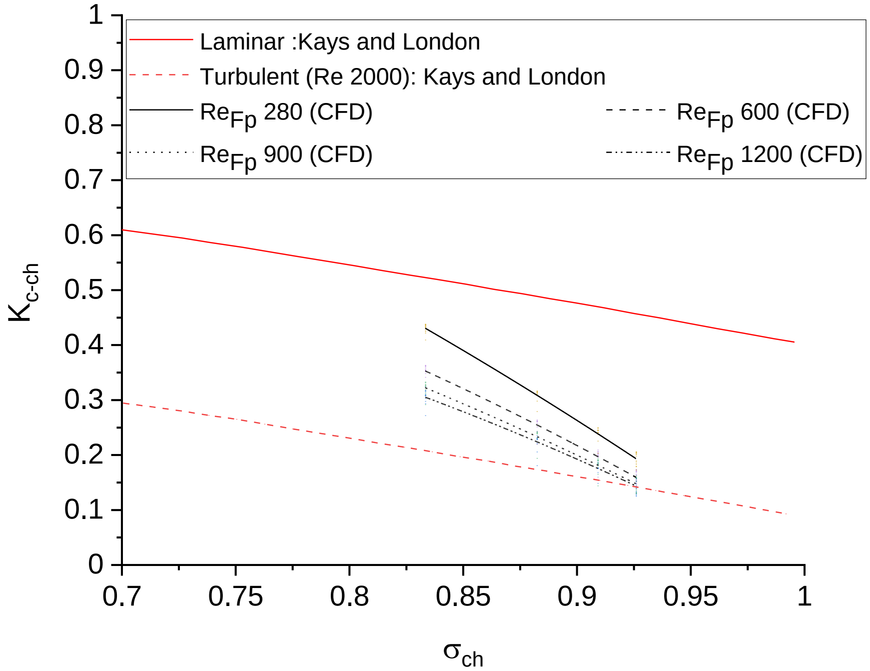

Figure 4-40: Entrance pressure loss coefficient for a channel entrance with contraction ratio.

Figure 4-41 shows the comparison of the predicted K_c for channel entrance using the above correlation with the CFD data. A total of 75 different geometrical configurations and 280 observations are used to develop the correlation. The discrepancy lies within ±10%.

After the fluid flows across the abrupt entrance change due to the fins, it encounters the tubes. Since the considered geometry consists of fins attached to the tube and the fact that the flow may be in the developing region when it encounters the tube contraction, it is difficult to measure the exact value of the entrance loss due to the tube contraction effects. Hence, K_c is considered from Kays and London(1984) for the turbulent range of Reynolds number. In this instance, the abrupt contraction coefficient($K_{c\text{-}tu}$) for the tube entrance is derived from the diagrams of Kays and London(1984). Because these losses may be less than 10% of the overall pressure drop for long ducts, even a 20% discrepancy in the abrupt contraction coefficient for tube entrance ($K_{c\text{-}tu}$) measurement would cause a 2% maximum difference in overall pressure drop.

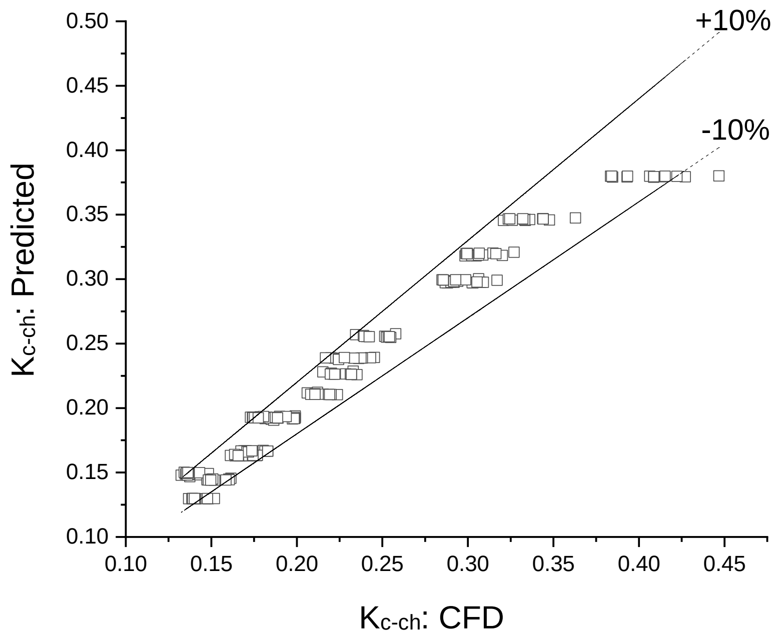

Figure 4-41: Comparison of predicted expansion coefficient for channel entrance with CFD data.

The exit pressure recovery is predicted using equation (4-4), where the coefficients for the abrupt exit from channel and tube bundles are derived from the diagrams in Kays and London (1984) for turbulence regimes.

$$\frac{\Delta P_{ex}}{0.5\,\rho {V_1}^2} = \left(1 - {\sigma_{tu}}^2 - K_{e_{tu}}\right) + \left(1 - {\sigma_{ch}}^2 - K_{e_{ch}}\right) \quad 4\text{-}4$$

where

$$V_1 = \frac{V_{up}}{\sigma_{tu}\sigma_{ch}} \quad 4\text{-}5$$

Figure 4-42 shows the plot of the exit pressure recovery with the Reynolds number for the predicted data using Kays and London and the current CFD data. It can be seen that Kays and London (1984) follow the same Reynolds number variation as the CFD data with an discrepancy of $\pm$20%.

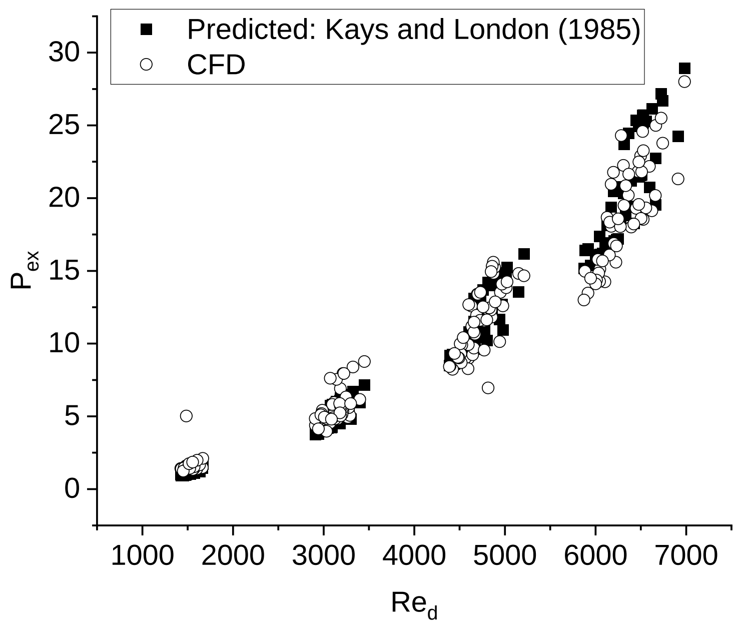

Figure 4-42: The variation of total exit pressure recovery with Reynolds number.

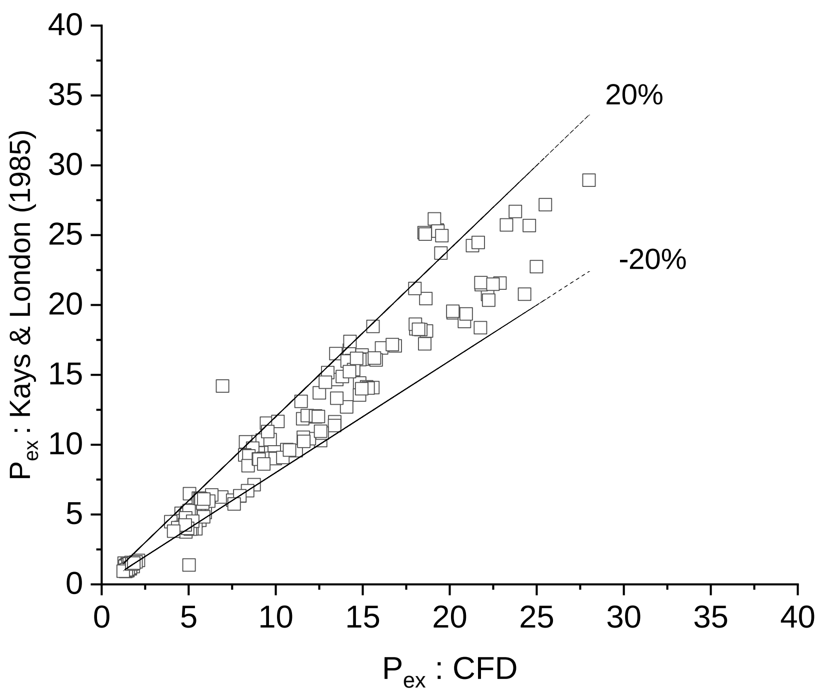

Figure 4-43: Comparison of predicted exit pressure recovery with CFD data.

4.3.4. Correlation

A total of 280 simulations were performed for the parameter space with 3 to 6 tube rows with the tube pitch of 3 to 4 diameters; a fin pitch of 0.25 to 0.65 diameters and Reynolds number from 1450 to 7000. In *Figure 4-44* and *Figure 4-45*, the dimensionless heat transfer and pressure drop from these simulations are presented.

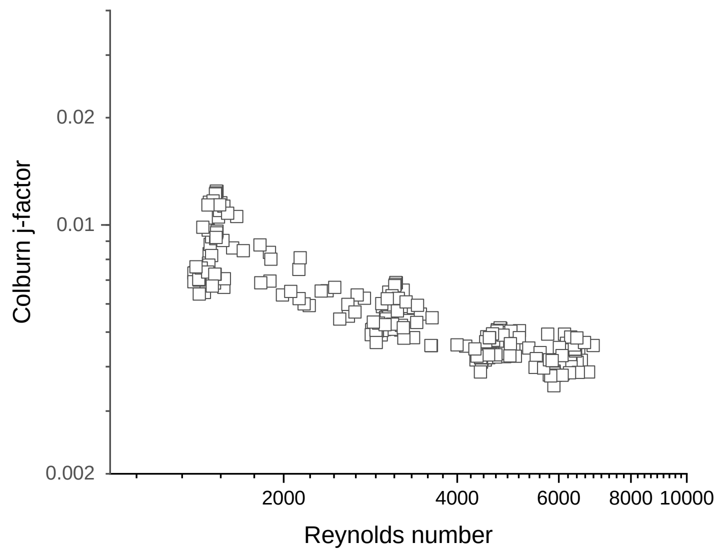

Figure 4-44: Colburn j-factor with Reynold's number for the entire population.

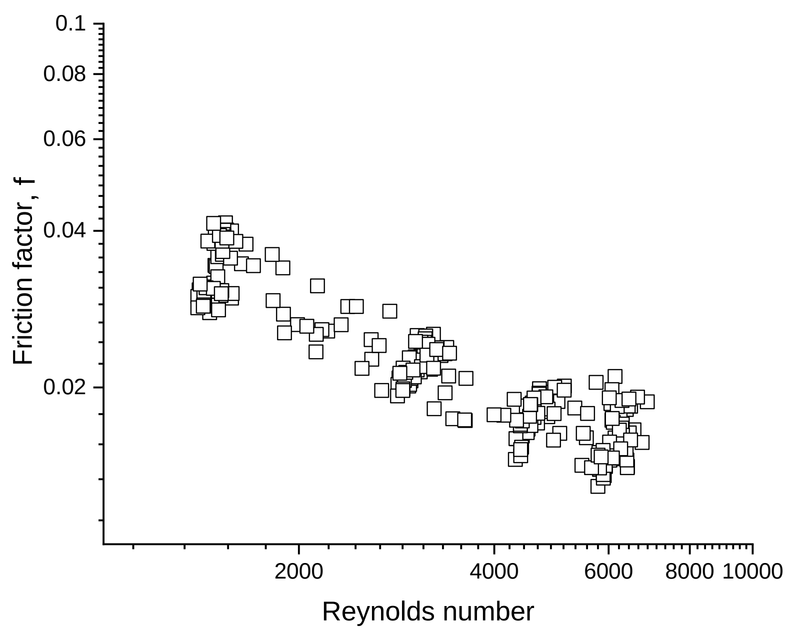

Figure 4-45: Friction factor, f with Reynold's number for the entire population.

It was found that the correlations of Wang [9] can capture the j-factor and f-factor with the geometrical parameters fairly accurately. Here, Wang's correlation has been adopted and modified to improve the accuracy of the cases studied. Multiple regression techniques were used to correlate the data. The Gauss square algorithm was used to minimize the sum of the error squared. The correlation adopted is given below, and the coefficients from the regression analysis are provided in Table 4-3.

$$j = C_1 * (Re_{Dc}^{P3}) * (\frac{F_P}{D_o})^{P5} * (\frac{F_P}{D_h})^{P6} * (\frac{F_P}{P_t})^{C_{13}} * N^{P4} \quad \text{4-6}$$

$$\text{P3} = C_2 + \frac{C_3 * N}{Ln(Re_{Do}^1)} + C_4 * Ln(N * (\frac{F_P}{D_c})^{C_5}) \quad \text{4-7}$$

$$\text{P4} = C_6 + \frac{C_7 * (\frac{P_1}{D_h})^{C_8}}{Ln(Re_{Do}^1)} \quad \text{4-8}$$

$$\text{P5} = C_9 + \frac{C_{10} * N}{Ln(Re_{Do}^1)} \quad \text{4-9}$$

$$P6 = C_{11} + C_{12} * Ln(\frac{Re_{Dc}^1}{N}) \quad \text{4-10}$$

The predicted results from the correlation and original CFD data are compared in Figure 4-46. Ninety-eight percent of the deviations are within ±8%, and the root-mean-square error is around 4.3%, indicating that the correlation is of sufficient accuracy.

Table 4-3: Coefficient for j-correlation For Fully Ducted Geometry

C_1	C_2	C_3	C_4	C_5	C_6	C_7	C_8
1.1407	-0.5516	0.0042	0.8826	0.2769	-12.6861	40.8495	0.0499
C_9	C_{10}	C_{11}	C_{12}	C_{13}			
-2.98	0.4016	-2.2253	0.2008	0.8492			

The above correlation for the Colburn j-factor is complex and difficult to implement. A simpler correlation was sought for the parameter space with 3 to 6 tube rows with tube pitch of 3 to 4 diameters; a fin pitch of 0.25 to 0.65 diameters and Reynolds number in the range 2000 to 7000. The low Reynolds number data showed significant deviation and was omitted so that the Reynolds number sample space was reduced as specified above. The resulting correlation is given by equation (4-11). The deviations are within 10%, as shown in Figure 4-47, and the root-mean-square difference is around 4.45%.

$$j_s = 0.221 * (Re_{Do}^{-0.43939}) * (\frac{F_P}{D_o})^{-0.48157} * (\frac{F_P}{P_t})^{0.23086} * N^{-0.0405} \quad \text{4-11}$$

Similar procedures were adopted to develop correlations for the friction factor. Multiple regression techniques using the Gauss-Newton iterative algorithm [71] was used to obtain the correlation for the friction factor as

$$f = A_1 * (Re_{Do}^{P3}) * N^{P4} * (\frac{F_P}{D_o})^{P5} * (\frac{F_P}{D_h})^{P6} * (\frac{F_P}{P_t})^{A_{13}} \quad \text{4-12}$$

$$\mathrm{P3} = A_2 + \frac{A_3 * N}{Ln(Re_{Do}^{1})} + A_4 * Ln(N * (\frac{F_P}{D_o})^{A_5}) \quad \text{4-13}$$

$$\mathrm{P4} = A_6 + \frac{A_7 * (\frac{P_1}{D_h})^{A_8}}{Ln(Re_{Do}^{1})} \quad \text{4-14}$$

$$\mathrm{P5} = A_9 + \frac{A_{10} * N}{Ln(Re_{Do}^{1})} \quad \text{4-15}$$

$$P6 = A_{11} + A_{12} * Ln(\frac{Re_{Do}^{1}}{N}) \quad \text{4-16}$$

Table 4-4:Correlation for f-correlation for Fully Ducted Geometry

A_1	A_2	A_3	A_4	A_5	A_6	A_7
24.2951	-0.6027	0.1791	0.6355	0.0538	-9.9696	26.94
A_8	A_9	A_{10}	A_{11}	A_{12}	A_{13}	
0.1036	-1.7091	0.3518	-3.573	0.3387	1.4539	

The predicted results from the correlation and the original CFD data are compared in *Figure 4-48*. The deviations are within 10%, and the root-mean-square difference is around 5.4%.

A simpler correlation was also developed for the friction factor and is given by equation (4-17). The deviations are within 15%, as shown in Figure 4-49, and the root-mean-square difference is around 7.26%.

$$f_s = 3.0644 * (Re_{Do}^{-0.5304}) * N^{-0.05434} * (\frac{F_P}{D_o})^{-0.8615} * (\frac{F_P}{D_h})^{-0.07812} * (\frac{F_P}{P_t})^{0.61771} \qquad 4\text{-}17$$

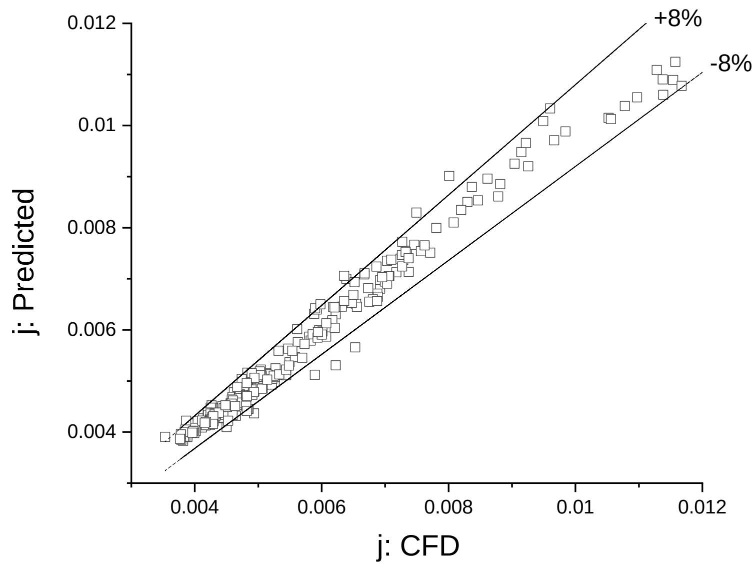

Figure 4-46: Comparisons of the present heat transfer correlations with the CFD data.

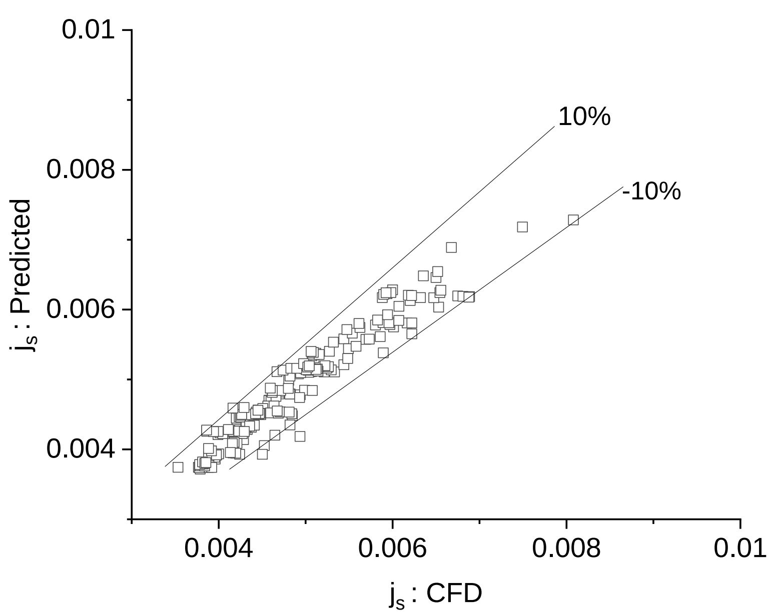

Figure 4-47: Comparisons of the present heat transfer correlations with the CFD data for simple correlation.

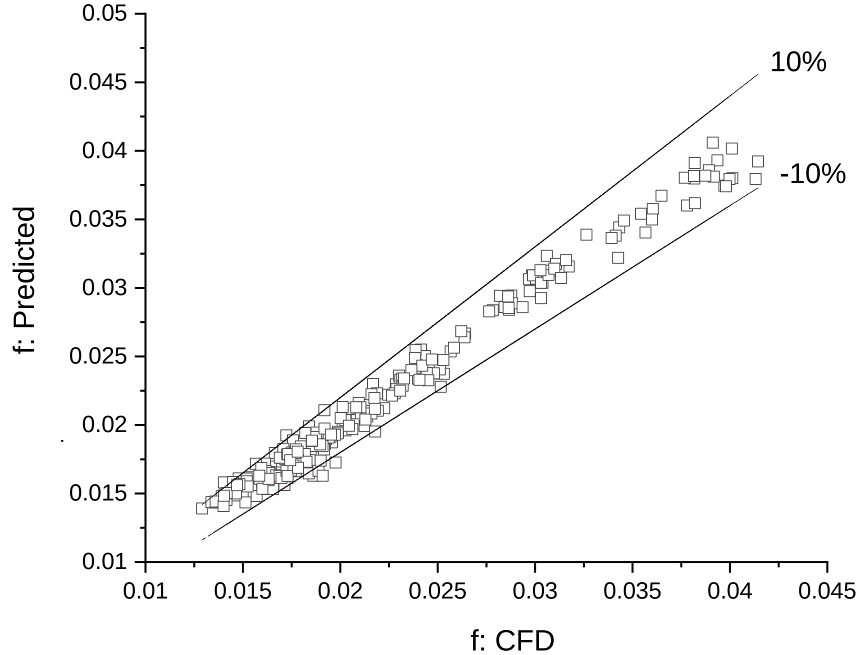

Figure 4-48: Comparisons of the present frictional factor correlations with the CFD.

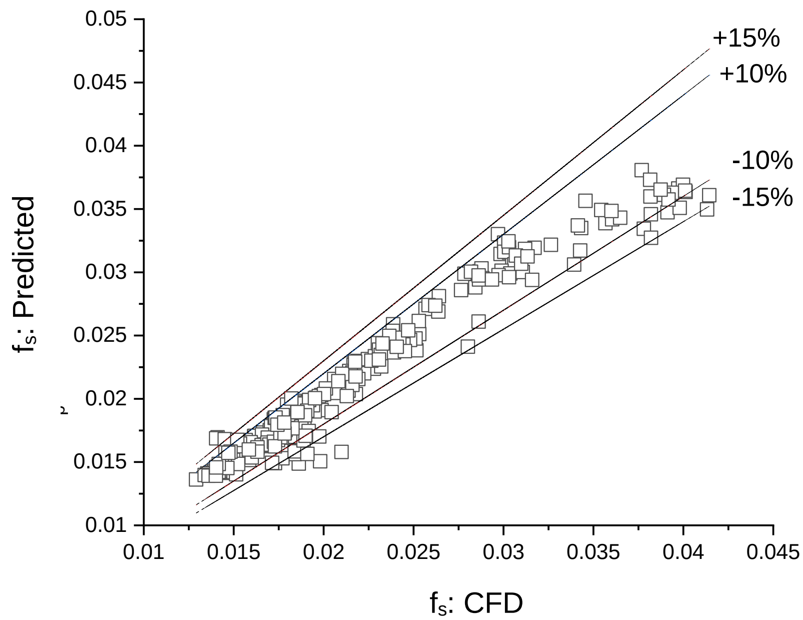

Figure 4-49: Comparisons of the present friction factor correlations with the CFD data for simple correlation.

Chapter 5.

Partially Ducted Heat Exchangers

In many applications, the flat plate and tube heat exchangers are mounted in airflow with significant clearance on the top and the sides. The heat exchanger provides a higher resistance to the flow, and some of the flow will bypass around the heat exchanger, resulting in reduced thermal performance. The effect of flow bypass on the performance of flat plate and tube heat exchangers is investigated numerically in this chapter.

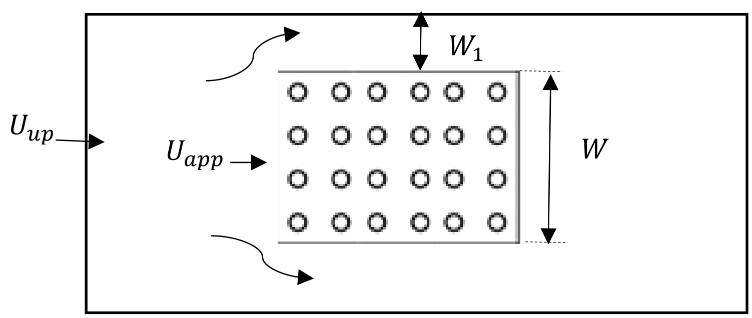

a) Top view

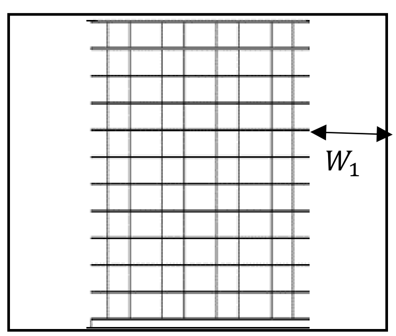

b) Front view

Figure 5-1: Top and Front View of Partially Ducted (PD) Flat Plate and Tube Heat Exchanger

The heat transfer from a fully ducted (FD) finned tube heat exchanger depends on its geometrical parameters and velocity of the flow entering the heat exchanger, as seen in the previous chapter. In the partially ducted case, the velocity of the flow entering the heat exchanger is less than the upstream velocity and is an essential factor for predicting the heat transfer. The velocity of flow just upstream of the heat exchanger entering into the heat exchanger is termed the approach velocity (U_{app}) and flow velocity bypassing is the bypass velocity (U_{by}). Depending on the clearance (W_1) around the heat exchanger, the clearance ratio (CLR) is defined as

$$\boldsymbol{CLR = \frac{2W_1}{W}} \tag{1}$$

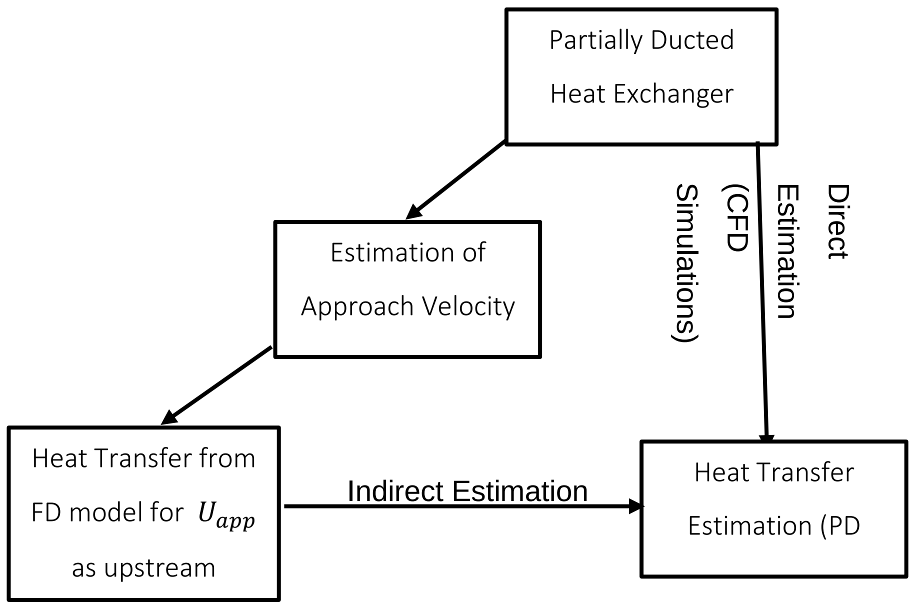

Figure 5-2: Modelling Strategy for Heat Transfer Estimation for Partially Ducted Heat Exchanger

The amount of flow bypass depends on the resistance of the heat exchanger core and the bypass region to the flow. The flow resistance of the heat exchanger core depends upon the geometrical parameters like fin pitch, tube pitch, number of tube rows and Reynolds number. The flow resistance of the bypass region depends upon the clearance width and Reynolds number, with the clearance width being the most significant factor that affects the flow bypass [43] [41]. This study is limited to the effect of the clearance ratio and Reynolds number for one of the most common geometrical configurations used by our industrial partner. The geometry considered has 6 number of tube rows, a transverse tube pitch of 3.5 diameters, a longitudinal tube pitch of 4 diameters and a fin pitch of 0.5 diameters.

Two possible approaches for estimating the heat transfer for a partially ducted model are (i) direct estimation from CFD simulations, which is not very time and cost-effective and (ii) estimation from existing fully ducted models using the approach velocity as the upstream velocity. The second approach requires the evaluation of the approach velocity. In this study, the various components of the pressure drop are compared against the available correlations, so that the approach velocity could be modelled using a resistance network approach in the future.

The Reynolds number is defined based on the velocity defined by U_{up}/σ, which is much higher than the actual maximum velocity inside the domain due to flow leakage to the bypass region. So, the flow inside the partially ducted heat exchanger cannot be compared with the fully ducted case based on the Reynolds number, rather it shall be compared based on the actual measure of the velocity for a given geometry.

5.1. Effect of bypass clearance ratio

The flow in a partially ducted flat plate and tube heat exchanger is similar to the flow over a porous rectangular block. Some of the approaching flow circumvents around the heat exchanger due to high pressure in the front. There is a low pressure at the back, which helps in the suction of the flow through the heat exchanger towards its back end. There is a continuous pressure drop on the side bypass path similar to channel flow.

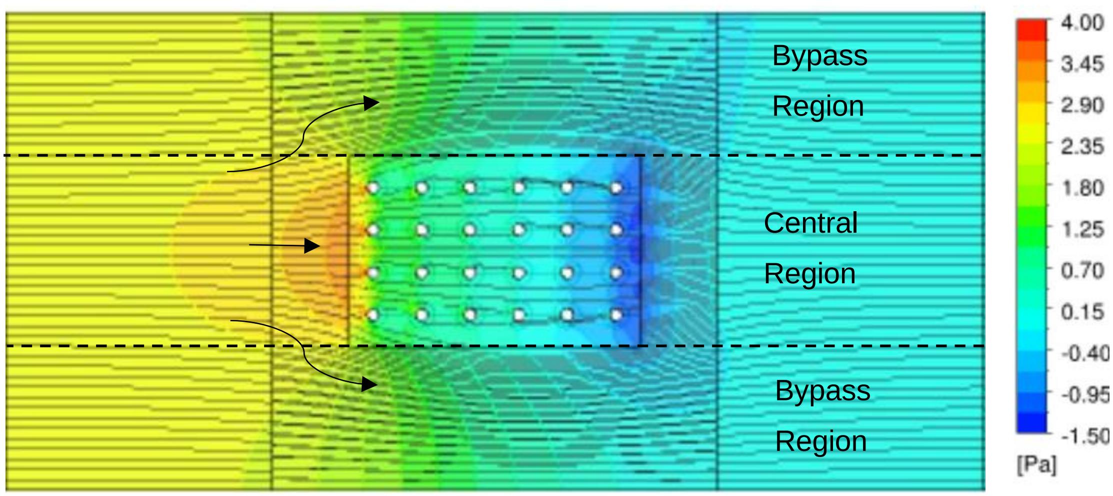

Figure 5-3: Streamlines with the Pressure Contours on Central Plane (CLR = 1.5).

The streamlines around the heat exchanger on the central plane for the partially ducted geometry with a clearance ratio of 0.25 and 24 for the Reynolds number of 2300 are shown in Figure 5-4. There is a higher bypass flow for the higher clearance ratio geometry, which reduces the approach velocity. Even after the flow enters and interacts with the first tube, there is a continuous leakage of the flow to the bypass region in the streamwise direction, and the effect is more pronounced for the higher clearance ratio geometry. Thus, the mass flow rate within the heat exchanger continuously decreases until it starts recovering due to low pressure at the back. It is also interesting to note that there is fluid circulating the corner tube of the second and the third row, unlike in the fully ducted heat exchanger. There is a development of horse-shoe vortices around the tubes, which would increase the heat transfer around these corner tubes.

The streamlines on the planes around the tubes with a clearance ratio of 0, 0.25 and 24 at Re_{Do} of 2300 are shown in Figure 5-5 to Figure 5-7. There is a difference in the streamlines around the second and third tube. Around the second tube, there are two primary vortices, one secondary vortex and one corner vortex for a clearance ratio of 0.25 and 24, which are not present for the fully ducted geometry (CLR 0). There is a similar horseshoe vortex system around the third tube for clearance of 24. Also, there is a strong single primary vortex for the smallest clearance ratio of 0.25. Around the last tube, there is a vortex at the 0° plane for the partially ducted geometry.

The wall heat flux on the fin surface for the finned tube heat exchanger with a clearance ratio of 0, 0.25 and 24 at Re_{Do} of 2300 is shown in Figure 5-8. The heat transfer in the partially ducted case would depend on the approach velocity as well as the continuous reduction in mass flow rate as the flow moves downstream through the heat exchanger. The wall heat flux decreases with the clearance ratio at the entrance of the fin, around the first row of tubes and on the fin surface, which can be attributed to the reduction in approach velocity. There is a further reduction in the wall heat flux on the downstream corner of the fin, which is due to the continuous leakage flow out of the domain. There is a greater reduction at the higher clearance ratio geometry due to a greater fluid loss. It is interesting to note the increase in wall heat flux around the second or posterior rows of tubes for the clearance ratio of 0.5 as well as 24. This is due to the formation of horseshoe vortices around the latter rows of tubes. To quantitively analyze the effect of the leakage flow on the heat transfer from the fin, a near tube region of radius equal to the outer diameter of the tube is defined, and the rest of the area is defined as the extended fin area. Figure 5-10 shows the heat transfer from these regions for clearance ratios of 0.25 and 24. The results are compared with the fully ducted model at an equivalent upstream velocity equal to the approach velocity of the individual partially ducted cases. The extended region of the partially ducted model transfers 13-14% less heat than the fully ducted model. However, the heat transfer in the near tube region for the partially ducted case is around 50% higher than the fully ducted case.

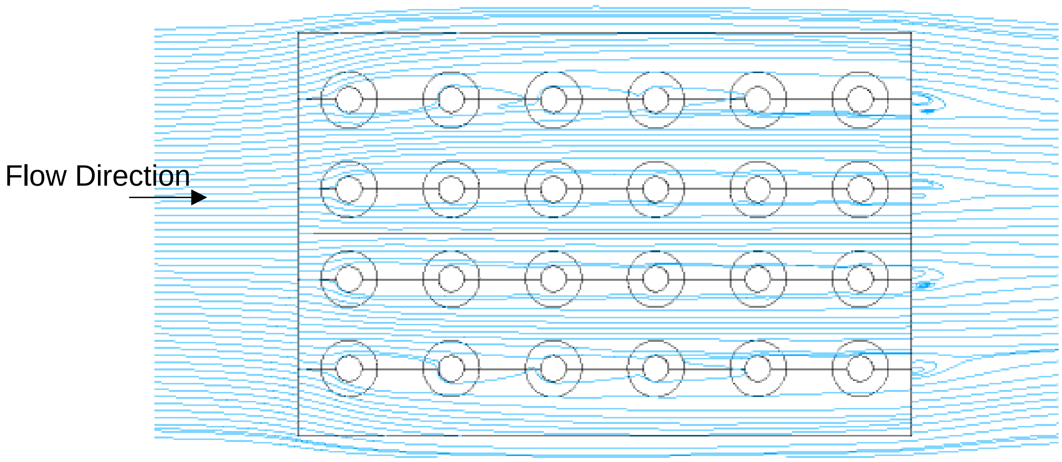

a) Clearance ratio: 0.25

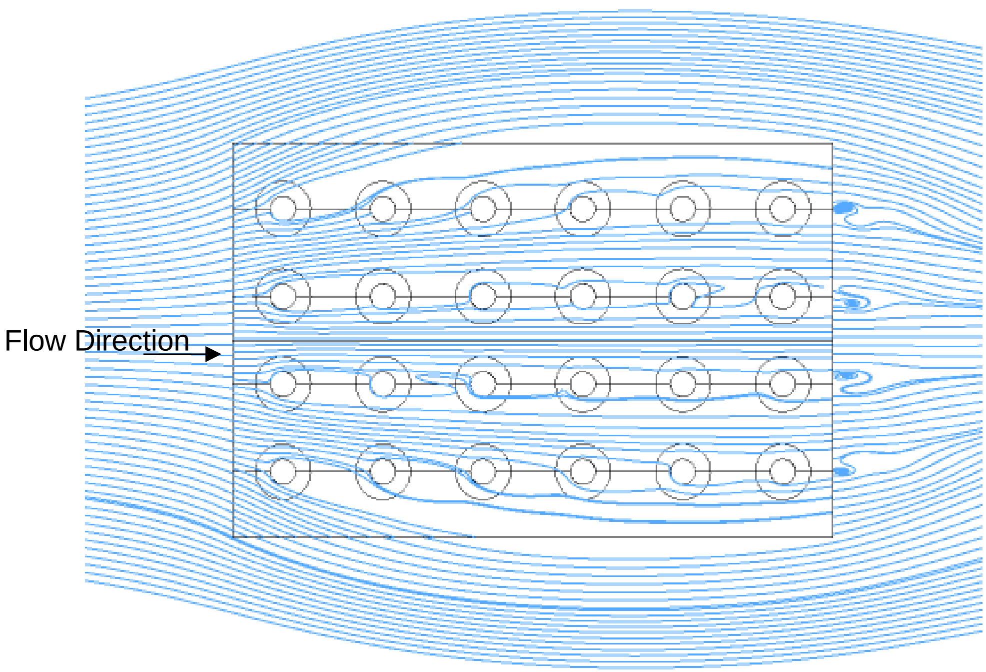

b) Clearance Ratio 24

Figure 5-4: Streamlines on a central plane around the tube for the partially ducted case for CLR 0.25(Top picture), 24 (Bottom picture) for Re_{Do}=2300.

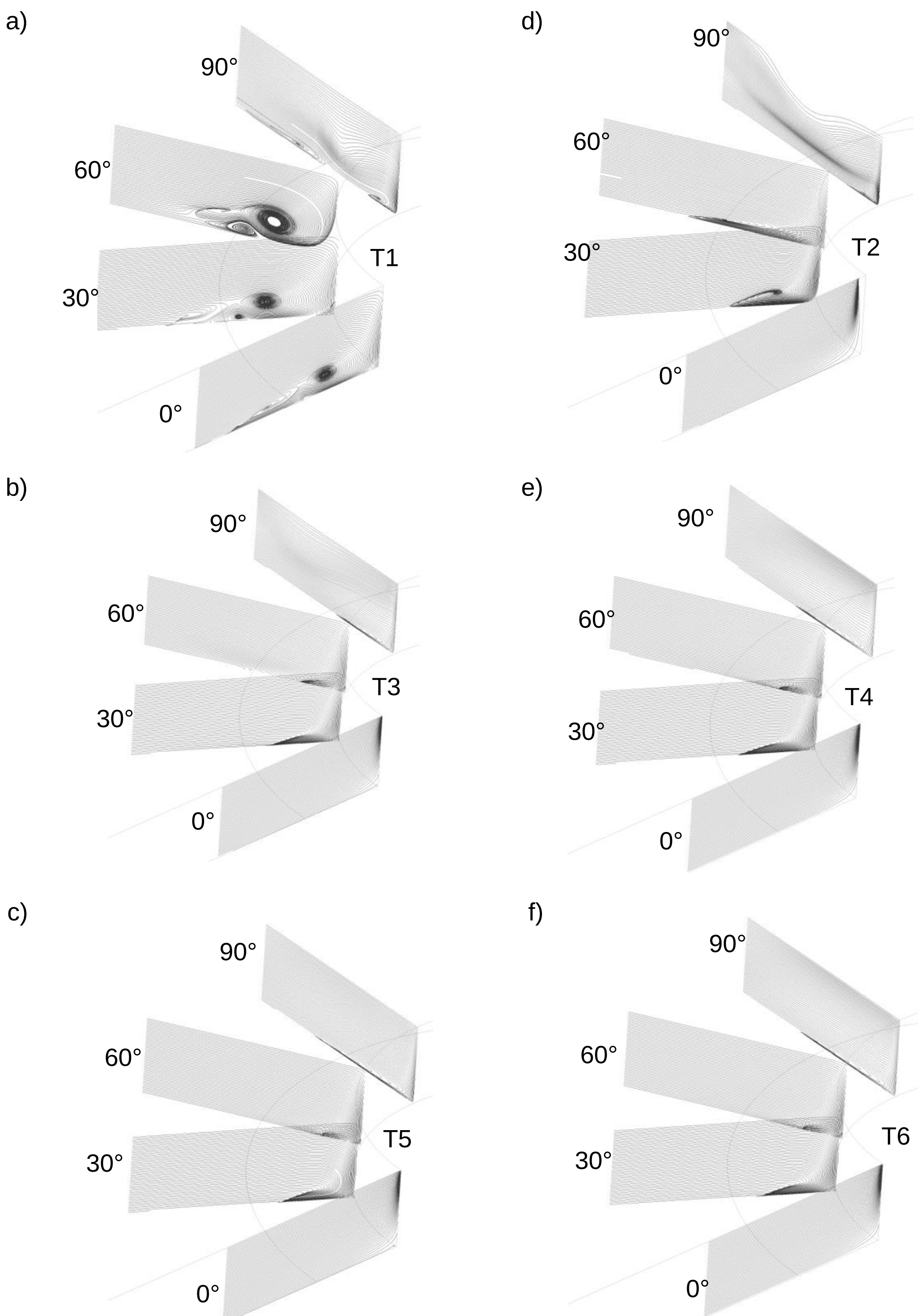

Figure 5-5: Streamlines on a different plane around the tube for the fully ducted case for Re_{Do}=2300.

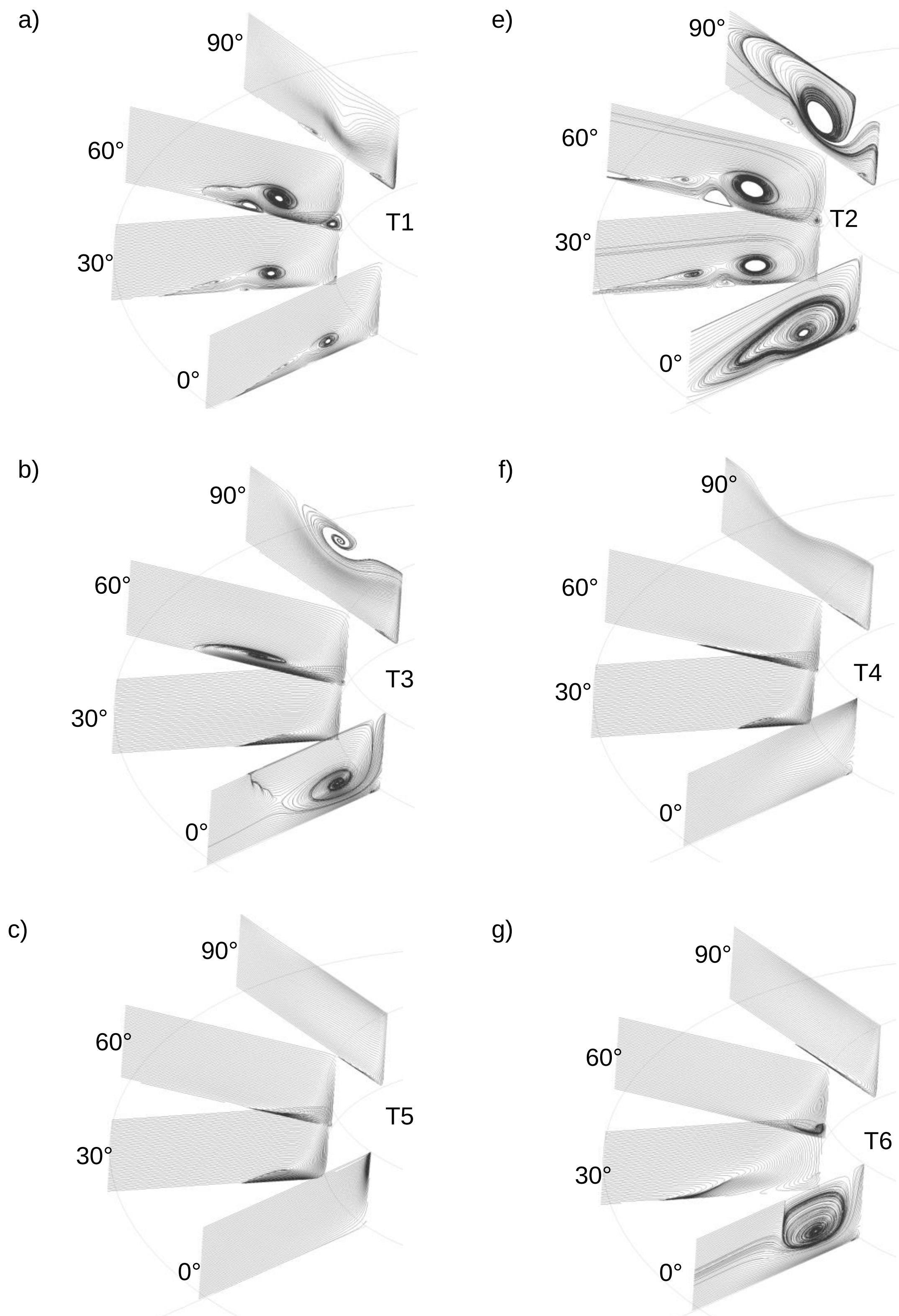

Figure 5-6: Streamlines on a different plane around the extreme column of the tube for the partially ducted case for CLR 0.25 for Re_{Do}=2300.

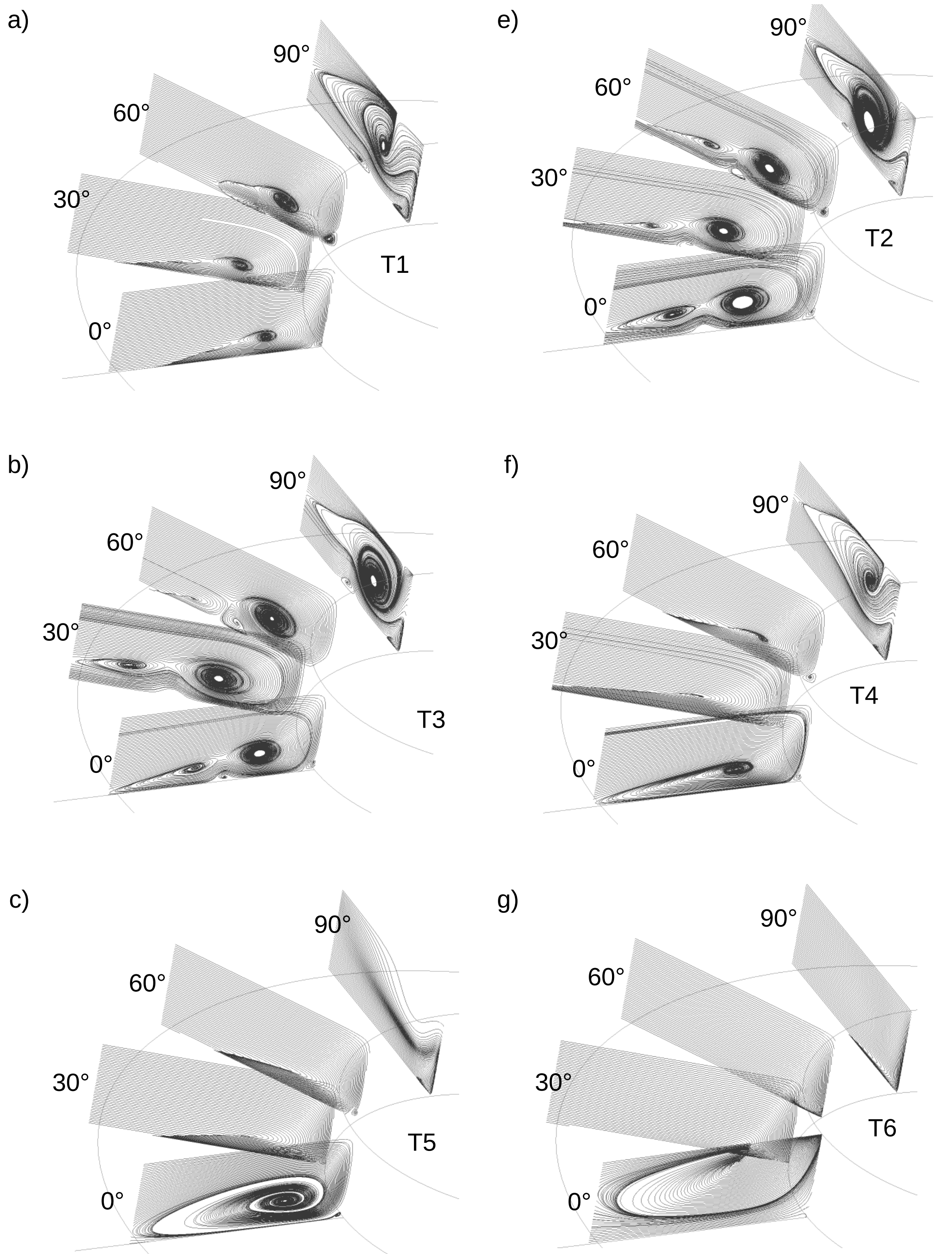

Figure 5-7: Streamlines on a different plane around the extreme column of the tube for the partially ducted case for CLR 24 for Re_{Do}=2300.

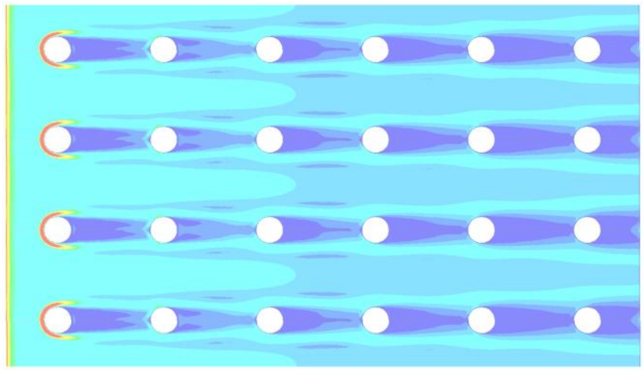

a) Fully ducted geometry

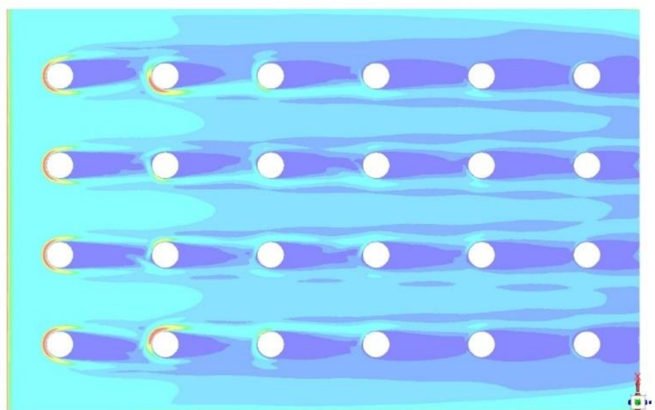

b) Partially ducted: CLR 0.25

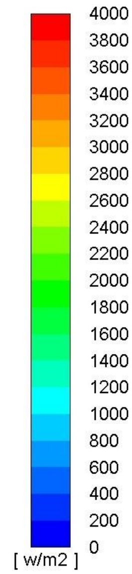

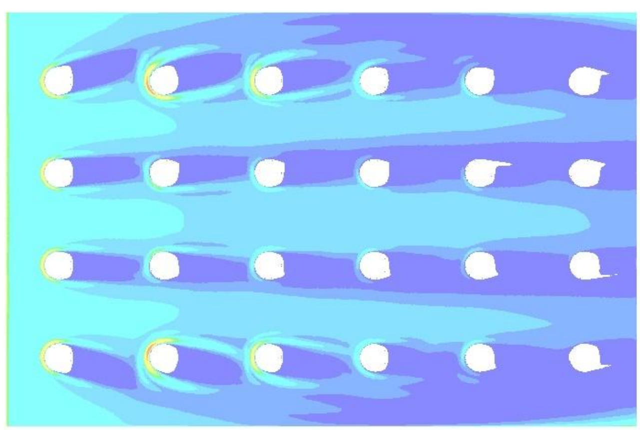

c) Partially ducted: CLR 24

Figure 5-8: The effect of the clearance ratio on wall heat flux on the fin surface for the fully ducted geometry and partially ducted geometry at Re_{Do}=2300.

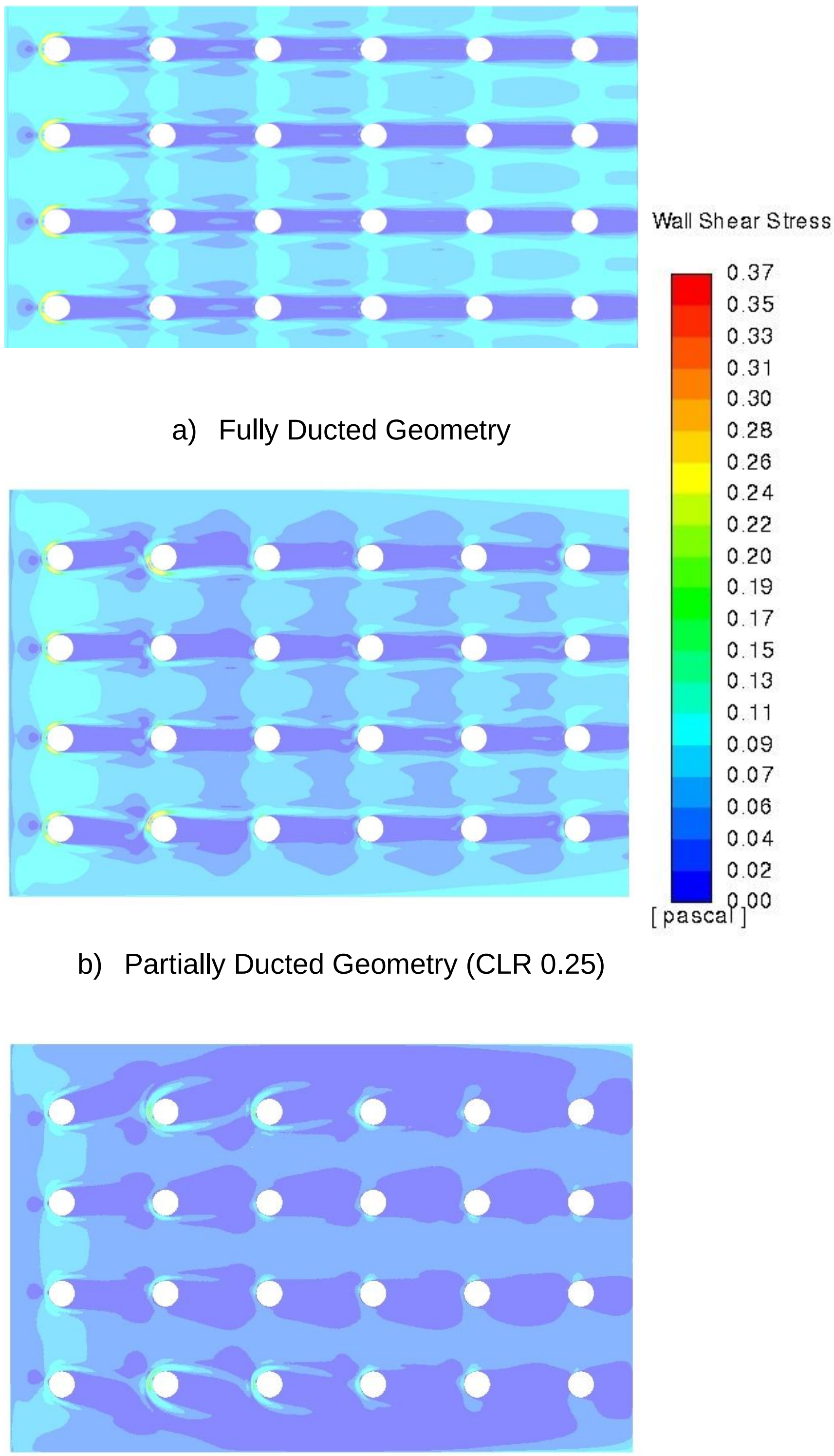

a) Fully Ducted Geometry

b) Partially Ducted Geometry (CLR 0.25)

c) Partially Ducted Geometry (CLR 24)

Figure 5-9: The effect of the clearance ratio on wall shear stress on the fin surface for the fully ducted geometry and partially ducted geometry at Re_{Do}=2300.

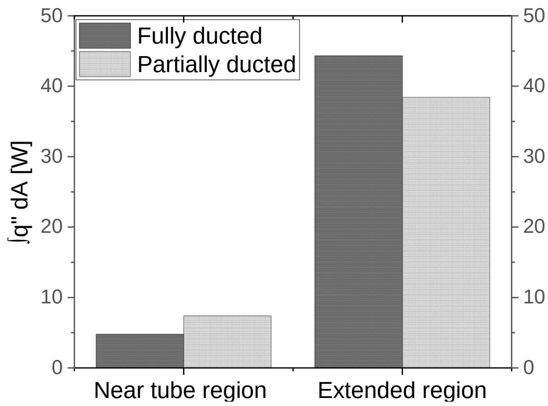

a) Clearance ratio: 0.25

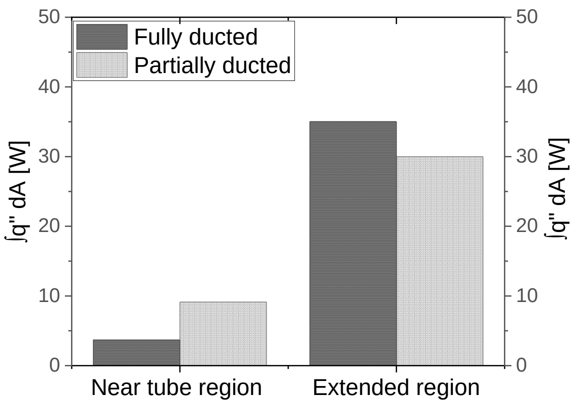

b) Clearance ratio: 24

Figure 5-10: Heat transferred from the near tube region and extended region from the fully ducted and partially ducted geometry for the clearance ratio of 0.25, 24.

The wall shear stress on the fin surface for the finned tube heat exchanger with a clearance ratio of 0, 0.25 and 24 at Re_{Do}=2300 are presented in Figure 5-9. Similar to the heat flux, the wall shear stress is reduced around the first row of tubes and on the fin surface as the clearance ratio is increased. A further decrease can be noticed on the downstream corner of the fin, which increases with the clearance ratio. A high wall shear around the second or posterior rows of tubes can be noticed due to the formation of horseshoe vortex.

A velocity ratio (VR) is defined as the ratio of the area average velocity at any cross-sectional plane to the upstream velocity. Similarly, a mass ratio (MR) is defined as the ratio of the mass flow rate at any cross-sectional plane to the upstream mass flow rate. These are represented as

$$Velocity\ Ratio, VR = \frac{\int U\, dA_f}{A_f U_{up}} \tag{5-1}$$

$$Mass\ Ratio, MR = \frac{\int (\rho U)\, dA_f}{A_{up} \rho_{up} U_{up}} \tag{5-2}$$

where, A_f is the fluid area at any cross-sectional plane.

The mass ratio for the central region (central region marked in Figure 5-3) with streamwise distance for different clearance ratios are plotted in Figure 5-11. There is a continuous decrease in the mass ratio in the central region as it approaches the heat exchanger. The decrease continues inside the heat exchanger due to the leakage of flow from the central region to the bypass region. Beyond the lowest pressure location downstream in the central region, the mass ratio begins to recover as the flow deviates back to the central region from the bypass region. After exiting the heat exchanger, the mass ratio continues to increase but does not fully recover. The mass ratio begins to decrease further upstream as the clearance ratio is increased. Also, the flow recovery is much later for a higher clearance ratio downstream of the heat exchanger. The flow leakage to the bypass region inside the heat exchanger increases on increasing the clearance ratio up to a CLR of 1.5, and a further increase in the CLR has a negligible effect on the leakage flow.

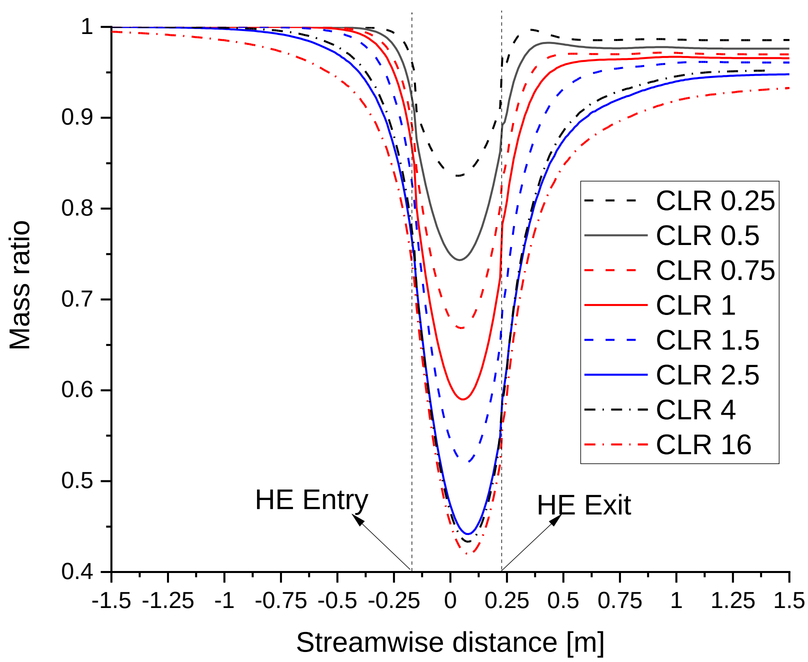

Figure 5-11: The effect of clearance ratio on the streamwise variation of mass ratio with streamwise distance in the central region for Re_{Do}=2300.

Due to the significant leakage of the flow after entering the heat exchanger, the nominal velocity is defined as the volume average velocity inside the heat exchanger core. The contraction ratio is incorporated to take into effect the area contraction, and the nominal velocity is defined as

$$Nominal\ Velocity, NV = \sigma_{ov}(\int \frac{U\ dV_f}{V_f}) \tag{5-3}$$

The ratio of approach velocity and the nominal velocity to the upstream velocity with the clearance ratio for a Reynolds number of 2300 is plotted in Figure 5-12. The approach velocity and the nominal velocity decreases rapidly with an initial increase in the clearance ratio. The approach velocity and the nominal velocity asymptotes to a constant value with a minimal change beyond a clearance ratio of 15. The nominal velocity is much lower than the approach velocity, especially for a high clearance ratio due to the flow leakage. Figure 5-13 shows the variation of the Colburn j-factor with the clearance ratio for the Reynolds number of 2300, which is defined as follows.

$$j = \frac{h}{\rho * c_p * U_{max}} Pr^{2/3} \tag{5-4}$$

$$U_{max} = \frac{U_{up}}{\sigma_{tu} * \sigma_{ch}} \tag{5-5}$$

The Colburn j-factor decreases with the clearance ratio until a clearance ratio of about 15 and there is little change beyond this clearance ratio.

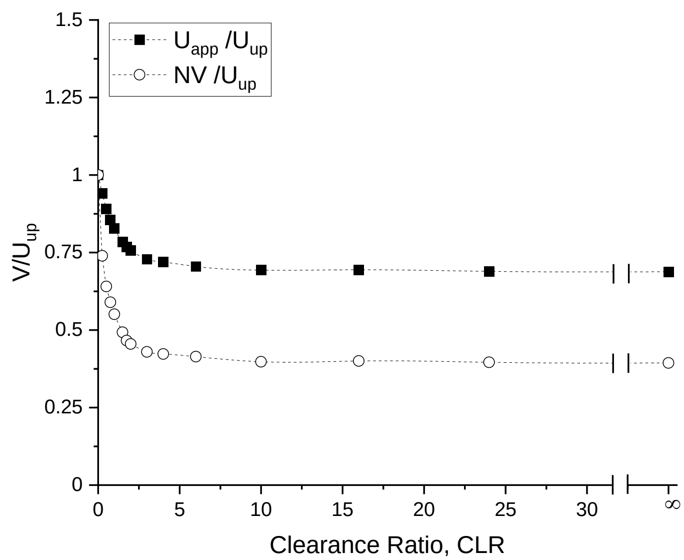

Figure 5-12: The effect of the clearance ratio on approach velocity and the nominal velocity variation for Re_{Do}=2300.

The streamwise pressure distribution in the central and bypass regions are shown in Figure 5-14. Figure 5-15 shows the variation of pressure with streamwise distance for different clearance ratios for the Reynolds number of 2300. A rise in the pressure can be seen before entering the heat exchanger and after exiting the heat exchanger. The increase in the streamwise pressure gradient upstream of the heat exchanger begins sooner with an increase in the clearance ratio. The maximum pressure is reached just before the inlet, which increases with the clearance ratio. The inlet pressure decreases with an increase in the clearance ratio to a value of nearly zero. Figure 5-16 shows the pressure coefficient, Cp, for the variation in total pressure with a clearance ratio for the Reynolds number of 2300, which is defined as follows.

$$C_{p,}\text{Total pressure diff.} = \frac{\Delta P_T}{0.5\rho {U_{up}}^2} \qquad \text{5-6}$$

There is a hyperbolic variation of C_p with the clearance ratio and reaches the value of 0 for the clearance ratio of infinity.

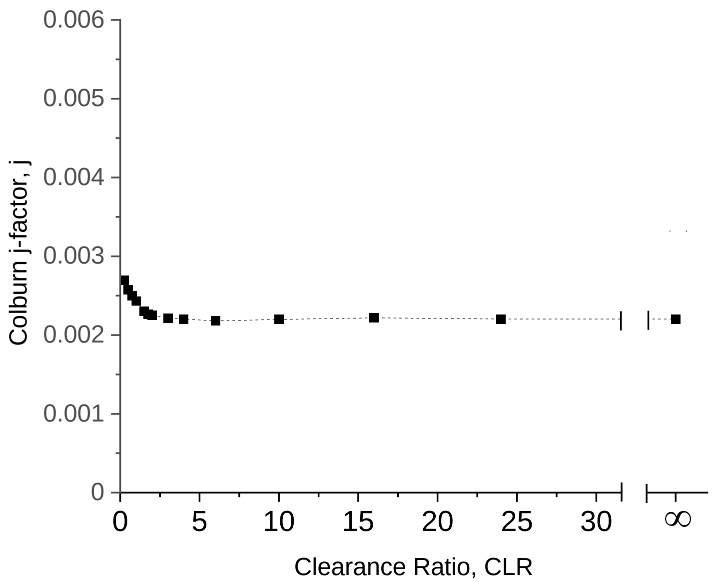

Figure 5-13: The effect of the clearance ratio on the Colburn j-factor with the clearance ratio for Re_{Do}=2300.

Figure 5-17 shows the variation of the friction factor for the partially ducted model with the clearance ratio for the Reynolds number of 2300, which is defined as follows.

$$f_1 = \frac{P_{fr} - P_b}{0.5\rho {U_{max}}^2}\frac{A_c}{A_o} \qquad \text{5-7}$$

where, P_{fr} and P_b is the average cross-sectional pressure in the central region just in front of and the back of the heat exchanger core, as shown in Figure 5-14. The friction factor decreases rapidly with the initial increase in the clearance ratio. The friction factor reaches a nearly constant value after a clearance ratio of 15 with minimal difference observed for higher clearance. There is a steep decrease in friction factor from fully ducted for the low clearance ratio of 0.25.

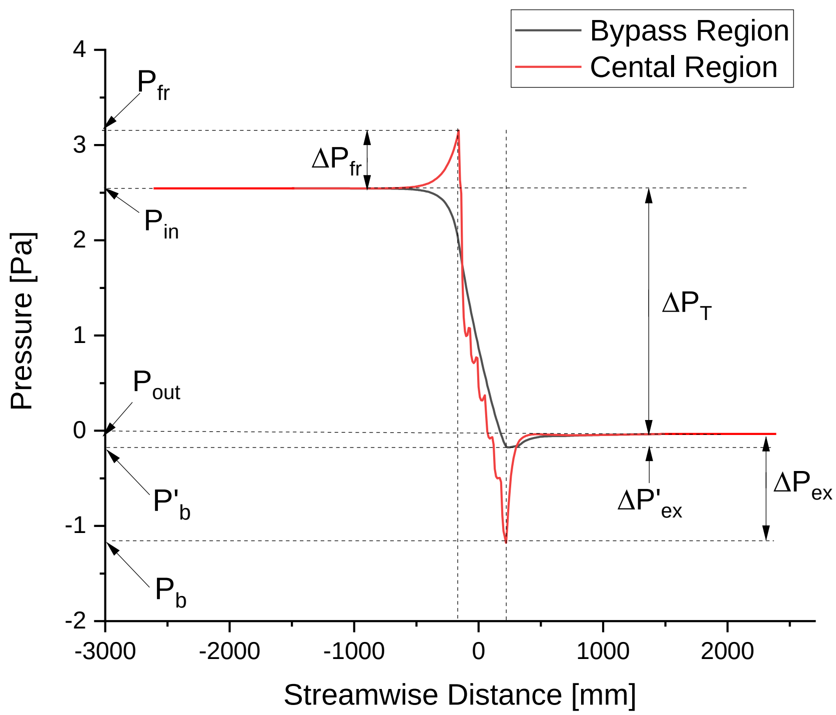

Figure 5-14: The pressure development in the central and the bypass region.

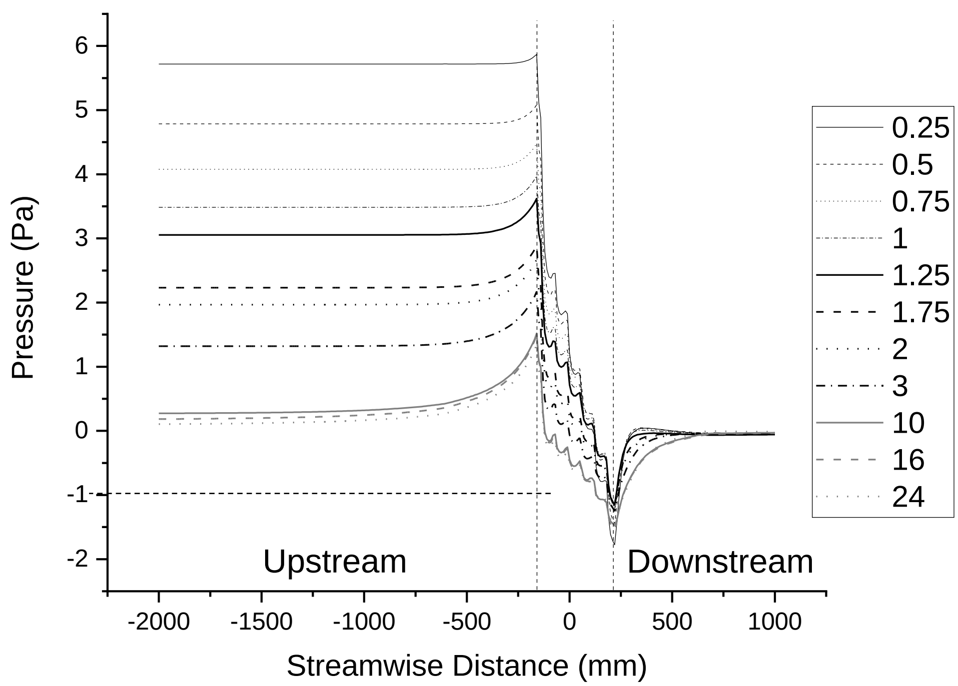

Figure 5-15: The effect of the clearance ratio on streamwise pressure variation for Re_{Do}=2300

The pressure coefficient for frontal pressure rise with a clearance ratio for the Reynolds number of 2300 is shown in Figure 5-18, which is defined as follows.

$$C_{p,}\text{Frontal pressure rise} = \frac{\Delta P_{fr}}{0.5\rho {U_{up}}^2} \quad \text{5-8}$$

The Cp (front pressure rise) increases rapidly with the initial increase in the clearance ratio. It reaches an almost constant value after the clearance ratio of 15 with minimal difference observed for higher clearance.

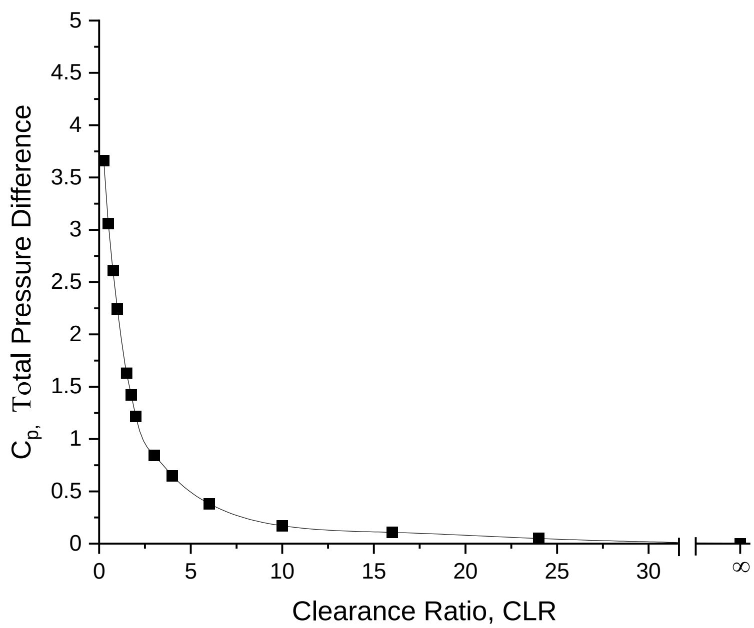

Figure 5-16: The effect of the clearance ratio on the variation of pressure coefficient for total pressure change for the Reynolds number of 2300.

The pressure coefficient for exit pressure change for the central region ($P_{out} - P_b$) and the bypass region ($P_{out} - P'_b$) with the clearance ratio for the central and the bypass region for the Reynolds number of 2300 is shown in Figure 5-19, which is defined as follows.

$$C_{p,}\text{Pressure recovery} = \frac{\Delta P_{ex}}{0.5\rho {U_{up}}^2}\ \text{(Central region)} \quad \text{5-9}$$

$$C_{p,}\text{Pressure recovery} = \frac{\Delta P'_{ex}}{0.5\rho {U_{up}}^2}\ \text{(Bypass region)} \quad \text{5-10}$$

The pressure coefficient decreases with the clearance ratio until CLR 1.5 and later increases to a constant value for high clearance ratios for the central region. For the bypass region, a steep decrease in the pressure coefficient with a clearance ratio is observed, which then asymptotes to a constant value after a clearance ratio of about 15.

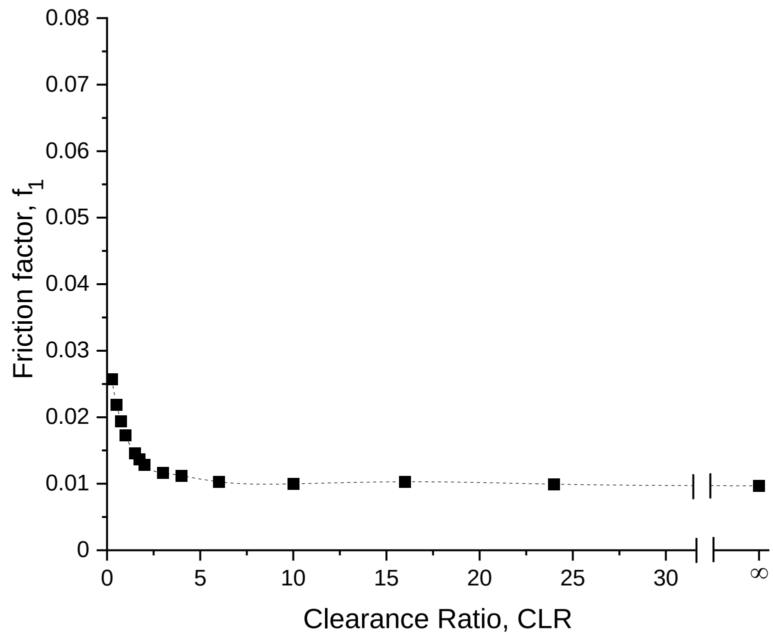

Figure 5-17: The effect of the clearance ratio on the friction factor for the Reynolds number of 2300

The total exit pressure change at the rear end is a function of two different causes. The first is the pressure recovery due to abrupt exit effects (***Δ****P_{ae}*). The second is the pressure change at the rear end of the heat exchanger due to the flow around the heat exchanger, similar to the negative pressure at the back face of a blunt-body (***Δ****P_{be}*). *P_{be}* is usually a pressure recovery for the central region, but a pressure loss for the bypass region.

ΔP_{ae} depends upon the square of the velocity before exiting the abrupt contraction area [29]. For the central region, as the clearance ratio increases, the approach velocity decreases, thereby decreasing the ***ΔP_{ae}***. Similarly, ***Δ****P_{be}* is usually dependent on the rise of the square of velocity downstream after exiting the heat exchanger[45], which increases with the clearance ratio, thereby increasing the ***Δ****P_{be}* for the central as well as the bypass region. The dominance of the pressure change at the exit due to the flow around the heat exchanger (***Δ****P_{be}*) after the clearance ratio of 1.5 could be the reason for the increase of the total pressure recovery.

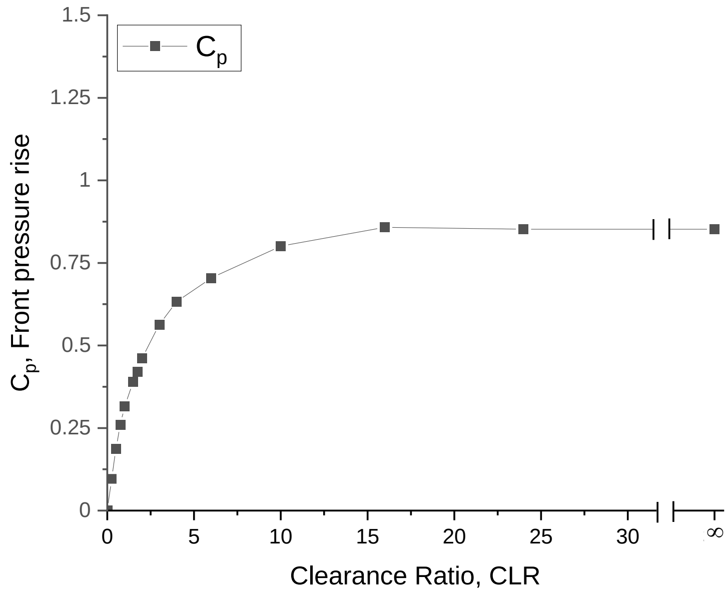

Figure 5-18: The effect of clearance ratio on pressure coefficient for front pressure riseVariation for the Reynolds number of 2300.

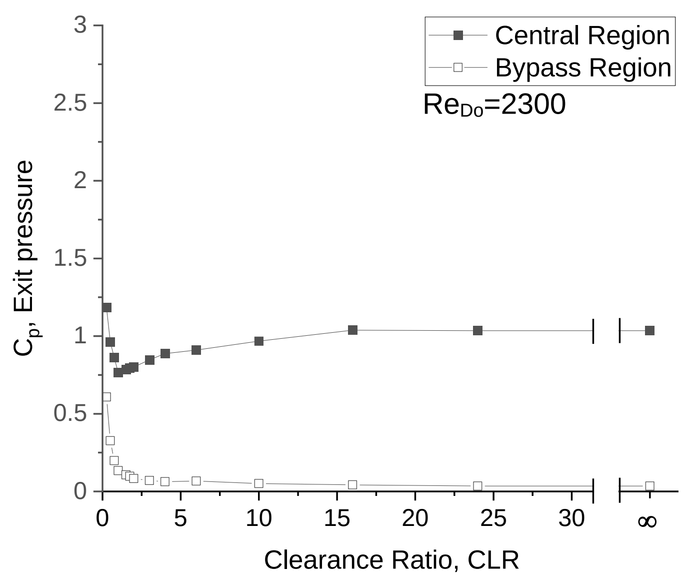

Figure 5-19: The effect of the clearance ratio on pressure coefficient for the exit pressure change for the central and the bypass region for the Reynolds number of 2300.

5.2. The variation with Reynolds number

The effect of Reynolds number and clearance ratio is considered for four different clearance ratio (CLR = 0.25, 1.5, 6, 16) in this section.

The streamwise variation of velocity ratio and mass ratio for the central and bypass regions for different Reynolds numbers for the different clearance ratios is shown in Figure 5-20 and Figure 5-21. There is a continuous decrease in velocity ratio and mass ratio in the central region until it approaches the heat exchanger due to the stagnation pressure. The leakage of flow from the central region to the bypass region further continues inside the heat exchanger. The stream starts recovering before exiting the heat exchanger, which increases the velocity ratio and mass ratio. The flow leakage decreases with an increase in the Reynolds number for all clearance ratios. As seen earlier for Re_{Do} of 2300, the flow leakage increases with the clearance ratio for the other Reynolds numbers as well. There is a sudden jump in the velocity ratio at the entrance and exit of the heat exchanger due to channel contraction and expansion effects. The velocity within the heat exchanger core is lower than the approach velocity for clearance ratios greater than 0.25 due to the flow leakage, while the mass ratio is always less than the velocity ratio due to the continuous decrease in density as the flow moves downstream. After exiting the heat exchanger, the overall mass ratio recovers back to one, while it is lower than one for the central region and higher than one for the bypass region. The velocity ratio is higher than one due to the conservation of mass.

The ratio of the approach and nominal velocity to the upstream velocity with the Reynolds number for different clearance ratios is presented in Figure 5-22. The approach and nominal velocity ratio slightly increase with the Reynolds number for all clearance ratios. The nominal velocity ratio is consistently lower than the approach velocity ratio for any Reynolds number due to flow leakage. As seen earlier for Re_{Do} of 2300, the approach and nominal velocity ratio decrease with the clearance ratio and this difference decreases as the clearance ratio is increased. The variation of the velocity ratio is more dependent on the Reynolds number for a high clearance ratio and less dependent on a low clearance ratio of 0.25.

The Colburn j-factor with the Reynolds number for different clearance ratios is shown in Figure 5-23. The Colburn j-factor decreases with the Reynolds number for all the clearance ratios. For clearance ratios higher than 1.5, the difference in j-factor becomes negligible for higher Reynolds numbers, while there is a small difference for low Reynolds numbers.

Figure 5-24 shows the pressure coefficient with streamwise distance for three different Reynolds numbers for the bypass region and the central region for a clearance ratio of 1.5, which is defined as follows.

$$C_p = \frac{P - P_{in}}{0.5\rho {U_\infty}^2} \qquad \text{5-11}$$

The total pressure drop across the path is equal for the bypass and central regions as expected. The increase and decrease in pressure in the central region and the bypass region, respectively, upstream of the heat exchanger are seen in this figure. The increase in streamwise pressure begins nearly 600mm upstream of the heat exchanger and does not vary much with the Reynolds number. Pressure recovery is observed at the exit from the central region. For the bypass region, a pressure loss is observed at the exit for the lowest Reynolds number and a pressure recovery is observed for the high Reynolds numbers.

Figure 5-25 shows the friction factor with Reynolds number for the different clearance ratios. The friction factor is decreasing with the Reynolds number for all the clearance ratios. For a clearance ratio greater than 1.5, the difference in friction factor with clearance ratio reduces with an increase in the Reynolds number.

The front pressure rise coefficient with Reynolds number for the different clearance ratios is presented in Figure 5-26. For the clearance ratio of 0.25, the pressure coefficient is nearly constant with the Reynolds number while a decrease in pressure coefficient with Reynolds number is seen for a high clearance ratio. This is consistent with the increasing dependence of velocity ratio on Reynolds number with increasing clearance ratio.

The exit pressure recovery (ΔP_{ex}) coefficient with Reynolds number for the central region for different clearance ratios is presented in Figure 5-27. An increase in the pressure coefficient is observed for the initial increase in the Reynolds number and it gradually decreases later for all the clearance ratios. The pressure coefficient is lowest for the clearance ratio of 1.5, which indicates the exit pressure recovery coefficient initially decreases with the clearance ratio of about 1.5 for all the Reynolds numbers and then increases with a further increase in the clearance ratio.

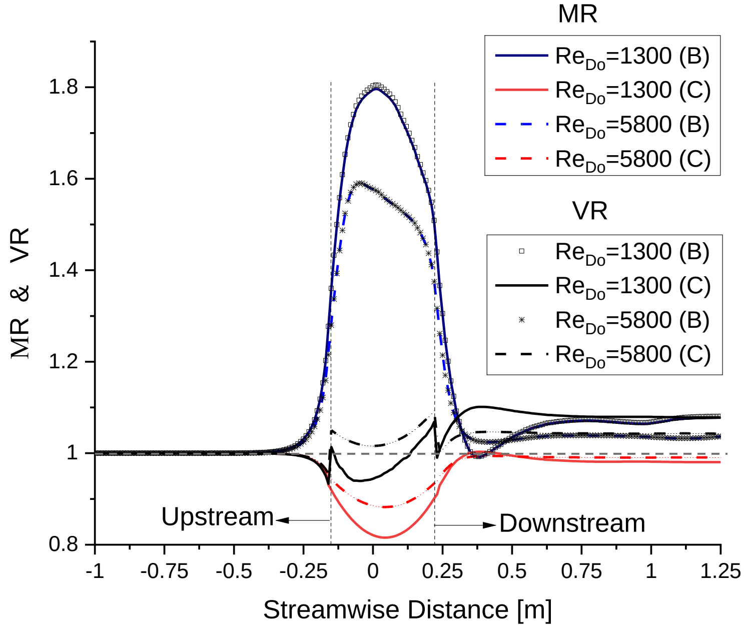

a) Clearance ratio of 0.25

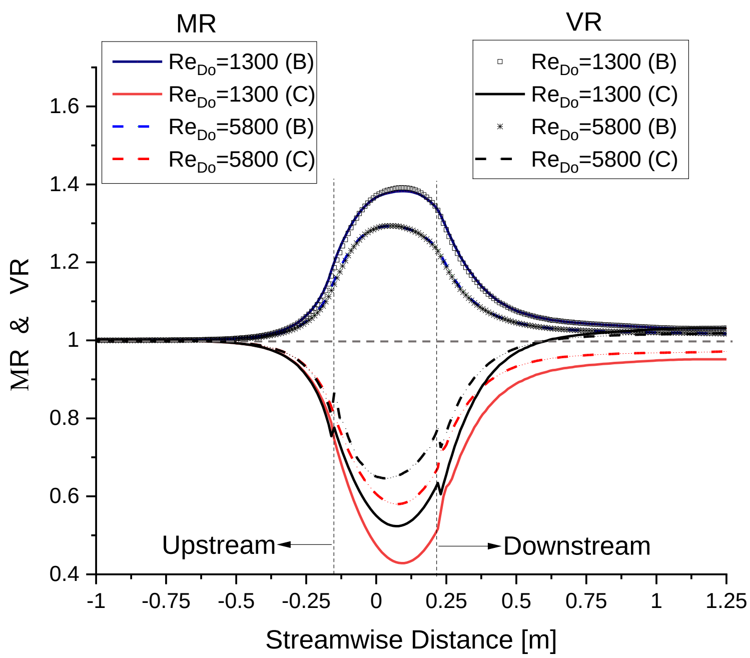

b) Clearance ratio of 1.5

Figure 5-20: The effect of Reynolds number on the velocity ratio and mass ratio with streamwise distance for the central region and bypass region for the clearance ratio of 0.25,1.5. B refers to the bypass region, C refers to the central region, VR is the velocity ratio, MR is the mass ratio

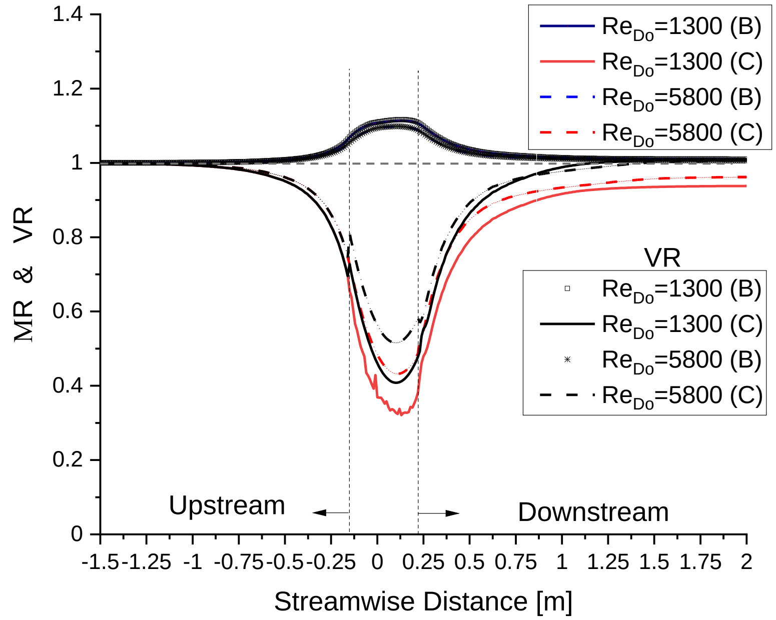

a) Clearance ratio of 6

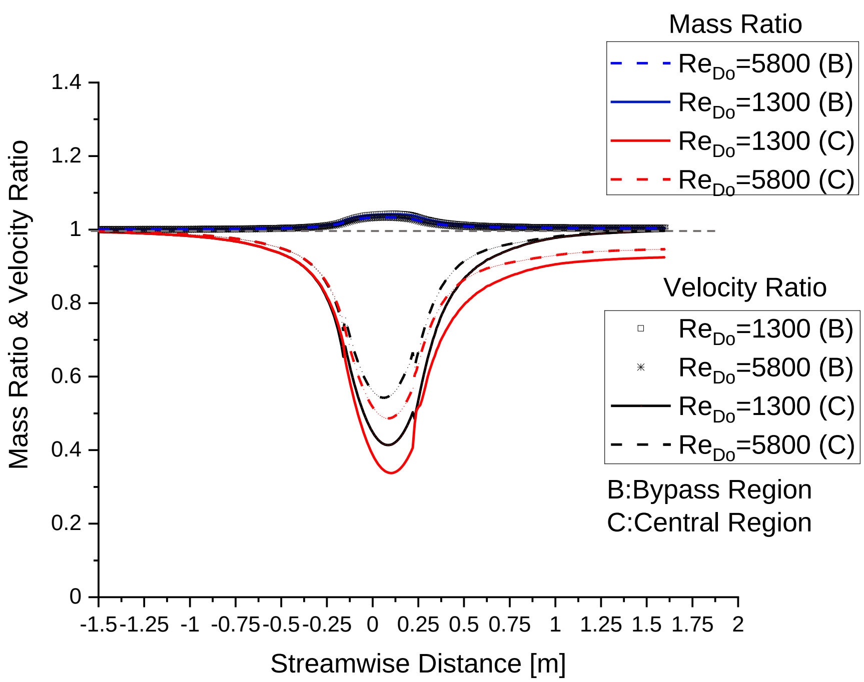

b) Clearance ratio of 16

Figure 5-21: The effect of Reynolds number on the velocity ratio and mass ratio with streamwise distance for the central region and bypass region for a clearance ratio of 6 and 16. B refers to the bypass region, C refers to the central region, VR is the velocity ratio, MR is the mass ratio

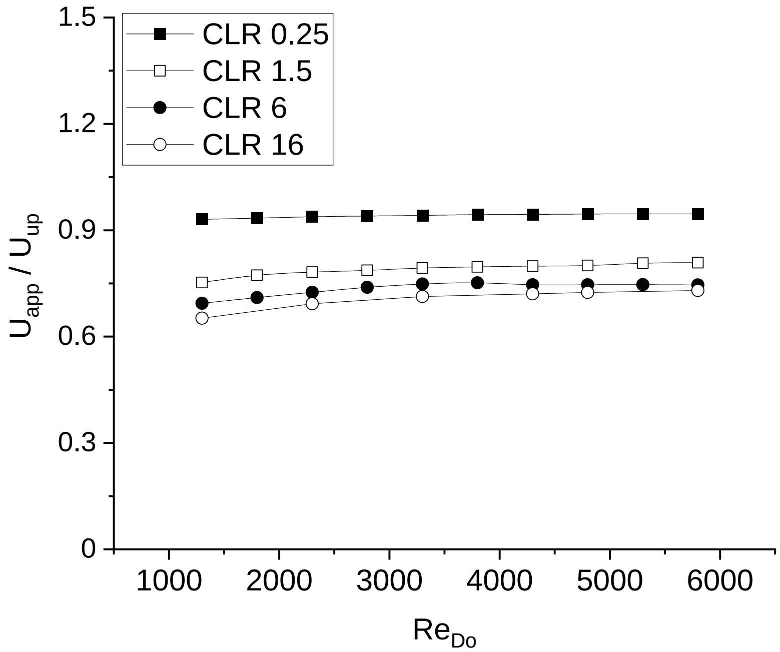

a) Approach Velocity

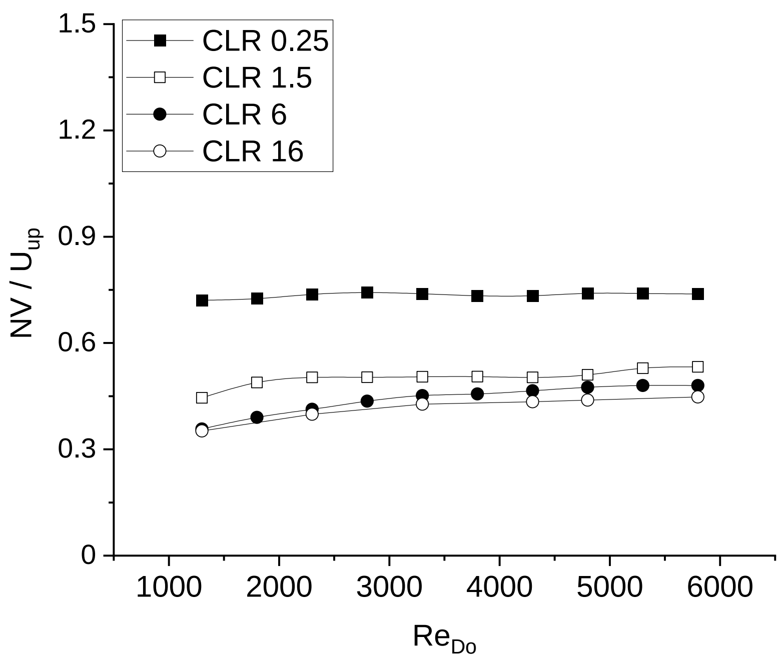

b) Nominal Velocity (NV)

Figure 5-22: The effect of Reynolds number on the ratio of the approach and nominal velocity (NV) with the upstream velocity for different clearance ratio.

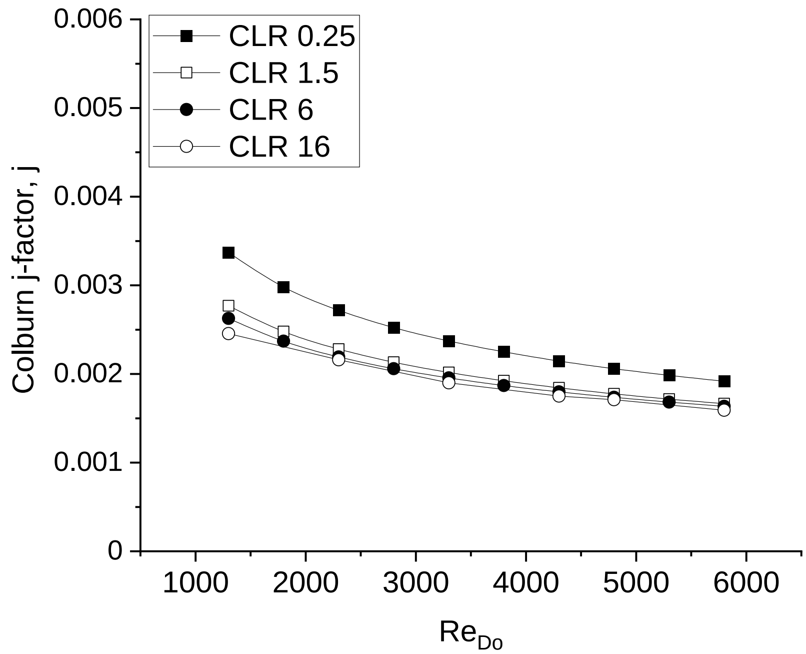

Figure 5-23: The effect of Reynolds number on the Colburn j-factor for different clearance ratios.

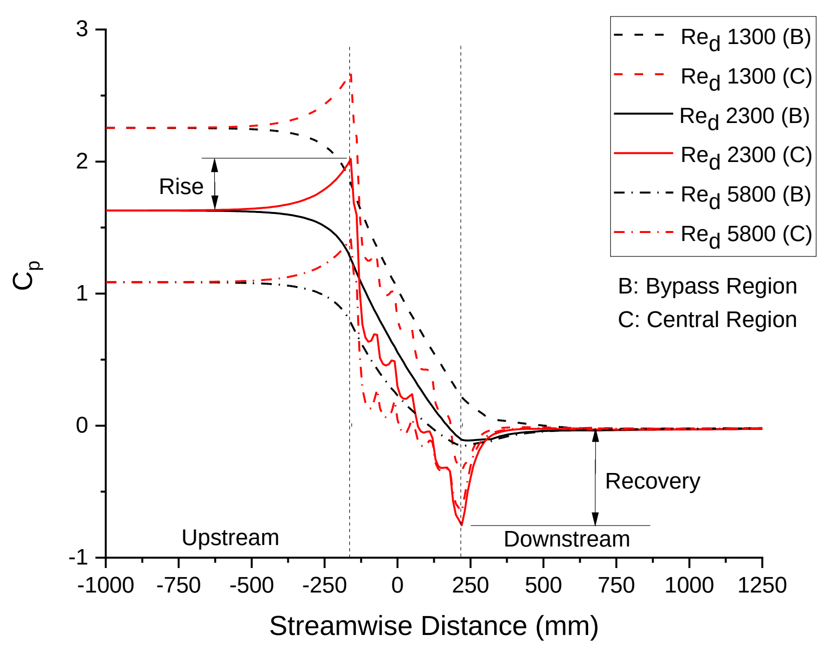

Figure 5-24: The effect of Reynolds number on Variation of Cp with streamwise distance for partially ducted geometry with CLR 1.5.

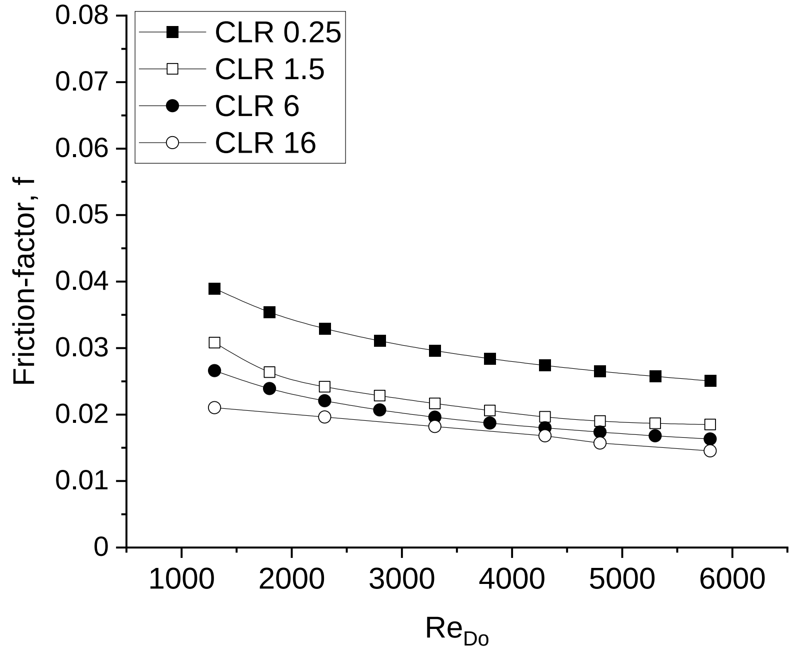

Figure 5-25: The effect of Reynolds number on the friction factor for different clearance ratios.

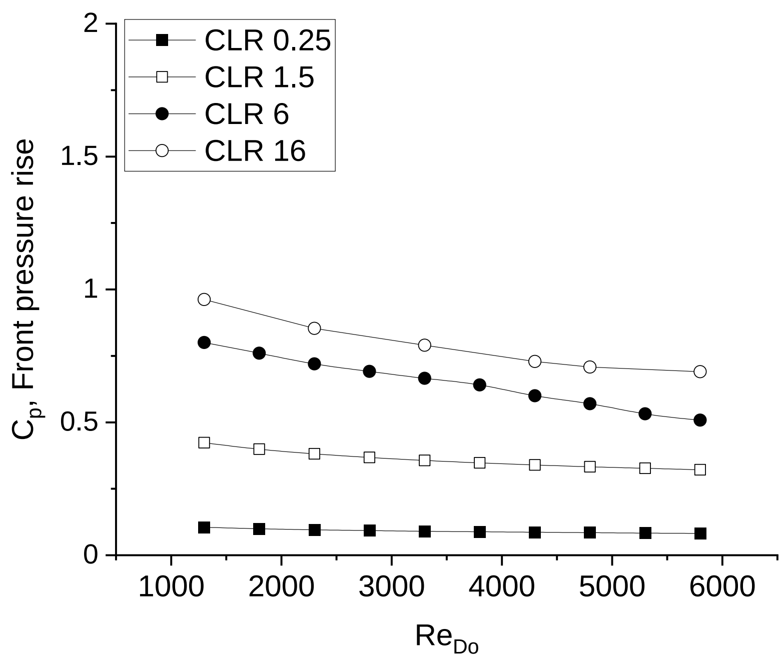

Figure 5-26: The effect of Reynolds number on the pressure coefficient for the front pressure rise for different clearance ratio.

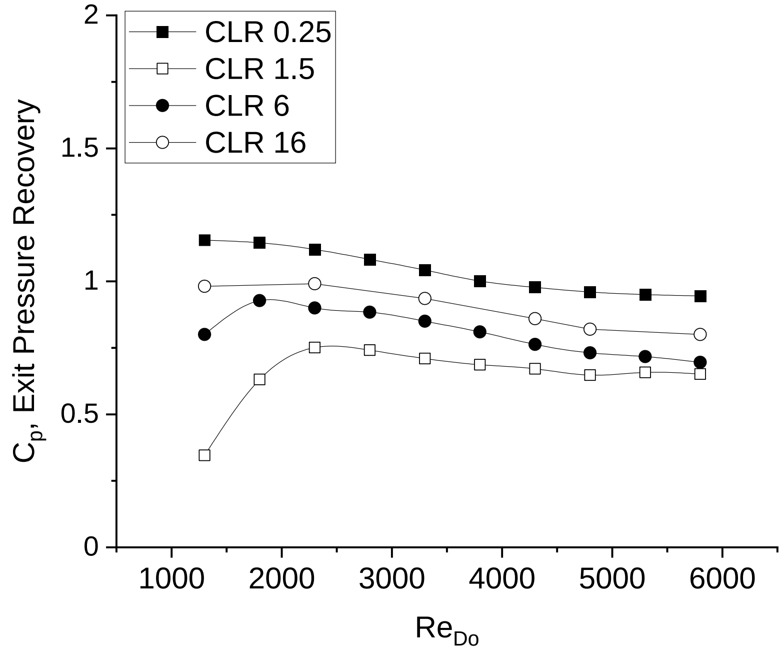

Figure 5-27: The effect of Reynolds number on the pressure coefficient for exit pressure recovery (***Δ***P_{ex}) for the central region.

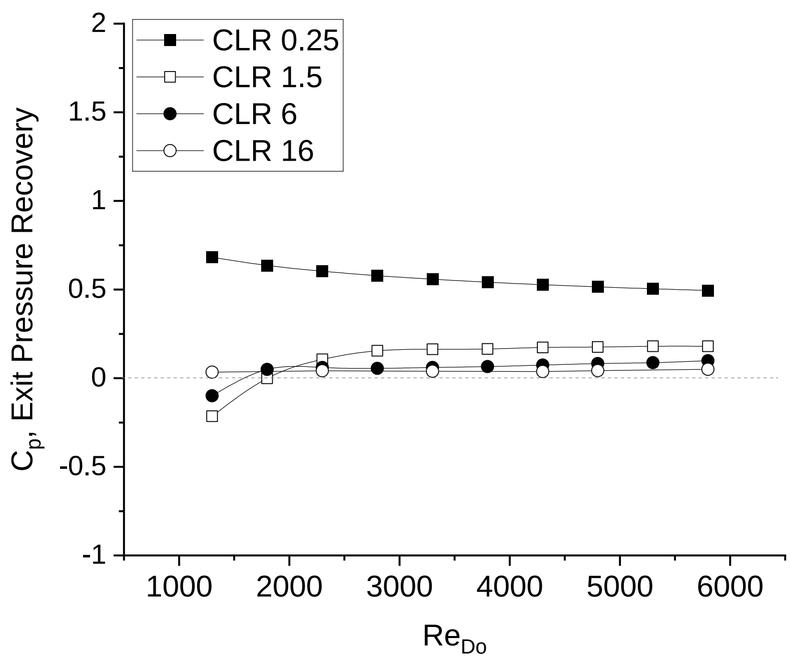

Figure 5-28: The effect of Reynolds number on the pressure coefficient for exit pressure recovery (***Δ***P_{ex}) for the Bypass region.

The pressure coefficient for exit pressure change (***Δ***P'ex) with the Reynolds number for the bypass region for different clearance ratios is shown in Figure 5-28. Negative values indicate a pressure loss and positive values represent a pressure recovery at the exit. A pressure loss is observed for the Reynolds number of 1300 for the clearance ratio of 1.5 and 6, while a pressure recovery is observed at all other Reynolds number for all clearance ratios studied. For the lowest Reynolds number, the pressure coefficient initially decreases until a clearance ratio of about 1.5 and then increases with a further increase in clearance ratio. At the higher Reynolds numbers, there is a decrease with the clearance ratio.

5.3. Estimation of heat transfer and pressure drop

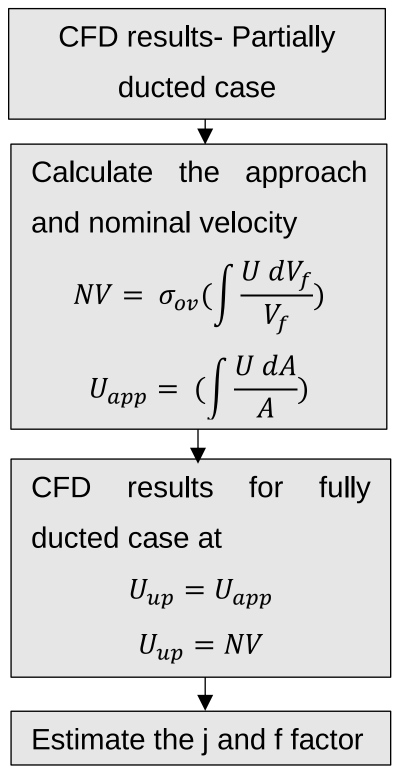

Figure 5-29: Flow chart to estimate the Colburn j-factor and friction factor for PD model.

A methodology is investigated here to estimate the heat transfer and pressure drop for the partially ducted configuration. Here, the correlations developed for the j-factor and friction factor for the fully ducted case is used, where the inlet velocity is replaced by either the approach velocity or nominal velocity for the partially ducted case. Figure 5-29 shows the flow chart for the estimation of the Colburn j-factor and friction factor using the nominal and approach velocity. Figure 5-30 shows the estimated Colburn j-factor for the partially ducted model at various clearance ratios and Reynolds number using the approach velocity and nominal velocity as upstream velocity in a fully ducted heat exchanger. The

Colburn j-factor for the partially ducted model estimated using the approach velocity is within ±10% of the CFD data. The predicted values using the nominal velocity shows a significant difference with the CFD data. This may be due to the high heat transfer rate at the entrance and around the first tube for the inline geometry, which reduces for nominal velocity in comparison to the partially ducted model.

Figure 5-31 shows the predicted friction-factor for the partially ducted model at various clearance ratios and Reynolds number from fully ducted heat exchangers using the approach velocity and nominal velocity as the upstream velocity. The friction factor can be estimated within +10% using the nominal velocity but is in the discrepancy of greater than 80% when using the approach velocity at a higher clearance ratio. The nominal velocity accounts for both the decrease in density as well as the flow leakage from the central region to the bypass region. The effect of the flow leakage is negligible on the heat transfer but quite significant for the friction factor, which makes the inclusion of flow leakage essential for estimating the approach velocity with the Resistance model.

Steiros [72] showed that the mean streamwise velocity upstream in front of a porous plate can be represented by the Taylor model, originally adopted by Graham (1976). Steiros [72] estimated the front pressure rise using the Bernoulli equation as

$$\Delta P_{fr} = \frac{\rho}{2}\left({U_\infty}^2 - U^2 - V^2\right) \quad \text{5-12}$$

where $U_\infty, U\ and\ \ V$ is the upstream, approach and the crosswise approach velocity.

However, Butterbaugh [43] recommended that the average value of pressure rise on the front face of the partially ducted heat exchanger can be defined by the following equation.

$$\Delta \mathrm{P}_{\mathrm{fr}} = \mathrm{C}_{\mathrm{d}}\frac{\rho}{2}\left({\mathrm{U}_{\mathrm{up}}}^2 - {\mathrm{U}_{\mathrm{app}}}^2\right) \quad \text{5-13}$$

where $\mathbf{C_d}$ is the dynamic pressure coefficient with a value of 0.8, as suggested by Butterbagh [43]. Figure 5-32 compares the pressure coefficient for the front pressure rise with the predictions from Butterbaugh [43] and Steiros [72] for various clearance ratio and Reynolds number. It can be seen that there is no significant difference in the pressure coefficient estimated using the Butterbaugh or Steiros methods, and it is within 20% of the CFD data for the clearance ratio of 1.5. However, the discrepancy increases as the clearance ratio are further increased. It should be noted that the test geometry used by Butterbaugh was limited to a clearance ratio of 2. The applicability of the Bernoulli equation was verified on a point to point basis before the flow enters into the heat exchanger.

However, due to the velocity profile effect, the average square of velocity is not equal to the average velocity before the entrance, which gives rise to an error in the prediction of front pressure rise using the Steiros [72] equation at a higher clearance ratio.

As stated earlier, there are two different sources for the pressure change at the exit for the central as well as bypass regions for a partially ducted heat exchanger. The first is the pressure recovery due to abrupt exit effects (ΔP_{ae}), which is considered from Kays and London [29]. For the bypass region, the exit area is open in the fin gap and the abrupt area change is only due to the small fin thickness which is usually ignored [43] and the pressure change due to irreversible free expansion is only considered. Hence, the following equation is the modified Kays and London equation.

$$P_{ae} = (-K_e)\frac{\rho}{2}{V_{ex}}^2 \qquad \text{5-14}$$

The second source of the pressure change is due to flow around the heat exchanger (ΔP_{be}). The flow separates at the edge of the heat exchanger causing a negative pressure at the end of the heat exchanger, leading to a pressure recovery at the heat exchanger exit in the central region. There is a corresponding pressure loss in the bypass region. For the central region, Kays and London[29] defined the expansion factor $\mathrm{K_e}$ for low turbulent flows and high turbulence flows. Figure 5-33 shows the pressure recovery due to the abrupt expansion using both regimes. It can be seen that the exit pressure drop predicted by Kays and London decreases rapidly and later asymptotes to a constant value with the clearance ratio. The pressure is higher for a low turbulent regime than the fully turbulent regime. Butterbaugh [43] correlated the second part of the pressure recovery due to flow around the heat exchanger, as shown by eq(5-13). Here, $\mathrm{C_d}$ is the dynamic pressure coefficient with a value of 0.2 for this pressure drop. It can be seen that the pressure increases and asymptotes to a constant value with the clearance ratio. Figure 5-34 shows the total pressure, using the low turbulence and high turbulence pressure drop due to abrupt expansion and the Butterbaugh estimation for $\mathrm{\Delta P_{be}}$. It can be seen that none of the correlations can predict the pressure rise beyond the clearance ratio of 1.5. It is probably because the $\mathrm{\Delta P_{be}}$ would dominate over $\mathrm{\Delta P_{ae}}$, which the Butterbaugh equation is not able to predict. However, the total pressure recovery can be estimated within sufficient accuracy for the geometry with a clearance ratio of less than 1.5 using the abrupt exit pressure drop for turbulent region estimated from Kays and London (1985) in addition to Butterbaugh estimation for the pressure drop due to flow around at the rear end.

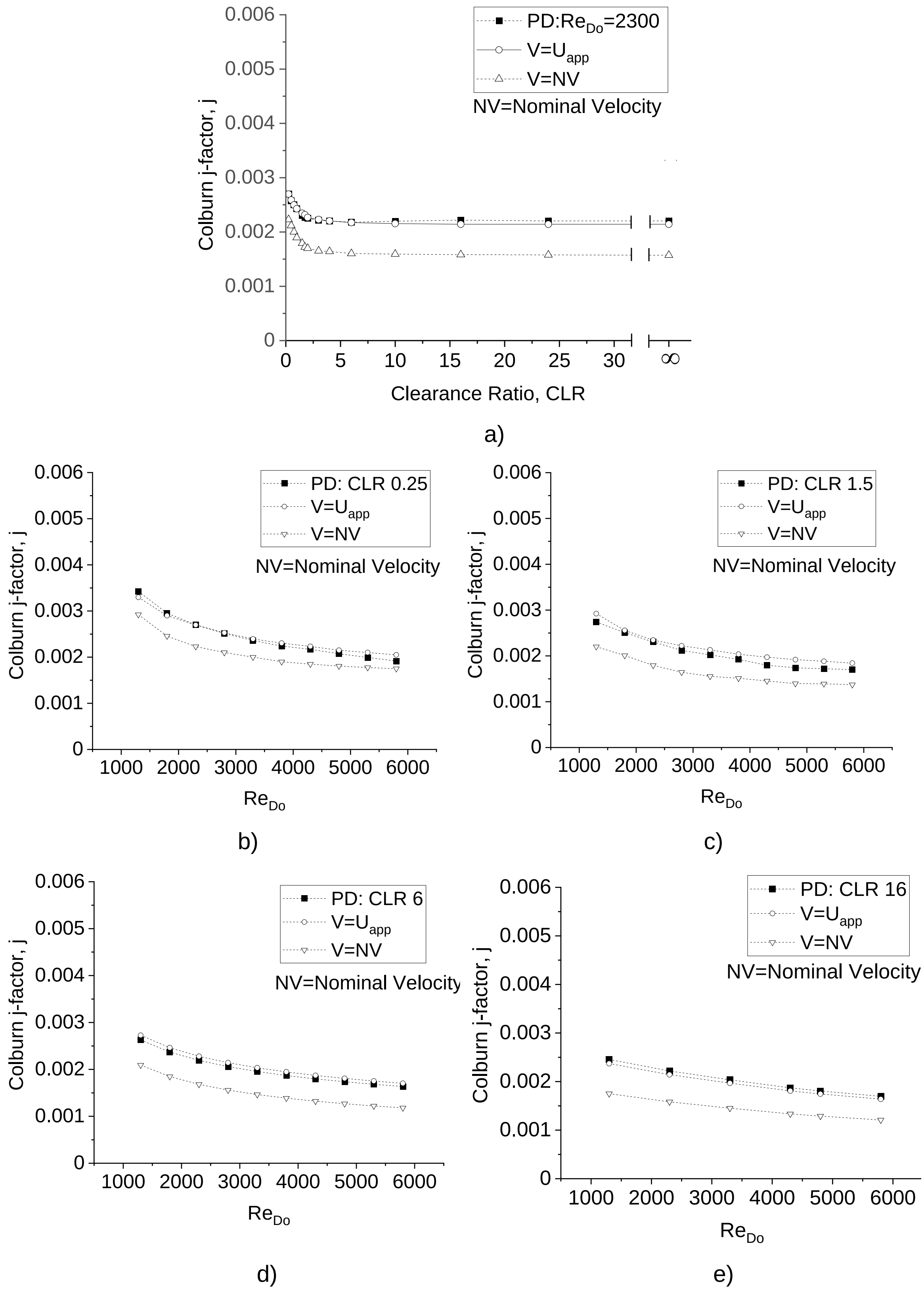

Figure 5-30: The prediction of the Colburn j-factor for partially ducted heat exchangers using a fully ducted heat exchanger at approach velocity as upstream velocity.

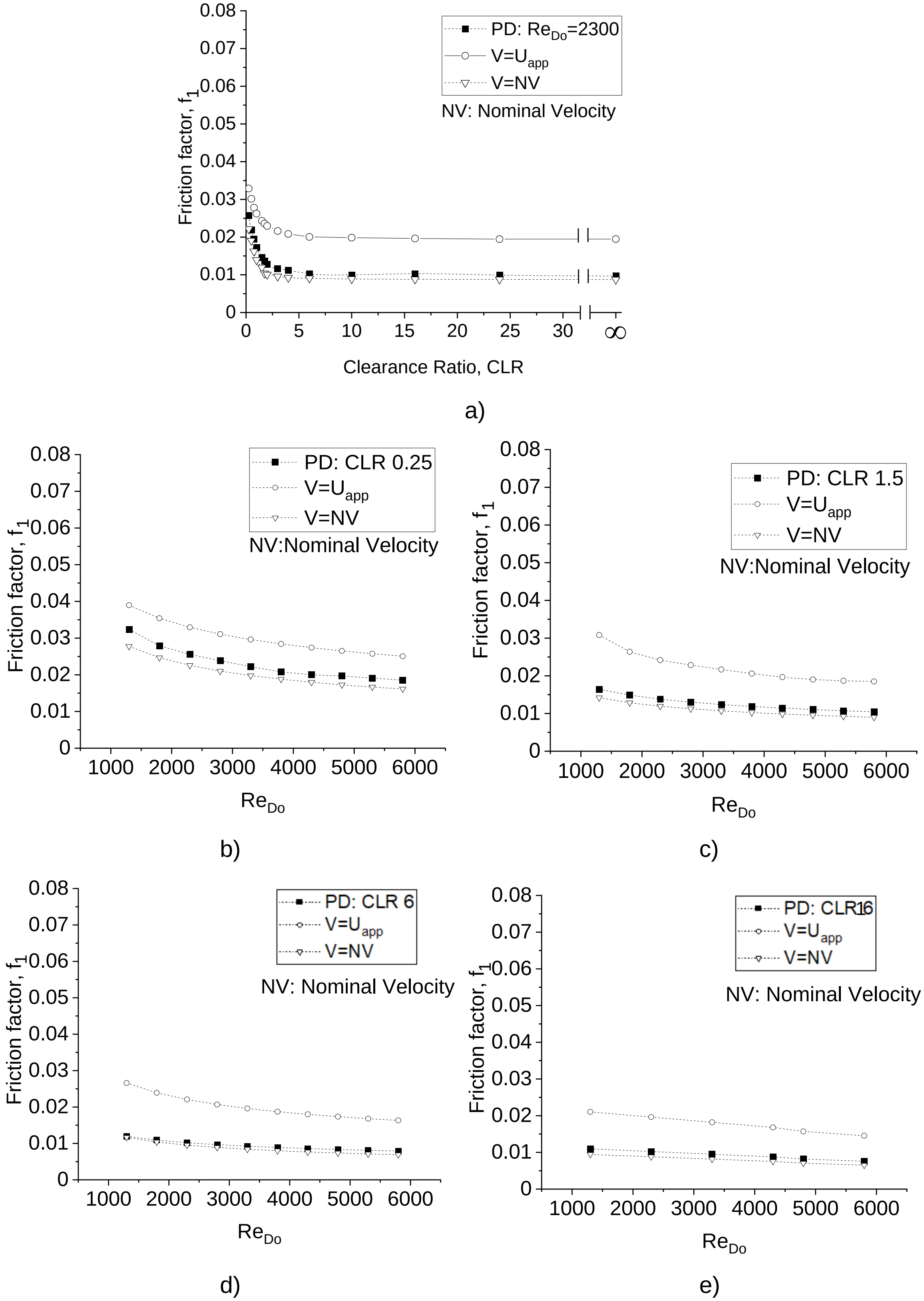

Figure 5-31: The prediction of the friction-factor for partially ducted heat exchangers using a fully ducted heat exchanger at approach velocity as upstream velocity.

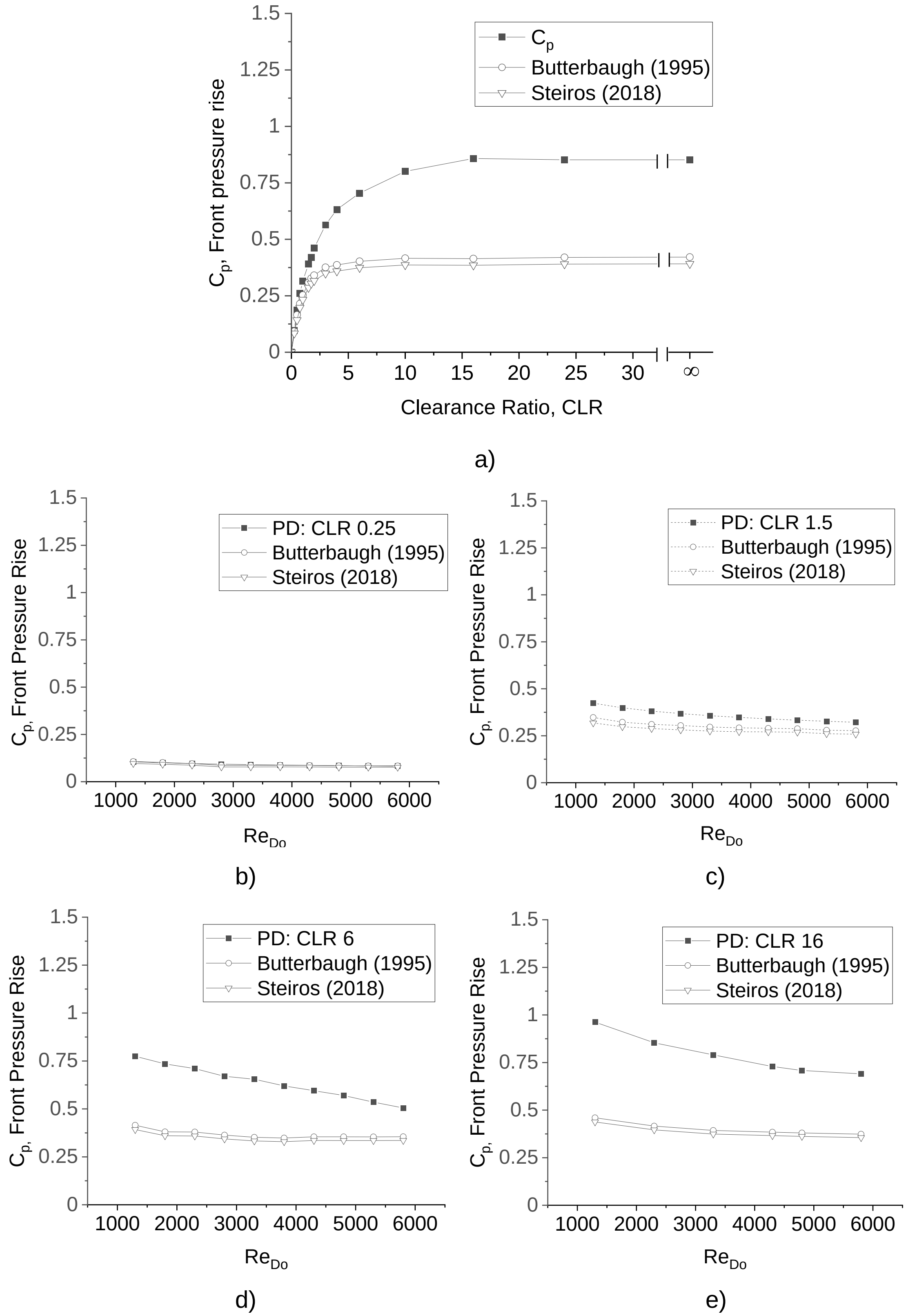

Figure 5-32: The dynamic pressure coefficient for the front pressure rise for the partially ducted case for different clearance ratios and the Reynolds number.

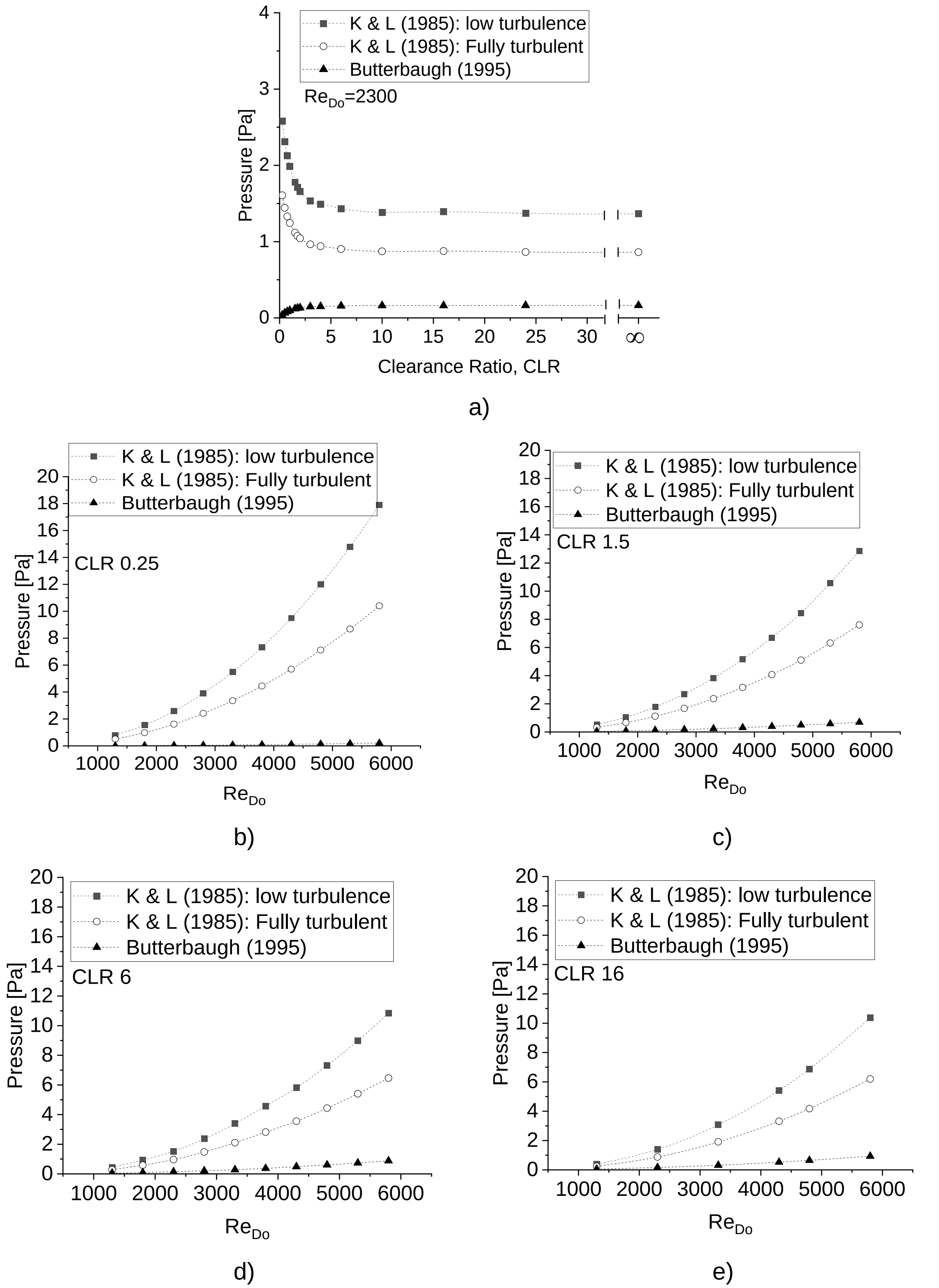

Figure 5-33: Estimation of various components of pressure recovery at the exit of the heat exchanger. Kays and London (1985) account for the abrupt exit effect for transitional and turbulent regimes. Butterbaugh (1995) accounts for pressure loss due to the flow around the heat exchanger.

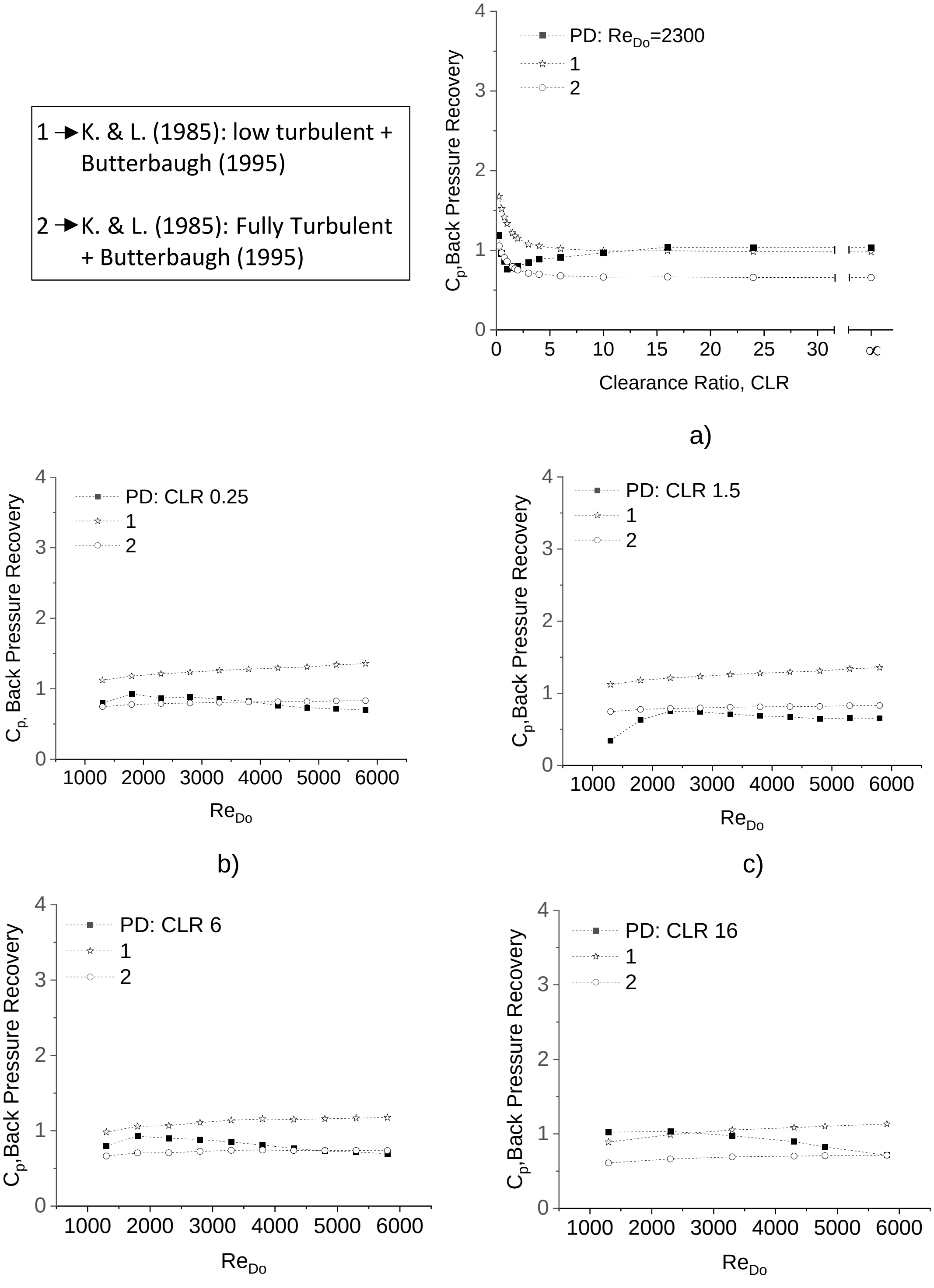

Figure 5-34: Pressure coefficient for back pressure recovery and the estimation using Kays and London(1985) and Butterbaugh's (1995) correlation. Here, legend 1 and 2 represent the sum of Kays and London's (1985) correlation for transitional and turbulent regimes for abrupt exit effect from heat exchanger core, respectively, with the correlation of Butterbaugh (1995) for the pressure loss due to the flow around the heat exchanger.

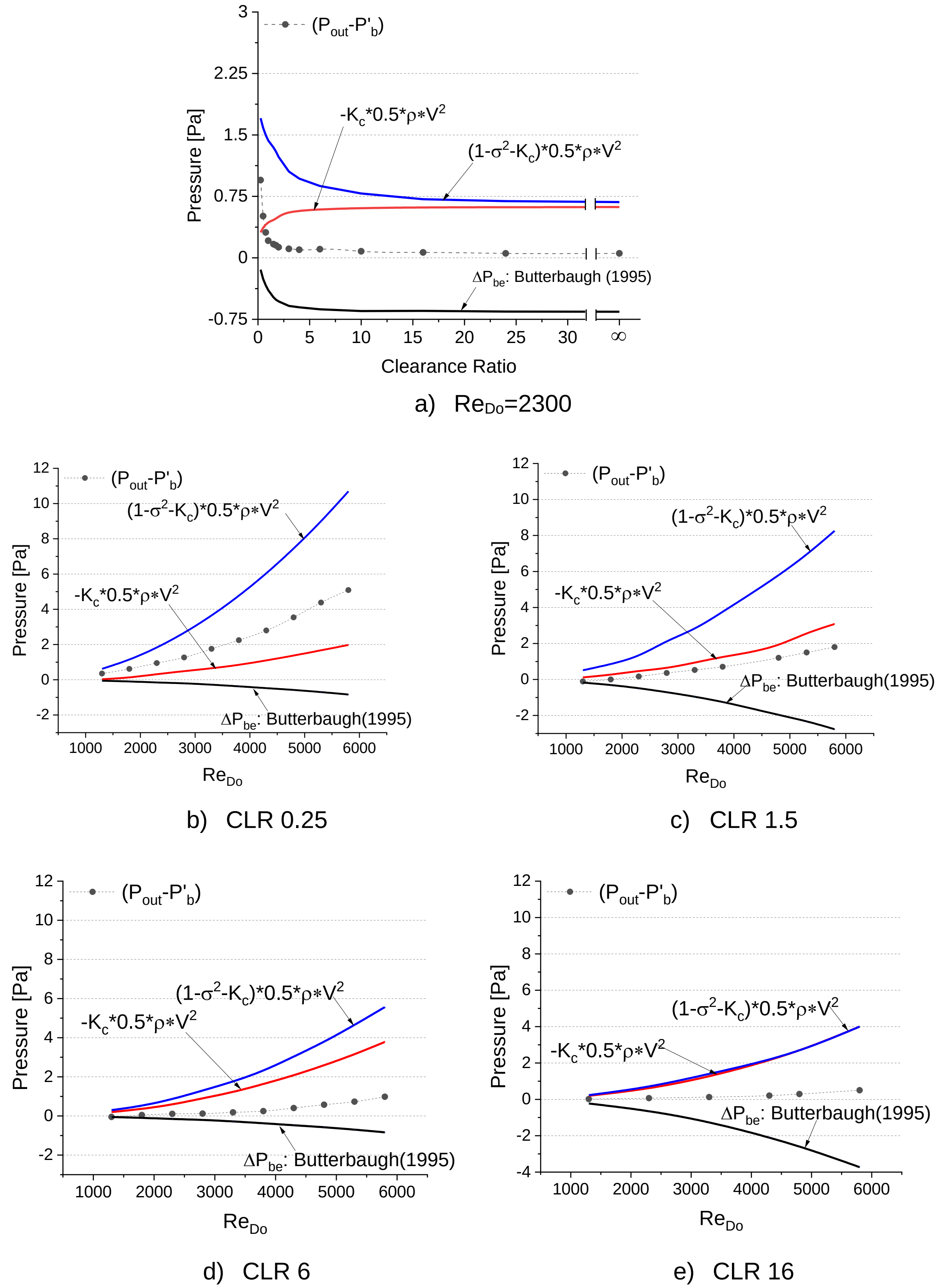

Figure 5-35: Estimation of various components of pressure recovery at the exit of the heat exchanger in the bypass region.

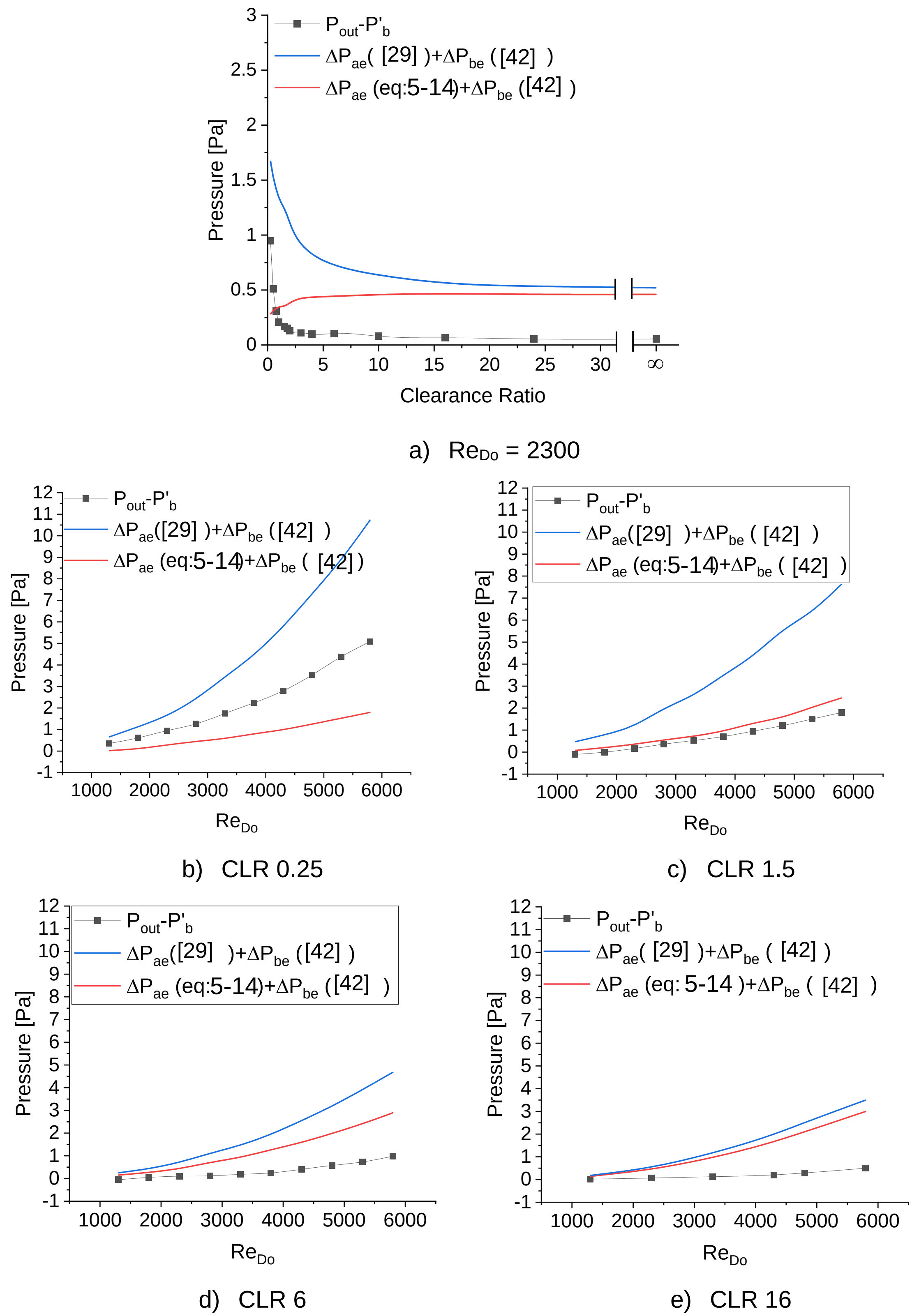

Figure 5-36: The exit back pressure change for the bypass region and estimation using Kays and London (1985) and Butterbaugh's (1985) correlation.

For the bypass region, there is a pressure recovery at the exit due to ΔP_{ae} and pressure loss at the exit due to ΔP_{be}. Figure 5-35 shows the estimation of ΔP_{ae} using Kays & London and its modified eq. (5-14). It also shows an estimation of $-\Delta P_{be}$ (pressure loss is taken negatively) using Butterbaugh's (1985) correlation. The sum of ΔP_{ae} and $-\Delta P_{be}$ is the overall pressure change in the bypass region. Figure 5-36 shows the estimation of total exit pressure change in the bypass region using the sum of estimated ΔP_{ae} and $-\Delta P_{be}$. The redline shows the typical correlation used in previous work [43]. It can be seen that none of the correlation predicts the $\Delta P'_{ex}$. As discussed above, the Butterbaugh estimation for ΔP_{be} seems correct till the CLR 1.5. For low clearance ratios where ΔP_{be} is very small, ΔP_{ae} should be close to the $\Delta P'_{ex}$. However, the pressure recovery, ΔP_{ae} is not predicted accurately using either Kays and London (1985) or its modified equation.

5.4. Effect of tube arrangement

Figure 5-37 shows the mass ratio in the central region for the inline and staggered partially ducted geometry with a clearance ratio of 0.25 and 6. Upstream of the heat exchanger, the mass ratio reduces with a slightly higher streamwise gradient for the staggered geometry than the inline geometry. As a result, the approach velocity of the staggered tube geometry is marginally less than the inline partially ducted geometry. Within the heat exchanger, the flow leakage from the central region to the bypass region for the staggered geometry is higher than the inline geometry. Also, the mass ratio recovery before exiting the heat exchanger lags for the staggered tube geometry than the inline partially ducted geometry.

The comparison of wall heat flux on the fin surface for staggered partially ducted geometry for the clearance ratio of 0.25 and 6 with the fully ducted case at the corresponding approach velocity is shown in Figure 5-38. The heat flux decreases at the downstream side of the fin due to the flow leakage. The figure shows a much higher decrease in heat flux for the higher clearance ratio of 6. There is a reduction in the heat flux around the tubes for the clearance ratio of 6. However, the effect is less for the lower clearance ratio due to less flow leakage. Also, there is a slight increase in heat flux around the corner tube of the third row as compared to the fully ducted geometry for the lower clearance and is not present for the clearance ratio of 6.

Figure 5-39 compares the wall heat flux for partially ducted geometry for staggered and inline for the clearance ratio of 0.25 and 6 for Reynolds number of 2300. For the clearance ratio of 0.25, the heat transfer for the staggered tube arrangement is higher due to much higher heat transfer around the tubes. Although inline transfers slightly higher heat flux at the downstream side of the fin. For the clearance ratio of 6, the heat flux at the downstream side of the fin is higher for the inline arrangement. However, it is slightly higher around the center tube for the second and third rows for the staggered arrangement. But, Inline transfers overall higher heat than the staggered for larger clearances.

The plot of approach velocity with the clearance ratio for staggered and inline partially ducted geometry for the Reynolds number of 2300 is shown in Figure 5-40. The approach velocity decreases exponentially with the initial increase in clearance ratio, similar to the inline tube arrangement and does not change much after the clearance ratio of 10. The staggered tube arrangement always has a marginally lower velocity ratio than the Inline arrangement.

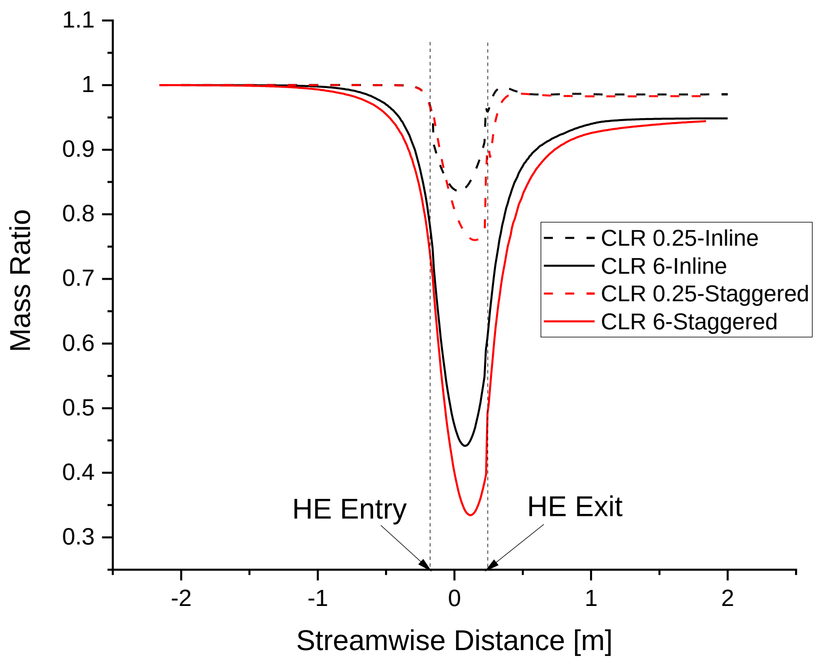

Figure 5-37: Effect of tube arrangement on the mass ratio in the central region with the streamwise distance for staggered and the inline geometry for the clearance ratio of 0.25,6 for Re_{Do}=2300.

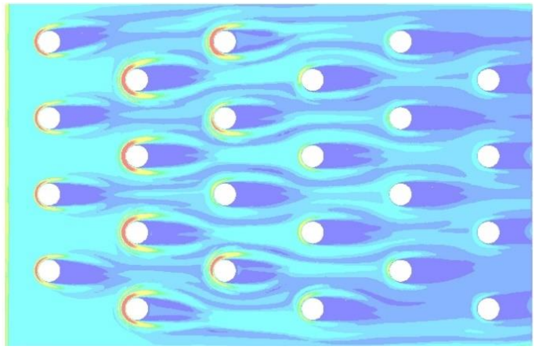

a) Staggered-PD Geometry (CLR 0.25)

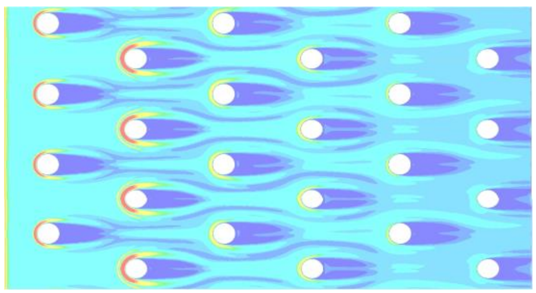

b) Staggered FD (U_{app}- CLR 0.25)

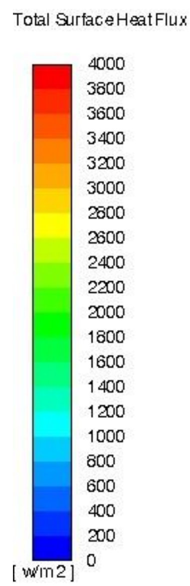

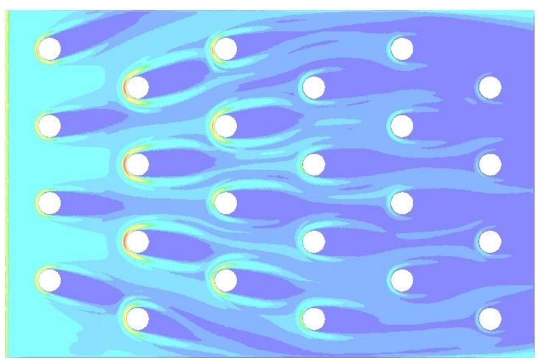

c) Staggered-PD Geometry (CLR 6)

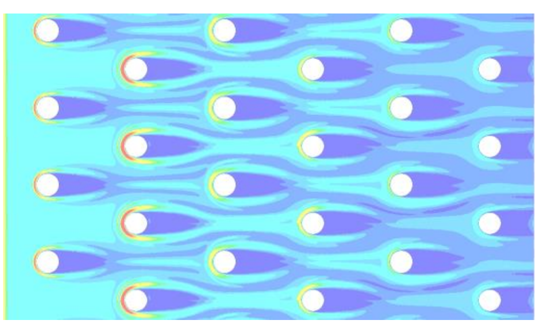

d) Staggered FD (Uapp- CLR 6)

Figure 5-38: Wall heat flux on the fin surface for staggered partially ducted and fully ducted geometry for Re_{Do}=2300.

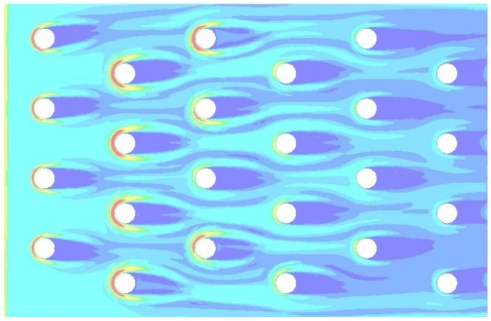

a) Staggered-PD Geometry (CLR 0.25)

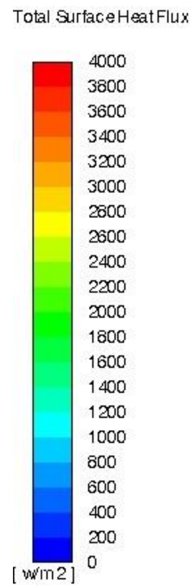

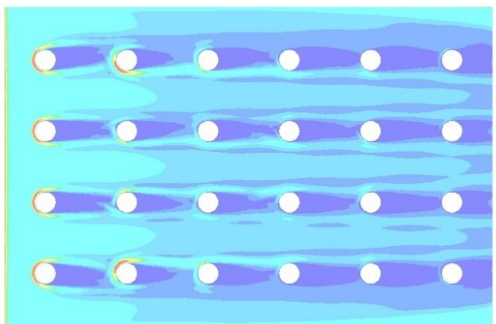

b) Inline-PD Geometry (CLR 0.25)

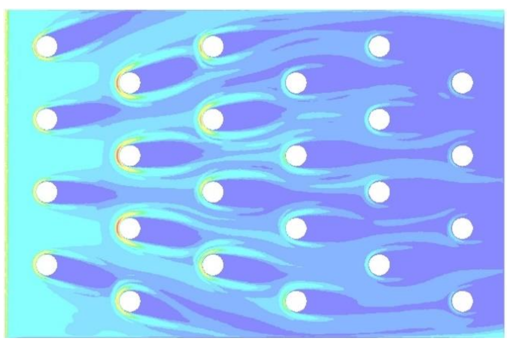

c) Staggered- PD Geometry (CLR 6)

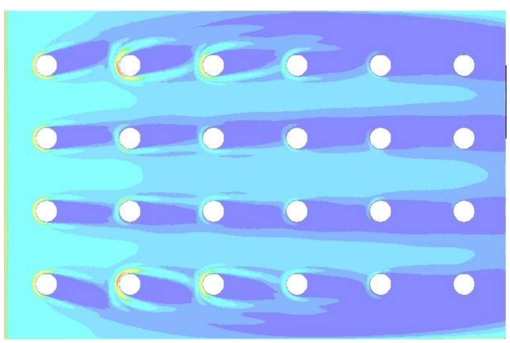

d) Inline-PD Geometry (CLR 6)

Figure 5-39: The effect of tube arrangement on wall heat flux from the fin surface for the clearance ratio of 0.25 and 6 for Reynolds number of 2300.

The plot of the Colburn j-factor with the clearance ratio for staggered and inline partially ducted geometry for the Reynolds number of 2300 is shown in Figure 5-41. The Colburn j-factor decreases with the steeper slope for the staggered tube arrangement than the inline arrangement at the lower clearance ratio. This could be due to higher flow leakage for the staggered tube arrangement. At the clearance ratio of 2, the j-factor for the inline and the staggered arrangement is almost identical. After the clearance ratio of 2, the inline has a higher Colburn j-factor than the staggered tube arrangement, suggesting that the inline could be a better choice for the partially ducted geometry, especially at a higher clearance ratio.

The pressure coefficient for the total pressure difference with the clearance ratio for staggered and inline partially ducted geometry for the Reynolds number of 2300 is shown in Figure 5-42. The C_p decreases rapidly with the clearance ratio for the staggered similar to inline tube arrangement with the much steeper decrease at lower clearances. The C_p approaches the value of zero for the infinite clearance for both the tube arrangements.

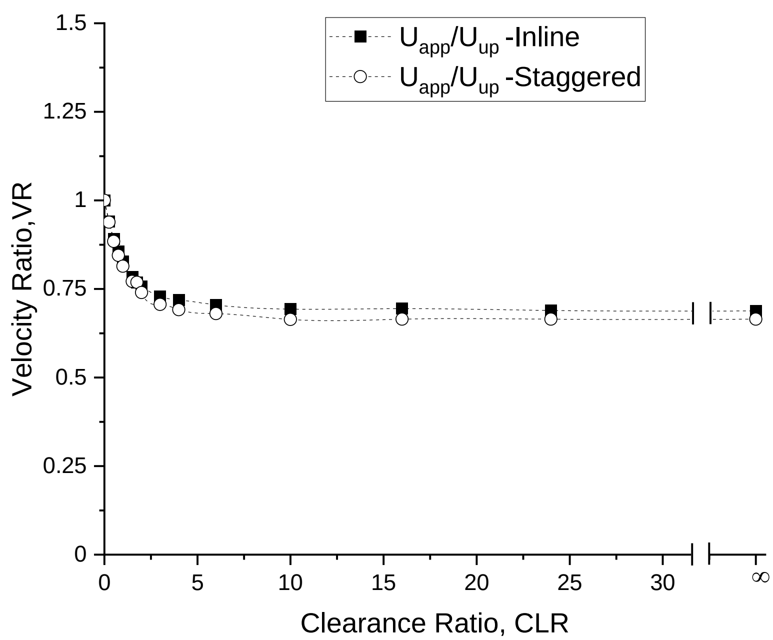

Figure 5-40: The effect of tube arrangement on the approach velocity ratio with the clearance ratio for Re_{Do}=2300.

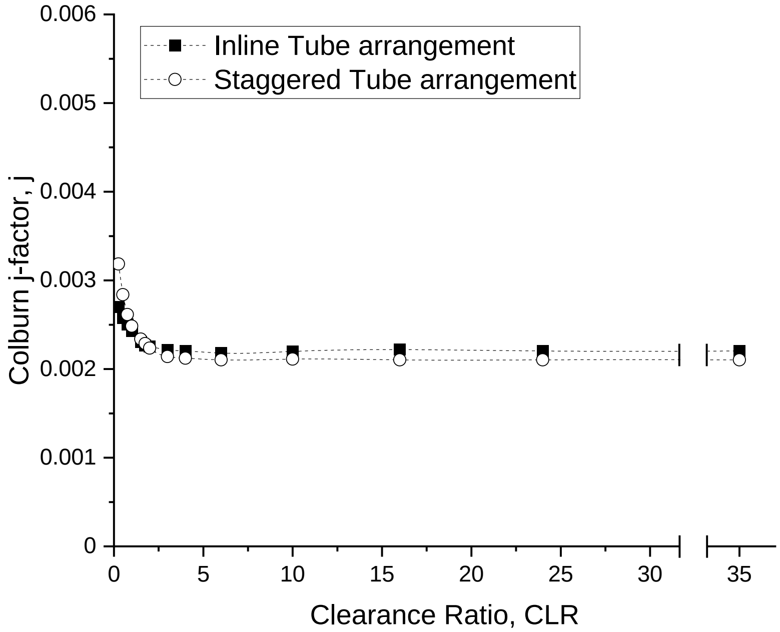

Figure 5-41: The effect of tube arrangement on the Colburn j-factor with the clearance ratio for inline and staggered partially ducted geometry for Re_{Do}=2300.

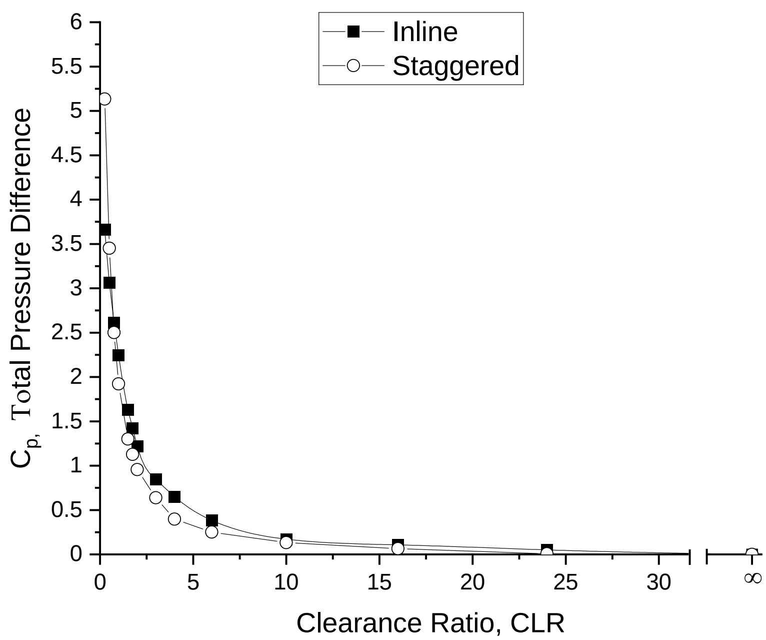

Figure 5-42: The effect of tube arrangement on Cp (Total pressure difference) with the clearance ratio for Re_{Do}=2300.

Chapter 6.

Conclusion and Recommendation

The heat transfer and pressure drop characteristics of plate-fin and tube heat exchangers were numerically investigated in this study. The numerical simulations were performed using the finite volume method on the commercial CFD code ANSYS FLUENT. The computational domain consisted of plain fin and tube heat exchangers, and the low Reynolds number k-ω SST turbulence model was used. Two heat exchanger configurations, inline and staggered tube arrangements, were considered. The emphasis of this study, however, was on the inline tube arrangement as it was the configuration used in an application that motivated the investigation and is also less studied in the literature. The case where the heat exchanger is placed in a fully ducted airflow was considered first, and the effect of the geometrical parameters and Reynolds number on the heat exchanger performance was studied. In the second part of the study, the impact of bypass flow around the heat exchanger when it is in a partially ducted airflow was investigated.

For the fully ducted case, the present study initially compares the local flow behaviour with the heat transfer characteristics for the inline and the staggered tube arrangement for a range of tube pitch. As the air flows through the inter-fin spacing and approaches the tubes, it flows around the tube creating a recirculation zone (dead zone) behind each tube. Strong horseshoe vortices are seen to develop in all tube rows for the staggered case, but only for the initial tube row for the inline tube arrangement. These vortices increase the wall heat flux and wall shear stress around the tube and can contribute about 15-30% of the total heat transfer. Therefore, an improved heat transfer coefficient and a higher-pressure drop are observed for the staggered tube arrangement.

The Colburn j-factor decreased as the tube pitch to diameter ratio was increased for the staggered arrangement, but not much for the inline case. For a higher tube pitch of 3.5 diameters, the Colburn j-factor of the staggered tube arrangement decreased from 30% higher value than inline tube arrangement for the Reynolds number of 1450 to 8% for Reynolds number of 6000. However, the expense in the pressure drop for the staggered tube arrangement is still more than 40% than the inline arrangement for all the Reynolds number. The higher goodness factor for the inline tube arrangement along with less heat transfer difference between the inline and the staggered tube arrangement suggests that the inline tube arrangement may be beneficial in pressure drop limited application or applications with substantial by-pass such as considered here.

The simulations were performed for finned tube heat exchanger with inline tube arrangement with 3 to 6 tube rows, tube pitch of 3 to 4 diameters, fin pitch of 0.25 to 0.65 diameters and Reynolds number of 1450 to 7000. The Colburn j-factor and the friction factor was seen to be strongly dependent on the fin pitch and the Reynolds number. The vorticity of the vortex around the tube reduces and the radial distance is increased as the fin pitch is increased. However, there was no change observed in the extent of the horseshoe vortex system for the deeper rows with the fin pitch. The horseshoe vortex system was seen to be more developed with the increase in the Reynolds number.

The contraction and the expansion pressure drop was separated from the overall pressure drop to obtain the frictional pressure drop. The Kays and London correlation predicted the exit pressure recovery within 20% accuracy. The abrupt contraction coefficient for channel entrance was between the turbulent and laminar correlation by Kays and London. Finally, the correlations were developed for the Colburn j-factor and friction factor based on 280 simulations for the range of geometry specified above.

The simulations for the partially ducted case were performed for the inline and the staggered tube arrangement with the clearance ratio in the range 0.25 to infinity, longitudinal tube pitch of 4 diameters, transverse tube pitch of 3.5 diameters, fin pitch of 0.5 diameters for the Reynolds number of 2300. For the clearance ratios of 0.25, 1.5, 6 and 16, simulations were performed for the inline arrangement for the Reynolds number in the range 1300-5800.

For partially ducted geometry, similar to flow around a porous block, there is a high-pressure development in front and a low pressure at the rear of the heat exchanger. The incoming airflow bypasses the heat exchanger on encountering the high pressure and low pressure at the back creates a suction that sucks the air into the heat exchanger. This reduces the mass flow rate entering into the heat exchanger (Approach velocity), which decreases the heat transfer performance substantially. The approach velocity decreases rapidly as the clearance ratio is increased, which later asymptotes to a constant value after the clearance ratio of 15. Even after entering into the heat exchanger core, the flow slips into the bypass region is seen. The total mass rate slipped out of domain from the heat exchanger core increases rapidly with the clearance ratio and later asymptote to the constant value. Therefore, the rapid decrease in the heat transfer performance was seen with the increase in the clearance ratio.

The increased circulation of the flow around the later tubes was seen for the inline geometry due to the flow inclination towards the corner. The horseshoe vortices were seen to develop in the vicinity of the corner downstream tubes as well for the inline geometry. So, the decrease of the heat transfer due to flow slip inside the heat exchanger is somewhat counterbalanced by the increased heat transfer around the tubes. This limits the effect of the inside flow slip on the heat transfer performance to a maximum of 10% decrease at the higher clearance ratio.

The significant effect of the tube arrangement on the heat transfer characteristics was seen for the partially ducted case as well. The approach velocity for the staggered case was found to decrease quickly with the clearance ratio, similar to the inline case. The approach velocity for both the tube arrangement is almost identical with a marginally lower value for the staggered tube arrangement. Also, the flow slip from the heat exchanger core into the bypass region was seen to be higher for the staggered tube arrangement than the inline tube arrangement. Therefore, the steeper drop in the Colburn j-factor was seen for the staggered tube arrangement than the inline tube arrangement for the initial increase in the clearance ratio. The performance of the staggered tube arrangement worsens than the inline tube arrangement for the clearance ratio greater than 1.5. This makes the inline tube configuration a better choice, especially for a higher clearance ratio.

A methodology was developed to estimate the heat transfer when there is a bypass flow in the partially ducted case using existing correlations for the fully ducted case. In this method, the approach velocity to the partially ducted heat exchanger is used in the J-factor correlation, instead of the upstream velocity to estimate the heat transfer. The results from this method agreed with the computational results to within ±10 percent. The approach velocity can be estimated using a pressure resistance model balancing the pressure drop across various air travel path. Therefore, the various pressure drop in the air path was compared with the existing correlation in the literature, which could be used for in the future studies for modelling the approach velocity.

6.1. Recommendations

Based on the results of this study and the existing literature, the following recommendations are made for future study:

1. The results here indicate that the difference in heat transfer between the staggered and inline tube geometries reduce for high Reynolds number and large tube pitch geometry. The effect of the tube arrangement in the higher Reynolds number range for large tube pitch geometry should be examined in detail.
2. The experimental study by Gao and Tifti (2003) revealed a strong dependence on the inlet flow angle on the performance of a multi-louvred fin heat exchanger. The effect of the flow inclination on a plain fin and tube heat exchangers is not well understood, including the impact on the vortices behind the tube for staggered as well as inline tube arrangement. This should be an area for future study.
3. Almost all studies on finned tube heat exchangers neglect the effect of gravity, which is a good approximation for heat exchangers placed in the horizontal orientation. However, the heat exchangers are placed vertically in many applications. Thus, it is important to understand the impact of mixed convection on the performance of the finned tube heat exchangers.
4. For a partially ducted finned tube heat exchanger, the conventional pressure resistance technique for approach velocity measurement, as used in Butterbaugh [43], is not valid. Hence, it is important to understand the pressure drop for the partially ducted model in detail, including the development of the model to estimate the approach velocity.

References

[1] C. F. McQuinston and D. R. Tree, "Heat transfer and flow friction data for two fin–tube surfaces," *ASME J. Heat Transfer,* vol. 93, no. 2, pp. 249-250, 1971.

[2] D. G. Rich, "The effect of the number of tubes rows on heat transfer performance of smooth plate fin-and-tube heat exchangers," *ASHRAE Trans.,* vol. 81, pp. 266-293, 1975.

[3] D.G. Rich, "The effect of fin spacing on the heat transfer and friction performance of multi-row, plate fin-and-tube heat exchangers," *ASHRAE Transactions,* p. 137–145, 1973.

[4] C. F. McQuiston, "Heat mass and momentum transfer data for five plate–fin–tube heat transfer surfaces," *ASHRAE Trans,* vol. 1, no. 84, pp. 266-293, 1978.

[5] F. McQuiston, "Correlation of heat, mass and momentum transport coefficients for plate-fin-tube heat transfer surfaces with staggered tubes," *ASHRAE Transaction,* vol. 84(1):, pp. 294-309, 1978.

[6] D. L. Gray and R. L. Webb, "Heat transfer and friction correlations for plate finned-tube heat exchangers having plain fins," in *International Heat Transfer Conference Digital Library*, Begel House Inc., 1986.

[7] C. C. Wang, Y. J. Chang, Y. C. Hsieh and T. L. Lin, "Sensible heat and friction characteristics of plate fin-and-tube heat exchangers having plane fins," *International Journal of Refrigeration,* vol. 19, no. 4, pp. 223-230, 1996.

[8] C. C. Wang and K. Y. Chi, "Heat transfer and friction characteristics of plain fin-and-tube heat exchangers, part I: new experimental data," *International Journal of Heat and Mass Transfer,* vol. 43, no. 15, pp. 2681-2691, 2000.

[9] C. C. Wang, K. Y. Chi and C. J. Chang, "Heat transfer and friction characteristics of plain fin-and-tube heat exchangers, part II: Correlation," *International Journal of Heat and Mass Transfer,* vol. 43, no. 15, pp. 2693-2700, 2000.

[10] A. Bastani, M. Fiebig and N. K. Mitra, "Numerical studies of a compact fin-tube heat exchanger," *Design and Operation of Heat Exchangers,* pp. 154-163, 1992.

[11] J. Y. Jang, M. C. Wu and W. J. Chang, "Numerical and experimental studies of three-dimensional plate-fin and tube heat exchangers," *International Journal of Heat and Mass Transfer,* vol. 39, no. 14, pp. 3057-3066, 1996.

[12] A. A. Bhuiyan, A. S. Islam and M. Amin, "Numerical prediction of laminar characteristics of fluid flow and heat transfer in finned-tube heat exchangers," *Innovative Systems Design and Engineering,* vol. 2, no. 6, pp. 1-12, 2011.

[13] A. A. Bhuiyan, M. R. Amin, R. Karim and A. K. Sadrul Islam, "Plate fin and tube heat exchanger modeling: Effects of performance parameters for turbulent flow regime," *International Journal of Automotive and Mechanical Engineering,* vol. 9, no. 1, pp. 1768-1781, 2014.

[14] Z. Q. Chen and J. X. Ren, "Effect of fin spacing on the heat transfer and pressure drop of a two-row plate fin and tube heat exchanger," *International Journal of Refrigeration,* vol. 11, no. 6, pp. 356-360, 1988.

[15] A. Y. Herchang, Y. J. Jiin and N. Y. Jer, "Local heat transfer measurements of plate finned-tube heat exchangers by infrared thermography," *International Journal of Heat and Mass Transfer,* vol. 45, no. 20, pp. 4069-4078, 2002.

[16] Y. Kim and Y. Kim, "Heat transfer characteristics of flat plate finned-tube heat exchangers with large fin pitch," *International Journal of Refrigeration,* vol. 28, no. 6, pp. 851-858, 2005.

[17] D. Kundu, A. Haji-Sheikh and D. Y. Lou, "Pressure and heat transfer in cross flow over cylinders between two parallel plates," *Numerical Heat Transfer; Part A: Applications,* vol. 19, no. 3, pp. 345-360, 1991.

[18] T. W. Sheui, S. F. Tsai and T. P. Chiang, "Numerical study of heat transfer in two-row heat exchangers having extended fin surfaces," *Numerical Heat Transfer; Part A: Applications,* vol. 35, no. 7, pp. 797-814, 1999.

[19] C. H. Huang, I. C. Yuan and H. Ay, "An experimental study in determining the local heat transfer coefficients for the plate finned-tube heat exchangers," *International Journal of Heat and Mass Transfer,* vol. 52, no. 21-22, pp. 4883-4893, 2009.

[20] R. R. Méndez, M. Sen, K. Yang and M. Rodney, "Effect of fin spacing on convection in a plate fin and tube heat exchanger," *International Journal of Heat and Mass Transfer,* vol. 43, no. 1, pp. 39-51, 2000.

[21] M. Tutar and A. Akkoca, "Numerical analysis of fluid flow and heat transfer characteristics in three-dimensional plate fin-and-tube heat exchangers," *Numerical Heat Transfer; Part A: Applications,* vol. 46, no. 3, pp. 301-321, 2004.

[22] J. V. Simo Tala, D. Bougeard, S. Russeil and J. L. Harion, "Tube pattern effect on thermalhydraulic characteristics in a two-rows finned-tube heat exchanger," *International Journal of Thermal Sciences,* vol. 60, pp. 225-235, 2012.

[23] A. P. Colburn, "A method of correlating forced convection heat-transfer data and a comparison with fluid friction," *Int J Heat Mass Transfer,* no. 1359–84, p. 174–210, 1964.

[24] D. Bacellar, V. Aute and R. Radermacher, "CFD-based correlation development for air side performance of finned and finless tube heat exchangers with small diameter tubes," in *International Refrigeration and Air Conditioning Conference*, Purdue, 2014.

[25] B. M. Jacimovica, S. B. Genica and B. R. Latinovic, "Research on the air pressure drop in plate finned tube heat exchangers," *International Journal of Refrigeration,* vol. 29, pp. 1138-1143, 2006.

[26] G. Xie, Q. Wang and B. Sunden, "Parametric study and multiple correlations on air-side heat transfer and friction characteristics of fin-and-tube heat exchangers with large number of large-diameter tube rows," *Applied Thermal Engineering,* vol. 29, no. 1, pp. 1-16, 2009.

[27] Z.-Y. Chen, M. Cheng, Q. Liao, Y.-D. Ding and J.-N. Zhang, "Experimental investigation on the air-side flow and heat transfer characteristics of 3-D finned tube bundle," *International Journal of Heat and Mass Transfer,* vol. 131, pp. 506-516, 2019.

[28] N. H. Kim, B. Youn and R. L. Webb, "Air-side heat transfer and friction correlations for plain fn-and-tube heat exchangers with staggered tube arrangements," *Journal of Heat Transfer,* vol. 121, no. 3, p. 662, 1999.

[29] W. M. Kays and A. L. London, Compact Heat Exchanger, McGraw-Hill, 1985.

[30] Y. Seshimo and M. Fujii, "An experimental study of the performance of plate fin and tube heat exchangers at low Reynolds number," in *3rd ASME/JSME Thermal Engineering Joint Conference*, 1991.

[31] J. Y. Jang, M. C. Wu and W. J. Chang, "Numerical and experimental studies of three-dimensional plate-fin and tube heat exchangers," *Elsevier Science Ltd.,* vol. Vol. 39, no. 14, p. pp. 3057 3066, 1996.

[32] E. M. Sparrow and D. S. Kadle, "Effect of tip-to-shroud clearance on turbulent heat transfer from a shrouded, longitudinal fin array," *ASME. J. Heat Transfer,* vol. 108, no. 3, pp. 519-524, 1986.

[33] E. M. Sparrow, B. R. Baliga and S. V. Patankar, "Forced convection heat transfer from a shrouded fin array with and without tip clearance," *ASME. J. Heat Transfer,* vol. 100, no. 4, pp. 572-579, 1978.

[34] E. M. Sparrow and T. J. Beckey, "Pressure drop characteristics for a shrouded longitudinal-fin array with tip clearance," *ASME. J. Heat Transfer,* vol. 103, no. 2, pp. 393-395, 1981.

[35] K. S. Lau and R. L. Mahajan, "Effects of tip clearance and fin density on the performance of heat sinks for VLSI packages," *IEEE transactions on components, hybrids, and manufacturing technology,* vol. 12, no. 4, pp. 757-765, 1989.

[36] R. Lee, H. Huang and W. Chen, "A thermal characteristic study of extruded-type heat sinks in considering air flow bypass phenomenon," in *Sixth Annual IEEE Proceedings Semiconductor Thermal and Temperature Measurement Symposium*, Phoenix, 1990.

[37] K. Azar and C. D. Mandrone, "Effect of pin fin density of the thermal performance of unshrouded pin fin heat sinks," *Journal of Electronic Packaging, Transactions of the ASME,* vol. 116, no. 4, pp. 306-309, 1994.

[38] H. Shaukatullah and M. A. Gaynes, "Effect of pin fin heat sink size on thermal performance of surface mount plastic quad flat packs," in *Proc. 1994 Int. Electronics Packaging Conference*, Atlanta, 1994.

[39] C. L. Chapman, S. Lee and B. L. Schmidt, "Thermal performance of an elliptical pin fin heat sink," in *Proceedings of 1994 IEEE/CHMT 10th Semiconductor Thermal Measurement and Management Symposium (SEMI-THERM)*, San Jose, CA, USA, 1994.

[40] H. Jonsson and B. Moshfegh, "Modeling of the thermal and hydraulic performance of plate fin, strip fin, and pin fin heat sinks - Influence of flow bypass," *IEEE Transactions on Components and Packaging Technologies,* vol. 24, no. 2, pp. 142-149, 2001.

[41] H. Jonsson and B. Palm, "Thermal and hydraulic behavior of plate fin and strip fin heat sinks under varying bypass conditions," in *IEEE Transactions on Components and Packaging Technologies*, 2000.

[42] E. R. Simons, "A simple method to estimate heat sink air flow bypass," *Electronics Cooling,* 1997.

[43] M. A. Butterbaugh, "Effect of airflow bypass on the performance of heat sinks in electronic cooling," *Advances in Electronic Packaging.,* vol. 10, no. 2, pp. 843-848, 1995.

[44] A. Barrett and I. Obinelo, "Characterization of longitudinal fin heat sink thermal performance and flow bypass effects through CFD methods," in *Thirteenth Annual IEEE. Semiconductor Thermal Measurement and Management Symposium*, 1997.

[45] Y. Sata, H. Iwasaki and M. Ishizuka, "Development of prediction technique for cooling performance of finned heat sink in uniform flow," IEEE Transactions on Components, Packaging, and Manufacturing Technology: Part A, 1997.

[46] I. F. Obinelo, "Characterization of thermal performance of longitudinal fin heat sinks for system level modeling using CFD Methods," in *Proceedings of the ASME International, Intersociety and Photonic Packaging Conference and Exhibition*, Hawaii, 1997.

[47] A. Radmehr, K. M. Kelkar, P. Kelly, S. V. Patankar and S. S. Kang, "Analysis of the effect of bypass on the performance of heat sinks using flow network modeling (FNM)," in *Fifteenth Annual IEEE Semiconductor Thermal Measurement and Management Symposium (Cat. No. 99CH36306)*, 1999.

[48] S. Prstic, M. Iyengar and A. Bar-Cohen, "Bypass effect in high performance heat sinks," in *Thermal Sciences 2000. Proceedings of the International Thermal Science Seminar*, Connecticut, 2000.

[49] H. Jonsson and B. Moshfegh, "Modeling of the thermal and hydraulic performance of plate fin, strip fin, and pin fin heat sinks-influence of flow bypass," in *IEEE Transactions on Components and Packaging Technologies*, 2001.

[50] E. M. Sparrow and C. F. Hsu, "Analytically determined fin-tip heat transfer coefficients," *ASME. J. Heat Transfer,* vol. 103, no. 1, pp. 18-25, 1981.

[51] R. A. Wirtz, W. Chen and R. Zhou, "Effect of flow bypass on the performance of longitudinal fin heat sinks," *ASME. J. Electron. Packag,* vol. 116, no. 3, pp. 206-211, 1994.

[52] W. Leonard, P. Teertstra, J. R. Culham and A. Zaghol, "Characterization of heat sink flow bypass in plate fin heat sinks," *ASME International Mechanical Engineering Congress and Exposition,* vol. 36363, pp. 189-196, 2002.

[53] C. B. Coetzer and J. A. Visser, "Compact modeling of forced flow in longitudinal fin heat sinks with tip bypass," *Journal of Electronic Packaging,* vol. 125, no. 3, pp. 319-324, 2003.

[54] J. Y. Min, S. P. Jang and S. J. Kim, "Effect of tip clearance on the cooling performance of a microchannel heat sink," *International Journal of Heat and Mass Transfer,* vol. 47, no. 5, pp. 1099-1103, 2004.

[55] M. B. Dogruoz, A. Ortega and R. V. Westphal, "A model for flow bypass and tip leakage in pin fin heat sinks," *Journal of Electronic Packaging,* vol. 128, no. 1, p. 53, 2006.

[56] W. A. Khan and M. M. Yovanovich, "Effect of Bypass on Overall Performance of Pin-Fin Heat Sinks," *Journal of Thermophysics and Heat Transfer,* vol. 21, no. 3, pp. 562-567, 2007.

[57] R. Hossain, J. R. Culham and M. M. Yovanovich, "Influence of bypass on flow through plate fin heat sinks," *Twenty-Third Annual IEEE Semiconductor Thermal Measurement and Management Symposium,* pp. 220-227, 2007.

[58] S. F. Tsai and T. W. H. Sheu, "Some physical insights into a two-row finned tube heat exchanger," *Computers & Fluids,* vol. 27, no. 1, pp. 29-46, 1998.

[59] K. Kritikos, C. Albanakis, D. Missirlis, Z. Vlahostergios, A. Goulas and P. Storm, "Investigation of the thermal efficiency of a staggered elliptic-tube heat exchanger for aeroengine applications," *Applied Thermal Engineering,* vol. 30, pp. 130-142, 2010.

[60] C. W. Lu, J. M. Huang, W. C. Nien and C. C. Wang, "A numerical investigation of the geometric effects on the performance of plate finned-tube heat exchanger," *Energy Conversion and Management,* vol. 52, no. 3, pp. 1638-1643, 2011.

[61] Tala, J. V. S. Russeil, S. Bougeard and D. Harion, "Numerical analysis of the fin spacing effect on the horseshoe vortex system evolution in a two-rows finned-tube heat exchanger," *International Journal of Numerical Methods for Heat and Fluid Flow,* vol. 23, no. 7, pp. 1136-1154, 2013.

[62] F. R. Menter, "Two-equation eddy-viscosity turbulence models for engineering applications," *AIAA Journal,* vol. 8, no. No.8, pp. 1598-1605, 1994.

[63] D. C. Wilcox, "Reassessment of the scale-determination equation for advanced turbulence model," *AIAA Journal,* vol. 26, no. 11, pp. 1299-1310, 1988.

[64] P. G. Huang, P. Bradshaw and T. J. Coakley , "Assessment of closure coffiecient for compressible-flows turbulence models," NASA TM-103882, March 1992.

[65] F. Menter, "Influence of freestream values on k-omega turbulence model predictions," *AIAA Journal,* vol. 30, no. 6, pp. 1657-1659, 1992.

[66] J.-M. Huang, W.-C. Hsieh, X.-J. Ke and C.-C. Wang, "The effects of frost thickness on the heat transfer of finned tube heat exchanger subject to the combined influence of fan types," *Applied Thermal Engineering,* vol. 28, pp. 728-737, 1 5 2008.

[67] M. Fiebig, A. Gorsse-Georgemann, Y. Chen and N. K. Mitra, "Conjugate heat transfer of a finned oval tube part B: heat transfer behaviors," *Numerical Heat transfer, Part A Applications,* vol. 33, no. 4, pp. 387-401, 1998.

[68] S. R. Philippe and C. L. Rumsey, "Effective Inflow Conditions for Turbulence Models in Aerodynamic Calculations," *American Institute of Aeronautics and Astronautics,* vol. 45, no. 10, pp. 2544-2553, 2007.

[69] U. Gross, "Reflux condensation heat transfer inside a closed loop thermosyphon," *International Journal of Heat and Mass transfer,* vol. 35, no. 2, pp. 279-294, 1992.

[70] M. Nacer-Bey, S. Russeil and B. Baudoin, "PIV visualizations ot the flow structure upstream of the tubes in a two-rows plate-fin-and-tube heat exchanger," *Proceeding of 4th International Conference on Compact Heat Exchangers and Enhancement Technology for the Process Industries,* vol. 3, pp. 63-68, 2003.

[71] G. A. F. Seber, Nonlinear Regression, The Wiley-Interscience Paperback Series, 2015, pp. 117-128.

[72] K. Steiros and M. Hultmark, "Drag on flat plates of arbitrary porosity," *Journal of Fluid Mechanics,* vol. 853, p. R3, 2018.